Characterization of a Unique Mouse Model of Multiple Myeloma and its Use as a Preclinical Testing Platform for Novel Inhibitors of the Mevalonate Pathway to Target Multiple Myeloma

Mònica Gómez Palou

Division of Experimental Medicine

Department of Medicine

McGill University

Montréal, Québec

August 2018

A thesis submitted to McGill University in partial fulfillment of the requirements of the degree of Doctor of Philosophy

Abstract

Multiple Myeloma (MM) is a hematological disorder characterized by malignant proliferation of plasma cells in the bone marrow. MM related bone disease is the most challenging feature that MM patients suffer. MM mouse models are essential in order to study MM biology and the mechanisms behind MM bone disease.

This thesis presents a novel mouse model of MM and MM bone disease, the Vk*MYC/KaLwRij model. The goal was to generate a model that presents earlier disease onset and higher burden and that develops MM bone disease similar to the one observed in MM patients. Results showed that Vk*MYC/KaLwRij mice secrete monoclonal protein (M-protein) in the same manner that MM patients do and the levels increase as the mice age. In addition, treatment of Vk*MYC/KaLwRij mice with bortezomib, a drug clinically used in MM, decreased MM disease burden in all Vk*MYC/KaLwRij mice tested. Micro-CT results showed an abnormal trabecula architecture in aged Vk*MYC/KaLwRij and histological analysis revealed decreased numbers of active osteoblasts and osteoclasts in the bone marrow of these mice. Significant increased levels of osteoprotegerin (OPG) in serum were observed in the model which may cause the bone forming unit to be unbalanced leading to the characteristic bone disease observed. Finally, mesenchymal stem cells (MSCs) isolated from the Vk*MYC/KaLwRij mice presented an impairment in their differentiation towards osteoblasts. RNA sequencing of the MSCs revealed an enrichment in inflammatory pathways which may cause the improper differentiation of these cells in this model.

Bisphosphonates (BPs) are the mainstay of treatment for MM bone disease and this thesis presents the design and testing of novel bisphosphonate-like compounds that inhibit the geranylgeranyl pyrophosphate synthase (GGPPS) in the mevalonate pathway. These compounds showed improved pharmacological properties and higher potency targeting MM disease. GGPPS inhibitors are effective in blocking *in vitro* proliferation of MM cells and they do so by blocking protein prenylation in the MM cells. In addition, increased endoplasmic reticulum stress and activation of the unfolded protein response was shown as a consequence of the GGPPS inhibition. Finally, these novel compounds were tested in the Vk*MYC/KaLwRij mouse model and reduction of M-protein in the serum was observed, as well as downregulation of Rap1A geranylgeranylation.

The final part of this thesis presents data on genetically knocking-down GGPPS and farnesyl pyrophostate synthase (FPPS) in a MM cell line. The goal was to validate GGPPS as a target and

to generate a new MM cell line that lacks the expression of this enzyme. shRNA and CRISPR/Cas9 were used to accomplish this goal and high levels of knock-down were shown (80%) using both strategies. Geranylgeraniol (GGOH) can rescue the pathway and protect cells from apoptosis when there is GGPPS knock-down. However, shRNA knock-down of GGPPS was not stable over time and a new cell line was created with GGPPS knock-out using CRISPR/Cas9. This new cell line will be a very useful tool to further validate GGPPS as a target and to study the inhibition of the mevalonate pathway and its importance in MM.

In summary, this thesis presents a full characterization of a novel mouse model of MM and a detailed analysis of its bone disease. In addition, work was published on the first GGPPS inhibitors that are able to inhibit MM cell proliferation *in vitro* and *in vivo* providing a valuable therapeutic target in oncology, specifically in MM. Finally, genetic validation of GGPPS was done using shRNA and CRISPR/Cas9 technology to further understand the mechanism of action of these novel BPs and the involvement of the mevalonate pathway in cancer biology.

Resumé

Le myélome multiple (MM) est une maladie hématologique caractérisée par une prolifération maligne des plasmocytes dans la moelle osseuse. La caractéristique qui présente le plus grand défi aux patients qui souffrent de MM est la maladie osseuse liée au MM. Les modèles murins (souris) MM sont essentiels pour permettre l'étude de la biologie et des mécanismes derrière la maladie osseuse MM.

Cette thèse présente un modèle murin novateur de MM et de la maladie osseuse MM, le modèle Vk*MYC/KaLwRij. L'objectif était de créer un modèle qui présente la survenue précoce de la maladie – en l'occurrence un cas grave – et qui développe une maladie osseuse de MM semblable à celle que l'on observe chez les patients MM. Les résultats démontrent que les souris Vk*MYC/KaLwRij sécrètent la protéine monoclonale de la même façon que les patients MM et que ces niveaux s'élèvent avec l'âge chez les souris. De plus, la charge corporelle de la maladie a diminué chez toutes les souris Vk*MYC/KaLwRij testées qui ont reçu un traitement de bortézomib, un médicament dont on se sert en clinique pour traiter le MM. Les résultats du micro CT-scan montrent une architecture anormale de la trabécule chez les Vk*MYC/KaLwRij âgées et une analyse histologique révèle une diminution du nombre d'ostéoblastes et d'ostéoclastes actifs dans la moelle osseuse de ces souris. Dans ce modèle, des niveaux considérablement plus élevés de OPG ont été observés dans le sérum, ce qui pourrait causer un déséquilibre de l'unité qui forme les os, aboutissant à la maladie osseuse caractéristique observée. Enfin, les cellules souches mésenchymateuses (CSM) isolées des souris Vk*MYC/KaLwRij montrent une déficience au niveau de leur différentiation vers les ostéoblastes. Les séquences ARN des CSM révèlent un enrichissement des voies inflammatoires qui pourrait causer une différentiation inappropriée des cellules de ce modèle.

Les bisphosphonates (BP) sont le traitement de base pour la maladie osseuse MM et cette thèse montre la conception et le testage de composés novateurs ressemblant aux bisphosphonates qui bloquent la synthase géranylgéranyl diphosphate (SGGDP) dans la voie mévalonate. Ces composés présentent des propriétés pharmacologiques améliorées et une plus grande activité thérapeutique qui cible la maladie MM. Les inhibiteurs SGGDP bloquent la prolifération des cellules MM *in vitro* d'une façon efficace en bloquant la prénylation de la protéine dans les cellules MM. De plus, une augmentation du stress du réticulum endoplasmique et l'activation de la réaction

de la protéine dépliée ont été montrées comme conséquence de l'inhibition de la SGGPP. Finalement, des tests avec ces nouveaux composés furent effectués sur des souris Vk*MYC/KaLwRij et une réduction de la protéine monoclonale dans le sérum fut observée, ainsi qu'une régulation négative de la géranylgéranylation Rap1A.

La dernière partie de cette thèse présente les données préliminaires sur le « knocking-down » génétique de la SGGPP dans une lignée cellulaire MM. Le but était de valider la SGGPP en tant que cible et de générer une nouvelle lignée cellulaire MM dépourvue de l'expression de cette enzyme. Deux stratégies furent utilisées pour atteindre cet objectif : shRNA et CRISPR/Cas9. Dans les deux cas, des niveaux élevés de « knock-down » furent atteints (80 %). Géranylgéraniol (GGOH) peut sauver la voie et prévenir l'apoptose des cellules lorsque le « knock-down » de la SGGPP se produit. Toutefois, le « knock-down » shRNA de la SGGPP n'était pas stable avec le temps et une nouvelle lignée de cellules fut créée avec un « knock-out » SGGPP à l'aide de CRISPR/Cas9. Cette nouvelle lignée cellulaire s'avérera un outil très utile qui fera avancer la validation de la SGGPP en tant que cible et pour étudier l'inhibition de la voie mévalonate et son importance dans le MM.

En résumé, cette thèse présente une caractérisation complète d'un modèle murin novateur de MM et une analyse détaillée de la maladie osseuse liée à MM. De plus, une étude a été publiée sur les premiers inhibiteurs de la SGGPP qui arrivent à inhiber la prolifération MM *in vitro* et *in vivo*, fournissant une cible thérapeutique importante en oncologie, particulièrement en ce qui concerne MM. Et enfin, la validation génétique de la SGGPP a été faite à l'aide de la technologie shRNA et CRISPR/Cas9, pour permettre de mieux comprendre le mécanisme de l'action de ces BP innovateurs et le rôle du la voie mévalonate dans la biologie du cancer.

Acknowledgments

I arrived in Montreal on a very cold February in 2013 and I was very lucky to get a position in Dr. Sebag's laboratory. Although I did not start my PhD until September this was where this adventure started.

First and foremost, I want to thank my supervisor Dr. Michael Sebag for giving me the opportunity to work in his laboratory. I was very new to research back then so I am very grateful for his support and for believing in me since the beginning. It has been a long journey and I feel I have become a better and more confident researcher thanks to the years of hard-work. There have been very few set-backs during these years but on each occasion Dr. Sebag was very reassuring and gave me the confidence to continue and not give up.

There are a few more people I want to thank for being there with me during these 5 years. Fang, I met you on the first day of being in the laboratory and you were so welcoming and patient teaching me. I think we have become a bit of a team as time passed by and for that I am extremely happy. We have been able to rely on each other on testing moments but we have also been able to celebrate the good times. I would also like to thank you Dan. You have taught me so much during the last 4 years (new techniques, tips, tricks, so much knowledge!) and I want to thank you for always answering everything, every question, email and text message I have sent you. Who knows how many of those we have exchanged after all this time. I hope we can keep in touch after finishing the PhD because I feel I will continue to have questions for you.

Next, it is time to thank everybody else I have met during these years and it is a lot of people. Karina, you were one of the first friends I had at the Royal Victoria and I am so happy that we met. We have been through a lot during our degrees and I wouldn't change any of that for the world. We have studied together, trained together, celebrated together, moved to a new hospital together, traveled together and hopefully we will finish the PhDs together. What a great time it has been. And Yassemine and Cristiana, I am so lucky to have met you and shared so many good times together, mostly eating events (lunches, second lunches, dinners at your place with amazing food, parties, etc.). I am sure that we will have so many more adventures the four of us and I can't wait for it.

I would also like to mention all the people I met while I was part of the EMGSS council. Being part of that council was something very new but I met some amazing and very driven people that

became in the end very good friends during my PhD. I am very thankful that I got to meet all of you.

I ara és el moment de dir gràcies a unes persones i animalets molt especials per a mi. El pare, la mare, la Marta, l'Stephane, la Buffy i la Fosca. Tots heu estat part d'aquest doctorat des del primer dia i sense vosaltres no podria haver arribat fins aquí. Al pare i la mare, gràcies per tot el que heu fet per mi tots aquests anys, m'heu ensenyat a ser forta i m'heu servit d'exemple per entendre com ser independent i treballadora. Moltes gràcies per escoltar-me en moments bons i dolents durant totes les xerrades telefòniques, skype, facetimes, messengers que hem fet durant aquests anys, han estat moltes! A la Marta, l'Stephane i la Fosqueta els hi vull donar les gràcies per ser els primers en adoptar-me quan vaig venir a Canadà. Vosaltres vau ser la meva segona família i vull agrair tots els consells i ajuda que m'heu donat durant aquests anys. Ens ho hem passat molt i molt bé i ara amb el Quim i el Ferran encara més!

També vull donar les gràcies a les amigues de Barcelona, Mireia, Ana, Míriam, Ángela, Laura i Anna. Se que he estat lluny durant aquests anys però em sabut mantenir el contacte i cada any que ens hem vist durant el doctorat ha estat una alegria. Sense el vostre suport i entusiasme el llarg camí d'aquest doctorat hagués estat més complicat.

Finally, I want to thank you Matt. I should start by mentioning the great summer we had when we first met playing softball. It took us a while to find each other after that summer but ChemEng events here and there plus all the dragon boating brought us together again. Thank you for all the support and laughs and love, it has been a very special year. I am so happy that we are finishing together our PhDs and I am looking forward to all the good things that are to come.

Table of Contents

List of Figures

List of Tables

Contributions of Authors

This thesis is presented and organized as a manuscript-based document composed of three manuscripts and the contributions of each author are stated below.

CHAPTER 2: ENDOGENOUS OPG EXPRESSION BY PLASMA CELLS INHIBITS THE BONE PHENOTYPE IN A TRANSGENIC MURINE MODEL OF MULTIPLE MYELOMA

This paper has been submitted to the Journal of Clinical Investigation. The author of this thesis contributed to the design of all the experiments performed in this manuscript with the supervision of Michael Sebag. Furthermore, all the experimental assays of this manuscript were entirely performed by the author of this thesis. Daniel D. Waller contributed with advice on the design of experimental assays and interpretation of results. Xian Fang Huang took care of the mouse colony and was in charge of ordering all products necessary for the assays. Radia Johnson performed the bioinformatic analysis of the RNA sequencing data. Richard Kremer and Daniel D. Waller helped reviewing the final manuscript. The author of this thesis and Michael Sebag wrote the manuscript. Funding acquisition and supervision was performed by Michael Sebag.

CHAPTER 3: UNRAVELING THE PRENYLATION-CANCER PARADOX IN MULTIPLE MYELOMA WITH NOVEL GGPPS INHIBITORS

This paper has been published in the Journal of Medicinal Chemistry. The work on this article was a collective effort between several research groups. Cyrus M Lacbay, Daniel D. Waller and the author of this thesis contributed equally to this article (co-first authors). Synthesis of the library of compounds and *in vitro* evaluation was performed by Cyrus M. Lacbay. Hematology, cellular and *in vivo* experiments were designed and coordinated by Michael Sebag. All biological studies were performed by the author of this thesis, Daniel D. Waller, and Xian Fang Huang. These include *in vitro* proliferation assays, study of apoptosis, protein immunoblotting and DNA electrophoresis as well as all *in vivo* experiments. Cloning, protein production and crystallography were performed by Jaeok Park, Viviane Ta and Albert M. Berghuis. DSF and bone affinity studies were performed by Félix Vincent. The author of this thesis also contributed in the writing of the materials and methods section of the manuscript. Conceptualization and coordination of the execution and the interpretation of the experiments was performed by Youla S. Tsantrizos. Michael Sebag and Youla

S. Tsantrizos wrote and revised the manuscript. Funding acquisition and supervision was performed by Youla S. Tsantrizos, Michael Sebag and Albert M. Berghuis.

CHAPTER 4: GGPPS AND FPPS KNOCK-DOWN AND KNOCK-OUT WITH SHRNA AND CRISPR/CAS9

This paper is in the early phases of preparation to be submitted. The author of this thesis contributed to the design and performed all the cellular and bacterial biology experiments presented in this manuscript with the supervision of Michael Sebag. Daniel D. Waller contributed designing the primers used for genetic validation in shRNA experiments. Daniel D.Waller also designed the RNA guide sequences and inserted them in competent stable cells for the use of CRISPR/Cas9 strategy. Xian Fang Huang took care ordering all products necessary for the assays. Daniel D. Waller helped reviewing the final manuscript. The author of this thesis and Michael Sebag wrote the manuscript. Funding acquisition and supervision was performed by Michael Sebag.

List of Abbreviations

AID – Activation induced deaminase

ALL – Acute lymphoblastic leukemia

ALP – Alkaline phosphatase

ASCT – Autologous stem-cell transplant

ASCT – Hematopoietic stem cell transplant

ATCC – American Type Culture Collection

ATP – Adenosine triphosphate

BAFF – B-cell activating factor

BCMA – B-cell maturation antigen

BM – Bone marrow

BMECs – Bone marrow endothelial cells

BMP – Bone morphogenetic protein

BMSCs – Bone marrow stromal cells

BMUs – Basic multicellular units

BPs - Bisphosphonates

CAR-T cells – Chimeric antigen receptor T-cells

CSR – Class switch recombination

CTX – C-terminal telopeptide

DKK – Dickkopf-1

DKK1 - Dickkopf-1

DMSO – Dimethyl sulfoxide

ECM – Extracellular matrix

ELISA – Enzyme-linked immunosorbent assay

ER – Endoplasmic reticulum

FGF – Fibroblast growth factor

FPP – Farnesyl pyrophosphate

FPPS – Farnesyl diphosphate synthase

Fzd - Frizzled

GAGE – Generally applicable gene set enrichment

GGOH - Geranylgeraniol

GGPP – Geranylgeranyl pyrophosphate

GGPPS – Geranylgeranyl pyrophosphate synthase

GTPases – GTP-binding proteins

HGF – Hepatocyte growth factor

HSC – Hematopoietic stem cell

HSC – Hematopoietic stem cells

IGF1 – Insulin-like growth factor 1

IL6 – Interleukin 6

IMiDs – Immunomodulatory drugs

JAK/STAT – Janus kinase/signal transducers and activators of transcription

LRP – Lipoprotein receptor-related protein

MAPK – Mitogen-activated protein kinase

M-CSF - Colony-stimulatory factor

MGUS – Monoclonal Gammopathy of Undetermined Significance

MIP1α - Macrophage inflammatory protein

MM – Multiple Myeloma

MSCs – Mesenchymal stem cells

N-BP – Nitrogen-containing bisphosphonates

NCI – National Cancer Institute

NF-κB – Nuclear factor kappa-light-chain enhancer of activated B cells

NOD/SCID – Non-obese diabetic/Severe combined immunodeficiency

NTX – N-terminal telopeptide

OCN - Osteocalcin

ONJ – Osteonecrosis of the jaw

OPG - Osteoprotegerin

PBMC – Peripheral mononuclear cell

PCR – Polymerase chain reaction

PCT - Plasmacytoma

PFA - Paraformaldehyde

PI3/AKT – Phosphoinositide-3-kinase and protein kinase B

PIs – Proteasome Inhibitors

PTHrP – Parathyroid hormone-related protein

KD – Knock-down

KO – Knock-out

qRT-PCR or qPCR – Quantitative reverse transcription PCR

RANK – Receptor activator of NF-κB

RANKL – Receptor activator of NF-κB ligand, TRANCE or TNFSF11

RUNX2 – Runt-related transcription factor 2

SCID – Severe combined immunodeficiency

SDF1α - Stromal cell-derived factor 1 alpha

sFRP – Secreted frizzled-related protein

SHM – Somatic hypermutation

SMM – Smoldering Multiple Myeloma

SOST - Sclerostin

SPEP – Serum protein electrophoresis

SREs – Skeletal related events

TGF-β - Transforming growth factor beta 1

ThP-BP - Thienopyrimidine-based bisphosphonate

TNF – Tumor necrosis factor

TNFα - Tumor necrosis factor alpha

TRACP – Tartrate-resistant acid phosphatase

UPR – Unfolded protein response

VEGF – Vascular endothelial growth factor

XBP-1 – X-box binding protein 1

ZOL - Zoledronate

μCT – Micro computed tomography

CHAPTER 1. INTRODUCTION

1.1. Overview of Multiple Myeloma

Multiple Myeloma (MM) is a B-cell malignancy characterized by the clonal expansion of malignant plasma cells in the bone marrow and it is the second most common hematological malignancy[1]. MM is associated with monoclonal immunoglobulin protein secretion by abnormal plasma cells (also known as M protein or monoclonal protein). The clinical manifestations of MM known as CRAB are caused by the monoclonal protein accumulation and they include signs of end-organ damage, such as hyperCalcemia, Renal insufficiency, Anemia, and/or Bone disease with lytic lesions[1].

Monoclonal Gammopathy of Undetermined Significance (MGUS) is known as a premalignant plasma-cell proliferative stage characterized by infiltration of clonal plasma cells into the bone marrow and the secretion of M protein. MGUS is asymptomatic and consistently precedes the development of MM. Approximately 15% of MGUS patients will progress to MM over 25 years[2]. The diagnosis of MGUS, smouldering multiple myeloma (SMM, intermediate state that presents a much higher risk of progression to MM) and MM requires the detection of serum monoclonal protein levels, assessment of the bone marrow and myeloma-defining events (including biomarker assessment and the presence or absence of CRAB features) (**Table 1.1**).

Table 1-1: International Working Group Criteria for the Diagnosis of Multiple Myeloma[1]

Feature	**MGUS**	**SMM**	**Multiple Myeloma**
Serum monoclonal protein levels	<3 g per dl and	≥3 g per dl and/or	-
Clonal BMPC infiltration*	<10%	10-60%	≥10% or a biopsy-proven plasmacytoma‡
Symptomatology	Absence of CRAB features	Absence of MDE or amyloidosis	Presence of MDE

*The clonality of BMPCs has to be established by restriction of the light chain, kappa or lambda, by flow cytometry, immunohistochemistry or immunofluorescence. Assessing the infiltration of these cells into bone marrow should be done by morphology, either in the aspirate or biopsy. ‡If the BMPC infiltration is <10%, more than one lytic lesion is required to confirm a diagnosis of multiple myeloma.

1.1.1. Epidemiology of MM

Multiple Myeloma is the second most common lymphoid malignancy in adults and it represents 1% of all cancers. MM incidence is highest in more developed countries, such as the United States, western Europe and Australia (availability of better diagnostic techniques might be a contributing factor). In 2017, 2,900 Canadians were diagnosed with MM (7.1 cases/100,000) and it affected slightly more men than women. In addition, incidence of MM is 2-3 times higher in African-American individuals than in caucasian individuals and is lower in Asian and Hispanic populations[3,4]. The median age of patients at diagnosis is approximately 66-70 years with 37% of patients being younger than 65 years of age.

In the past decade, MM survival rates have improved significantly with the largest increase between 2006 and 2008[5]. Collaborative research has led to an improvement in the understanding of the monoclonal gammopathies, including a better knowledge of the mechanisms underlying MM disease and the introduction of novel and more effective therapies. Autologous stem cell transplants as well as modern therapies such as immunomodulatory drugs (IMiDs) and proteasome inhibitors (PIs) have led to a tremendous improvement in the survival of MM patients[5,6].

1.1.2. Mechanism of Development of MM Disease

1.1.2.1. The Biology of Normal and Malignant Plasma Cells

In order to define how MM develops it is essential to have a proper insight into B cell development and plasma cell biology. Hematopoietic stem cells (HSC) are the precursor cells to B cells and subsequently plasma cells and they undergo several rounds of differentiation in the bone marrow and lymph nodes to become mature plasma cells. Pre-B cells undergo functional V(D)J (variable (V), diversity (D), and joining (J) gene segments) rearrangements of *IGH* (immunoglobulin heavy chain) and *IGL* (immunoglobulin light chain) genes in the bone marrow to generate immature B cells that express functional Ig on the cell surface. Next, these cells exit the bone marrow as mature B cells and home to the secondary lymphoid tissues. Mature B cells are exposed to antigen that stimulates the formation of a lymphoblast which differentiates into a non-switched (IgM), or switched (IgG, IgA, IgE, or IgD) plasma cell. Later in the immune response, the lymphoblast enters the germinal center, where it undergoes somatic hypermutation (SHM) of its *IGH* and *IGL* genes, and antigen selection of cells with high affinity Ig receptor[7]. The enzyme in charge of initiating diversity in V(D)J and heavy chain genes is known as activation induced deaminase (AID), which

is a cytosine deaminase that enzymatically converts cytosine to uracil[8]. The production of the secondary, or memory, repertoire of antibodies in mature B cells is produced thanks to class-switch recombination (CSR) and it occurs after antigen binds to the receptor, which initiates a cascade of signaling events that cause cellular activation[8]. The result of this activation is the differentiation of B cells into plasma or memory cells, which now express a large repertoire of antibodies to clear different foreign antigens. Finally, these plasma cells home to the bone marrow where they differentiate into a long-lived plasma cell[8].

The initial event that leads to the development of MM is thought to occur in the germinal center with the introduction of double-strand DNA breaks in the immunoglobulin loci during somatic hypermutation and class-switch recombination. These breaks lead to fusions with other DNA breaks in the genome. Although most of these breaks and fusions are inconsequential as these cells do not produce progeny, translocations that involve specific oncogenes can give cells a growth advantage, which could lead to the development of MGUS, SMM and eventually MM. The incidence of translocations increases with the stage of disease: 50% in MGUS, 60-65% in MM, 70-80% in extramedullary MM, and >90% in MM cell lines[9,10].

1.1.2.2. Chromosomal Defects and Secondary Mutations

Translocations that involve IgH represent an important group of primary events identified in MGUS, SMM and MM[11]. Translocation t(11;14) is found in 14% of all MM patients which results in increased expression of *CCND1*, whose product, cyclin D1, is important for cell cycle progression. Furthermore, translocation t(4;14) can be found in 11% of MM patients which upregulates *NSD2* and *FGFR3.* Additional translocations such as t(14;16), t(14;20) and t(6;14) that involve IgH can also be found though in lower percentages. The different MM subgroups are associated with different levels of aggressiveness and with different prognoses. For example, it has been reported that the median progression from SMM to MM is shorter in patients with t(4;14) than in patients with t(11;14) which suggests that t(4;14) cases might suffer a secondary event at a higher rate than t(11;14) cases. It is especially important to define risk status if high risk cases are to be managed appropriately because of their aggressive clinical course, high rates of early relapse and the need to maintain therapeutic pressure on the clone[11].

Secondary or later oncogenic events in MM pathogenesis include frequently occurring mutations such as *KRAS* (in 23% of patients), *NRAS* (20%), *FAM46C* (11%), *DIS3* (11%) and *TP53* (8%).

Other less frequent but recurrently mutated genes are *BRAF*, *TRAF3*, *PRDM1*, *CYLD*, *RB1*, *IRF4*, *EGR1*, *MAX*, *HIST1H1E* and *ACTG1*[12]. In addition, it has been reported that although c-*MYC* is dysregulated by primary translocations in some B-cell malignancies, it is dysregulated by secondary translocations as myeloma tumors become more proliferative and at later stages of progression (observed in up to 45% of patients with advanced MM). In addition, recent NGS studies have shown that *MYC* translocations occur in early stages of the disease as well. Dysregulation of *MYC* is also very often observed in cell lines and is characterized by a different structure at the underlying breakpoints[13,14].

The high variety in the number of primary and secondary events that lead to MM makes it a very challenging disease to treat. In some patients there is no change in the subclonal composition found at diagnosis and at relapse, suggesting that different subclones have responded in a similar way to the treatment[15]. However, there are also cases where the subclones have changed after treatment and one clone has become more dominant than another. The presence of these subclones has consequences for treatments that target the mutated protein[15]. There are several mutations that are targetable such as *BRAF* mutation but it is very challenging to create a strategy that is capable of destroying all malignant clones at once, some of which may not harbor the target mutation[15].

1.1.3. Role of the Bone Marrow Microenvironment in MM

The bone marrow microenvironment is a very complex system and has a crucial role in MM development, therefore it is acquiring primary interest as a pathogenic factor in MM. MM growth is largely restricted to this microenvironment. The microenvironment is formed by hematopoietic stem cells, progenitor and precursor cells, immune cells, macrophages, dendritic cells, fibroblasts, erythrocytes, bone marrow stromal cells (BMSCs), bone marrow endothelial cells (BMECs), as well as mesenchymal stem cells (MSCs), osteoclasts and osteoblasts. All these cells interact with myeloma cells and the outcome is enhanced expression and release of cytokines that will activate signaling pathways which mediate growth, survival, drug resistance, cell trafficking and homing of myeloma cells. In addition, myeloma interactions in the bone marrow result in abnormally enhanced osteoclastogenesis and decreased osteoblastogenesis as well as alteration of angiogenesis[16,17].

Some of the factors being secreted by cells comprising the bone marrow microenvironment are interleukin-6 (IL6), insulin-like growth factor 1 (IGF1), vascular endothelial growth factor

(VEGF), B-cell activating factor (BAFF), fibroblast growth factor (FGF), stromal cell-derived factor 1α (SDF1α), and tumor necrosis factor-α (TNFα) and they can be upregulated by tumor cell adhesion to extracellular matrix (ECM) proteins and/or BMSCs[18]. Due to the interaction of myeloma cells with BMSCs and the release of these specific factors there are several important signaling pathways being activated: PI3K/AKT; I kappa B kinase (IKK)/nuclear factor-kappa B (NF-κB); Ras/Raf/mitogen-activated protein kinase (MAPK); mitogen-induced extracellular kinase (MEK)/ERK; Janus kinase (JAK)2/signal transducers and activators of transcription (STAT3)[19]. It is reported that IL6 can activate the JAK2/STAT3 pathway in plasma cells which results in the overexpression of antiapoptotic proteins Bcl-xL and Mcl-1, and inhibition of CD95 (Fas)-induced apoptosis. IL6 also triggers plasma cell proliferation via Ras/Raf/MEK/MAPK cascade. Another molecule involved in proliferation, survival and drug resistance of malignant plasma cells is IGF1. IGF1 can induce these effects in myeloma cells via Ras/MAPK and PI3K/AKT signaling cascades and it is known to be a more potent inducer of AKT signaling and NF-κB than IL6[20,21].

The secretion of these molecules within the bone marrow microenvironment in myeloma patients has severe consequences in drug resistance. For example, both IL6 and IGF1 are involved in resistance against drugs that target PI3K/AKT signaling as well as other cytotoxic chemotherapy and proteasome inhibitors[20,22].

Furthermore, osteoclasts and osteoblasts are cells responsible for bone resorption and formation, respectively. These cell types are in the bone marrow microenvironment and they are affected directly and in-directly by the interaction of the myeloma cells with them as well as with other cell types. The mechanisms by which these cells are affected will be discussed in detail in the Multiple Myeloma Bone Disease section of this introduction.

1.1.4. MM Treatment and Management

A better understanding of myeloma biology has led to several changes in the treatment of MM in the last decade. There are several classes of drugs that are available nowadays and the initial choice of treatment needs thorough consideration.

The initial goals of therapy include:

- Rapid and effective control of multiple myeloma.

- Reversion of complications or symptoms related to multiple myeloma.
- Enable the collection of stem cells in patients who are eligible for autologous hematopoietic stem cell transplantation (ASCT).

Induction therapy is the first phase of treatment in MM and its goal is to reduce the number of plasma cells in the bone marrow and the M-protein produced by these cells. Patients are initially classified according to the risk of disease progression in three groups, standard risk (t(11;14), t(6;14) and trisomies), intermediate risk (t(4;14)) and high risk (del(17p), t(14;16) and t(14;20)). All patients receive induction therapy although the regimen can be variable depending on what risk group they are and on the eligibility of the patient for ASCT.

The main factor in eligibility of ASCT is age with most clinical trials limiting this to patients ≤65 years of age. The second factor is the presence of comorbidities such as cardiac and pulmonary disorders or renal insufficiency. And finally, the patient preference to undergo ASCT plays an important part. If the patient is not eligible for ASCT they will continue to receive induction therapy until progression. When patients are eligible for ASCT they receive induction therapy for few months prior to the stem cell collection in order to reduce the number of tumor cells in bone marrow and peripheral blood[23].

Post-induction therapy is the next step in this process. ASCT eligible patients have several options, to receive high dose chemotherapy followed by ASCT, continued therapy reserving ASCT until relapse or high dose chemotherapy followed by allogeneic SCT[21].

Maintenance therapy is usually given after ASCT and it is also used after induction therapy in non ASCT eligible patients. The goal of maintenance therapy is to keep the patient in remission and prevent relapse. Often, maintenance therapy is given in low doses over long periods of time in order to cause fewer side effects and for the patient to have a better quality of life[24].

The development of effective drugs available for the management of multiple myeloma in newly diagnosed patients and in relapsed cases has continued to improve in the last years. The most currently used drugs in MM are proteasome inhibitors, immunomodulatory drugs, monoclonal antibodies, histone deacetylase inhibitors and alkylating agents (**Table 1-2**). Although dexamethasone is not aforementioned groups, it is is part of most combination therapies in MM. Dexamethasone is a steroid that is able to decrease swelling or inflammation and in combination with other chemotherapeutic drugs can target the myeloma disease[9,25].

The initial treatment of choice for patients that can undergo combination therapy is bortezomib plus lenalidomide plus dexamethasone (known as VRd). Other combinations of proteasome inhibitors and immunomodulatory drugs have been evaluated with promising results in progression-free survival in patients that also received ASCT following initial therapy[26]. Additional combinations with proteasome inhibitors and alkylating agents have also been studied[27].

Treatment in patients not eligible for ASCT is focused in the use of melphalan and prednisone. However, in phase 3 clinical trials the combination of these drugs with a proteasome inhibitor and immunomodulatory drugs shows improved progression-free survival. Although these triple combinations are the standard approach there are still patients treated with double drug combinations and for patients non-ASCT eligible treatment approaches can be variable since they depend on the patient characteristics[28].

Table 1-2: Currently used drugs in MM

Proteasome inhibitors	Bortezomib, carfilzomib, ixazomib
Immunomodulatory drugs	Thalidomide, lenalidomide, pomalidomide
Monoclonal antibodies	Daratumumab (anti-CD38), elotuzumab (anti-SLAMF7)
Histone deacetylase inhibitor	Panobinostat
Alkylating agents	Melphalan, cyclophosphamide, bendamustine
Others	Dexamethasone, prednisone, cisplatin, doxorubicin

Unfortunately, most of MM patients eventually relapse and need additional therapy. Because of the number of relapses that the patients go through, the efficacy of the treatments is reduced. This is caused by the increased genomic complexity of the tumor and acquired mutations and epigenetic alterations. For this reason, there are new types of drugs that are being developed in clinical trials such as small molecules and novel immune therapies. Small molecules that are being explored are protein inhibitors, new proteasome inhibitors as well as alkylating agents. And novel immune therapies target CD38, the PD1 and PDL1 checkpoint, CD19 or the B-cell maturation antigen (BCMA). Targeting of CD19 and BCMA is achieved using chimeric antigen receptor (CAR) T cell therapy[29]. There has been great success using this strategy to treat acute lymphoblastic leukemia (ALL) and new research is aiming to extend this treatment to other

hematologic malignancies such as MM. There are additional methods that are being studied for this purpose such as the use of natural killer cells or dendritic cell-based vaccines[29].

Health-related quality of life is a very important factor in MM patients since the features of this disease affect quality of life significantly. The improvement in patient survival has made health-related quality of life an important end point in clinical trials and a factor in treatment decisions[30]. Supportive and palliative care are essential for the improvement of quality of life in these patients and the main goal is to prevent and relief the suffering by treating the pain and other physical and psychosocial issues[31].

1.2. Multiple Myeloma Bone Disease

1.2.1. Biology of Normal Bone Remodeling

Bone disease is the most notable clinical feature of MM and it affects up to 80% of patients with MM. Patients present osteolytic bone lesions at diagnosis and skeletal related events (SREs) that are associated with increased morbidity and mortality[32]. The hallmarks of bone disease in MM are increased osteoclast activity in combination with osteoblast inhibition[33]. Understanding the mechanisms involved in MM bone disease is crucial to advance on the effective management and the improvement in the quality of life of MM patients.

An introduction to normal bone remodeling is necessary in order to better explain how MM bone disease develops in patients. Bone remodeling occurs throughout life and the remodeling process replaces about 5-10% of skeleton each year, with the entire adult skeleton replaced every 10 years[34]. In other words, bone remodeling is the replacement of old bone tissue by new bone tissue. In order to maintain structural integrity bone remodeling is under very tight control. The main cells involved in bone remodeling are osteoblasts and osteoclasts and they carry out bone formation and bone resorption, respectively. There are other cell types involved in bone remodeling such as osteocytes (which act as mechanosensor and as endocrine cells, and are derived from osteoclasts) and the bone lining cell[35]. Bone can be classified as cortical bone or cancellous bone and they present different structures and the mechanism by which they remove and replace are different as well. Cortical bone forms the cortex of most bones and it is much denser than cancellous bone, harder, stronger and stiffer. The cortical bone comprises a cutting zone covered with osteoclasts followed by differentiating osteoblasts, and with the space filled by blood vessels, nerves and

connective tissue. On the other hand, cancellous bone also known as trabecular bone is less dense, softer, weaker and less stiff. Trabecular bone is covered by mesenchymal stem cells, which are the precursor cells to osteoblasts, and with osteoclasts resorbing bone. The resorbed surface is cleaned up by lining cells and macrophages, and osteoblast precursors differentiate to fill the pits of bone that have been resorbed[34].

The bone remodeling process consists of five steps, activation, resorption, reversal, formation and termination. Basic multicellular units (BMUs) are the clusters of cells that are involved in resorption and formation of bone and include osteocytes, osteoblasts and osteoclasts. In normal bone there is a homeostatic equilibrium between resorption and formation so bone is continuously replaced by new tissue. Active BMUs are formed by resorbing osteoclasts which are covering the newly exposed bone. This surface will be covered by osteoblasts which will secrete and deposit unmineralized bone osteoid[36]. The order in which the cells arrange themselves is crucial for proper bone remodeling.

There are many different signals that can trigger the first stage of bone remodeling, activation. These signals can be hormonal (e.g. estrogen or parathyroid hormone) or mechanical. Osteocytes are the cells that will detect any physical forces that cause mechanical strain and/or microdamage to the skeleton. Once the signals have been detected, the bone lining cells retract and the endosteal membrane is digested by the action of collagenase. Next, there is migration of partially differentiated mononuclear preosteoclasts to the bone surface where they form multinucleated osteoclasts. The resorption phase is the next step and is defined by osteoclasts resorbing bone with break down of the bone matrix achieved by secretion of hydrogen ions and enzymes (e.g. cathepsin K). Hydrogen ions lower the pH within the bone resorbing compartment to mobilize bone mineral and in order to digest the organic bone matrix osteoclasts can also secrete other enzymes such as matrix metalloproteinases. The end result is the formation of lacunae on the surface of the trabecular bone. Osteoclasts will undergo apoptosis at the end of this phase[35,37]. After the completion of osteoclastic resorption, there is a reversal phase when mononuclear cells appear on the bone surface. The lacuna not only contains monocytes but also osteocytes and pre-osteoblasts. These cells prepare the surface for new osteoblasts to begin bone formation and provide signals for osteoblast differentiation and migration. There are a number of coupling signals involved in the beginning of bone formation being produced by the bone matrix and factors such as transforming growth factor beta (TGF-β) that are released. At this point, osteoclasts are replaced

by osteoblast cells which initiate bone formation. Osteoblasts will secrete molecules that ultimately form new bone. The main organic component of the newly formed matrix is collagen type I. The remaining part of the matrix is composed of non-collagenous proteins, including proteoglycans, glycosylated proteins and lipids. The termination step is the process of mineralization. Hydroxyapatite will be incorporated together with carbonate, magnesium and acid phosphate. The mineralization process is regulated by phosphoprotein kinases and alkaline phosphatase. In addition, vitamin D indirectly stimulates mineralization of unmineralized bone[38].

1.2.1.1. Osteoblast-Osteoclast Interactions

There are many cytokines and hormones released in the bone marrow microenvironment as well as signaling pathways that when activated contribute to bone remodeling. In the remodeling process, osteoblasts and osteoclasts are in close contact and it is known that they can communicate with each other through direct cell-cell contact, cytokines or by cell-bone matrix contact[39]. The contact between these two cell types vary during the stages of differentiation. Studies have shown that osteoblasts can regulate osteoclast formation and that osteoclasts can affect osteoblast activity[40,41].

It has been reported that osteoblasts can communicate with osteoclasts by direct contact. They can form gap junctions and small water-soluble molecules can passage between the two cell types. There are several inhibitors of osteoclasts that originate from osteoblasts. The best known inhibitor of osteoclastogenesis is osteoprotegerin (OPG) and is secreted by osteoblasts although the major source of OPG is B lymphocytes in the bone marrow. OPG is a decoy receptor that can bind RANKL and block activation of RANK and consequently, inhibit osteoclastogenesis. The RANKL/OPG system plays a major role in MM bone disease and it is described in detail in the next section[42]. In addition, osteoblasts can secrete Ephgb4 and Sema3A which are known to also inhibit osteoclast formation[43,44]. On the other hand, osteoblasts can promote osteoclastogenesis by secretion of RANKL and macrophage colony-stimulatory factor (M-CSF). M-CSF is an important cytokine for survival, differentiation, cell differentiation, cell migration and activity of both macrophages and osteoclasts. It can also enhance the differentiation of bone marrow precursors to osteoclastic precursors. Finally, osteoblasts can also produce monocyte chemoattractant protein-1 (MCP-1) which is a recruiter of osteoclast precursors. When MCP-1 binds to the precursors, they reposition to the bone surface to differentiate into active osteoclasts (**Figure 1-1**)[45].

In the same way that osteoblasts act on osteoclasts, osteoclasts also have effects on osteoblast function and activity. To begin with, sclerostin (SOST) is the best known osteoblast inhibitory molecule secreted by osteoclasts in human long bones and cartilages[46]. Furthermore, its expression was studied on mice at different ages and it was observed that SOST mRNA and protein levels were higher in 24-month old mice compared to 6-week old mice[45]. Another molecule known to be secreted by osteoclasts is semaphorin 4D which potently inhibits bone formation through its receptor plexin-B1 expressed by osteoblasts[47]. MicroRNAs are also shown to regulate osteogenic activity and osteoblastic bone formation. Specifically, MiR-214-3p has been shown to play a crucial role in skeletal disorders. It has been shown that MiR-214-3p is produced by osteoclasts and can affect the osteoblastic bone formation. Further studies are underway to understand better the role of microRNAs and exosomes in bone metabolism[48]. Finally, there are several molecules that can promote osteoblastogenesis such as EphB4 or complement component 3a which stimulate osteoblast differentiation in a co-culture system of osteoblasts and mature osteoclasts (**Figure 1-1**)[40,43].

Under physiological conditions, the resorption and formation of bone remain balanced thanks to all these molecules. However, when this balance is disturbed the bone architecture or function will be abnormal like in MM bone disease[49]. The mechanisms of MM bone disease will be discussed in the next section.

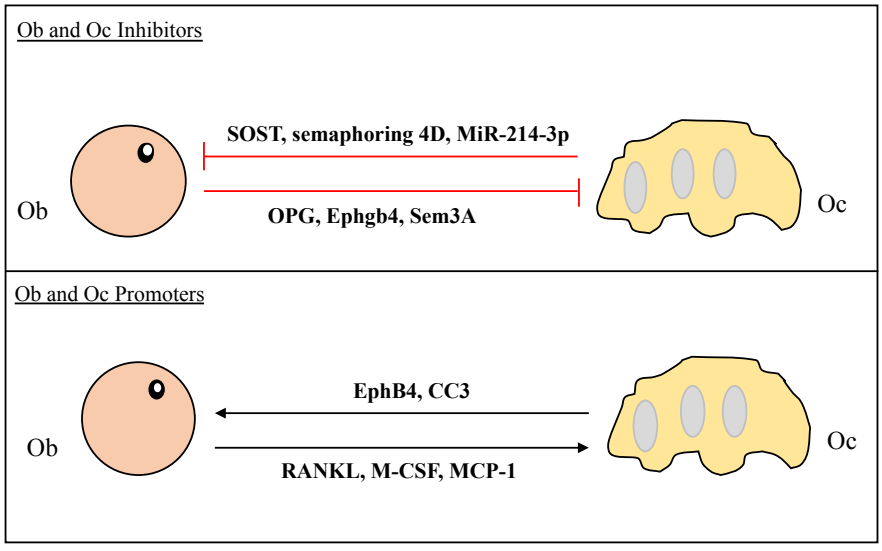

Figure 1-1: Interactions between osteoclasts and osteoblasts

1.2.2. MM Effects on Bone Resorption and Formation

MM bone disease shows in the form of classic discrete lytic lesions, widespread osteopenia, or multiple lytic lesions affecting spine, skull, and/or long bones. The balance of osteoclastic and osteoblastic activity is lost in MM and that is the basis for the pathogenesis of myeloma-related bone disease. It is the interaction between myeloma cells and the bone marrow microenvironment that leads to the activation of osteoclasts and suppression of osteoblasts, resulting in bone destruction. There are many signaling pathways that are implicated in this complex process and they will be discussed in this section[50].

It has been observed that osteolytic lesions appear in areas adjacent to myeloma cells which suggests that myeloma cells are releasing factors that stimulate osteoclastic activity to resorb bone and additionally, inhibit osteoblastic activity. The increased osteoclastic activity leads consequently to an increase in growth factors being released that will in turn increase growth in MM cells in a vicious cycle. There are several cytokines involved both in the activation of osteoclasts and inhibition of osteoblasts. In addition, the cell-cell interactions between myeloma cells and cells from the microenvironment will also increase the release of additional molecules that will feed into the unbalance in the bone forming and resorbing unit[51].

1.2.2.1. Mechanisms Behind the Increased Osteoclast Activity in MM

Osteoclasts are multinucleated cells that originate from monocytic cell lineage. Osteoclasts main function is bone resorption and there exist several markers to quantify their function. Markers of bone resorption that can be quantified are collagen cross-links, telopeptides of type I collagens (CTX, NTX) and tartrate-resistant acid phosphatase (TRACP 5b). In addition, osteoclasts can release cathepsins (e.g. cathepsin K) which are the most important proteases involved in bone resorption. There are several signaling pathways that regulate the differentiation of precursor osteoclasts and the activity of mature osteoclasts. This section presents different groups of factors that have an effect in osteoclastic activity in myeloma disease.

1.2.2.1.1. RANK/RANKL/OPG System

RANK (receptor activator of nuclear factor NF-κB) and RANK ligand (RANKL) are crucial for the regulation of bone remodeling. RANK is a transmembrane receptor that belongs to the tumor necrosis factor (TNF) superfamily and is expressed on the surface of osteoclast precursors. RANKL is a cytokine that is expressed as a membrane-bound protein by BMSCs and activated T

cells. In normal bone remodeling, RANKL binds to RANK on precursor osteoclasts thereby stimulating their differentiation into mature osteoclasts. In addition, osteoclast apoptosis is reduced which increases osteoclastic activity[42]. Osteoprotegerin is a member of the TNF superfamily and is mostly secreted by BMSCs and osteoblasts in the bone marrow. Osteoprotegerin expression in osteoblasts is regulated by hormones, cytokines and growth factors such as estrogen and tumor necrosis factor. Osteoprotegerin acts as a decoy receptor for RANKL. The blockade of RANKL binding to RANK receptor by OPG inhibits osteoclast maturation and bone destruction. Osteoprotegerin and RANKL expression can be modified by several stimuli such as 1,25-dihydroxyvitamin D, PTH, PTHrP, glucocorticoids and cytokines (IL-1, IL-7, TNFα)[42].

In MM bone disease the RANK/RANKL/OPG system is dysregulated. There are several factors that lead to the imbalance in this system. MM cells interact with the bone marrow microenvironment and activate signaling pathways that increase RANKL and decrease OPG production (**Figure 1-2**)[52]. It has also been reported that in MM myeloma cells, BMSCs, osteoblasts, endothelial cells and T lymphocytes overexpress RANKL and the production of soluble RANKL by MM cells has been directly linked to the bone destruction observed in MM patients[52]. The RANK/RANKL/OPG system can also be altered by myeloma cells binding to BMSCs and decreasing the secretion of OPG and increasing the expression of RANKL, thereby promoting osteolysis. Additionally, MM cells are able to express syndecan-1 which binds to OPG. Subsequently, OPG is taken up by endocytosis in the myeloma cell, where it is degraded. The end result of all these interactions is increased osteoclastogenesis with very high numbers of active osteoclasts and a very minimal expression of OPG thus leading to no inhibition of osteoclastogenesis (**Figure 1-2**)[18,52,53].

1.2.2.1.2. Notch Pathway

Notch signaling is known to be involved in MM induced osteoclastogenesis. Notch can get activated in MM in different ways. Myeloma cells express Notch 1, 2, 3 that bind to their ligands presented either on the same cells or on adjacent BMSCs and malignant plasma cells. When Notch signaling is activated there is production of the osteoclastogenic factor RANKL by myeloma cells. RANKL binds to RANK on the surface of osteoclast precursors and in turn Notch2 expression and activation are induced. The Notch2 signaling cascade in preosteoclasts may be further stimulated by binding to Jagged ligands on neighboring myeloma cells. RANKL production can also be increased by BMSCs expressing Notch receptors that may be triggered by Jagged ligands of

myeloma cells. In addition, Notch signaling has been involved in triggering the expression of adhesion molecules, migratory chemokines, and angiogenic factors in order to establish a pre-metastatic milieu in the bone[54,55].

1.2.2.1.3. Macrophage Inflammatory Protein 1α (MIP1α)

Another molecule that affects the RANK/RANKL/OPG system is MIP1α (also known as macrophage inflammatory protein-1α or chemokine (C-C motif) ligand3 (CCL-3)). MIP1α is secreted by MM cells and is a potent inducer of osteoclast formation. The main receptors of MIP1α are CCR1 and CCR5 and they are expressed on BMSCs, osteoclasts, osteoblasts, and myeloma cells (**Figure 1-2**). MIP1α can attract osteoclast precursors and induce osteoclastogenesis, while it potentiates RANKL and IL6 effects on osteoclasts. In addition, MIP1α inhibits osteoblast activity and mineralization by downregulating RUNX2 and osterix, major regulators of osteoblastic differentiation.[56]. High levels of MIP1α are detected in bone marrow and serum of MM patients and they correlate positively with the extent of bone disease and it is negatively associated with survival[57]. MIP1α can also act on myeloma cells since they express the CCR5 receptor. Binding of MIP1α will promote growth, survival and migration of myeloma cells and it will increase adhesion between myeloma cells and marrow stromal cells. This will result in an increased production of RANKL, IL6, VEGF and TNF-α by stromal cells, which will further enhance MM cell growth, angiogenesis and bone destruction[58].

1.2.2.1.4. Interleukin 6 and Interleukin 3

IL6 is a multifunctional cytokine involved in bone metabolism. It can activate certain pathways such as Ras/mitogen-activated protein (MAP), ERK, STAT3 and the PI3K/AKT cascade. IL6 is also involved in immune and inflammatory responses. IL6 acts as a growth factor for both myeloma cells and osteoclasts promoting their survival and preventing their apoptosis. IL6 is produced by stromal cells and osteoclasts in the bone marrow microenvironment. The effect of IL6 in osteoclasts is an increase in the number of early osteoclast precursors that will differentiate into mature and active osteoclasts[51]. It has been known for some years that IL6 levels in serum of MM patients are elevated and correlate positively with MM stage and with osteolytic bone disease[59]. There are anti-IL6 monoclonal antibodies and inhibitors of the PI3K/mTOR signaling that are being investigated which would provide restoration of bone remodeling[60,61].

IL3 is a cytokine secreted by activated lymphocytes and has a bifunctional profile. IL3 can stimulate osteoclast formation and inhibit osteoblast differentiation as seen in preclinical models of MM (**Figure 1-2**). MM patients present elevated protein levels of IL3 in bone marrow plasma and elevated IL3 mRNA levels in myeloma cells[62]. Furthermore, IL3 in combination with MIP1α or RANKL can significantly increase osteoclast formation and bone resorption[63].

1.2.2.1.5. TNF Superfamily

TNFα is a cytokine than can induce osteoclast formation, promote myeloma cell proliferation by increasing IL6 production by BMSCs, and also inhibit MSC proliferation. TNFα can also induce osteoclastogenesis by acting synergistically with RANKL (**Figure 1-2**). In addition, it is known that BAFF, a member of the tumor necrosis factor superfamily, is highly expressed in the bone marrow microenvironment of MM and enhances the survival of myeloma cells[64].

1.2.2.1.6. Others

Osteopontin is another molecule involved in osteoclast activation and local angiogenesis. Osteopontin is a non-collagenous bone matrix glycoprotein secreted by osteoclasts and in MM patients is described as a dual marker of bone resorption and angiogenic activity. High osteopontin levels have been associated with extensive osteolytic lesions and advanced disease[65]. Finally, activin A is a member of the TGFβ superfamily and induces RANK expression and activates NF-κB pathway and, therefore promotes osteoclast differentiation[33].

1.2.2.2. Mechanisms Behind the Suppressed Osteoblast Activity in MM

Mesenchymal stem cells have the potential to renew themselves and they are also multipotent progenitors that can differentiate into a variety of cell types, such as osteoblasts, adipocytes and chondrocytes. The differentiation pathway of MSCs includes the progression from osteogenic cells into preosteoblasts and finally into osteoblasts. Subsequently, the occurrence, proliferation, differentiation, and maturation of osteoblasts are closely related to the normal growth and development of bones[66]. Once MSCs have differentiated, osteoblasts deposit a dense organic extracellular matrix, primarily collagen I and then harden the matrix by producing an inorganic calcium and phosphate-based mineral, hydroxyapatite. Bone formation markers are direct or indirect products or enzymes of these active osteoblasts. They most often include total alkaline phosphatase (ALP) and osteocalcin (OCN)[67]. In addition, MSCs are thought to be involved in the

pathology and progression of MM disease. It has been reported that MSCs derived from MM patients are genetically and functionally different compared to MSCs derived from normal donors[68]. Furthermore, MSCs from MM patients have also an impaired osteogenic differentiation potential compared to normal donors and patients with MGUS[69]. Suppression of osteoblastogenesis and osteoblast activity can occur by functional inhibition of existing osteoblasts in addition to the impaired MSC differentiation. As a consequence of this osteoblastic suppression, MM patients with active osteolytic lesions showed extremely low serum markers of bone formation (such as osteocalcin and OPG) compared to patients without bone lesions[70]. Soluble factors that contribute to osteoblastic suppression include inhibitors of the two major signaling pathways governing osteoblastogenesis (Wnt signaling pathway and bone morphogenetic (BMP) signaling pathway), several cytokines and chemokines, as well as MM-induced apoptotic factors for osteoblasts[71]. The most important pathways involved in osteoblastogenesis that are affected by MM disease will be discussed next.

1.2.2.2.1. Wnt Signaling Pathway

Wnt signaling is known to play a key role in the regulation of bone mass, and there is increasing data that suggests a role for this pathway in the development of MM. Wnts are a family of 19 secreted glycoproteins that trigger several pathways involved in cell fate determination, proliferation, migration and polarity as well as embryogenesis and regeneration of adult tissues. It is also reported that Wnt signaling is critical in MSCs for osteoblastic differentiation and in turn, for bone metabolism. In the canonical pathway and in absence of Wnt stimulation, β-catenin is phosphorylated by a multi-protein destruction complex and undergoes ubiquitin-mediated degradation in the proteasome. When the canonical Wnt ligands bind to the Frizzled (Fzd) receptor and to the lipoprotein receptor-related protein (LRP) co-receptor, the destruction complex is inhibited which allows β-catenin to translocate into the nucleus. In the nucleus, β-catenin interacts with T-cell factor/lymphoid enhancer factors to activate transcription of target genes involved in osteoblastogenesis[72]. There are several secreted factors that will negatively regulate Wnt signaling and they can be divided into two functional classes. Members of the dickkopf (DKK) family and sclerostin which bind to the LRP5/6 component of the Wnt receptor complex, while secreted frizzled-related proteins (sFRP), such as sFRP2 and 3, bind to Wnt proteins (**Figure 1-2**). Since Wnt plays such an essential role in MSCs differentiation into osteoblasts, alterations in this pathway lead to skeletal disorders such as MM bone disease[71].

1.2.2.2.2. Dickkopf-1

Dickkopf-1 (DKK1) is a member of the DKK family that acts on the Wnt signaling pathway and plays an important role in osteoblastogenesis and skeletal development. DKK1 is expressed by osteoblasts and BMSCs (**Figure 1-2**). In addition, in bone marrow biopsies from MM patients immunohistochemical analysis showed that myeloma cells also overexpressed DKK1[73]. DKK1 binds to LRP5/6 and forms a complex that induces the internalization of LRP consequently inhibiting Wnt signaling. The end result is inhibition of osteoblastogenesis due to the prevention of MSCs to differentiate into mature osteoblasts by suppressing the Wnt signaling. There are additional feedback signaling cascades occurring that involve DKK1 like for example, non-differentiated MSCs can secrete IL6 that stimulates proliferation of myeloma cells secreting DKK1 increasing the presence of this molecule in the bone marrow microenvironment. In fact, MM patients that were newly diagnosed showed elevated DKK1 and sclerostin (SOST) levels compared to healthy donors in bone marrow and peripheral blood plasma, correlating with the presence of bone lesions[74,75].

1.2.2.2.3. Sclerostin

Sclerostin is a secreted glycoprotein produced by osteocytes. Sclerostin induces the apoptosis of mature osteoblasts by activating the caspase pathway and inhibits osteoblast-driven bone formation (**Figure 1-2**)[76]. Sclerostin binds to the extracellular domain of LRP5/6 transmembrane receptors that are found on osteoblast-lineage cells. Consequently, Wnt ligands cannot bind to LRP5/6 and subsequently β-catenin undergoes proteasomal degradation. In the nucleus, transcription factors will be repressed and gene expression promoting bone formation is suspended[77]. In addition, sclerostin together with noggin (protein involved in the development of many tissues including bone) prevents type I and type II BMPs from binding to their receptors and in consequence BMP-mediated mineralization in osteoblasts is downregulated. It has been shown that myeloma cells derived from bone marrow of patients secrete sclerostin and consequently levels of circulating sclerostin are elevated in MM patients compared to patients with MGUS[75,78]. MM patients who present fractures at diagnosis have very high levels of circulating sclerostin compared with all others, whereas sclerostin correlates negatively with bone-specific phosphatase (bone formation marker) and positively with C-telopeptide of collagen 1a (bone resorption marker)[51].

Interestingly, both DKK1 and sclerostin further increase the RANKL/OPG ratio on MSCs and osteoprogenitor cells by upregulating the expression of RANKL and reducing that of OPG, thus indirectly enhancing osteoclast differentiation and activity[79,80].

1.2.2.2.4. Runx2

Runt-related transcription factor 2/core-binding factor Runt domain subunit 1 (RUNX2/CBFA1) is part of the non-canonical Wnt signaling pathway and is a key regulator in the formation and differentiation of osteoblasts from MSCs. When RUNX2 is activated in BMSCs and preosteoblasts there is high expression of osteoblastic markers such as alkaline phosphatase and osteocalcin. Myeloma cells are capable of inhibiting RUNX2 activity in BMSCs and osteoblast precursor cells, blocking osteoblast differentiation[81]. Expression of RUNX2 has been reported to be lower in patients with myeloma bone disease than in normal population and MM patients without bone disease[51].

1.2.2.2.5. BMPs

BMPs are included in the TGFβ superfamily and act through Smad-dependent and Smad-independent pathways. Specifically, BMP2 is in charge of inducing osteoblastogenesis and promoting bone formation. It is known that myeloma cells can secrete several molecules such as hepatocyte growth factor (HGF) and Pim-2 kinase that act as negative regulators of BMP-mediated osteoblast differentiation.

1.2.2.2.6. TNF Superfamily

It was previously discussed how TNFα plays a role in promoting osteoclastogenesis but it is also reported that it can inhibit osteoblast precursor recruitment from progenitor cells and suppress RUNX2 as well as osterix.

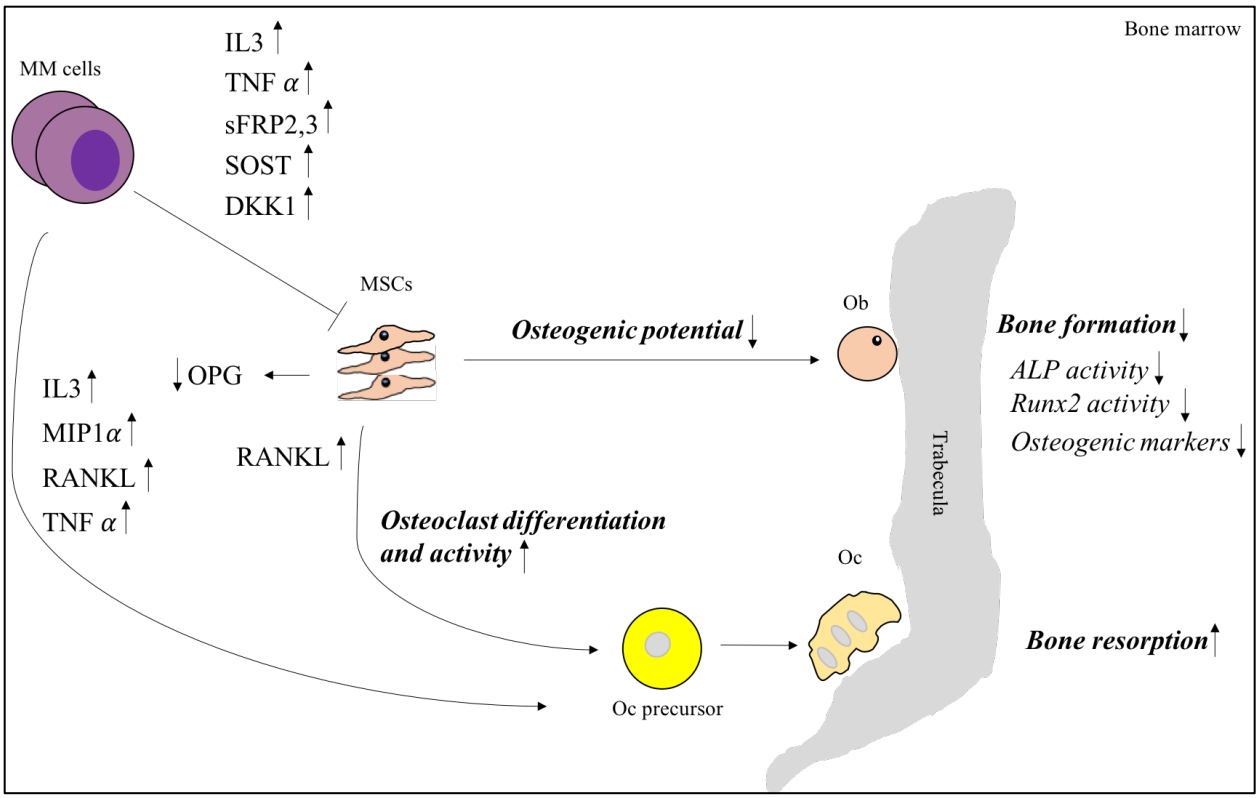

Figure 1-2: Interactions between MM cells and the bone forming unit in the MM disease

1.2.2.3. Targeting the Bone Disease in MM

The mainstay treatment of MM bone disease is bisphosphonates (BPs). BPs are potent inhibitors of osteoclast recruitment and osteoclast activity and longevity. BPs are absorbed by osteoclasts or they can also be absorbed by macrophages which derive into osteoclasts. BPs induce the apoptosis of osteoclasts in two different ways depending on the type of BP. Non-nitrogen containing BPs act accumulating non-hydrolysable ATP metabolites and nitrogen-containing BPs (N-BPs) inhibit the mevalonate pathway. In particular, N-BPs inhibit the enzyme farnesyl pyrophosphate synthase (FPP synthase), which prevents the formation of isoprenoid lipids such as geranylgeranyl pyrophosphate (GGPP). GGPP is required for the post-translational prenylation of proteins especially Ras, Rho, Rab and Rac. Decreased numbers of these proteins will interfere with cellular function and induce apoptotic cascades. BPs also reduce osteoclast activity via disruption of the cytoskeleton and the osteoclast ruffled border[82]. Zoledronic acid is the most commonly used BP since it demonstrated a superior reduction of myeloma SRE than clodronate and also reported a survival advantage in patients who had evidence of bone disease at onset[83]. In addition, there is evidence that zoledronic acid has some anti-tumor activity in MM[84]. However, BPs have poor

biopharmaceutical properties, such as their high polarity and affinity for bone or poor cell membrane permeability[83,85]. A deeper analysis of BPs will be done in the last section of this introduction.

There are other non-bisphosphonate treatment modalities that are under study to target bone disease in MM.

First, proteasome inhibitors are an important class of agents that emerged to treat multiple myeloma in the past two decades. Bortezomib is a highly effective proteasome inhibitor that has become the mainstay of treatment worldwide in myeloma. As a consequence of proteasome inhibition there is reduced degradation of β-catenin which is a common mediator of osteoblastogenic Wnt signaling pathway. Additional proteasome inhibitors such as carfilzomib have improved side effect profiles and are also achieving positive effects on bone remodeling by stimulating Wnt signaling pathway[86,87].

Second, as observed by the regulation of all these signaling pathways the RANK/RANKL/OPG system plays a crucial role in osteoclast differentiation and activation in myeloma bone disease. The increased expression of RANKL in the bone marrow has demonstrated to be a key factor in the bone destruction observed in MM patients. A novel agent was designed to target RANKL and it is known as Denosumab. Denosumab (anti-receptor activator of nuclear factor-kappaB ligand antibody) is a fully human monoclonal antibody that inhibits osteoclastic-mediated bone resorption by binding to osteoblast-produced RANKL. By reducing RANKL binding to RANK, bone resorption and turnover decrease[88]. Denosumab has shown encouraging results in the treatment of MM bone disease in patients. Phase 3 clinical trials revealed that denosumab is not inferior to zoledronic acid, commonly used to treat bone disease in MM, while having a safer renal profile and with the potential to increase the progression-free survival[89].

Third, the production of DKK1 by myeloma cells which inhibits osteoblast activity has been the subject of interest as a target as well. The anabolic effects of a DKK1 neutralizing antibody (BHQ880) have been previously evaluated in vitro. BHQ880 was able to increase osteoblast differentiation, neutralizing the negative effect of myeloma cells on osteoblastogenesis, and reduced IL6 secretion. BHQ880 was also used to treat a mouse model of MM and treatment led to a significant increase in osteoblast number, serum osteocalcin levels, and trabecular bone[90]. In addition, increased bone anabolic activity was observed in a phase 2 clinical trial[33].

Finally, an important target for the development of agents targeting osteoblast suppression in MM is sclerostin. A monoclonal antibody against sclerostin has been developed, Romosozumab, that has increased the bone mass in patients with post-menopausal osteoporosis. Use of this antibody in clinical trials for MM is highly anticipated[91].

1.3. Mouse Model Systems of MM and MM Bone Disease

Mouse models of MM and MM bone disease are essential tools to study the biology of MM and its associated bone disease as well as to select novel candidate therapeutics for clinical development. Over the last decade several different murine models of MM have been developed which include xenograft models using human myeloma cells and different strains of severe combined immunodeficient (SCID) mice, in addition to transgenic or syngeneic models that develop murine MM in immunocompetent mice. These mouse models aim to recapitulate the disease and to provide insights on the interactions between myeloma cells and the bone marrow microenvironment. The microenvironment is becoming a key factor in the study of MM disease and bone disease since it is involved in proliferation, viability, and drug resistance of MM cells *in vivo*. For these reasons there is emphasis in the creation of models in which myeloma cells can form bone lytic lesions in the skeleton and the mice are not immunocompromised. Lastly, due to the differences between models it is important to take into careful consideration which model should be used for preclinical evaluation of the disease and to develop specific therapeutic agents[92].

In this section, existing mouse models of MM and MM bone disease will be discussed in detail and at the end of the section a summary of all models described is available (**Table 1-4**).

1.3.1. Syngeneic murine models of MM

1.3.1.1. BALB/c Models

The best available mouse model to study MM in the early 1960s was the peritoneal plasma cell tumor (PCT) model in BALB/c mice. In this model, plastics and paraffin oils were administered intraperitoneally in BALB/c mice which would chemically induce tumors that secreted monoclonal immunoglobulin (plasmacytomas). The benefit of this model was that BALB/c mice are immune competent, and so it would be possible to study the interaction between the cell tumors and the immune system. Because of this reason this model would be a good model to study the mechanism of action of novel immunomodulatory drugs for the treatment of MM. However, this

model does not present MM in the same form as in the human since the plasma cells were localized to the peritoneum and in the subcutaneous space, but not in the bone marrow[93]. The only instance in which bone disease was observed in this model was when MOPC315 cells (cells that had infiltrated the bone marrow of immunocompetent BALB/c mice treated with mineral oils) were re-injected intravenously in BALB/c mice. These mice developed MM in bone marrow and had limited extramedullary involvement. In addition, they presented osteolytic disease, detectable paraprotein and end-stage paraplegia[94].

1.3.1.2. 5T MM Models

The C57BL/KaLwRij mouse strain develops proliferative B-cell disorders with a high frequency when they are aged. Approximately 80% of these mice present MGUS and in a few cases (0.5%) they develop MM when they are older than two years. Subsequent transplantation of bone marrow cells from C57BL/KaLwRij mice with myeloma to young C57BL/KaLwRij mice results in a reproducible murine myeloma model in which features of human myeloma are recapitulated (e.g. tumor growth within the bone marrow, increase in M-protein, renal dysfunction and development of bone disease). Recently, the genetic determinants underlying the MGUS predisposition of the KaLwRij strain were identified using whole genome and exome sequencing. The variants identified include the deletion of *Samsn1* and the deleterious point mutations in *Tnfrsf22* and *Tnfrsf23*[95]. These variants significantly affected multiple cell types including B-cells, macrophages, and bone marrow stromal cells. These data points to the contribution of several cell types in MM development prior to the acquisition of somatic driver mutations in KaLwRij mice[95]. The MM cell lines originated in this mouse strain are called the 5T MM series and can be transferred in mice that will in consequence develop MM. It was reported that the MM development was achieved in 100% of the cases in the first and in subsequent cell transfer generations. There are several MM lines obtained from this model and they can present different features. For example, some cell lines grow slowly and with little bone destruction. Those cell lines tend to retain these characteristics in the next transplanted generations. Other cell lines gradually develop a more aggressive growth with greater bone destruction and excessive M-protein production (**Table 1-3**). Certain cell lines have been extremely well characterized, in particular the 5T2 MM and 5T33 MM lines.

Table 1-3: List of documented 5T MM in aging C57BL/KaLwRij mice

5T MM number	Transplanted	Growth	Osteolytic bone lesions
5T2 MM	+	Moderate	Pronounced
5T7 MM	+	Slow, smoldering	Sporadic
5T8 MM	-	-	-
5T13 MM	+	Moderate	Sporadic
5T14 MM	+	Aggressive	Mainly osteolytic, some sublines
5T21 MM	+	Aggressive	Not studied
5T30 MM	+	Moderate	Not studied
5T33 MM	+	Aggressive	Diffuse
5TF	+	Moderate	Mainly peripheral
5TGM1	+	Aggressive	Pronounced

Adapted from "*Animal Models of Human Disease*". Jiri Radl MD, Joan Willem Croese MD, Chris Zurcher MD, Margit H. M. Van den Enden-Vieveen, and A. Margreet de Leeuw PhD. American Journal of Pathology, Vol. 132, No. 3, September 1988 and from "*The 5TMM series: a useful in vivo mouse model of human multiple myeloma*". Kewal Asosingh[1], Jiri Radl[2], Ivan Van Riet[1], Ben Van Camp[1] and Karin Vanderkerken*,

1.3.1.2.1. 5T2 MM Model

The most commonly used cell line from the 5T MM series to develop MM in mice is the 5T2 MM. The 5T2 MM model represents the most common forms of human MM and has moderate growth with recapitulation of features of human myeloma and the associated bone disease within approximately 3 months. After intravenous transplantation, these bone marrow 5T2 MM cells can only be found on the bone marrow of the recipient mice. As the disease progresses, the myeloma cells occupy most of the bone marrow space and will replace the normal hematopoietic tissue. Bone disease in this model is observed as osteolytic focal destruction of cortical bone and as a decrease in the amount of trabecular bone. In addition, cortical destruction is most commonly seen where blood vessels pass[96]. Animal models such as the 5T2 MM have been used to predict efficacy of new chemical entities advancing into clinical trials and can in turn validate the use of these models. For instance, the 5T2 MM model was used to test the bisphosphonate drug, zoledronic

acid, and data showed that zoledronic acid was able to inhibit the development of myeloma bone disease with decrease of osteolysis, tumor burden and angiogenesis, and increased survival[97]. In addition, it was observed that MM propagates outside of the bone marrow and can be seen surrounding muscles, into the vertebral canal and the spleen is usually affected as well[96]. The 5T2 MM cells however, do not survive well *in vitro* and can only be maintained by direct passage from mouse to mouse, limiting their utility for *in vivo* studies[98].

1.3.1.2.2. 5T33 MM Model

The 5T33 MM model causes a highly aggressive form of MM with rapid tumor growth in mice. Tumor in marrow is evident after approximately 4 weeks after inoculation with a significant increase in M-protein after 2 weeks. This model might be a better representation of advanced or relapsed MM compared to the 5T2 MM model, which depicts a patient with less aggressive early disease. In addition, in contrast to the 5T2 MM model where the myeloma cells are mainly located in the bone marrow, in the 5T33 MM model the bone marrow infiltration is accompanied by a massive infiltration of both liver and spleen in nearly all mice[99]. The involvement of the spleen in these models is not surprising since it is a hematopoietic organ in the mouse. Furthermore, compared to the 5T2 MM model, injected mice with 5T33 MM cells do not have measurable focal lytic bone disease and instead exhibit "diffuse" lytic bone lesions. For this reason, this model cannot be used for the testing of therapeutics to target the bone disease or for bone formation induction[100]. Nonetheless, this model shows an advantage compared to the 5T2 MM model and it is that the 5T33 MM cells can be grown *in vitro*. This allows the cells to be transduced to express GFP or luciferase in order to identify them *in vivo*[101].

1.3.1.2.3. 5TGM1 Inoculated Mice

Due to the lack of MM bone disease observed in the 5T33 MM model an additional model was created in order to investigate mechanisms of MM induced bone disease. This model is called the 5GTM1 model which was achieved by continual *in vivo* passage of the 5T33 MM cells. This model develops MM aggressively like the 5T33 MM model and paraplegia is usually observed in these mice after 21-35 days post-injection. The 5TGM1 cell can also be cultured in vitro like the 5T33 MM cells. After injection, 5TGM1 cells home to the bone marrow and in some cases, they can also be localized in the spleen and ovaries. At the end-stage of the disease there is detectable M-protein in these mice[102]. The advantage of this model over the 5T33 MM, is the presence of

"pronounced" osteolytic lesions compared to the "diffuse" lesions observed in the 5T33MM[100]. This model is a reproducible model of human MM disease and can be used to test agents that not only target MM but also the bone disease[98].

1.3.1.2.4. Advantages and Limitations of the 5T MM Models

The main advantage of the 5T series of MM mouse models is that they have an intact immune system that other immunocompromised mice do not have. The cellular structure of the bone marrow microenvironment is intact in these mice which is essential since it is known that the microenvironment plays a key role in MM development. In addition, these models demonstrate high cell engraftment and low variability. For these reasons, the 5T MM models are ideal for the study of efficacy of novel anti-MM agents as well as for agents developed to prevent bone disease. In addition, the different 5T MM cell lines allow the investigator to define the profile of the MM disease that they need for their studies (slow, moderate or aggressive growth) and the presence or absence of MM bone disease.

A limitation of the 5T MM series is that these models do not capture the diverse spectrum of genetic heterogeneity of human MM since they only represent single clonal murine MM-like diseases. It is possible that this could be improved in the future with the generation of 5T sublines. Furthermore, the disease in some of these models is often not localized to the bone marrow compartment which does not recapitulate what is observed in the human MM, limiting their pre-clinical use. An additional disadvantage is that these models develop murine MM and not human MM and because of that the mechanism by which plasma cells become malignant might be different. The mechanisms by which these mice develop MM are not fully understood yet and it should be taken into consideration when performing studies using the 5T MM models.

1.3.1.3. Transgenic Models of MM

There have been a number of transgenic MM mouse models developed in the last ten years in an attempt to model the mutations that exist in human MM and with the additional goal to better replicate the pathogenesis of human MM. Early studies focused on the role of IL6 in MM. Mineral induced plasmacytomas growth relies heavily on the expression of IL6 and it is also known to not only be a growth factor, but also a survival factor in MM, which inhibits apoptosis in myeloma cells. IL6 interacts with many molecules within the bone marrow microenvironment including adhesion molecules, tumor suppressor genes and oncogenes[103]. Based on this information, an IL6

transgene driven by the promotor of L^d gene of the major histocompatibility complex (H2-L^d) was generated in C57Bl/6 mice and showed the development of massive polyclonal plasmacytomas. Only with the introduction of BALB/c genetic background into the IL-6 transgenic mice, monoclonal transplantable plasmacytomas could be generated[104]. These early studies unveiled the importance of IL6 in MM growth and the importance of tumor microenvironment *in vivo*. However, these mice developed plasmacytomas that would resemble at best extramedullary MM cases and would not fully recapitulate the human disease.

1.3.1.3.1. The Vk*MYC Model

MYC was identified 25 years ago as the gene dysregulated in Burkitt's lymphoma, mouse plasmacytomas and by complex translocations in human MM, however, no model was developed that can recreate these diseases in mice. The Vk*MYC mouse model is the first mouse model generated that relies in the activation of the oncogene *MYC*.

In the Vk*MYC model the activation of *MYC* is under the control of the kappa light chain gene regulatory elements and it occurs sporadically thanks to somatic hypermutation in the germinal center in B cells, once B cells have committed to terminal differentiation[105]. In more detail, a vector was generated with a V-kappa exon sequence splicing in frame with the human *MYC* locus. The transgene harbors a stop codon within V-kappa exon that generates a DGYW motif. This motif is targeted by SHM, which can randomly revert the stop codon and promote *MYC* expression. AID (activation-induced deaminase) is the enzyme responsible for inserting DNA mutations during SHM which causes *MYC* expression in this model. In this way, *MYC* becomes activated along the germinal center reaction, preferentially affecting plasma cell differentiation. As the Vk*MYC mice age, the malignant plasma cells accumulate in the bone marrow and secondary lymphoid organs and they develop MGUS/MM. Only in rare cases the MM disease escapes the bone marrow confinement and becomes extramedullary plasmacytoma. This model resembles the human MM since the mice produce monoclonal protein quantifiable in serum as early as 40 weeks. These mice also present significantly lower hemoglobin concentration at necropsy indicating anemia. Kidneys are also affected with Igs detected in the tubuli and glomeruli in the form of protein deposition. The bone disease in Vk*MYC mice is not severe, discrete bone lytic lesions and vertebral collapse can occasionally be detected but are uncommon, although bone mineral density is significantly lower. In addition, significantly decreased trabecular number is also observed in these mice. The development of MM in this model is very slow, similar to MM patients, and mice live almost 2

years although with shorter median survival compared to wild type. Furthermore, Vk*MYC mice with significant M-protein levels were treated with clinically used drugs in to order to evaluate their potential as a drug testing platform. Profound and statistically significant reduction in M-protein levels were observed after mice were treated with melphalan, dexamethasone, and bortezomib[105].

1.3.1.3.1.1. Advantages and Limitations of the Vk*MYC Mouse Model of MM

The Vk*MYC mouse model fulfills many of the biologic and genetic characteristics to be an ideal MM mouse model, showing high resemblance to the human MM. The first advantage of this model is that the Vk*MYC mice are immunocompetent which translates into the malignant cells interacting with a complete immune system in the same way as in the human MM. In addition, it was shown that it is possible to successfully transplant the MM disease from the Vk*MYC mice into syngeneic recipient mice with the mice developing a very aggressive MM phenotype. Another advantage of this model is that the MM is restricted to the bone marrow while other immunocompetent models presented extramedullary plasma cell proliferation. Furthermore, response to clinically used therapies in this model demonstrates that the Vk*MYC model can be a good preclinical validation tool for novel therapies[105]. Finally, in this model there is reproduction of the existing cross talk between clonal plasma cells and the surrounding bone marrow microenvironment. This characteristic is essential to be able to study the dynamics in this disease which englobes both malignant myeloma cells and cells of the microenvironment.

The indolent disease and late onset of MM in these mice has both advantages and disadvantages. The disease in these mice faithfully models clinical features of human MM but the mice only start showing signs of disease as early as 40 weeks of age. Consequently, the colony needs to be maintained for long time with an appropriate number of mice, which makes it very costly. In addition, due to the strategy used these mice lack important characteristic human myeloma cytogenetic events, limited to murine malignant cells in a murine bone marrow microenvironment. Finally, the rare occurrence of bone disease or bone lytic lesions does not recapitulate what is observed in human MM. Bone disease is a hallmark of MM and the lack of this features marks this model as unsuitable to test novel bone anabolic drugs.

1.3.1.3.2. The XBP-1 Model

Additional transgenic models of MM disease have been developed over the years and a good example is the XBP-1 model. XBP-1 (X box binding protein 1) is a basic-leucine zipper transcription factor and it is a major regulator of the unfolded protein response (UPR) and plasma cell differentiation[106]. XBP-1 is particularly required for the last stages of B-cell differentiation into plasma cells. It has been reported that XBP-1 is overexpressed in human carcinogenesis and tumor growth under hypoxic conditions. Specifically, high expression of XBP-1 has been detected in human MM cells and can be induced by IL6[107,108]. MM patients with high XBP-1 treated with the proteasome inhibitor, bortezomib, showed improved outcome although no correlation between XBP-1 RNA expression and response to therapy was found[109]. Considering the involvement of XBP-1 in malignant plasma cell differentiation in MM, a Eμ-XBP-1 transgenic mouse, with a prominent expression of transgenic product in spleen, lymph nodes, bone marrow and thymus was generated. These mice presented M-protein in their serum by 40 weeks of age, antibody-based cast nephropathy and bone marrow plasma cell infiltrate <10%. When these mice age they present up >10% bone marrow plasma cells and bone lytic lesions, although with late onset (after 2 years). The Eμ-XBP-1 mouse model represents a suitable platform to study the consequences of targeting UPR modulators in MM, however their production of an IgM monoclonal protein as well as the spacial distribution of the disease make this model very un-like human MM[106].

1.3.1.3.3. Advantages and Limitations of Transgenic Models of MM

The main advantage of transgenic mouse models of MM is that there is a representation of different phases of MM development starting with mice developing MGUS and evolving to MM which in some cases can be extramedullary. This can be advantageous depending on the therapeutics to be tested and their target. On the other hand, these are less well characterized models and are difficult to manipulate to reliably reproduce a MM-like disease. Finally, due to the longer latency period, transgenic models are not as commonly used because of time constrain and cost.

1.3.2. Xenograft models of MM

As mentioned previously, one of the limitations of the 5T MM series is the genetic murine myeloma that those models present. The Vk*MYC also falls in that category in the sense that they present murine malignant cells in the mouse bone marrow microenvironment. The aim of the xenograft models is to test innovative drugs against human MM cells in their microenvironment.

In order to achieve that goal, engraftment of human MM cells in a mouse recipient has been attempted. The methods used have been injection either subcutaneously (s.c.) or systemically (intravenously, i.v. or intraperitoneally, i.p.) of MM cell lines in immune compromised mice (e.g. severe combined immunodeficient (SCID), nude, non-obese diabetic (NOD)/SCID, etc.) [98]. A variety of MM cell lines have been administered to SCID and NOD/SCID mice. The MM cell lines used include: ARH-77[110,111], RPMI8226[112], U266[113], KMS11[114], KMS-12-BM[115] and MM1S[116]. In addition, monoclonal protein in serum as well as additional biomarkers such as beta 2 microglobulin can be detected in both models and used as an indirect biomarkers of disease burden. The administration route of these cells lines is relevant due to the different development of the tumors[117].

It has been observed that mice injected subcutaneously develop palpable tumors only in the injection site. There are several ways to identify if there is MM tumor growth in these models, for example in mice that have been injected subcutaneously MM growth is measured by a caliper or ultrasound and effects of specific drugs are quantified by tumor volume and mouse survival. A disadvantage of this model is that there is no myeloma cell and bone marrow microenvironment interaction which it is known to sustain the MM expansion and drive the development of bone disease. Furthermore, MM cell lines used for engraftment have been isolated from extramedullary sites and have lost their dependence from the bone marrow which means that their genetic background has changed significantly to a late stage disease[117].

In the systemic injection model there is MM infiltration in different organs such as spleen, liver, lungs and bone marrow depending on the cell line used. In this model, MM growth is diffuse and disease burden needs to be evaluated by microCT, MRI or PET scan[118]. In addition, in the intravenous injection model the bone marrow of the mice can be infiltrated which allows for malignant myeloma cells to interact with the microenvironment and reproduce the MM bone disease. Something uncommon in the human disease that this model presents is the accumulation of myeloma cells in organs other than the bone marrow[117].

These two models are good models to test new cytotoxic drugs because they are easy to handle and assessment of drug activity can be done quickly. However, they do not provide an understanding on the interactions between myeloma cells and bone marrow microenvironment. This information is relevant to allow the novel compounds to translate into the clinical setting. It

is essential that the selective mechanism of action that most commonly involves the bone marrow niche in MM is known[117].

In order to surpass these limitations novel "humanized" models of MM have been developed (SCID-hu, SCID-synth-hu and SCID-rab). In brief, to reproduce the human MM in these models there needs to be implantation of human fetal bone chips in the flank of irradiated SCID mice and seeding of freshly isolated primary myeloma cells in the chips. The main advantage of this system is that the cells home to the human but not the murine bone marrow.

1.3.2.1. The SCID-hu Model

In the SCID-hu model, SCID irradiated mice have been implanted with human fetal bone tissue before intravenous injection of primary human myeloma cells or human myeloma cells lines such as RPMI8226, U266, ARH-77[119]. It has been reported previously that successful engraftment of various MM cell lines into human bone chips was achieved with no dissemination to other organs and M-protein was detected in serum in these mice[119]. In the same way, injection of human primary myeloma cells resulted in positive engraftment and increase in M-protein. In addition to these features, SCID-hu mice showed evidence of neovascularization, increased osteoclast numbers and reduced bone density compared to SCID mice with empty human bone implants[120].

The advantage of using MM cell lines is the high reproducibility of the data which represents more accurately the human disease. As an example, there is the inoculation of INA-6 cells into SCID-hu mice. INA-6 cells are fully dependent on human BMSCs and/or human IL6 and after engraftment an increase in soluble human IL6 receptor is observed, a marker for the IL6 dependent INA-6 cell line and tumor burden[121].

Another advantage of the SCID-hu model is the use of human bone versus using murine bone which allows higher tumor engraftment of myeloma cells into a human bone chip. However, the main limitation is the use of fetal bone as opposed to adult bone because it does not fit with the age demographic of MM disease. In addition, human fetal bone is difficult to acquire due to ethical reasons. Finally, this model does not recapitulate an important feature of the disease which is the homing and metastasis of tumor cells due to direct injection of malignant cells into the bone chip[98].

These models have been used to identify key MM signaling pathways and to investigate several novel agents to treat the disease. For example, MAPK is constitutively activated in MM and

contributes to tumor growth. When MAPK is abrogated within MM osteoclast activity is attenuated and there is bone restoration in SCID-hu mice[122,123].

Due to the ethical limitations in acquiring human fetal bone chips a novel model was designed, the SCID-rab model.

1.3.2.2. The SCID-rab Model

In the SCID-rab model the human bone chips have been substituted with rabbit bones. This resulted in 85% bone marrow engraftment, with no dissemination to other organs. The features of these mice recapitulate human MM with M-protein in serum, neovascularization and increased osteoclast numbers which are responsible for the observed bone disease[124]. This model has been the main tool to investigate the bone anabolic effects of proteasome inhibitor, bortezomib. When these mice are injected with bortezomib they present reduced tumor burden, increased bone mineral density and increased trabecular bone volume and bone formation which sets the basis to further explore the bone building potential of novel drugs in this model[125]. In addition to bortezomib, the effects of anti-DKK1 monoclonal antibody were investigated in this model. Anti-DKK1 was able to increase bone mineral density in the presence of malignant plasma cells. In addition, the neutralization of DKK-1 led to an increase in osteoblastic numbers while osteoclasts remained significantly reduced[90].

The SCID-rab is a good model to investigate preclinical molecules although it has the limitation that the implanted bone is from rabbit. Although ontogenically related, rabbit bone cannot be compared to the human bone[117].

1.3.2.3. The SCID-synth-hu Model

Similar to the SCID-hu and the SCID-rab models, the SCID-synth-hu provides a system for myeloma cell engraftment. The SCID-synth-hu model is based on a synthetic 3D-bone-like, cylindrical, poly-ε-caprolactone polymeric scaffold coated with mouse or human bone marrow stromal cells subcutaneously implanted into the flank of a SCID mouse. Engraftment of MM cell lines, human MM primary cells and peripheral blood plasma-cell leukemia cells on scaffolds coated with human bone marrow stromal cells has been demonstrated in this model. These models can be very useful because of their ability to recapitulate MM disease which allows them to become platforms to test a variety of innovative therapeutic approaches. For example, the SCID-synth-hu model was used to study the effects of bortezomib/dexamethasone. After whole bone marrow

aspirates were engrafted directly *in vivo*, these mice were treated with bortezomib/dexamethasone which led to a significant decrease of myeloma cells in mouse serum and clearance of myeloma cells from the scaffold[126].

Additionally, primary human myeloma cells can be engrafted to scaffolds coated with their own (autologous) bone marrow stromal cells and present long-term survival (3-4 months) with detectable human monoclonal protein production in mouse serum. This feature makes the SCID-synth-hu model interesting for *in vivo* screening of preclinical MM agents[127].

1.3.2.4. Advantages and Limitations of Xenograft Models

The first advantage of xenograft models is the high percentage of engraftment that they show, almost 100% in some cases. In addition, they present specific bone marrow homing of myeloma cells and in some cases bone disease. An additional advantage is that xenograft models use human cell lines or patient-derived primary cells which allows a better recapitulation of the human MM disease.

The main disadvantage of these models is the lack of competent and complete immune system. Mice are either irradiated which profoundly affects the immune status and bone marrow microenvironment or are intrinsically immunodeficient. The irradiation of these mice will likely affect the disease response to treatments and will show differences in results when comparing to immunocompetent models and human MM. For this reason, results obtained using these models need to be treated with caution. Furthermore, there is very wide selection of cell types that can be used, from primary MM cells to all the different human MM cell lines that exist. Each cell line presents different characteristics and may result in differences in latency periods, M-protein production, tumor dissemination and production of bone disease. However, cell lines per se are thought to represent advanced MM disease rather than the indolent nature of primary human MM thus results obtained using these models may not truly reflect the clinical reality. Finally, the selection of appropriate endpoints is crucial when selecting cell lines in order to obtain reliable results after the therapeutic administration.

Table 1-4: Summary of MM mouse models.

	Characteristics	Bone disease	Limitations
Syngeneic models			
BALB/c[94]	Development mainly of plasmacytomas. Are immune competent.	Only when MOPC315 cells are re-injected in BALB/c.	Plasma cells in peritoneum, does not resemble human MM.
5T MM series[96,100]	MM originated from KaLwRij mice. 5T2, 5T33 and 5TGM1 most widely used models. Transplantable cells.	Only observed in the 5T2 MM model and in the inoculated 5TGM1 model.	Development of murine MM and no genetic heterogeneity.
Transgenic models			
Vk*MYC[105]	Based on *MYC* activation and dependent on SHM and CSR in B cells.	Rare occurrence.	Murine MM and slow and late onset of MM. Costly.
XBP-1 model[106]	XBP-1 overexpression is key in MM development. Ideal model for the study of the UPR in MM.	Some present bone lytic lesions.	Production of M-protein and spacial distribution of disease does not resemble human MM.
Xenograft models			
SCID-hu model[119]	Irradiated mice implanted with human fetal bone tissue with intravenous injection of human MM or MM cell lines.	Dependent on cell line or primary cell injected.	Not immune competent. Difficulty in acquiring the human fetal bone plus no match to the MM demographic (old age).
SCID-rab model[124]	Irradiated mice implanted with rabbit bone and injected with human MM or MM cell lines.	Dependent on cell line or primary cell injected.	Not immune competent. Implanted bone originates from rabbit, cannot be compared to human bone.
SCID-synth-hu[126]	Based on a synthetic 3D-bone-like scaffold coated with mouse or human bone marrow stromal cells implanted in SCID mice.	Dependent on cell line or primary cell injected.	Not immune competent.

1.3.3. Immunotherapy and MM Mouse Models

As mentioned in the first section of this introduction, the treatment of MM has evolved significantly over the last decades. Integration of immunotherapy into standard treatment is the next step in the improvement of MM treatment[128].

The discovery of immune checkpoints and the fast development of inhibitory monoclonal antibodies to these molecules has raised the question on what the most suitable MM mouse model is to investigate these immune-modulatory agents.

The ideal model needs a fully competent immune system able to mount an effective anti-cancer response. Several immunocompetent mouse models of MM, including the 5T MM and Vk*MYC models, have been widely used to investigate the role of different immunosuppressive cell populations and the activity of checkpoint inhibitors such as anti-PD1 monoclonal antibodies[129,130]. Specifically, cellular immunity in Vk*MYC mice was studied in order to compare it to newly diagnosed and relapsed/refractory MM patients. Vk*MYC mice were able to replicate changes in the memory T cell population observed in patients with MM, although results revealed that the Vk*MYC model resembles more closely the relapsed/refractory stage of human MM. It was suggested that in the Vk*MYC model, the most appropriate role for testing immunomodulatory therapies was likely to be in refractory/relapsed MM that remains an area of clinical need for novel therapies[131].

Finally, the SCID-hu and SCID-synth-hu are strong candidates as good models since it has been reported that immune populations, such as dendritic cells are present and functionally active in the latter model[132].

1.4. The Role of Bisphosphonates in MM

Bisphosphonates (BPs) are the standard choice for the prevention of bone disease in MM[32]. In 1992, a clinical study on the effects of oral clodronate (first generation BP) demonstrated a significant reduction in the proportion of patients developing progression of osteolytic bone lesions[133]. In the last 10 years, intravenous administration of BPs became part of routine clinical management of MM patients thanks to a study on intravenously administered pamidronate (second generation nitrogen-containing BP, N-BP) that demonstrated that the proportion of patients developing SREs was significantly lower, with improved quality-of-life scores, performance

status, pain scores and incidence of pathologic fractures[134]. Both pamidronate and zoledronic acid (third generation N-BP) are widely used for the prevention of bone destruction in MM. However, pamidronate was compared to zoledronic acid *in vitro* and findings showed that zoledronic acid is 10 times more potent which translates into increased osteoclast and tumor cell apoptosis via increased inhibition of protein prenylation[135]. Results from a multicenter cohort also showed a reduced risk of death by 22% when treating patients with zoledronic acid versus pamidronate. In addition, zoledronic acid also reduced the risk of SREs by 25%[136]. Finally, zoledronic acid also showed increased overall survival in MM patients when compared to clodronate in a Crochane meta-analysis[137]. Interestingly, in the late 90s, BPs were also shown to cause proapoptotic effects on a variety of tumor cell lines, including MM cell lines, in a concentration and time-dependent manner[138-141]. The number of studies in the anti-myeloma activity of BPs has increased in the last years with promising results. A short review of the mechanisms of action involved in inhibition of osteoclastogenesis and anti-myeloma activity of these compounds will be done in this section.

1.4.1. Mechanisms of Action of BPs

Bisphosphonates are analogs of pyrophosphate (P-O-P), an endogenous regulator of bone mineralization, in which the central oxygen atom is replaced with a carbon atom (P-C-P)(**Figure 1-3**)[142].

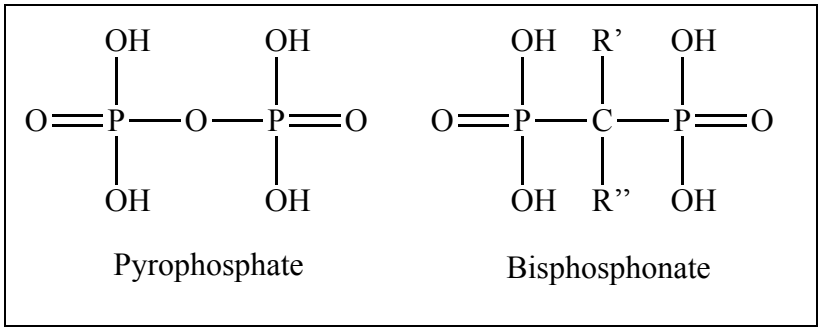

Figure 1-3: Basic chemical structures of pyrophosphate and bisphosphonates.

1.4.1.1. Inhibition of Osteoclastogenesis by BPs

Like in pyrophosphate, the flanking phosphate groups provide BPs with a strong affinity for hydroxyapatite crystals. Additional changes in the BP structure like adding a hydroxyl group to the central carbon (R') provide these compounds with the ability to bind to calcium as well. It is

known that bisphosphonates incorporate in zones of active remodeling and they do not only inhibit calcification but also effectively suppress bone resorption[143].

BPs bind to exposed mineralized bone and are taken up by osteoclasts during bone resorption, inhibiting osteoclast recruitment and maturation, preventing the development of monocytes into osteoclasts, inducing osteoclast apoptosis and interrupting their attachment to the bone[144].

The mechanism of action of BPs depends on their chemical structure. As mentioned previously, there are two types of BPs, nonnitrogen-containing BPs and more potent nitrogen-containing BPs (**Figure 1-4**)[143].

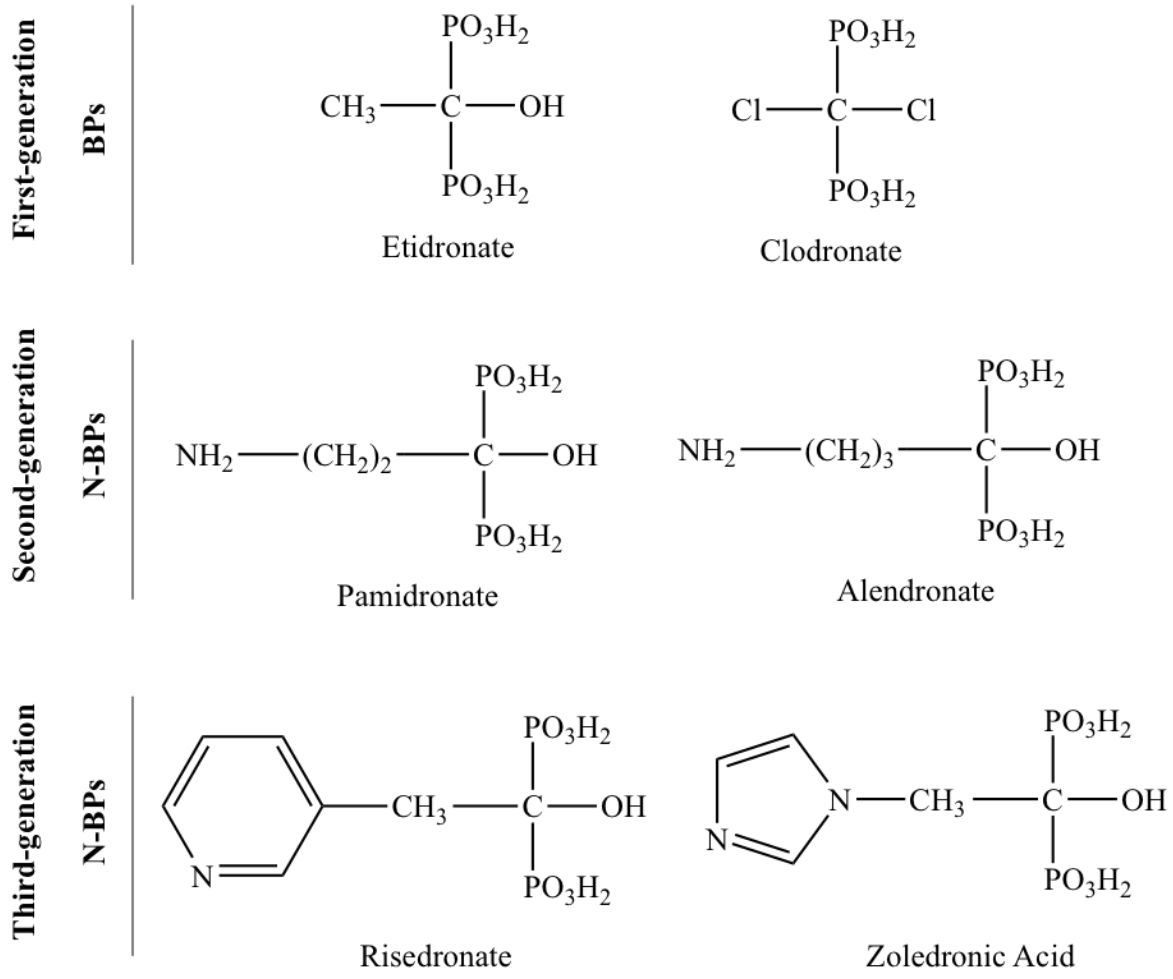

Figure 1-4: Chemical structures of first-generation nonnitrogen containing BPs and of second- and third-generation nitrogen-containing BPs.

Nonnitrogen containing BPs are considered first generation BPs and they include etidronate, clodronate, and tiludronate (**Figure 1-4**). Because of their structural similarity to PP*i* they

incorporate into molecules of newly formed adenosine triphosphate (ATP) after osteoclast-mediated uptake from the mineral bone surface. Intracellular accumulation of nonhydrolyzable ATP analogues is thought to be the cause for the cytotoxic activity to osteoclasts. These BPs inhibit multiple ATP-dependent cellular processes, leading to osteoclast apoptosis[143].

In BPs, the potency for inhibition of bone resorption relies on the groups attached to the central carbon (R'') which can contain nitrogen or amino groups. Nitrogen-containing BPs (N-BPs) include second- and third- generation BPs (alendronate, risedronate, ibandronate, pamidronate, and zoledronic acid) and they have nitrogen-containing R'' side chains **(Figure 1-4)**. The presence of these chains increases the N-BP potency by 10 to 10,000 relative to nonnitrogen containing BPs[143]. The mechanism of action of N-BPs relies on their capability of inhibiting a specific step in the mevalonic acid pathway (**Figure 1-5**)[145]. The mevalonic acid pathway is an important metabolic pathway. The core of this pathway involves the synthesis of farnesyl diphosphate (FPP), and geranylgeranyl diphosphate (GGPP) which are involved in multiple cellular processes by synthesizing sterol isoprenoids, such as cholesterol, and non-sterol isoprenoids[146,147].

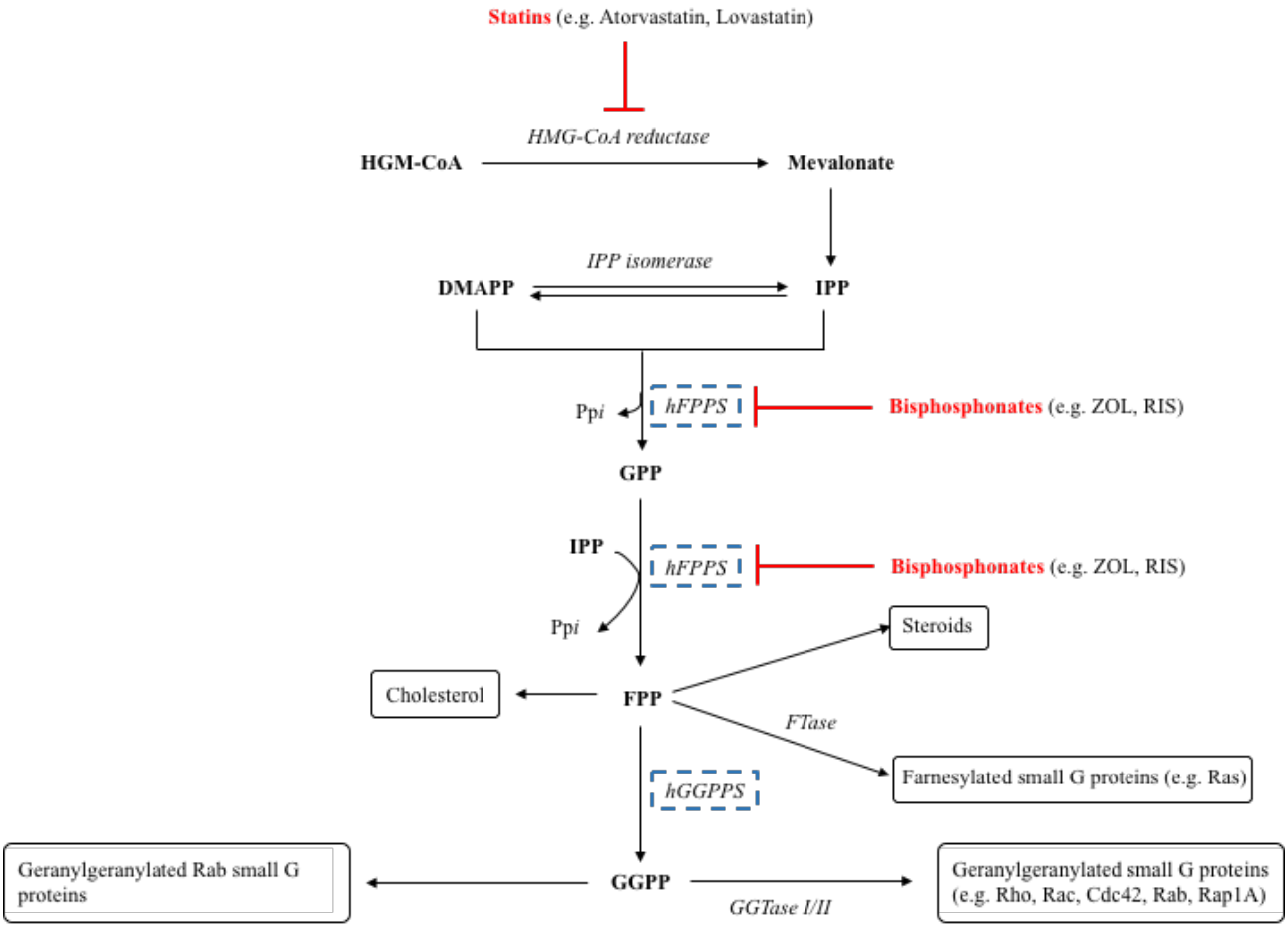

Figure 1-5: The mevalonic acid pathway

In 1999, van Beek et. al. confirmed that the specific molecular target of N-BPs is FPP synthase (*hFPPS* in **Figure 1-5**)[148]. FPP synthase is a key enzyme in isoprenoid biosynthesis that catalyzes the formation of FPP. As mentioned previously, FPP is a precursor for several classes of essential metabolites including sterols, carotenoids, and ubiquinones. FPP also serves as substrate for protein farnesylation and gernaylgeranylation. N-BPs bind to the geranyl diphosphate binding site of FPPS and act upon it[145]. However, N-BPs anti-resorptive properties do not raise from farnesylation inhibition but from the inhibition of protein geranylgeranylation. It has been reported that inhibition of protein geranylgeranylation prevents the formation of osteoclasts, disrupts osteoclast cytoskeleton, and induces apoptosis of osteoclasts[149]. In brief, the resorptive property of osteoclasts relies heavily on their ability to form the sealing zones and ruffled membranes at resorptive sites. It has been found that Cdc42, Rac and Rho are crucial to initiate the formation of the sealing zones and membrane ruffling[150]. N-BPs prevent geranylgeranylation of these GTP-binding proteins which has significant effects in the actin dynamics crucial for osteoclast function.

These small G-proteins that are being inhibited by N-BPs are also part of the integrin signaling pathway which is crucial for osteoclast survival and functions[151].

1.4.1.2. Antitumoral Effects of BPs

Although BPs are highly effective therapeutic agents for the treatment of MM bone disease there are additional *in vitro* studies that also demonstrate some anti-proliferative activity of N-BPs in MM and other cancer cell lines in a time and concentration-dependent manner[138,140,141,152-154]. The results from these studies demonstrated that various N-BPs decrease myeloma cell proliferation and induce apoptosis, while nonnitrogen containing BPs such as clodronate had little or no effect[152]. The mechanism of action for the anti-tumor activity of N-BPs is still not fully understood but the inhibition of FPPS, in the mevalonic pathway, is known to interfere with a variety of key cellular functions. FPP and GGPP are intermediates of this pathway and are required for the post-translational modification of G-proteins such as Ras, Rho, and Rac. These signaling molecules as mentioned previously are involved in the regulation of cell proliferation, cell survival, and cytoskeletal organization. Inhibition of the mevalonate pathway at the FPPS step is thought to be the main cause for the antitumoral activity of N-BPs[155]. Additionally, it has also been reported that when geranylgeraniol and farnesol, two intermediates of the mevalonate pathway, are added, they prevent the N-BP-induced apoptosis and partially reverse the cell cycle arrest[152]. Furthermore, inhibitory effects of N-BPs on tumor cell adhesion, invasion and migration *in vitro* also appear to be related to the inhibition of protein prenylation[156]. In addition, the high N-BP concentration in bone may have effects not only osteoclasts but also in additional cell types of the bone marrow microenvironment such as stromal cells or monocytes. By inhibiting osteoclastic activity, N-BPs could be affecting the secretion of growth factors from bone leading to a decreased tumor growth. N-BPs will not only affect the secretion of molecules from osteoclasts but will also decrease the secretion of growth factors and cytokines from osteoblasts, bone marrow stromal cells, monocytes and macrophages[157]. Finally, N-BPs could be exerting their antitumoral effect by inhibiting angiogenesis. Zoledronic acid has been shown to inhibit *in vitro* proliferation of human umbilical vein endothelial cells induced by bFGF, VEGF, or serum[158]. Furthermore, the antiangiogenic effect of N-BPs has also been confirmed in the 5T2 *in vivo* model of MM. Treatment of tumor-bearing mice with zoledronic acid reduced microvessel density in the myelomatous bone lesions[97].

However, antitumor effects of N-BPs observed in humans are considered minimal specially when used in single therapy and that might be due to the poor cell-membrane permeability and almost negligible distribution to non-skeletal tissues of these type of compounds[159,160].

In addition, several *in vivo* studies were performed using MM animal models and reported that BPs can be effective at reducing tumor burden in that setting[97,161]. 5T2 MM mice received zoledronic acid treatment and their survival was prolonged. Additionally, increased apoptosis of tumor cells *in vivo* has also been demonstrated both in murine models and in patients with MM[123,162]. The limitation of *in vivo* studies is to elucidate the mechanism underlying the antitumor effects since the antiresorptive effect of BPs by itself may influence tumor growth and survival in the bone marrow by reducing the levels of tumor growth and survival factors in the bone microenvironment[163,164]. Another mechanism of action of BP might be the effect on proliferation and survival of myeloma cells *in vivo* by inhibiting the release of growth factors from osteoblasts and bone marrow stromal cells[140,165].

1.4.1.3. ER Stress and UPR Response upon BP treatment of MM cells

The most important hallmark of MM is the high production of monoclonal protein by malignant plasma cells in the bone marrow of patients. For myeloma cells to produce such degree of antibodies they require very specific machinery. The endoplasmic reticulum (ER) is key in the protein folding process and in myeloma cells it needs marked restructuring and expansion during their differentiation[166]. When there is accumulation of unfolded proteins in the ER there is a consequent activation of an adaptive signaling cascade known as the unfolded protein response (UPR). Upon activation of the UPR there is regulation at all levels of gene expression including transcription, translation, translocation into the ER lumen and ER-associated degradation. This degradation occurs when there are misfolded proteins in the ER lumen which are directed towards degradation through the 26S proteasome or through autophagy. However, if the protein folding defect is not corrected and ER homeostasis is not reestablished there is chronic activation of the UPR signaling which eventually induces an apoptotic response[167]. Due to the increased requirement for dealing with secretory proteins within the ER, myeloma cells are highly dependent on the UPR pathway. Targeting the UPR has become a new strategy to target myeloma disease due to the high sensitivity of these cells to compounds that target the proteasome (e.g. proteasome inhibitor, bortezomib)[168]. However, it has also been reported that compounds that target the isoprenoid biosynthesis in the mevalonic pathway disrupt light chain trafficking and lead to

accumulation of light chain in the ER, activating the UPR pathway and inducing apoptosis. This could be an additional mechanism of action of N-BPs that induce apoptosis in myeloma cells[169].

1.4.1.4. Adverse Effects of BPs on Patients

An advantage of BPs is their high affinity for, and consequent deposition into bone relative to other tissues. This feature allows BPs to achieve a high local concentration throughout the entire skeleton[143]. BPs that are not bound to the skeleton are rapidly cleared from the circulation via renal elimination. An additional characteristic of BPs is their extreme hydrophilic profile and that they are only poorly absorbed from the gastrointestinal tract[170].

Due to the pharmacological features of BPs, patients suffer from short-term and long-term adverse effects during therapy. Examples of short-term side effects of BPs are upper gastrointestinal effects due to intolerance to oral BPs or acute phase reaction characterized by fever, myalgias, and arthralgias. This reaction probably reflects the activation of γδ T cells which causes the activation of antigenic receptor and induction of cytokine release, leading to inflammation. In addition, severe musculoskeletal pain and hypocalcemia might arise. Hypocalcemia occurs frequently after intravenous infusion and is often observed in patients with hypoparathyroidism or with impaired renal function. The most widely reported long-term adverse effect of BPs is osteonecrosis of the jaw (ONJ). The incidence of ONJ in patients with cancer who have received high doses of intravenous BPs has been estimated to be 1 to 10 per 100 patients. The risk of suffering ONJ increases in patients with poor oral hygiene, invasive dental procedures or denture use, and prolonged high doses of intravenous BPs. Lately, a new reduced dosing schedule in patients with MM showed to decrease the incidence of ONJ. Once established, care of ONJ is mostly supportive, with antiseptic oral rinses and antibiotics[171].

RESEARCH OBJECTIVES

The primary goal of this thesis is to present the MM field with a novel mouse model of MM and MM bone disease. The goal when developing our model was to improve upon the MM disease observed in the parental strain as well as the bone disease. This novel mouse model can then be used as a platform to study the disease and to test novel chemical entities that can target the malignant plasma cells as well as the osteolytic bone disease commonly observed and that causes many complications in MM patients.

The second goal of this thesis is to design and test novel bisphosphonate-like compounds that can inhibit proliferation of malignant plasma cells *in vitro* and that can also be used to treat our novel mouse model preclinically *in vivo*.

Finally, the third goal of this thesis is to genetically validate the target of the newly designed compounds (GGPPS) and to uncover in more detail the mechanism of action of these compounds.

A detailed summary of the objectives that were pursued can be found therein,

Objective 1. To develop and characterize a new hybrid transgenic model of MM and MM bone disease (Vk*MYC/KaLwRij).

- To characterize the MM disease in this model (incidence, disease burden, response to clinically used drugs, etc.).
- To characterize the MM bone disease that this mouse model develops:
    1. Focus on the abnormal osteoclast activity of the bone forming unit in our model
    2. Focus on mesenchymal stem cell impaired differentiation into osteoblasts.

Objective 2. To design and test bisphosphonate-like compounds that target GGPPS in the mevalonate pathway in order to target the MM disease.

- To test the effects on proliferation of the novel compounds *in vitro* using MM cell lines.

- To understand the mechanism of action of the novel bisphosphonate-like compounds (study of ER stress and UPR in MM cell lines treated with the compounds).

- To test the compounds *in vivo* using our novel Vk*MYC/KaLwRij mouse model of MM (e.g. efficacy of compounds and toxicity).

Objective 3. To genetically validate GGPPS as the better target of the newly created bisphosphonate-like compounds.

- To knock-down GGPPS and FPPS in the RPMI8226 MM cell line using lentiviral transduction of shRNAs.
- To knock-out GGPPS and FPPS using CRISPR/Cas9 novel technology in RPMI8226 MM cell line.
- To validate GGPPS as a target by assessing cell proliferation after GGOH withdrawal.
- To create a novel cell line with complete GGPPS KO after isolation of single cell clones.

CHAPTER 2. ENDOGENOUS OPG EXPRESSION BY PLASMA CELLS INHIBITS THE BONE PHENOTYPE IN A TRANSGENIC MURINE MODEL OF MULTIPLE MYELOMA

Mònica Gómez Palou[†], Daniel D. Waller, Xian Fang Huang, Radia Marie Johnson, Richard Kremer, Michael Sebag.

2.1. Abstract

Multiple Myeloma (MM) is the second most common hematological malignancy and up to 80% of MM patients develop osteolytic bone disease. Mouse models of MM are essential to study MM biology and bone disease development as well as to serve as preclinical platforms to test new chemical entities. We have generated a novel transgenic mouse model of MM by crossbreeding the original Vk*MYC strain with a substrain of C56/Bl6, KaLwRij, that is the basis for the 5T MM cell lines. This new transgenic substrain, the Vk*MYC/KaLwRij model, shows earlier onset of MM in addition to increased disease burden compared to the parental strain. Furthermore, we have characterized the bone phenotype of these mice and results show abnormal architecture of trabecular bone and affected bone surface. Further analysis has revealed an imbalance in the bone forming and resorbing unit in the skeleton of aged mice with quantifiable MM disease. Osteoclastic function and numbers were reduced in the Vk*MYC/KaLwRij mice opposed to what is expected in a model with MM. This model presents significantly increased serum levels of osteoprotegerin (OPG) and it was later confirmed that OPG is expressed by the malignant plasma cells in the bone marrow of these mice. An additional feature of the bone disease in this model was the impaired differentiation potential of the mesenchymal stem cells (MSCs) towards osteoblasts. RNA sequencing of MSCs from Vk*MYC/KaLwRij revealed a set of inflammatory signaling pathways (e.g. TNFα and NF-κB) significantly enriched which may be the reason behind osteoblastic inhibition in this model. In summary, we present a unique MM model that shows an uncoupling of the osteoblastic and osteoclastic units which can serve for the future development of strategies targeting MM and its associated bone disease.

2.2. Introduction

Multiple Myeloma (MM) is the second most common hematologic malignancy and one of the leading causes of cancer deaths[172]. The disease is characterized by the slow accumulation of malignant but fully differentiated B cells, plasma cells, in the bone marrow which interact with their microenvironment to alter their milieu in order to make it more favorable for their survival[9,173]. This interaction almost invariably leads to bone destruction leaving lytic lesions, pathologic fractures, vertebral collapses, pain, osteoporosis and hypercalcemia. Myeloma bone disease is the direct result of the disruption of the normal homeostatic mechanisms of bone in

which there is normally an equilibrium between bone formation and destruction by osteoblasts and osteoclasts respectively[17,50]. Uncoupling osteoclastic stimulation from osteoblastic function is the hallmark of this disease and a number of osteoclastogenic factors have been identified over the years including, IL-3, IL6, IL1b, and Macrophage Inflammatory Protein 1 alpha (MIP1alpha) also known as chemokine ligand 3 (CCL3). Many of these factors will ultimately work through the NF-kB receptor pathway (RANK), its ligand (RANKL) and its decoy inhibitor (OPG)[174,175]. OPG appears to play a pivotal role in osteoclastic function in MM bone disease, its absence and therapeutic implications of the pathway in which it acts have functional clinical significance. While the factors which stimulate osteoclasts are well identified, those that uniquely suppress the osteoblasts in MM bone disease are poorly identified and understood. It has been recognized early on that the unique hallmark of MM bone disease was osteoblastic impairment as bone samples from patients revealed no bone regeneration and functional impairment when osteoblasts are co-cultured with myeloma cells[176]. There is evidence for the inhibition of WNT signaling in mesenchymal stem cells (MSC) through DKK1 or sFRP3 as well as inhibition through soluble factors such as Hepatocyte Growth Factor (HGF), IL7, activin and sclerostin[177-179]. While these factors have been more recently identified to account for osteoblastic inhibition, many may converge on transcription factors such as Runx2/Cbfa1, crucial in MSC differentiation to osteoblasts, enabling the expression of osteocalcin and alkaline phosphatase, markers of terminal MSC/osteoblastic differentiation[180]. The net result is either a defect in the differentiation of MSCs to mature osteoblasts and/or a dysfunction of osteoblastic function. The mainstay of treatment for MM bone disease centers around good disease control as well as adjunctive agents such as bisphosphonates like zoledronic acid and recently targeted approaches such as RANKL inhibition by the monoclonal antibody, denosumab[89]. These strategies target the osteoclast but do little to reverse the osteoblastic impairment.

Mouse models of multiple myeloma bone disease are critical in understanding pathogenesis and to facilitate the development of novel therapeutic strategies. Although a number of MM mouse models have been described, few are able to faithfully reproduce the specific microenvironment of the malignant plasma cell in its intact bone marrow milieu in an immune competent context. The 5T2 mouse model relies upon the syngeneic transfer of MM cells from mouse to mouse and while useful it is difficult to propagate and its aggressive nature belies the slow indolent nature of human MM. In the SCID/Hu model human or rabbit (SCID/Rab) fetal bones are implanted in a

SCID mouse and are used as substrate for marrow microenvironment for subsequently injected primary myeloma cells[92]. These models are useful but do not represent the actual anatomical nature of this disease nor are they immunocompetent and therefore are not fully reflective of the microenvironmental reality in which MM cells live.

The Vk*MYC model has distinguished itself as one in which the characteristics of human MM are most faithfully reproduced. It involves the spontaneous activation of MYC in fully mature post germinal B cells and leads to the universal development of monoclonal gammopathies in mice as they age. As these mice accumulate CD138 positive plasma cells in their bone marrows they also manifest the features of MM, including bone disease, albeit an attenuated form with osteopenic bone as its principle characteristic[105]. The foundation of the 5T2 model is a substrain of C57/Bl6 mice, KaLwRij, which spontaneously develops gammopathies at a higher frequency than their parent strain and in which this predisposition has been mapped to the deletion of a single gene[95]. In this article we back-cross the Vk*MYC model to that of the KaLwRij mice in order to accelerate the myeloma phenotype and accentuate the bone phenotype. We characterize the resultant bone phenotype by radiological, histological and molecular techniques and elucidate a unique uncoupling of osteoclastic and osteoblastic activities. This model proves to be a unique platform for the study of osteoblastic function in the context of Multiple Myeloma.

2.3. Materials & Methods

2.3.1. Mice

Experiments were performed according to the guidelines of the Canadian Council on Animal Care and approved by the Animal Care Committee of the Research Institute of the McGill University Health Centre.

The Vk*MYC model, based on a C57/Bl6 background, was described previously in *Chesi, M., et al. (2008)*[105]. Vk*MYC (C57/Bl6) mice were backcrossed with KaLwRij mice more than ten times generating the Vk*MYC/KaLwRij mouse model. The presence of MYC transgene in all mice was confirmed by polymerase chain reaction (PCR) using tail genomic DNA as described elsewhere[105]. See supplemental data for nucleotide sequences. All experiments were performed with $n \geq 6$ mice per group.

Vk*MYC and KaLwRij mice strains were obtained from M. Chesi, Mayo Clinic Scottsdale, AZ and from Envigo (Envigo, Netherlands), respectively.

Mice heterozygous for the osteoprotegerin mutant allele (OPG knockout, *Tnfrsf11b*^{tm1Eac}) were obtained from the Jackson Laboratory (The Jackson Laboratories, Bar Harbor, ME) and bred with Vk*MYC/KaLwRij mice. Mice were genotyped by PCR using tail genomic DNA as described elsewhere[181]. Three groups of mice were bred to 60-70 weeks of age prior to analysis: OPG+/- Vk*MYC/KaLwRij, OPG-/- Vk*MYC/KaLwRij and OPG-/-KaLwRij.

2.3.2. Micro-computed Tomography Analysis and X-ray

Dissected L4 vertebrae of mice were immersed in a saline solution and scanned by micro-computed tomography (μCT) in a Bruker Skyscan 1172 (software Version 1.5, Kontich, Belgium). AI 0.5 filter with a spatial resolution of 8 μm and a voltage of 49 kV were used as scanning parameters. NRecon (Bruker, Version 1.6.8.0) and CTAn (Bruker CT Analyser software, Version 1.12.0.0) were used to construct 3D models and analyze the data, respectively. Three-dimensional morphological parameters including trabecular number (Tb.N.), trabecular thickness (Tb. Th.), connectivity density (Conn. Dn.) and bone surface (BS/BV) were recorded. Selected mice were also imaged using high resolution X-ray (In-Vivo Xtreme, Bruker, Billerica, MA).

2.3.3. Histomorphometric Analysis

Mouse vertebrae were embedded in plastic and sections were cut prior to histologic analysis as described previously[182]. To analyze osteoblastic and osteoclastic content, alkaline phosphatase (ALP) and tartrate resistant acid phosphatase (TRAP) stains were applied following sample processing. Regions of interest away from cortical bone and growth plates were selected and imaged using light microscopy (Leica DMR, ProgRes C14 camera, Wetzlar, Germany). Cells of interest were quantified by software analysis (Bioquant Nova Prime V 6.90.10., Bioquant, Nashville, TN).

2.3.4. Serum Analysis

Serum levels of osteocalcin, TRAP5b, MIP-1 α, osteoprotegerin and RANKL were measured using commercially available enzyme-linked immunosorbent assay (ELISA) kits following manufacturers' instructions. Osteocalcin levels were measured using Mouse Osteocalcin EIA Kit (Alfa Aesar, Haverhill, MA); TRAP 5b levels were measured using Mouse TRAP (TRAcP 5b)

ELISA (Immunodiagnostic Systems, The Boldons, UK). MIP-1 α, osteoprotegerin and RANKL levels were measured using Quantikine Elisa Mouse CCL3/MIP1α, Quantikine Elisa Mouse Osteoprotegerin/TNFRSF11B and Quantikine Elisa Mouse TRANCE/RANKL/TNFSF11 (R&D Systems, Minneapolis, MN), respectively.

2.3.5. Gene Expression Analysis

Bone marrow (BM) samples were collected by femoral flushing, red blood cells were lysed and plasma cells were enriched using CD138 immunomagnetic bead selection (Miltenyi Biotech, Bergisch Gladbach, Germany) and an autoMACS Pro Cell separator (Miltenyi Biotech, Bergisch Gladbach, Germany). Total RNA was isolated by RNeasy Mini Kit, (Qiagen, Germantown, MD) from both the CD138+ and CD138- BM fractions. Then reverse-transcribed into cDNA prior to further analysis with High-capacity cDNA Reverse Transcription kit (Applied Biosystems, Foster City, CA). Quantitative real-time PCR (qRT-PCR) was performed using the StepOne Plus Real Time PCR System and SYBR Green Master Mix (Applied Biosystems, Foster City, CA). Changes in relative gene expression between Vk*MYC/KaLwRij and KaLwRij samples were calculated using the $2^{-\Delta\Delta CT}$ method with normalization to β-actin. The following primer sets were used: OPG, forward primer (5'-CGGAAACAGAGAAGCCACGCAA-3') and reverse primer (5'-CTGTCCACCAAAACACTCAGCC-3'), and b-actin, forward primer (5'-CAGAAGGAGATTACTGCTCTGGCT-3') and reverse primer (5'-GGAGCCACCGATCCACACA-3').

2.3.6. Mesenchymal Stem Cell Isolation, Culture and Differentiation

Mesenchymal stem cell (MSC) isolation and culture protocol was performed as described previously[183], with the following modifications: following the isolation of bone marrow cells these were resuspended in Complete MesenCult Mouse Medium + Mesenpure (Stemcell Technologies, Vancouver, BC), followed by plating at a maximum cell density of 1.5 million cells/cm^2 and incubation at 37ºC and 5% CO_2 for 24 hours. After 24 hours, adherent cells were washed with phosphate-buffered saline and fresh media was added for an additional 48 hours of incubation following which they were counted and plated at a fixed density of $3x10^4/cm^2$ in 6-well plates. MSC differentiation was induced by 21 days of exposure to either MesenCult Osteogenic Stimulatory Mouse Media for osteoblasts or to MesenCult Adipogenic Stimulatory Mouse Media (Stemcell Technologies, Vancouver, BC) for adipocytes. Osteoblastic differentiation was

determined by quantifying *in vitro* mineralization (calcium deposits) using Alizarin Red S (Sigma, St. Louis, MO) and adipogenic differentiation was determined quantifying lipid vesicles using Oil Red O (Sigma, St. Louis, MO).

2.3.7. Quantification of *In Vitro* Mineralization

Cells were fixed with 4% paraformaldehyde (PFA) and stained with 40 mM Alizarin Red for 10 minutes. Images of wells were taken at 20x magnification using EVOS XL Core Cell Imaging System (Thermo Fisher, Waltham, MA). Percentage of area stained with Alizarin Red was quantified using ImageJ (Version 1.48v)[184] and values normalized to CFUs (colony formation units) stained with Methylene Blue.

2.3.8. Flow Cytometry

Flow cytometry for MSC surface characteristics was performed using antibodies against CD105 PE, CD138 PE and CD45 PE-Cy 5 according to the manufacturer's instructions (BD Biosciences, San Jose, CA), analyzed on a FACSCanto II cytometer (BD Biosciences, San Jose, CA) with FlowJo software (FlowJo, Version 10.0.7, Ashland, OR).

2.3.9. RNA Sequencing Data Analysis

RNA sequencing (RNAseq) of 3 KaLwRij and 3 Vk*MYC/KaLwRij mice MSCs was performed on total RNA isolated with RNAeasy Mini Kit (Qiagen, Germantown, MD) using a HiSeq 2500 (Illumina, San Diego, CA). Following sequencing, the reads were aligned to the mm10 mouse genome using STAR (Version 2.4.2) and counted with --quantMode GeneCounts[185]. Differential expression analysis was performed with the DESeq2 (Version 1.16.1) R Bioconductor package[186]. Pathway analysis was performed using the GAGE (Version 2.26.1) R Bioconductor package and mouse KEGG database[187]. All clustering and heatmap visuals were generated using ComplexHeatmap (Version 1.17.1) R Bioconductor package. Default parameters for this package were used[188].

2.3.10. Statistical Analysis

All assays were performed with 6 or more mice per group and all results are presented with standard deviations. Comparison between groups was accomplished using standard Student's T test and ANOVA regression analysis where appropriate.

2.3.11. Serum Protein Electrophoresis Analysis (SPEP)

Hydragel agarose gel and HYDRASIS LC (Sebia, Lisses, France) were used to perform SPEP on mice serum samples following manufacturer's instructions. Gels were scanned and SPEP band density was quantified using ImageJ (Version 1.48v)[184]. M-protein was considered as any band appearing below β_2 band on the gamma-zone of the gel. Monoclonal protein abundance was reported as a percentage of the total protein as described elsewhere and mice were considered to have Multiple Myeloma if their M proteins represented at least 15% of their total serum proteins[189].

2.3.12. Bone Surface Lesion Quantification

3D reconstructed images from L4 vertebrae cuts were used to quantify the number of bone surface lesions. ImageJ (Version 1.48v) was used to visualize and quantify the number of surface bone lesions.

2.3.13. qPCR and PCR cycling conditions and nucleotide sequences

Cycling conditions for gene expression analysis by qPCR of OPG and b-actin were the following: 95ºC for 10 min, 40 cycles of 95ºC for 15 sec, 55ºC for 30 sec, 72ºC for 30 sec, and melt curve conditions were 95ºC for 15 sec, 60ºC for 1 min and 95ºC for 15 sec.

Nucleotide sequences for MYC PCR:

Forward: 5'-ACATAATACACTGAAATGGAGCCC-3'

Reverse: 5'-ATACAGTCCTGGATGATGATG-3'

Cycling conditions for MYC PCR were the following: 94ºC for 15 min, 42 cycles of 94ºC for 30 sec, 56ºC for 1 min and 72ºC for 1 min, followed by 72ºC for 10 min.

Nucleotide sequences for OPG ($Tnfrsf11b^{tm1Ea}$) PCR:

5'-GGT CCT CCT TGA TTT TTC TAT GCC-3'

5'-TGC CCT GAC CAC TCT TAT ACG GAC-3'

5'-TGA CCG CTT CCT CGT GCT TTA C-3'

Cycling condition for OPG PCR were the following: 94ºC for 2 min, 10 cycles of 94ºC for 20 sec, 65ºC for 15 sec (-0.5ºC/cycle decrease) and 68ºC for 10 sec. These 10 cycles are followed by 28 cycles of 94ºC for 15 sec, 60ºC for 15 sec, 72ºC for 10 sec. Final step is 72ºC for 2 min.

2.3.14. Proliferation Capacity of MSCs

Proliferation capability of MSCs isolated from KaLwRij and Vk*MYC/KaLwRij mice was compared using a commercial MTS proliferation assay (Promega, Madison, WI) following the manufacturer's instructions. In short, MSCs isolated from KaLwRij and Vk*MYC/KaLwRij mice were seeded in 96-well plates at a density of 5,000 cells per well. Cells were incubated for 24 hours prior to addition of the MTS reagent. Plates were then incubated at 37ºC and 5% CO_2 for 2 hours prior to recording OD490 using a Tecan Infinite M200Pro microplate reader.

2.4. Results

2.4.1. Vk*MYC/KaLwRij MM Tumor Burden and Bone Loss.

C57Bl/KaLwRijHsd, a substrain of C57/Bl6 mice are known to have a higher and earlier incidence of monoclonal gammopathies than their parent strain[95].

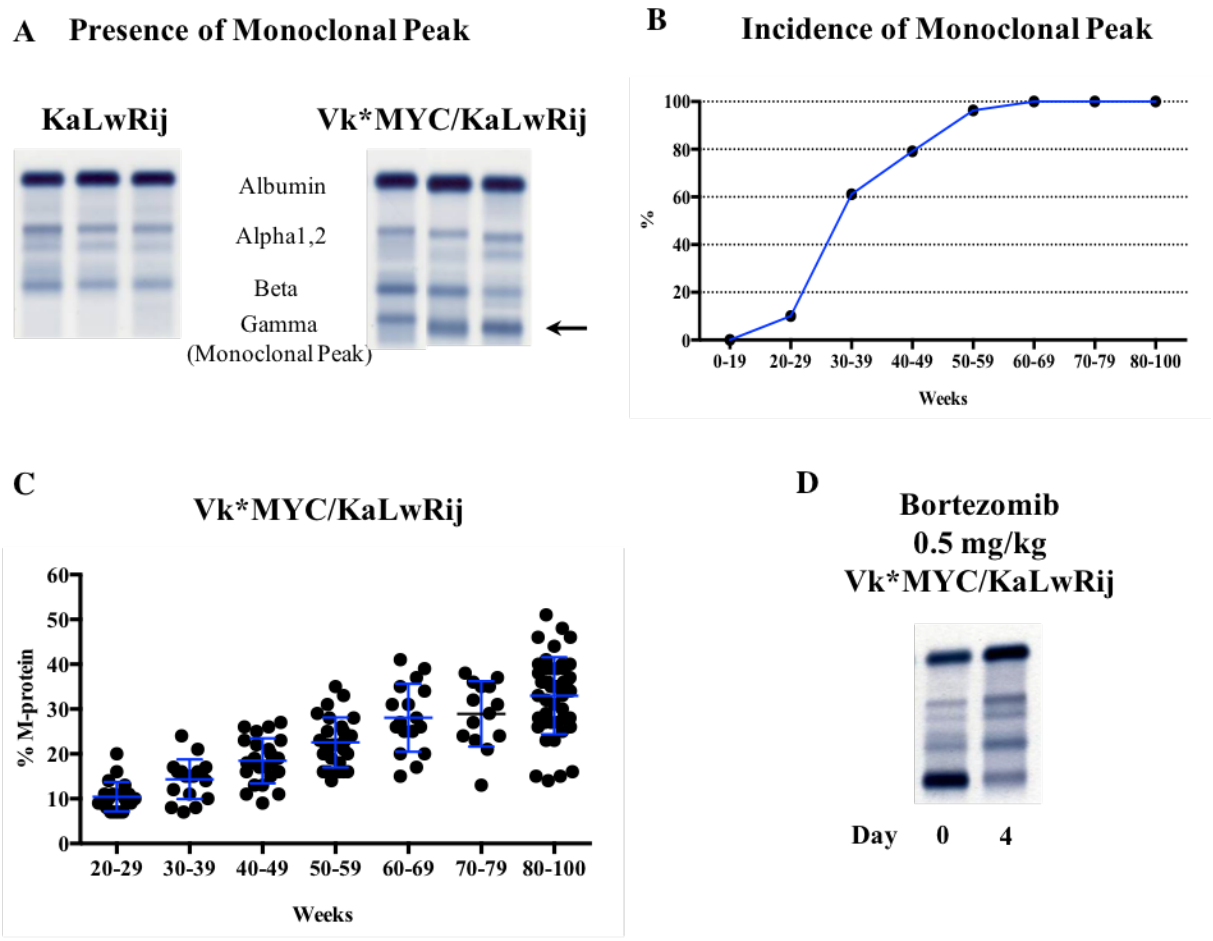

E

Weeks	% M-protein		Incidence
	Median	*Range*	*%*
20-29	10.45	(7.23-13.67)	10
30-39	14.23	(9.88-18.57)	61.11
40-49	18.38	(13.33-23-42)	79.16
50-59	22.56	(16.95-28.17)	96.29
60-69	27.99	(20.43-35.54)	100
70-79	28.89	(21.55-36.23)	100
80-100	32.98	(24.37-41.60)	100

Figure 2-1: Multiple Myeloma Disease Burden in the Vk*MYC/KaLwRij mouse model. (A) Representative SPEP gels from three KaLwRij and three Vk*MYC/KaLwRij mice. Serum albumin and alpha, beta, and gamma globulins are indicated. Arrow emphasizes monoclonal peak in Vk*MYC/KaLwRij mice. (B) Incidence of monoclonal peaks in Vk*MYC/KaLwRij for each age group. (C) Percentage of M-protein in total serum for each age group of Vk*MYC/KaLwRij mice. (D) In vivo treatment: M-protein decrease of 50% in Vk*MYC/KaLwRij mouse treated with four doses of Bortezomib (0.5 mg/kg). (E) Numerical summary of % M-protein and Incidence for each age group.

We crossbred this strain with Vk*MYC mice to potentiate the MM phenotype. We observed an age dependent increase in the incidence and quantity of monoclonal immunoglobulins which appears earlier in Vk*MYC/KaLwRij mice as compared to the Vk*MYC mice (**Figure 2-1A, B and E**). Additionally, the Vk*MYC/KaLwRij mice appeared to have higher burdens of disease at a given matched age, evidenced by a greater amount of M peak secreted as compared to the previously published original Vk*MYC mice (**Figure 2-1C and E**)[105]. To show that the Vk*MYC/KaLwRij mice strain have a similar pattern of clinical behavior to its parent strain, these were treated with four doses of bortezomib at 0.5 mg/kg and a similar but profound decrease in disease burden post treatment was observed suggestive of clinical phenotypic equivalency (**Figure 2-1D**)[15].

We next evaluated the extent of bone loss by Micro-CT analysis performed on the L4 lumbar vertebra of 50-week old Vk*MYC/KaLwRij mice with high MM disease burden (M peak representing >15% of total serum proteins) and compared it to age and gender matched KaLwRij controls. 3D reconstructions of micro-CT images are shown as examples of markedly reduced trabecular bone mass in Vk*MYC/KaLwRij mice compared to wild type KaLwRij controls **(Figure 2-2A)**. Quantitative measurements of static parameters affecting bone remodeling show significantly reduced trabecular numbers (Tb. N.) in Vk*MYC/KaLwRij mice (median Tb. N. 1.26, range 0.58–1.93, vs control median 2.05, range 1.64–2.45, $P \leq 0.05$) while trabecular thickness (Tb. Th.) was significantly increased (median Tb. Th. 0.062, range 0.049-.075, vs control median 0.043, range 0.041-0.045, $P \leq 0.01$) (**Figure 2-2B, C and Table 2-1)**. Abnormal trabecular architecture was also seen with a significantly decreased connectivity density (Conn. D.) in the Vk*MYC/KaLwRij mice lumbar vertebrae (median Conn.D. 78.65, range 18.51-138.79, vs control median 161.33, range 112.08-210.59, $P \leq 0.05$) (**Figure 2-2D and Table 2-1**).

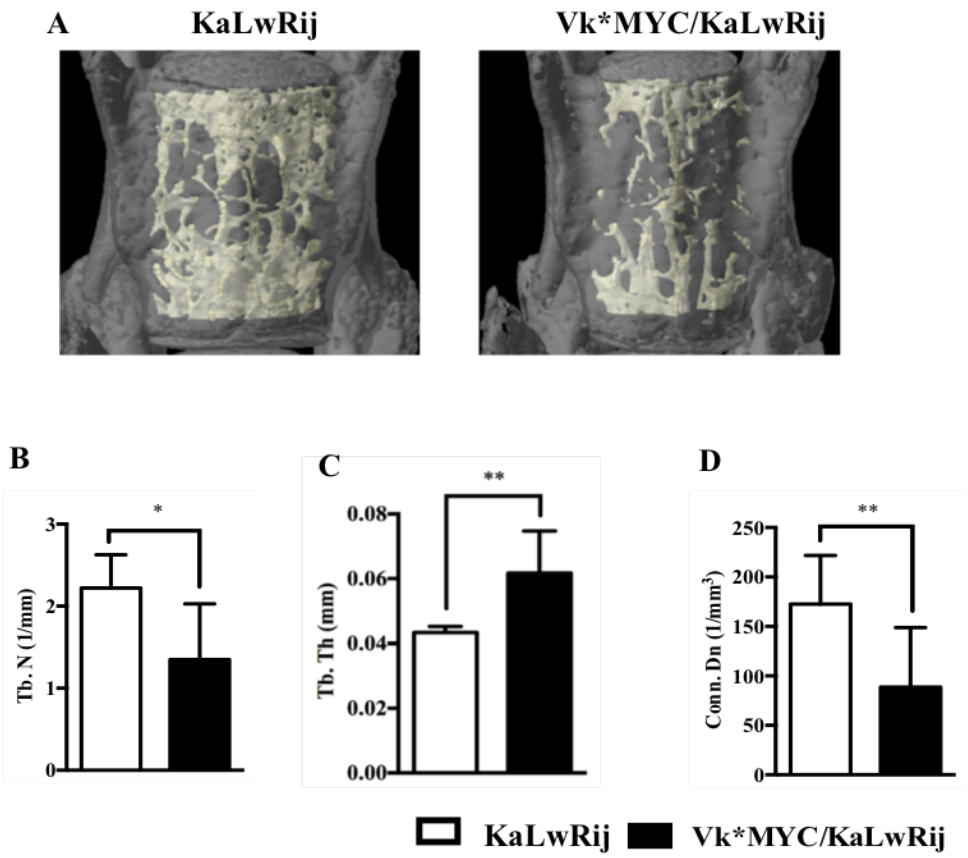

Figure 2-2: Micro-CT imaging demonstrates altered trabecular architecture in Vk*MYC/KaLwRij mice. (*A*) Representative 3D micro-CT images of L4 trabecular bone microarchitecture of KaLwRij and Vk*MYC/KaLwRij mice. Micro-CT quantitative analysis of KaLwRij and Vk*MYC/KaLwRij trabecular number (Tb.N.) (*B*), trabecular thickness (Tb.Th.) (*C*) and connectivity density (Conn.Dn.) (*D*). Error bars represent standard deviations. $^{*}P \leq 0.05$; $^{**}P \leq 0.01$.

Table 2-1: Trabecular number, thickness, connectivity density and bone surface/volume ratio number separation in KaLwRij and Vk*MYC/KaLwRij mice, analyzed by micro-computed tomography. Data given for all animals, with median and ranges indicated.

		KaLwRij		**Vk*MYC/KaLwRij**	
		Median	*Range*	*Median*	*Range*
Trabecular Number	1/mm	2.05	(1.64–2.45)	1.26*	(0.58-1.93)
Trabecular Thickness	mm	0.043	(0.041-0.045)	0.062**	(0.049-0.075)
Connectivity Density	$1/mm^3$	161.33	(112.08-210.59)	78.65*	(18.51-138.79)
Bone Surface/Volume Ratio	1/mm	76.73	(72.75-80.75)	67.22**	(60.75-73.70)

Vk*MYC/KaLwRij vs. KaLwRij
*$P \leq 0.05$ and **$P \leq 0.01$

In addition, micro-CT analysis shows that bone surface to volume ratio is significantly decreased in Vk*MYC/KaLwRij mice (median BS/BV 67.22, range 60.75-73.70, vs control median 76.73, range 72.75-80.75, P≤0.05) (**Figure 2-3A**), which correlates with the increased number of bone destructive lesions observed per fixed area (**Figure 2-3B**).

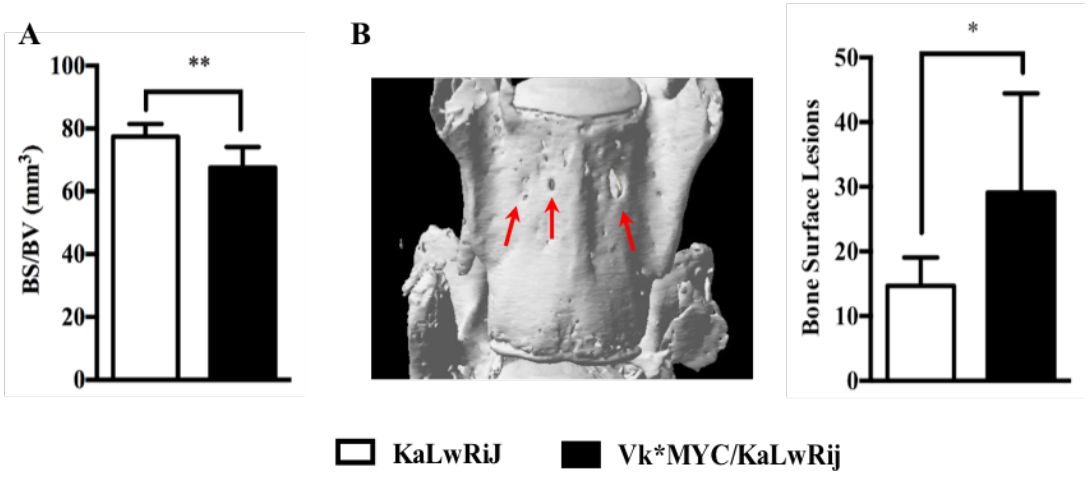

Figure 2-3: Bone surface to volume ratio and surface bone lesions. *(A)* Micro-CT analysis of bone surface to volume ratio (BS/BV). (*B*) Representative 3D micro-CT image of the bone surface of a Vk*MYC/KaLwRij mouse spine and number of bone surface lesions. The red arrows show surface bone lesions. Error bars represent standard deviations. *$P \leq 0.05$; **$P \leq 0.01$.

2.4.2. Both Osteoblast and Osteoclast Number and Function are Reduced in the Vk*MYC/KaLwRij Mouse Model.

Histomorphometric analysis of vertebrae (L4) from Vk*MYC/KaLwRij and control mice demonstrated in the former, a clear decrease in osteoblast number over a set bone perimeter (Ob/B.Pm.) as seen by alkaline phosphatase (ALP) staining **(Figure 2-4A and B)**. Osteoblastic function was also impaired in Vk*MYC/KaLwRij mice as shown by the significant decrease in osteocalcin serum levels **(Figure 2-4C)**.

To our surprise, histomorphometric analysis of L4 vertebrae also showed a decrease in tartrate-resistant acid phosphatase (TRAP) positive osteoclasts in Vk*MYC/KaLwRij mice as compared to controls (**Figure 2-4D and E**). Furthermore, biomarker serum analysis reveals significantly decreased levels of TRAP 5b, a marker of osteoclast activity, in Vk*MYC/KaLwRij mice compared to the wild type mouse strain (**Figure 2-4F**).

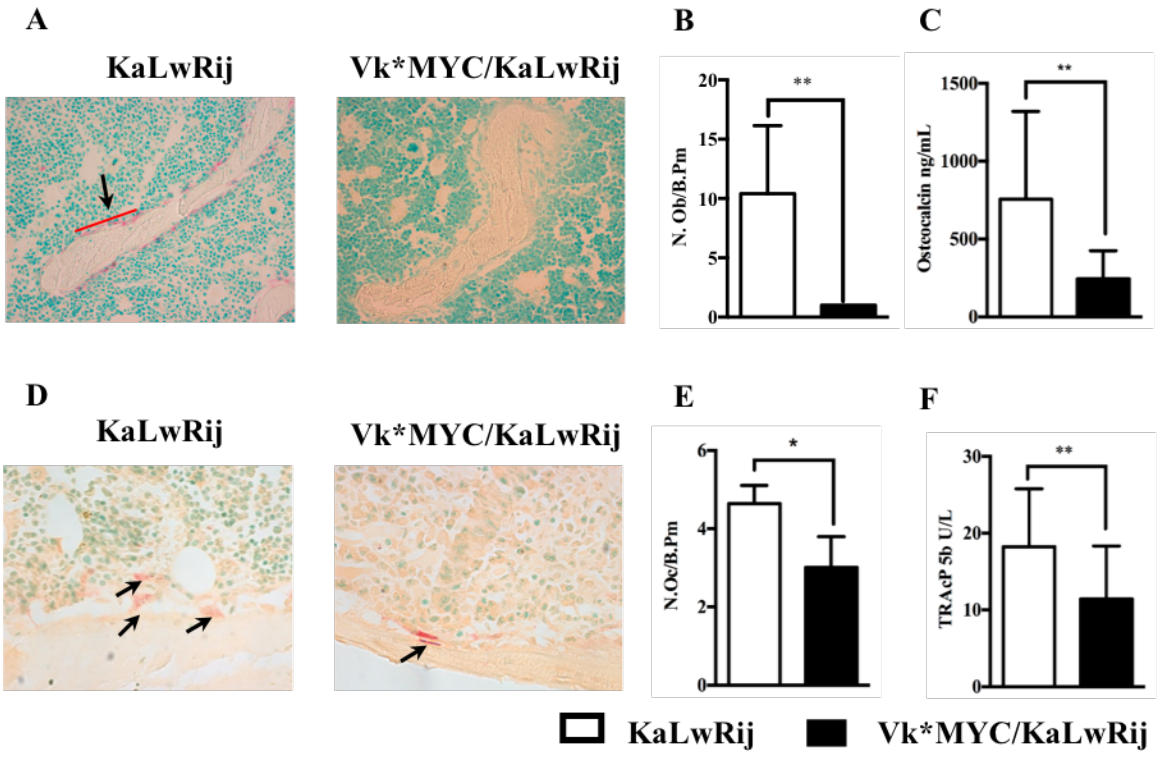

Figure 2-4: Vk*MYC/KaLwRij mice present significantly reduced osteoblast and osteoclast number and function. (*A*) Representative micrographs of KaLwRij and Vk*MYC/KaLwRij L4 vertebra sections stained with alkaline phosphatase (ALP). 20x Magnification. Arrow and red line point at positive staining of

osteoblasts. *(B)* Osteoblast number relative to bone perimeter (N.Ob/B.Pm) in L4 vertebra of KaLwRij and Vk*MYC/KaLwRij mice. *(C)* Osteocalcin serum levels in KaLwRij and Vk*MYC/KaLwRij mice. *(D)* Representative micrographs of KaLwRij and Vk*MYC/KaLwRij L4 vertebra sections stained with tartrate-resistant acid phosphatase (TRAP). 40x Magnification. Arrows point at positive stained osteoclasts (*E*) Osteoclast number relative to bone perimeter (N.Oc/B.Pm) in L4 vertebra of KaLwRij and Vk*MYC/KaLwRij mice. (*F*) TRAcP 5b serum levels in KaLwRij and Vk*MYC/KaLwRij mice. Error bars represent standard deviations. $^{*}P \leq 0.05$; $^{**}P \leq 0.01$; $^{***}P \leq 0.001$.

2.4.3. Rank-RankL Mediated Osteoclastogenesis is Intact in Vk*MYC/KaLwRij Mice with MM.

To investigate the mechanism of unexpected osteoclastic inhibition in this model, we first looked at serum levels of RANKL and osteoprotegerin (OPG) in Vk*MYC/KaLwRij mice and wild type mice by ELISA assay. We observed that OPG serum levels were surprisingly and significantly increased in Vk*MYC/KaLwRij mice compared to the wild type mice (median OPG 5376.15 range 7901.93-2850.37, vs control median 3811.54 range 5061.76-2561.31, P≤0.01) **(Figure 2-5A)**. We observed no difference in RANKL serum levels between these two strains (**Figure 2-5B**). We then looked at the correlation between osteoclastic activity in Vk*MYC/KaLwRij mice as determined by serum TRAP levels and serum levels of OPG (**Figure 2-5C**). We found a statistically significant inverse relationship between the amount of circulating OPG and the amount of osteoclastic activity in aged Vk*MYC/KaLwRij with MM. Interestingly, MM disease burden, as determined by M protein as a function of total serum proteins, also correlated with serum OPG levels (**Figure 2-5D**) in aged Vk*MYC/KaLwRij mice, suggesting that as these mice acquire an MM phenotype and plasma cells accumulate in their bone marrows, OPG production is paradoxically increased. To determine the origin of persistent OPG production in this model, bone marrow cells were harvested from both Vk*MYC/KaLwRij mice with high disease burden and from normal wild type mice. Immunomagnetic bead separation using an anti-CD138 antibody was used to isolate plasma cells from bone marrow specimens and OPG gene expression levels were examined in both the CD138 positive and negative fractions using qPCR. OPG gene expression was significantly elevated in the CD138 positive plasma cell population from Vk*MYC/KaLwRij mice, indicating that the major expression of OPG originates from plasma cells (**Figure 2-6A**).

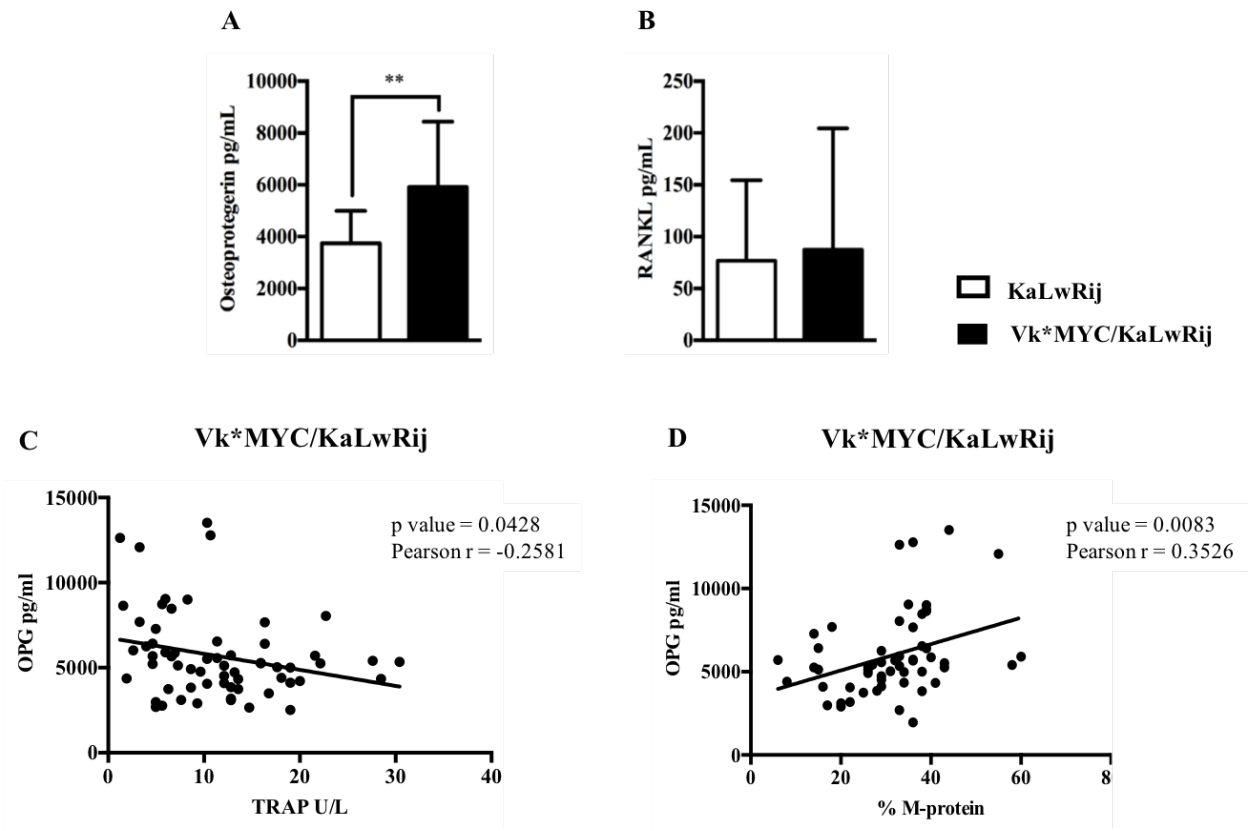

Figure 2-5: OPG and RANKL serum levels and correlation analysis. *(A,B)* OPG and RANKL serum levels. *(C)* Correlation of OPG with TRAcP 5b in Vk*MYC/KaLwRij. *(D)* Correlation between OPG serum levels and percentage of M-protein in serum of Vk*MYC/KaLwRij mice. Error bars represent standard deviations. $^{**}P \leq 0.01$.

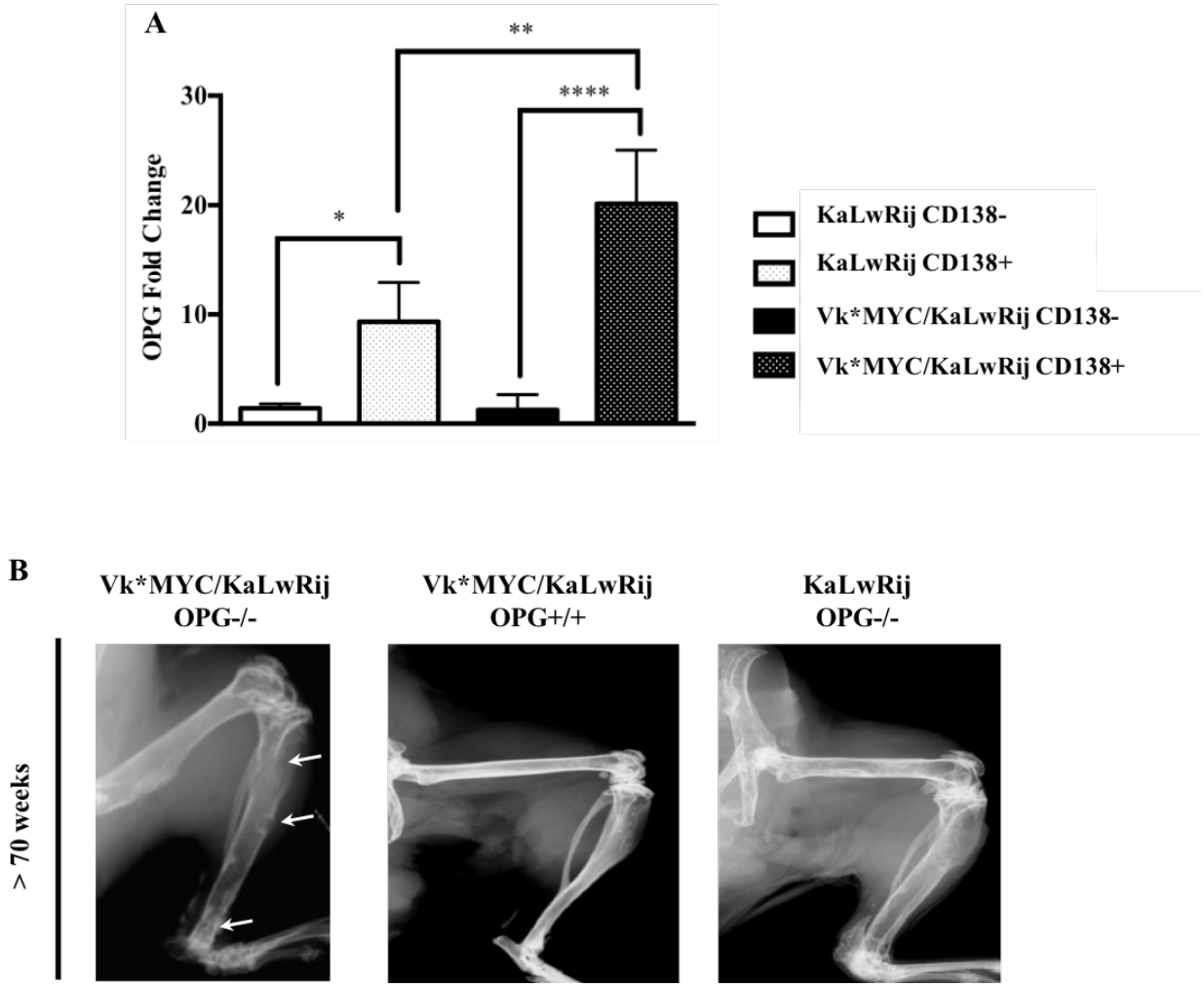

Figure 2-6: OPG gene expression levels and x-ray imaging analysis. *(A)* Osteoprotegerin gene expression analysis in CD138 positive and CD138 negative bone marrow cells from KaLwRij and Vk*MYC/KaLwRij mice. *(B)* Representative x-ray imaging of distal femur and proximal tibia of KaLwRij OPG-/- mice (left), Vk*MYC/KaLwRij OPG+/+ mice (middle), and Vk*MYC/KaLwRij OPG-/- mice (right). White arrows in left panel point to bone lytic lesions observed. Error bars represent standard deviations. $^{*}P \leq 0.05$; $^{**}P \leq 0.01$; $^{****}P \leq 0.0001$.

XBP1s expression was used to further confirm the identity of the OPG expressing plasma cells post CD138 selection (**Figure 2-7A**). In contrast, MIP1-α serum levels were found to be higher in Vk*MYC/KaLwRij than in controls **(Figure 2-7B)** suggesting that in absence of OPG downregulation, MIP1-α is not sufficient to promote osteoclastogenic activity. Finally, assuming that OPG plays a pivotal role in MM bone disease in our model, we attempted to reverse the

osteoclastic impairment phenotype by breeding Vk*MYC/KaLwRij mice with OPG knockout mice of the same C57/Bl6 background ***(Tnfrsf11b^{tm1Ea})*.** Though the parental OPG knockout strain of mice shows profound developmental abnormalities, are difficult to significantly age and invariably show severely osteoporotic bones (data not shown), they do not demonstrate outright lytic lesions (**Figure 2-6B**) by X ray imaging. Mice expressing the Vk*MYC transgene that are homozygous for the OPG knockout, survive beyond 70 weeks with measurable MM disease burden were seen to exhibit X-ray detectable macro lytic lesions of bone (**Figure 2-6B**). In contrast none of the Vk*MYC/KaLwRij mice with intact OPG production were seen to exhibit large enough lytic lesions to be detectable by X-ray.

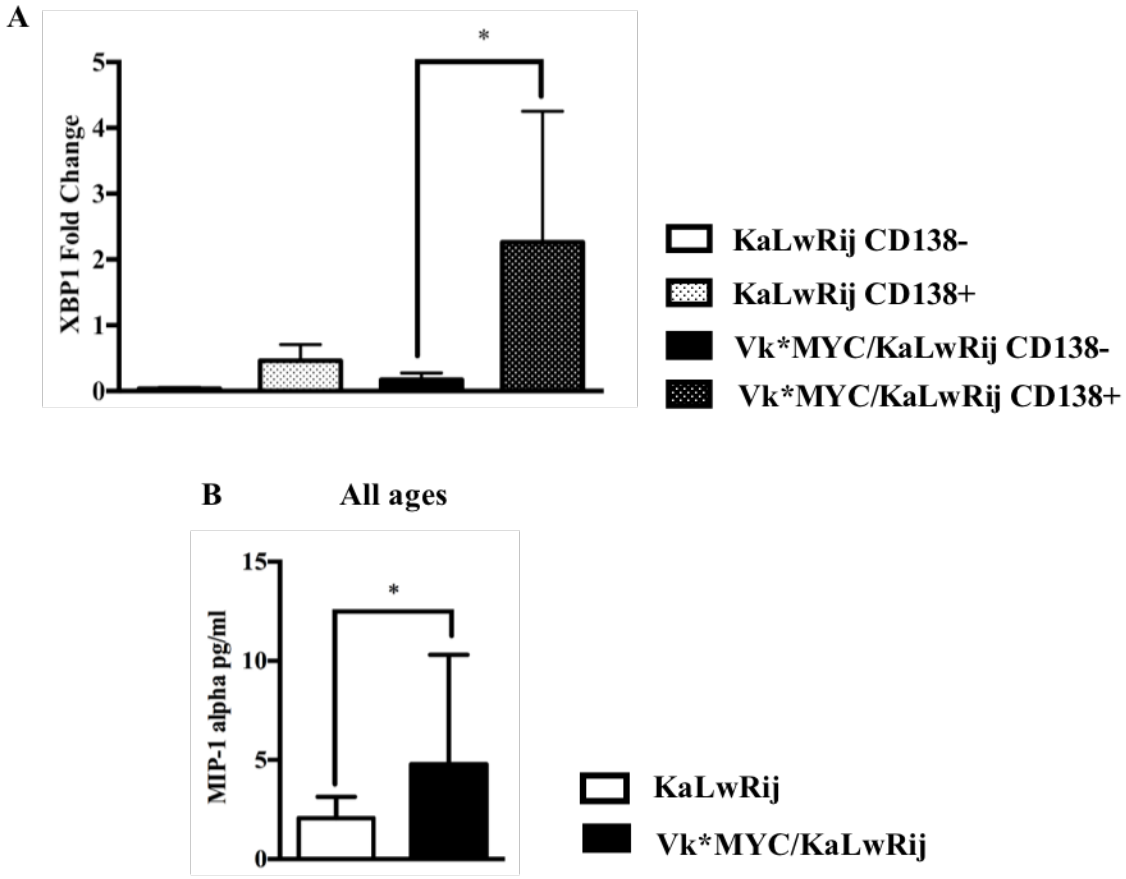

Figure 2-7: Xbp1 gene expression in plasma cells and MIP1-alpha levels in serum of mice. *(A)* XBP1 gene expression analysis in CD138 positive and CD138 negative bone marrow cells from KaLwRij and Vk*MYC/KaLwRij mice. Error bars represent standard deviations. $^{*}P \leq 0.05$. *(B)* MIP1-alpha serum levels

in KaLwRij and Vk*MYC/KaLwRij mice of all age groups. Error bars represent standard deviations. $^{*}P \leq 0.05$.

2.4.4. Vk*MYC/KaLwRij Mice Show Impaired Differentiation of Bone Marrow Mesenchymal Stem Cells (MSCs) into Osteoblasts.

To determine the mechanism of osteoblastic impairment we looked at the potential for *ex vivo* bone marrow derived mesenchymal stem cells to differentiate into osteoblasts in our mouse model. MSCs from both Vk*MYC/KaLwRij and controls were cultured from harvested mouse bone marrows using established protocols[183]. Flow cytometric analysis confirmed isolation of pure MSCs with low CD45 and high CD105 expression with little plasmacytic or lymphocytic (CD138 and 45) contamination (**Figure 2-8A**). We next evaluated the differentiation potential of purified MSCs by inducing them to differentiate into adipocytes (**Figure 2-8B and C**) or into osteoblasts following dexamethasone and vitamin C exposure.

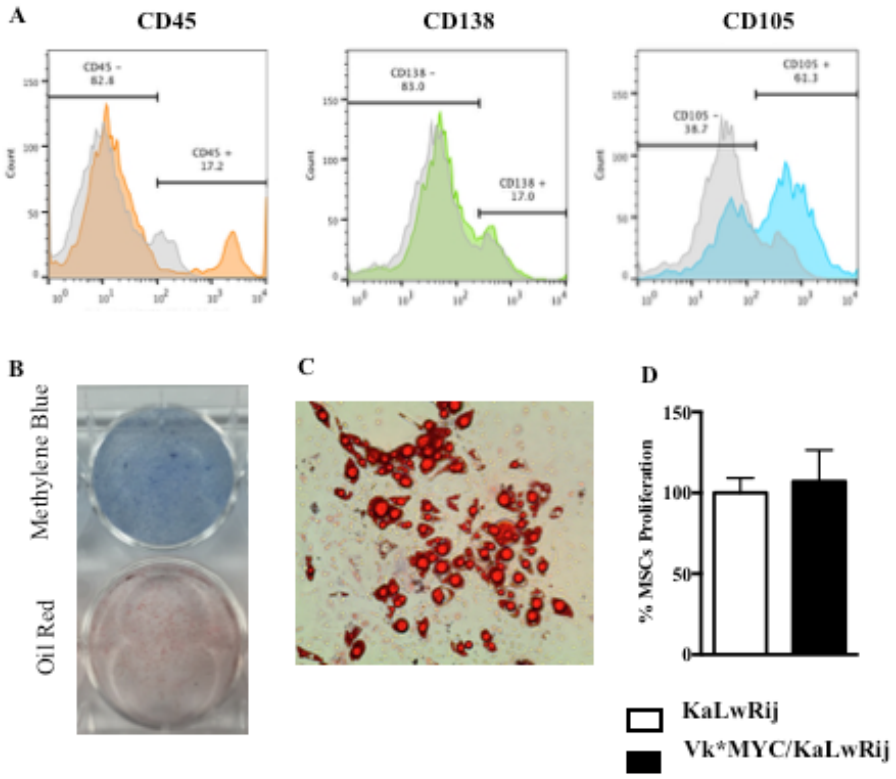

Figure 2-8: Characterization of MSCs from Vk*MYC/KaLwRij mice. *A*) Representative flow cytometry analysis of cell-surface markers of freshly isolated MSCs from a Vk*MYC/KaLwRij mouse. Proportion of CD45 negative, CD105 positive and CD138 negative cells in bone marrow is >80%, >60% and <17%,

respectively. (*B*) Oil Red staining of adipocyte differentiated MSCs isolated from bone marrow of KaLwRij mice. (*C*) Representative image of Oil Red stained adipocytes differentiated from MSCs. 20x Magnification. *(D)* Comparison of proliferative capacity of MSCs from KaLwRij and Vk*MYC/KaLwRij mice. Data normalized to proliferation capacity of KaLwRij MSCs. Error bars represent standard deviations.

Our results show a significantly reduced mineralization capacity of MSCs isolated from Vk*MYC/KaLwRij mice compared to the wild type mouse strain as evidenced by alizarin red staining for mineralization and methylene blue for cell colony content (**Figure 2-9A and B**). To show that the impairment lies with the differentiative rather than the proliferative capacity of MSCs from Vk*MYC mice we looked at the proliferation of MSCs from these two groups of mice over a 24hr period and we observed that these did not significantly differ (**Figure 2-8D**).

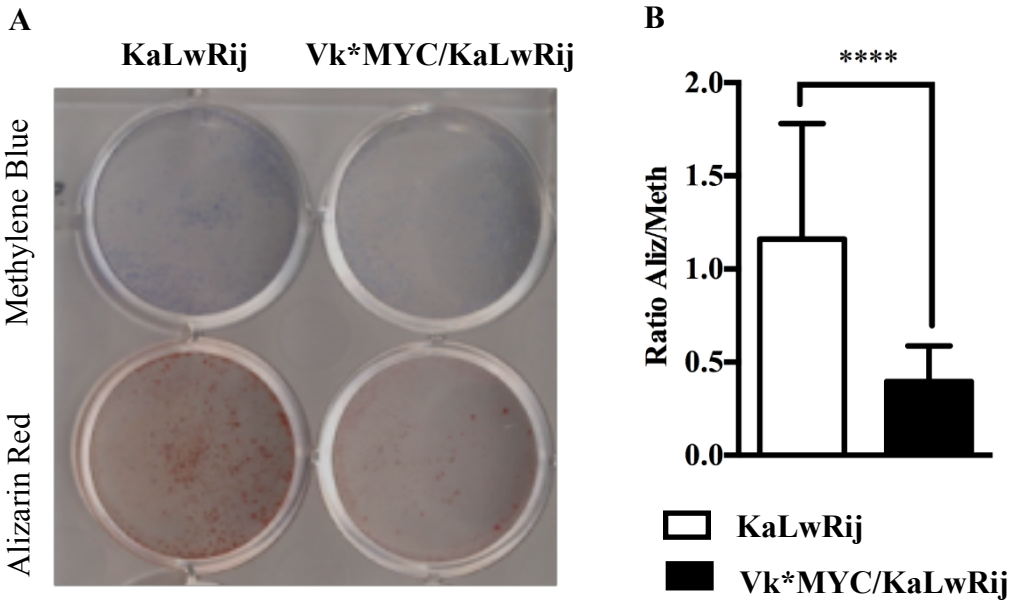

Figure 2-9: *In vitro* osteoblastic differentiation of MSCs from bone marrow of Vk*MYC/KaLwRij mice is impaired. (*A*) Methylene blue and Alizarin Red staining of osteoblast differentiated MSCs isolated from bone marrow of KaLwRij and Vk*MYC/KaLwRij mice. (*B*) Quantitative analysis of mineralization by Alizarin Red S/Methylene Blue ratio. Error bars represent standard deviations $^{****}P \leq 0.0001$.

2.4.5. RNA Sequencing of Mesenchymal Stem Cells Isolated from Vk*MYC/KaLwRij and Wild Type Mice.

We performed whole transcriptome analysis by RNA sequencing to elucidate differences between gene expression in MSCs from Vk*MYC/KaLwRij and those from wild type controls which have retained the ability to differentiate into osteoblasts.

Generally Applicable Gene-set Enrichment for Pathway Analysis (GAGE) was used to obtain a list of significantly up- and down-regulated signaling pathways that are differentially expressed in Vk*MYC/KaLwRij vs. wild type (**Table 2-2**). Heatmaps showing differential expression of genes across gene sets are also shown (**Figure 2-10).** We observed that Vk*MYC/KaLwRij derived MSCs exhibit an inflammatory like signature with upregulation of NFKB, NOD like receptor signaling and TNF receptor signaling. Interestingly TNFα features prominently in all of these gene sets, consistent with its role in impairment of osteoblastic differentiation[190].

Table 2-2: KEGG pathway enrichment results. Table presents top upregulated and downregulated enriched signaling pathways in MSCs from Vk*MYC/KaLwRij versus KaLwRij (qvalue < 0.2).

Upregulated

Signaling Pathway	Count	pvalue	qvalue	Genes
NOD-like receptor signaling pathway	8	2.64E-10	5.43E-08	*Gbp2, Gbp7, Casp1, Naip7, Ccl2, Tnf, Gbp2b, Casp8*
Toll-like receptor signaling pathway	2	8.74E-07	9.01E-05	*Tnf, Casp8*
NF-kappa B signaling pathway	3	0.0003	0.0192	*Card14, Plau, Tnf*
Antigen processing and presentation	3	0.0005	0.0192	*Rfx5, H2-Q2, Tnf*
RIG-I-like receptor signaling pathway	4	0.0006	0.0192	*Map3k1, Ifih1, Tnf, Casp8*
Lysosome	3	0.0008	0.0207	*Gla, Manba, Scarb2*
TNF signaling pathway	3	0.0029	0.0550	*Ccl2, Tnf, Il15*

Chemokine signaling pathway	3	0.0047	0.0816	*Lyn, Cxcl13, Ccl2*
Natural killer cell mediated cytotoxicity	3	0.0091	0.1448	*Tnf, Tnfsf10, Itgal*

Downregulated

Signaling Pathway	**Count**	**pvalue**	**qvalue**	**Genes**
Ribosome	2	1.63E-08	3.35E-06	*Rps3a1, Mrps6*
ECM-receptor interaction	4	0.0020	0.1302	*Comp, Lama1, Sv2c, Col4a1*
Metabolism of xenobiotics by cytochrome P450	3	0.0022	0.1302	*Gstm6, Gstm7, Gstm4*
Valine, leucine and isoleucine degradation	2	0.0027	0.1302	*Acadm, Hmgcs2*
Hippo signaling pathway	9	0.0031	0.1302	*Wtip, Nkd1, Wnt11, Gdf5, Gli2, Dlg2, Tead2, Lef1, Wwc1*
Glutathione metabolism	5	0.0046	0.1598	*Lap3, Gstm7, Gstm2, Gstm4, Gstm6*
Focal adhesion	8	0.0063	0.1874	*Comp, Lama1, Pak7, Col4a2, Col4a1, Parva, Actn4, Itga3*
Oxidative phosphorylation	2	0.0073	0.1891	*Atp4a, Cox6b2*
Pyruvate metabolism	3	0.0090	0.1947	*Fh1, Ldhb, Me3*
Propanoate metabolism	3	0.0094	0.1947	*Acadm, Ldhb, Bckdhb*
Protein digestion and absorption	4	0.0112	0.1948	*Col4a2, Col4a1, Col6a3, Xpnpep2*

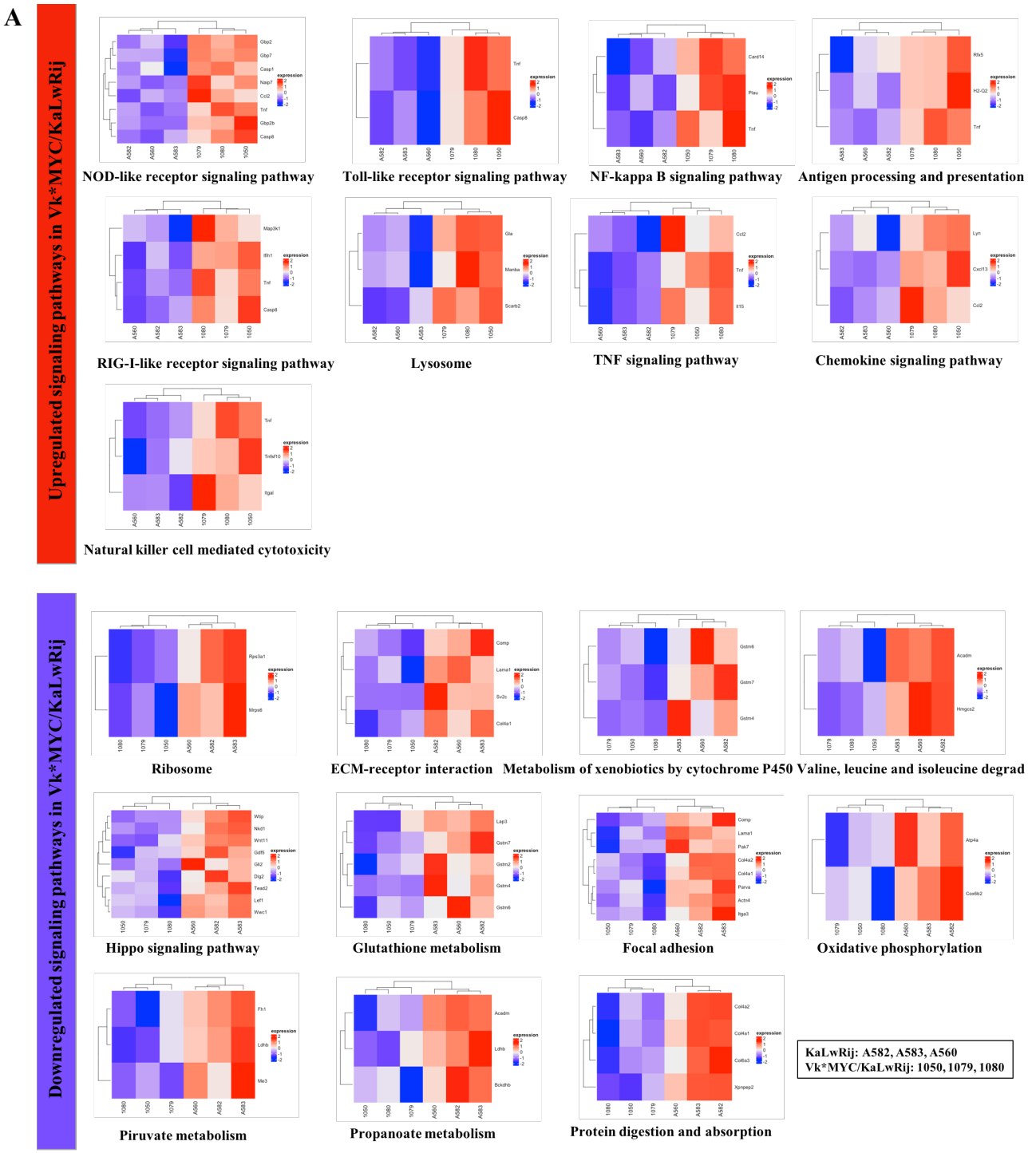

Figure 2-10: Heatmaps representing differential expression of genes upregulated and downregulated from each enriched signaling pathway from Vk*MYC/KaLwRij MSCs.

2.5. Discussion

While other mouse models of bone disease have existed for some time now, none have been described in the context of a model which faithfully recapitulates the clinical phenotype of human multiple myeloma. The transgenic Vk*MYC model with its C57Bl/6 background, has been shown to be clinically very similar to human MM, it invariably arises in older animals, it is a slow and indolent disease, its principle clinical manifestation is anemia and most importantly the bone marrow restricted clonal plasma cells appear to have the same sensitivity to pharmacologic intervention as its human counterpart[105]. In the original description of the model, however, osteopenia was the predominant bony manifestation with only the occasional lytic lesion or spinal compression observed. While the lack of dramatic bone disease in the Vk*MYC model may be due to the latency of onset of MM as well as slow MM cell doubling time and clinical progression, we set out to enhance the bone phenotype and understand its behavior. The KaLwRij mouse model was originally described almost 50 years ago by Radl *et al*.[191] and are said to be predisposed to developing the benign precursor to MM, MGUS, at a very high rate. While KaLwRij mice with MGUS may eventually develop MM, they do so at a very low rate and incidence, something akin to the rate of progression of the human equivalent. From this C57Bl/6 substrain, numerous mouse primary cell lines have been isolated and form the basis of a transplantable form of MM which does include an aggressive form of MM bone disease[92]. Further analysis of the background of KaLwRij mice has revealed several significant germline mutations and deletions which may explain its predisposition to gammopathy, these include a deletion of *Samsn1* which can increase B cell proliferation as well as affect the bone marrow microenvironment through macrophage functional alteration all of which can promote MM tumorigenesis[95]. We reasoned that combining the Vk*MYC model's ability to invariably produce MM with the increased propensity of the KaLwRij model to develop gammopathies may lead to an earlier and more enhanced MM and bone phenotype. Our first observation is that, indeed, the Vk*MYC/KaLwRij mice do develop gammopathies earlier than the parent Vk*MYC strain and that furthers their disease burden, as evidenced by a greater proportion of the M peak representation of the total serum protein. Despite this increased burden of disease this new strain seemed to exhibit the same sensitivity to at least one anti-MM drug suggesting that this has not altered its clinical phenotype to the point of not resembling the human clinical disease.

As our primary focus was to characterize the bone phenotype of this new strain, we observed significant bone loss, as evidenced by reduced trabecular numbers, increased trabecular thickness, deceased connectivity density and bone surface structural changes of the lumbar vertebrae of Vk*MYC/KaLwRij as compared to that of age and gender matched KaLwRij control mice. While these results are not directly compared to the parent Vk*MYC strain, they nonetheless represent a heavy burden of bone disease as well as some bone surface changes, however a frank preponderance of osteolytic lesions was still not apparent. While histomorphometric and serum analysis confirmed an undeniable decrease in the number and the function of bone osteoblasts in Vk*MYC/KaLwRij mice as compared to controls, we were not able to demonstrate the predicted increase in osteoclastic activity. This was consistent in both our histological and serum results. While the cornerstone of MM bone disease is undoubtedly osteoblastic inhibition, it is almost always accompanied by osteoclastic stimulation. Although soluble serum levels of RANKL were the same in both control and Vk*MYC/KaLwRij mice the OPG serum levels differed significantly and unexpectedly. In contrast to human MM where OPG levels are depressed and probably derived from bone marrow mesenchymal cells[174], the Vk*MYC/KaLwRij mice showed persistently increased OPG serum levels which appear to originate from the MM cells themselves. MIP-1 α has also been shown to be a powerful stimulator of osteoclastic function in MM and indeed levels of MIP-1 α are actually higher in Vk*MYC/KaLwRij than in the controls. These results suggest that despite other mechanisms of osteoclastic stimulation, an intact RANK-RANKL axis is absolutely necessary for osteoclastic function. OPG production alone may explain the lack of florid osteolytic lesions in this model. The mechanism of persistent OPG production by MM cells in this model remains unexplained and will be the focus of future studies. We do note however that OPG is normally produced by bone marrow stromal cells and osteoblasts, at least in humans[192]. A number of cytokines have been identified which promote osteoclastogenesis, including TNF-a, IL-6, IL-17, IFN-g, IL-4, IL10, IL-12 and IL-18. The results of our MSC RNAseq profiling suggests that these cytokines are most likely present in the bone marrow microenvironment since their downstream effects are evident in the upregulated gene sets. However, the presence of OPG alone is again, sufficient to abrogate the effects of these cytokines on osteoclastic production. Of interest, not all non-xenographic mouse models of MM demonstrate bone disease, the KaLwRij based 5T model appears to have several lines in which lytic bone lesions predominate while other lines in which it is absent[193]. The 5T2 line appears to be associated with aggressive bone disease while the

same mice when injected with 5T33 cells do not get bone disease[100]. In fact, it would appear that the 5T33 model appears to have high serum concentrations of OPG, possibly explaining its absence of osteoclastic activity, though the source of that OPG was not elucidated[194]. It would appear that mice with a C57BL/6 background (as are the KaLwRij) have B cells that produce OPG as they mature into plasma cells, in contrast to humans[195] where the OPG is derived from mesenchymal cells. This is consistent with our observation that even CD138 selected normal non MM plasma cells from normal (non-transgenic) mice showed expression of OPG. We suspect that for bone disease to appear in C57BL/6 derived mice, OPG has to somehow be repressed or its expression silenced. Non-xenographic murine models of MM that demonstrate bone disease, in particular the 5T2 model, has been specifically selected for its ability to cause osteolysis and in the course of its propagation, that cell line has silenced OPG, probably epigenetically, though this remains speculative.

By contrast, we report here that osteoblastic inhibition through the impairment of their differentiation from mesenchymal stem cells recapitulates what has been reported in human MM bone disease. Histomorphometric analysis showed a net decrease in osteoblast numbers in Vk*MYC/KaLwRij mice as compared to controls as well as decreased in osteoblastic function as evidenced by decreased osteocalcin serum levels. Bone marrow derived mesenchymal stem cells were carefully isolated and identified and while their ex vivo proliferative potential did not differ between experimental and control animals their ability to differentiate into osteoblasts was severely impaired despite being physically removed from both bone marrow MM cells and their native microenvironment. This is a phenomenon which is readily seen in human MM. RNAseq analysis of the MSCs derived from Vk*MYC/KaLwRij mice have upregulated inflammatory pathways which include the TNF and NF-κB signaling pathways. DKK1 suppression of the WNT signaling pathway is said to play a crucial role in the inhibition of osteoblastogenesis in human MM[196]. In addition, DKK1 may also have a role in increasing the RANKL/OPG ratio thereby contributing to osteoclastogenesis[79]. Both of these phenomena were not observed in this unique mouse model, leading us to believe that though the MSCs ability to differentiate into osteoblasts is as profound as it is in the human disease, its mechanism is more likely the result of cytokine exposure. Of the cytokine pathways that were upregulated in Vk*MYC/KaLwRij derived MSCs, TNF-α and NF-κB are the most prominent. Both have been shown to play a role in osteoblastogenesis: TNF-α has been shown to inhibit the recruitment of osteoblastic precursors

from progenitor cells as well as suppress RUNX2 and its co activator TAZ in addition to osterix, all leading to impairment of osteoblastic differentiation[197,198]. NF-κB likely also plays an important role in the cytokine mediated impairment of osteoblasts. Importantly, it has been shown that NF-κB can prevent MSC differentiation into osteoblasts by increasing the degradation of beta catenin[190]. In this mouse model, it may be that NF-κB and TNF-α play a far more important role in osteoblastic impairment than does DKK1 in human MM, though the end result and the mechanisms for that end result are likely very similar.

Of interest, we noted an increase in signaling pathways that are the direct result of TGF-β, though these did not individually reach significance, collectively they suggest that TGF-β may play an important role in this model. TGF-β is implicated in the terminal differentiation of osteoblasts, though our model appears to be impaired earlier in its differentiation[199]. In addition, TGF-β has also been shown to upregulate mouse OPG expression, making it an interesting target for both the osteoblastic and osteoclastic phenotype observed here[200].

Taken together, these results show that the Vk*MYC/KaLwRij transgenic model offers a unique and interesting platform for studying MM bone disease. We have demonstrated that OPG plays a crucial role in determining if bone disease is going to develop in murine models of MM and that the source of that OPG, unlike in human disease, is the plasma cell (both benign and malignant). The model itself remains of interest as the uncoupling of osteoblasts from osteoclasts observed here represents a novel opportunity to study and possibly intervene using strategies that specifically target osteoblastic function.

CONNECTING TEXT

In Chapter 2, a novel transgenic mouse model of MM and MM bone disease has been presented, the Vk*MYC/KaLwRij model. Mouse models of MM are essential tools to first, understand the mechanisms behind myeloma disease development and second, to use as preclinical models in the development and testing of novel chemical entities or molecules to treat MM. This study successfully characterized the MM disease in the Vk*MYC/KaLwRij mice by showing monoclonal protein secretion quantifiable by SPEP in addition to showing an increased disease burden compared to their parental strain, the Vk*MYC model. M-protein production is a surrogate biomarker of MM disease burden in humans and it is fundamental that MM mouse models recapitulate this feature since it is the most direct tool to quantify the effectiveness of novel administered drugs in the mice.

Bisphosphonates are the mainstay of MM bone disease treatment and have been associated with, albeit moderate, antitumoral properties. *N*-BPs drugs, such as zoledronic acid are clinically validated selective inhibitors of human farnesyl pyrophosphate synthase (hFPPS)[201]. This property predicts antitumoral activity, however, BPs are hampered by their poor biopharmaceutical properties such as their high polarity, poor cell-membrane permeability and high affinity for bone[85]. For these reasons the development of novel BPs is an area of interest not only because of their action inhibiting osteoclastogenesis in MM but also for their potential as anti-myeloma drugs.

The third chapter of this thesis focuses on the development and testing of novel bisphosphonates with improved pharmacologic properties. The goal of the next study was to design and test novel inhibitors that target the geranylgeranyl pyrophosphate synthase (GGPPS) which is downstream of hFPPS in the mevalonate pathway. MM cell lines were used to test the novel GGPPS inhibitors and the Vk*MYC/KaLwRij mouse model, previously characterized, was used to test the effectiveness of these compounds *in vivo*. The mechanism of action of the newly developed inhibitors of GGPPS was also studied.

CHAPTER 3. UNRAVELING THE PRENYLATION-CANCER PARADOX IN MULTIPLE MYELOMA WITH NOVEL GGPPS INHIBITORS

Cyrus M. Lacbay[†], Daniel D. Waller[†], Jaeok Park, Mònica Gómez Palou[†], Félix Vincent, Xian Fang Huang, Viviane Ta, Albert M. Berghuis, Michael Sebag, Youla S. Tsantrizos

3.1. Abstract

Post-translational prenylation of the small GTP-binding proteins (GTPases) is vital to a plethora of biological processes, including cellular proliferation. We have identified a new class of thienopyrimidine-based bisphosphonate (ThP-BP) inhibitors of the human geranylgeranyl pyrophosphate synthase (hGGPPS) that block protein prenylation in multiple myeloma (MM) cells leading to cellular apoptosis. These inhibitors are also effective in blocking the proliferation of other types of cancer cells. We confirmed intracellular target engagement, demonstrated the mechanism of action leading to apoptosis and determined a direct correlation between apoptosis and intracellular inhibition of hGGPPS. Administration of a ThP-BP inhibitor to a MM mouse model, confirmed *in vivo* downregulation of Rap1A geranylgeranylation and reduction of monoclonal immunoglobulins (M-protein, a marker of disease burden) in the serum. These results provide the first proof-of-principle that hGGPPS is a valuable therapeutic target and more specifically for the treatment of multiple myeloma.

3.2. Introduction

Post-translationally modified proteins, with either farnesyl pyrophosphate (FPP) or geranylgeranyl pyrophosphate (GGPP), constitute approximately 2% of the total mammalian proteome[202]. Known farnesylated proteins include members of the small GTP-binding proteins (GTPases), such as the Ras superfamily (e.g. H-Ras, K-Ras, N-Ras)[203], DnaJ chaperone proteins[204,205], and the precursor of the nuclear lamin A[206]. Geranylgeranylated GTPases include the Rho family of proteins (*e.g.* RhoA/B/C), the Ras-related proteins Rap1A and Rac-1, and Cdc42. Prenylation of small GTPases provides them with the ability to associate specifically with cellular membranes and participate in a plethora of cellular functions, including cell signaling and proliferation[207].

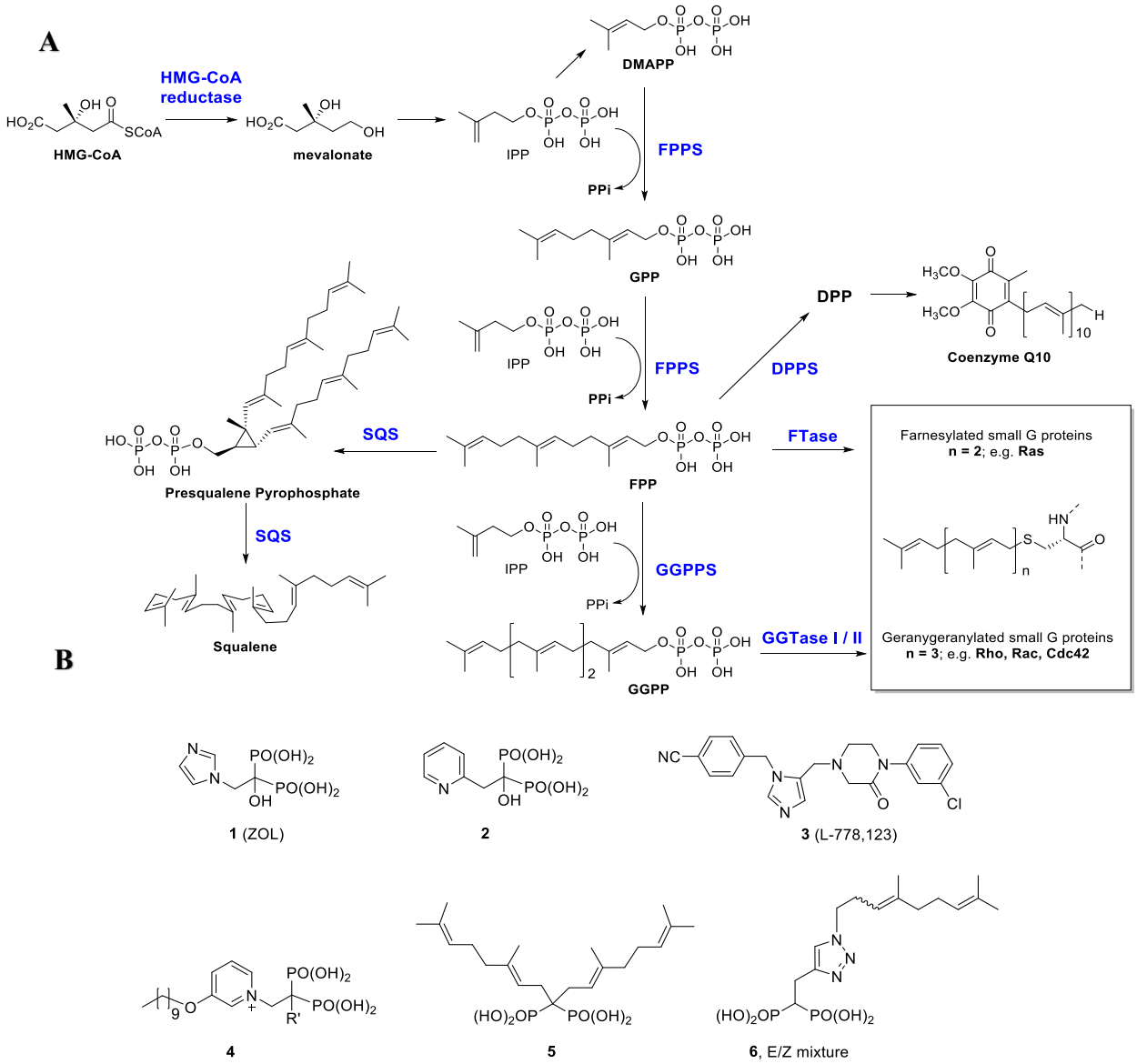

Figure 3-1: Isoprenoid substrates and inhibitors of prenylation. (a) Sequence of biochemical steps involved in the biosynthesis of isoprenoids. (b) Structures of inhibitors ZOL (1) and RIS (2) of hFPPS; L-778,123 (3) is a dual inhibitor of FTase and GGTase I; compound 4 is a dual inhibitor of hFPPS and hGGPPS; compounds 5 and 6 are selective inhibitors of hGGPPS.

There is a growing awareness that dysregulation of the mevalonate pathway plays a crucial role in oncogenesis and tumor cell survival[208-210]. In the past, targeting this pathway has focused mainly on inhibiting the human farnesyl pyrophosphate synthase (hFPPS) and the prenyl transferases FTase and GGTase I (**Figure 3-1A**). Indirect inhibition of prenylation with statins[211-213] has also been under clinical investigation and implicated in better survival of patients with multiple

myeloma (MM)[214]. Nitrogen-containing bisphosphonates (*N*-BPs; **Figure 3-1B**), such as zoledronic acid (**1**; ZOL) and risedronic acid (RIS; **2**) are clinically validated inhibitors of hFPPS that are used mainly for the treatment of skeletal disorders[215,216]. Additionally, the potential value of *N*-BPs as antitumor agents has been explored in numerous studies both *in vitro* and *in vivo*. For example, clinical trials in breast cancer[217-220] and MM[83,221] have shown improved outcomes for patients treated with standard of care chemotherapy plus ZOL (**1**) and the effects appeared to be unrelated to the skeletal benefits of this drug. However, there is an on-going debate as to whether *N*-BPs are *bona fide* antitumor agents, since their antitumor effects in humans are minimal when used in monotherapy. The modest clinical antitumoral efficacy of ZOL has been attributed to its poor cell-membrane permeability, rapid clearance from the systemic circulation, and almost negligible distribution to non-skeletal tissues[159,160]. Consequently, more recent drug discovery efforts have focused towards the identification of non-bisphosphonate allosteric inhibitors of hFPPS[222-225]. Numerous structurally diverse compounds have been reported; unfortunately, none of them exhibit any significant antitumor potency. Efforts directed at blocking the prenyl transferase enzymes FTase and GGTPase I have also received significant attention. Several compounds, including the dual FTase/GGTPase I inhibitors L-778,123 (**3**)[226,227], were advanced to clinical development. However, after a number of disappointing clinical trials with FTase inhibitors, it was realized that a biochemical redundancy mechanism allows cross prenylation and activation of Ras proteins (which are common drivers of oncogenesis) by GGTPase I, when FTase is inhibited[228,229].

The human geranylgeranyl pyrophosphate synthase (hGGPPS) is not yet a clinically validated therapeutic target. Only a few selective inhibitors of this enzyme have been reported and none advanced to clinical development. The precision with which hGGPPS identifies its substrates surpasses our current understanding of the molecular recognition elements required to design potent and highly selective inhibitors for this target. Although the volume of the hGGPPS active site cavity is larger than that of its functionally related upstream enzyme, hFPPS, this information alone does not provide sufficient guidance in the design of selective and drug-like inhibitors. Known inhibitors of hGGPPS include the pyridinium bisphosphonate **4**[230,231], and the substrate bioisosteres **5**[232] and **6**[233] (**Figure 3-1B**). Compound **4** exhibiting negligible selectivity between hFPPS and hGGPPS[230], whereas **5** and **6** are much more selective in inhibiting hGGPPS. Triazole

E/Z-**6** is currently the most potent hGGPPS inhibitor known (IC_{50} value of 45 nM)[233,234]. Interestingly, the *E/Z* mixture of **6** is more potent that either one of its pure isomers and presumed to bind cooperatively in both the FPP substrate and the GGPP product sub-pockets of hGGPPS[234]. However, crystallographic confirmation of the exact binding mode of this compound has yet to be realized.

In this report, we present a novel chemotype of thienopyrimide-based bisphosphonate (ThP-BP) inhibitors of hGGPPS. Analogs were identified that exhibit toxicity in various cancer cell lines and are particularly toxic to human myeloma cells, blocking prenylation and inducing apoptosis. The antimyeloma potency of some ThP-BP analogs is equivalent to that of doxorubicin while exhibiting far lower toxicity to healthy cells. Strong evidence of intracellular engagement of hGGPPS (by these inhibitors) was observed that correlates with their antimyeloma activity both in cellular assays and *in vivo*. The antimyeloma effects of prenylation inhibitors is a topic of significant interest. However, the necessity to develop selective inhibitors of hGGPPS has been intensely debated[231]. In principle, inhibitors of hFPPS are expected to directly block activation of FPP-dependent and indirectly GGPP-dependent GTPases; the latter as a consequence of intracellular depletion of the FPP substrate of hGGPPS (*e.g.* ZOL blocks geranylgeranylation of Rap 1A[235]). In this report, we provide data from a large panel of human MM cell lines and MM patient bone marrow specimens suggesting that hGGPPS is a far more valuable therapeutic target for multiple myeloma than hFPPS.

3.3. Materials & Methods

3.3.1. General Procedures for Purification and Characterization of Compounds

Chemicals and solvents were purchased from commercial suppliers and used without further purification. Normal phase column chromatography on silica gel was performed using a CombiFlash instrument using the solvent gradient, as indicated. Reverse phase preparative HPLC was carried out using a Waters Atlantis Prep T3 OBD C18 5µm 19 x 50 mm column; Solvent A: H_2O, 0.1% formic acid; Solvent B: CH_3CN, 0.1% formic acid; Mobile phase: gradient from 95% A and 5% B to 5% A and 95% B in 17 min acquisition time; flow rate: 1 mL/min. The homogeneity of final inhibitors was confirmed to be ≥ 95% by reversed-phase HPLC using a Waters ALLIANCE® instrument (e2695 with 2489 UV detector, 3100 mass spectrometer, C18 5µm

column): Solvent A: H_2O, 0.1% formic acid; Solvent B: CH_3CN, 0.1% formic acid; Mobile phase: linear gradient from 95% A and 5% B to 0% A and 100% B in 13 min. Key compounds were fully characterized by ^{1}H, ^{13}C, ^{31}P NMR and HRMS. Chemical shifts (δ) are reported in ppm relative to the internal deuterated solvent. The NMR spectra of all final bisphosphonate inhibitors were acquired in D_2O (either after conversion to their corresponding tri-sodium salt or by addition of ~2% ND_4OD) or in DMSO-d_6. In some cases, the Cα to the bisphosphonate was broad and overlapped with the solvent peak, as confirmed by HSQC NMR studies. The high-resolution MS spectra of final products were recorded using electrospray ionization ($ESI^{+/-}$) and Fourier transform ion cyclotron resonance mass analyzer (FTMS). The HRMS data for inhibitors **10a-c**, **11a-c**, and **12** were acquired from the corresponding trisodium salt of the bisphosphonic acid.

Synthesis - Part I:

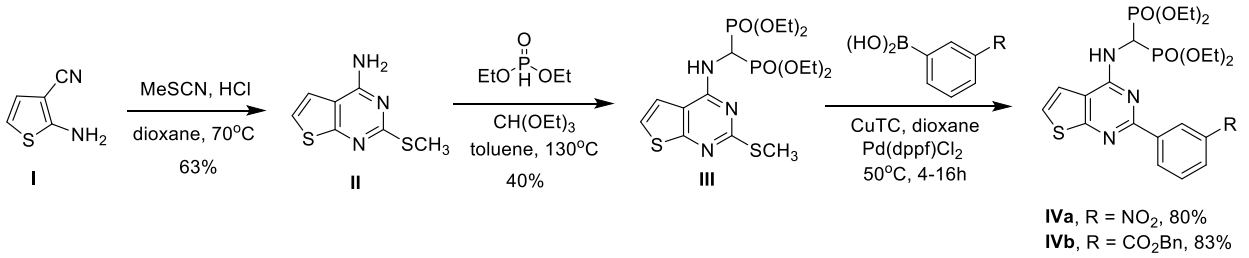

Synthesis - Part II:

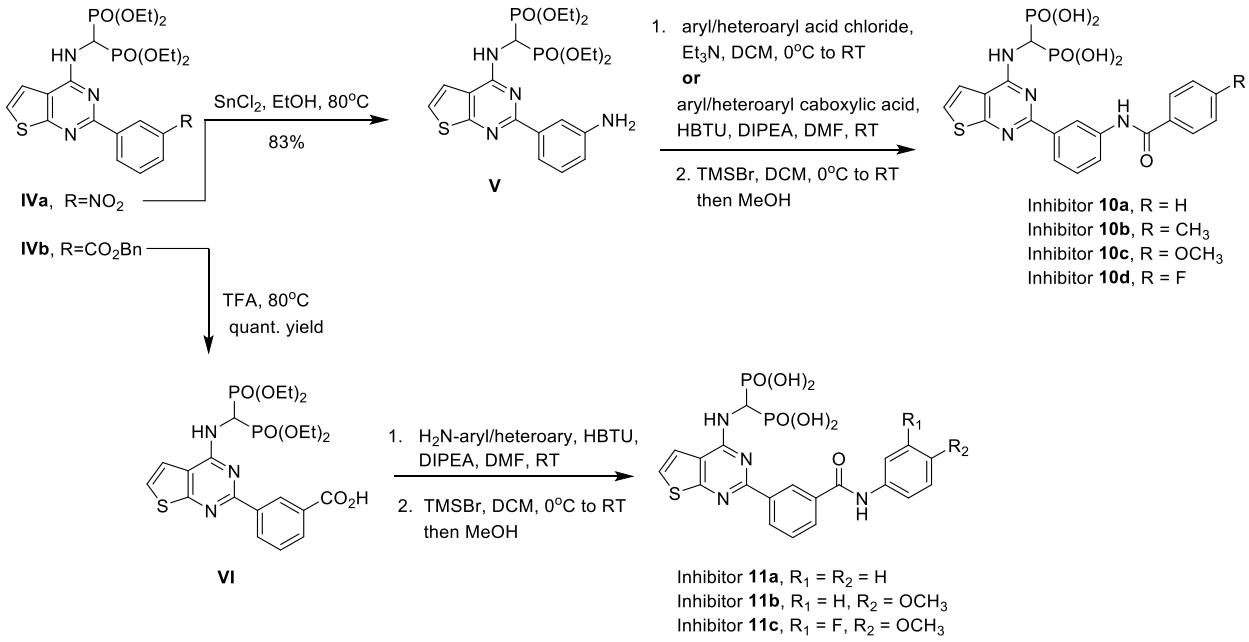

Figure 3-2: Parallel Synthesis of Compound Library. Part I-Synthesis of basic scaffolds IVa and IVb; Part II-Synthesis of analogs, including examples 10a-d and 11a-c

3.3.2. General Synthetic Protocols

Synthesis of 2-(methylthio)thieno[2,3-d]pyrimidin-4-amine (**II**):

2-Amino-5-methylthiophene-3-carbonitrile (**I**; 2.5g, 20 mmol) was added to HCl (4M in dioxane; 30.2 mL, 121 mmol), followed by methyl thiocyanate (1.4 mL, 20 mmol). The resulting suspension was heated to 70 °C in a sealed pressure tube for 36 h. The mixture was allowed to cool to RT and the resulting green precipitate was collected by vacuum filtration. The solid was dissolved in EtOAc, washed with saturated aqueous $NaHCO_3$, and the aqueous phase was extracted further

with EtOAc. The combined organic extracts were washed with brine, dried over Na_2SO_4, and concentrated *in vacuo*. Intermediate **II** was obtained as a light brown solid (2.52g, 63%), and was used in the next step without further purification. ^{1}H NMR (500 MHz, DMSO-d_6): δ 7.55 (br_s, 2H), 7.47 (d, *J* = 5.9 Hz, 1H), 7.36 (d, *J* = 5.9 Hz, 1H), 2.46 (s, 3H). ^{13}C NMR (126 MHz, DMSO-d_6): δ 167.5, 166.5, 158.3, 120.7, 120.2, 113.4, 13.8. MS [ESI$^+$] *m/z*: 198.0 [M + H$^+$].$^+$

Synthesis of tetraethyl (((2-(methylthio)thieno[2,3-d]pyrimidin-4-yl)amino)methylene)bis(phosphonate) **(III)**:

In a pressure vessel, diethyl phosphite (5.5 mL, 43 mmol) and triethyl orthoformate (1.7 mL, 10 mmol) were added to 2-(methylthio)thieno[2,3-d]pyrimidin-4-amine, **II** (1.2g, 6.1 mmol) in dry toluene (5.0 mL). The resulting mixture was heated at 130^{o}C for 40 h (monitored by TLC and/or LC-MS). The mixture was then cooled to RT, and concentrated *in vacuo*. Crude product was purified by silica gel column chromatography. The product, intermediate **III** eluted from the column with 10-20% MeOH in EtOAC and obtained as a light yellow solid (1.2 g, 41%). ^{1}H NMR (500 MHz, DMSO-d_6): δ 8.70 (d, *J* = 9.7 Hz, -NH), 7.97 (d, *J* = 6.0 Hz, 1H), 7.45 (d, *J* = 6.0 Hz, 1H), 5.70 (td, *J* = 23.6, 9.7 Hz, 1H), 4.14 – 4.02 (m, 8H), 2.50 (s, 3H), 1.21 (t, *J* = 7.1 Hz, 6H), 1.14 (t, *J* = 7.0 Hz, 6H). ^{31}P NMR (203 MHz, DMSO-d_6): δ 16.77 (s). ^{13}C NMR (126 MHz, DMSO-d_6): δ 167.3, 165.4, 155.12 (t, *J* = 4.1 Hz), 121.1, 120.1, 113.6, 62.9 - 62.7 (m), 44.4 (t, *J* = 147.3 Hz), 16.2 - 16.1 (m), 13.5. MS [ESI$^+$] *m/z*: 484.1 [M + H$^+$].$^+$

General protocol for the Liebeskind–Srogl cross-coupling reaction (synthesis of **IVa,b**):

This procedure was based on the literature with slight modifications[236,237]. Intermediate **III** (880 mg, 1.8 mmol), aryl boronic acid (4.6 mmol; obtained commercially or prepared using well established methods), CuTC (1.04 g, 5.5 mmol) and Pd(dppf)Cl_2•CH_2Cl_2 (150 mg, 0.18 mmol) were charged into an oven-dried round bottom flask. The flask was evacuated and purged with Ar, followed by addition of dry dioxane (10.0 mL). The flask was sealed and heated at 50^{o}C for 4-16h (under Ar balloon; monitored by TLC or LC-MS). The reaction mixture was cooled to RT, diluted with EtOAc, and filtered through celite. The filtrate was collected and washed with 10% aqueous NH_4OH (thrice), followed by brine. The combined organic extracts were dried over Na_2SO_4 and concentrated *in vacuo*. Crude product was purified by silica gel column chromatography with a gradient from 25% EtOAc in hexanes to 100% EtOAc and then to 20% MeOH in EtOAc. Product typically eluted from the column with 10%-20% MeOH in EtOAc and isolated in ~80-85% yield.

Tetraethyl (((2-(3-nitrophenyl)thieno[2,3-d]pyrimidin-4-yl)amino)methylene)bis(phosphonate) (**IVa**):

Isolated as light brown solid. ^{1}H NMR (500 MHz, DMSO-d_6): δ 9.12 (t, J = 1.9 Hz, 1H), 8.85 (d, *J* = 9.6 Hz, -NH), 8.80 (d, *J* = 7.9 Hz, 1H), 8.35 (ddd, *J* = 8.2, 2.4, 0.9 Hz, 1H), 8.14 (d, *J* = 6.0 Hz, 1H), 7.84 (t, *J* = 8.0 Hz, 1H), 7.72 (d, *J* = 6.0 Hz, 1H), 5.99 (td, *J* = 23.5, 9.6 Hz, 1H), 4.23 – 4.02 (m, 8H), 1.20 (t, *J* = 7.0 Hz, 6H), 1.12 (t, *J* = 7.0 Hz, 6H).^{31}P NMR (203 MHz, DMSO-d_6): δ 16.9.^{13}C NMR (126 MHz, DMSO-d_6): δ 167.8, 156.5 (t, *J* = 4.0 Hz), 156.4, 148.7, 139.6, 134.1, 130.8, 125.3, 124.9, 122.4, 120.8, 116.4, 63.4 - 63.2 (m), 45.0 (t, *J* = 147.2 Hz), 16.7 - 16.6 (m). MS [ESI$^+$] *m/z*: 559.1 $[M + H^+]^+$

Benzyl 3-(4-((bis(diethoxyphosphoryl)methyl)amino)thieno[2,3-d]pyrimidin-2-yl)benzoate (**IVb**):

Isolated as a light yellow solid. ^{1}H NMR (500 MHz, CD_3OD): δ 9.09 (s, 1H), 8.66 (d, *J* = 7.8 Hz, 1H), 8.14 (dd, *J* = 7.7, 1.1 Hz, 1H), 7.72 (d, *J* = 6.0 Hz, 1H), 7.64 – 7.58 (m, 1H), 7.55 (dd, *J* = 6.0, 1.5 Hz, 1H), 7.49 (d, *J* = 7.9 Hz, 2H), 7.41 (t, *J* = 7.5 Hz, 2H), 7.36 – 7.32 (m, 1H), 6.19 (t, *J* = 23.5 Hz, 1H), 5.42 (s, 2H), 4.24 – 4.18 (m, 8H), 1.27 – 1.21 (m, 12H). ^{31}P NMR (203 MHz, CD_3OD): δ 17.17 (s). ^{13}C NMR (126 MHz, CD_3OD): δ 169.5, 167.5, 159.4, 157.4 (t, *J* = 3.9 Hz), 139.7, 137.6, 133.6, 132.2, 131.8, 130.1, 129.9, 129.7, 129.3, 129.3, 125.3, 119.8, 117.1, 67.9, 65.2 - 65.1 (m), 45.5 (t, *J* = 150.0 Hz), 16.7 - 16.6 (m). MS [ESI$^-$] *m/z*: 648.3 $[M - H^+]^-$

Synthesis of tetraethyl (((2-(3-aminophenyl)thieno[2,3-d]pyrimidin-4-yl)amino)methylene)bis(phosphonate) (**V**):

In a pressure vessel containing intermediate **IVa** (500 mg, 0.90 mmol) in EtOH (9.0 mL), $SnCl_2$•$2H_2O$ (1.01 g, 4.5 mmol) was added and the mixture was stirred at 80^{o}C for 2-3 h. The reaction mixture was cooled to RT and then slowly poured into sat. $NaHCO_3$ solution (9.0 mL). It was then extracted with EtOAc (3x), brine (once), dried over anhydrous $MgSO_4$, filtered, and concentrated *in vacuo*. Intermediate **V** was obtained as a light yellow solid (392 mg, 83% yield), and was used in the next step without further purification. ^{1}H NMR (500 MHz, DMSO-d_6): δ 8.52 (d, *J* = 9.7 Hz, 1H), 8.06 (d, *J* = 6.0 Hz, 1H), 7.64 – 7.62 (m, 1H), 7.58 (d, *J* = 6.0 Hz, 1H), 7.53 (d, *J* = 7.7 Hz, 1H), 7.14 (t, *J* = 7.8 Hz, 1H), 6.67 (dd, *J* = 7.9, 1.5 Hz, 1H), 6.01 (td, *J* = 23.5, 9.7

Hz, 1H), 5.22 (s, 2H), 4.15 – 4.05 (m, 8H), 1.16 (t, *J* = 7.0 Hz, 6H), 1.11 (t, *J* = 7.0 Hz, 6H). ^{31}P NMR (203 MHz, DMSO-d_6): δ 17.18 (s).MS [ESI$^+$] *m/z*: 529.1 [M + H$^+$]$^+$

Synthesis of 3-(4-((bis(diethoxyphosphoryl)methyl)amino)thieno[2,3-d]pyrimidin-2-yl)benzoic acid (**VI**):

A solution of intermediate **IVb** (271 mg, 0.42 mmol) in neat TFA (4.6 mL) was stirred at 80^{o}C for 14h (monitored by TLC). TFA was then removed by evaporation *in vacuo* and the residue was dissolved in DCM and the solvent was evaporated again under reduced pressure (done at least twice). Crude product was purified by silica gel column chromatography using a gradient of 50% EtOAc in hexanes to 100% EtOAc and then to 15% MeOH in EtOAc. Product was isolated as a light brown solid (quantitative yield). ^{1}H NMR (400 MHz, $CDCl_3$ with ~0.1% CD_3OD): δ 9.20 (s, 1H), 8.70 (d, *J* = 7.9 Hz, 1H), 8.19 (d, *J* = 7.7 Hz, 1H), 7.70 (d, *J* = 6.0 Hz, 1H), 7.59 (t, *J* = 7.8 Hz, 1H), 7.40 (d, *J* = 6.0 Hz, 1H), 6.08 (t, *J* = 22.2 Hz, 1H), 4.29 – 4.18 (m, 8H), 1.29 (t, *J* = 7.0 Hz, 6H), 1.20 (t, *J* = 7.0 Hz, 6H). ^{31}P NMR (203 MHz, $CDCl_3$): δ 17.50 (s). ^{13}C NMR (126 MHz, $CDCl_3$ with ~0.1% CD_3OD) δ 169.2, 168.3, 158.4, 155.8, 138.4, 132.7, 131.5, 129.8, 128.6, 123.8, 118.8, 115.9, 115.8, 64.2 (br), 44.1 (t, *J* = 147.0 Hz, 1H), 16.2 (br). MS [ESI$^+$] *m/z*: 558.1 [M + H$^+$]$^+$

3.3.3. General Protocol for the Synthesis of Final Inhibitors 10 and 11

Step 1: Amide bond formation:

Method A: To a stirring solution of intermediate **V** (80 mg, 0.15 mmol) in dry DCM (1.5 mL) at 0^{o}C, dry Et_3N (97 µL, 0.45 mmol) was added, followed by an acid chloride (aryl-COCl or heteroary-COCl; 0.18 mmol), which was added dropwise. The solution was stirred and allowed to warm to RT (reaction progress was monitored by TLC or LC-MS). Once complete (typically, after ~1 h), the reaction was poured into sat. $NaHCO_3$ solution and extracted with EtOAc (2x), washed with brine, dried over anhydrous Na_2SO_4 and concentrated under vacuum. Crude product was purified by silica gel column chromatography using a gradient from 25% EtOAc in hexanes to 100% EtOAc and then to 20% MeOH in EtOAc. Product typically eluted with 10%-20% MeOH in EtOAc. Isolated yields typically ranged from 75% to quantitative.

Method B: Alternatively, to a mixture of intermediate **VI** (50 mg, 0.09 mmol) and an amine (aryl-NH_2 or heteroaryl-NH_2) (0.1 mmol) in dry DMF (2.0 mL), DIPEA (31 µL , 0.18 mmol) was added,

followed by HBTU (37.4 mg, 0.1 mmol). The solution was stirred at RT until complete conversion was observed by TLC (typically after ~1-2 h). The reaction mixture was then diluted with brine and was extracted with EtOAc. The organic phase was washed with sat. NH_4Cl solution, brine, dried over anhydrous Na_2SO_4 and concentrated *in vacuo*. Crude product was purified by silica-gel column chromatography as described for ***Method A*** above. Isolated yields typically ranged from 60-80%.

Step 2: Deprotection of bisphosphonate esters using TMSBr, followed by methanolysis was carried out as previously described[238]. Isolated yields ranged from 40-90%.

(((2-(3-benzamidophenyl)thieno[2,3-d]pyrimidin-4-yl)amino)methylene)bis(phosphonic acid) (**10a**):

The tetraethyl (((2-(3-benzamidophenyl)thieno[2,3-d]pyrimidin-4-yl)amino)methylene)-bis(phosphonate) was isolated as a light yellow solid. ^{1}H NMR (500 MHz, DMSO-d_6): δ 10.43 (s, -NH), 8.86 (t, *J* = 1.7 Hz, 1H), 8.65 (d, *J* = 9.7 Hz, -NH), 8.12 (d, *J* = 7.9 Hz, 1H), 8.10 (d, *J* = 6.0 Hz, 1H), 8.01 (d, *J* = 7.1 Hz, 2H), 7.91 (dd, *J* = 8.1, 1.1 Hz, 1H), 7.64 (d, *J* = 6.0 Hz, 1H), 7.63 – 7.59 (m, 1H), 7.57 – 7.53 (m, 2H), 7.51 (t, *J* = 7.9 Hz, 1H), 6.06 (td, *J* = 23.3, 9.5 Hz, 1H), 4.18 – 4.07 (m, 8H), 1.19 – 1.10 (m, 12H). ^{31}P NMR (203 MHz, DMSO-d_6) δ 17.01 (s).

Inhibitor **10a** was isolated as a pale yellow solid. ^{1}H NMR (400 MHz, D_2O): δ 8.36 (s, 1H), 8.18 (d, *J* = 7.9 Hz, 1H), 7.95 (d, *J* = 7.3 Hz, 2H), 7.89 (d, *J* = 8.2 Hz, 1H), 7.70 – 7.57 (m, 5H), 7.49 (d, *J* = 6.0 Hz, 1H), 5.13 (t, *J* = 18.6 Hz, 1H). ^{31}P NMR (162 MHz, D_2O): δ 13.79 (s). ^{13}C NMR (101 MHz, D_2O): δ 169.8, 165.5, 159.8, 157.0, 138.7, 137.5, 133.9, 132.4, 129.5, 128.8, 127.4, 125.3, 124.3, 123.1, 122.0, 119.0, 115.9. C-α to the bisphosphonate was observed by HSQC. HSQC (^{1}H-^{13}C): ^{1}H at δ 5.13 correlates to ^{13}C-α at δ 49.5. HRMS [ESI$^+$] calculated for $C_{20}H_{16}N_4Na_3O_7P_2S$ *m/z*, 586.9903; found 586.9898 $[M + H]^+$

(((2-(3-(4-methylbenzamido)phenyl)thieno[2,3-d]pyrimidin-4-yl)amino)methylene)-bis(phosphonic acid) (**10b**):

The tetraethyl (((2-(3-(4-methylbenzamido)phenyl)thieno[2,3-d]pyrimidin-4-yl)amino)methylene)bis(phosphonate) was isolated as a pale yellow solid. ^{1}H NMR (500 MHz, DMSO-d_6): δ 10.34 (s, -NH), 8.85 (t, *J* = 1.8 Hz, 1H), 8.65 (d, *J* = 9.7 Hz, -NH), 8.12 -8.09 (m, 2H), 7.93 (d, *J* = 8.2 Hz, 2H), 7.91 (ddd, *J* = 8.1, 2.1, 1.0 Hz, 1H), 7.64 (d, *J* = 6.0 Hz, 1H), 7.50

(t, *J* = 7.9 Hz, 1H), 7.35 (d, *J* = 7.9 Hz, 2H), 6.06 (td, *J* = 23.4, 9.7 Hz, 1H), 4.18 – 4.05 (m, 8H), 2.40 (s, 3H), 1.19 – 1.10 (m, 12H). ^{31}P NMR (203 MHz, DMSO-d_6): δ 17.00 (s). MS [ESI$^+$] m/z: 647.2 $[M + H^+]^+$

Inhibitor **10b** was isolated as a pale yellow solid. ^{1}H NMR (500 MHz, D_2O): δ 8.38 (s, 1H), 8.20 (d, *J* = 7.6 Hz, 1H), 7.93 (d, *J* = 7.1 Hz, 1H), 7.89 (d, *J* = 7.9 Hz, 2H), 7.68 - 7.63 (m, 2H), 7.51 (d, *J* = 5.9 Hz, 1H), 7.46 (d, *J* = 7.9 Hz, 2H), 5.15 (t, *J* = 18.9 Hz, 1H) , 2.47 (s, 3H). ^{31}P NMR (203 MHz, D_2O) δ 13.82 (s). ^{13}C NMR (101 MHz, D_2O): δ 169.3, 165.6, 159.5, 156.8, 143.5, 138.3, 137.5, 130.7, 129.4, 129.3, 127.5, 125.0, 124.1, 123.3, 121.6, 118.8, 115.8, 48.9 (t, *J* = 124.8 Hz), 20.6. HRMS [ESI$^+$] calculated for $C_{21}H_{18}N_4Na_3O_7P_2S$ *m/z*, 601.00590; found 601.00773 $[M + H]^+$

(((2-(3-(4-methoxybenzamido)phenyl)thieno[2,3-d]pyrimidin-4-yl)amino)methylene)bis-(phosphonic acid) (**10c**):

The tetraethyl (((2-(3-(4-methoxybenzamido)phenyl)thieno[2,3-*d*]pyrimidin-4-yl)amino)methylene)bis(phosphonate) was isolated as a pale yellow solid. ^{1}H NMR (500 MHz, DMSO-d_6): δ 10.27 (s, -NH), 8.84 (t, *J* = 1.7 Hz, 1H), 8.65 (d, *J* = 9.7 Hz, -NH), 8.11 – 8.09 (m, 2H), 8.02 (d, *J* = 8.8 Hz, 2H), 7.90 (dd, *J* = 6.9, 1.2 Hz, 1H), 7.64 (d, *J* = 6.0 Hz, 1H), 7.49 (t, *J* = 7.9 Hz, 1H), 7.08 (d, *J* = 8.9 Hz, 2H), 6.06 (td, *J* = 23.4, 9.7 Hz, 1H), 4.18 – 4.07 (m, 8H), 3.85 (s, 3H), 1.19 – 1.10 (m, 12H). ^{31}P NMR (203 MHz, DMSO-d_6): δ 17.01 (s). MS [ESI$^+$] m/z: 663.2 $[M + H^+]^+$

Inhibitor **10c** was isolated as pale yellow solid. ^{1}H NMR (400 MHz, D_2O): δ 8.36 (s, 1H), 8.19 (d, *J* = 7.8 Hz, 1H), 7.98 (d, *J* = 8.8 Hz, 2H), 7.91 (d, *J* = 8.1 Hz, 1H), 7.68 - 7.60 (m, 2H), 7.50 (d, *J* = 6.0 Hz, 1H), 7.17 (d, *J* = 8.9 Hz, 2H), 5.11 (t, *J* = 19.0 Hz, 1H), 3.94 (s, 3H). ^{31}P NMR (162 MHz, D_2O) δ 13.78 (s). ^{13}C NMR (126 MHz, D_2O): δ 169.1, 165.0, 162.2, 160.0, 156.8, 138.7, 137.6, 129.6, 129.5, 126.3, 125.1, 124.4, 122.6, 122.0, 119.2, 116.0, 114.1, 55.5. C-α to the bisphosphonate was observed by HSQC. HSQC (^{1}H-^{13}C): ^{1}H at δ 5.11 correlates to ^{13}C-α at δ 50.0.

HRMS [ESI$^+$] calculated for $C_{21}H_{18}N_4Na_3O_8P_2S$ *m/z*, 617.00082; found 617.00181 $[M + H]^+$

(((2-(3-(4-fluorobenzamido)phenyl)thieno[2,3-d]pyrimidin-4-yl)amino)methylene)bis-(phosphonic acid) (**10d**):

The tetraethyl (((2-(3-(4-fluorobenzamido)-phenyl)thieno[2,3-d]pyrimidin-4-yl)amino)methylene)bis(phosphonate) was isolated as a pale yellow solid (48 mg, 65%). ^{1}H NMR (500 MHz, $CDCl_3$): δ 8.39 (s, 1H), 8.28 (d, *J* = 7.9 Hz, 1H), 8.14 (d, *J* = 7.6 Hz, 1H), 8.03 – 7.90 (m, 3H), 7.52 (t, *J* = 8.0 Hz, 1H), 7.37 (d, *J* = 6.0 Hz, 1H), 7.21 (t, *J* = 8.5 Hz, 2H), 5.97 (d, *J* = 9.9 Hz, 1H), 5.78 (s, 1H), 4.35 – 4.08 (m, 8H), 1.29 – 1.19 (m, 12H). ^{31}P NMR (203 MHz, $CDCl_3$): δ 16.84.

Inhibitor 10d was isolated as a light beige solid (26.1 mg, 63%). ^{1}H NMR (400 MHz, D_2O): δ 8.37 (s, 1H), 8.20 (d, *J* = 7.9 Hz, 1H), 8.05 – 7.98 (m, 2H), 7.93 (d, *J* = 8.1 Hz, 1H), 7.70 – 7.60 (m, 2H), 7.51 (d, *J* = 6.0 Hz, 1H), 7.39 – 7.29 (m, 2H), 5.17 (t, *J* = 19.0 Hz, 1H). ^{31}P NMR (162 MHz, D_2O): δ 13.93 (s). ^{13}C NMR (126 MHz, D_2O): δ 168.5, 165.8, 165.4, 163.8, 159.7, 156.9, 138.5, 137.4, 130.1, 130.0, 129.4, 125.1, 124.1, 122.9, 121.7, 118.9, 115.8, 115.7, 115.5, 49.5 (t, *J* = 122.7 Hz). HRMS [ESI$^-$] calculated for $C_{20}H_{15}FN_4NaO_7P_2S$ *m/z* [M-2H+Na]$^-$ 559.0024; found 559.0010 [M-2H+Na]$^-$

(((2-(3-(phenylcarbamoyl)phenyl)thieno[2,3-d]pyrimidin-4-yl)amino)methylene)bis(phosphonic acid) (**11a**):

The tetraethyl (((2-(3-(phenylcarbamoyl)phenyl)thieno[2,3-*d*]pyrimidin-4-yl)amino)methylene)bis(phosphonate) was isolated as a light yellow solid. ^{1}H NMR (400 MHz, DMSO-d_6): δ 10.47 (s, -NH), 8.95 (s, 1H), 8.75 (d, *J* = 9.6 Hz, -NH), 8.57 (d, *J* = 7.9 Hz, 1H), 8.10 (d, *J* = 5.7 Hz, 1H), 8.07 (d, *J* = 7.9 Hz, 1H), 7.82 (d, *J* = 7.7 Hz, 2H), 7.71 - 7.66 (m, 2H), 7.39 – 7.35 (m, 2H), 7.12 (t, *J* = 7.4 Hz, 1H), 6.03 (br, 1H), 4.18 – 4.00 (m, 8H), 1.19 – 1.08 (m, 12H). ^{31}P NMR (162 MHz, DMSO-d_6) δ 17.05 (s). ^{13}C NMR (126 MHz, DMSO-d_6): δ 167.6, 165.5, 157.5, 156.0 (t, *J* = 3.7 Hz), 139.2, 137.7, 135.5, 130.4, 129.4, 128.7, 128.6, 127.1, 123.8, 123.7, 120.3, 120.2, 115.5, 62.9 - 62.7 (m), 16.2 - 16.1 (m). C-α to the bisphosphonate was observed by HSQC. HSQC (^{1}H-^{13}C): ^{1}H at δ 6.03 correlates to ^{13}C-α at δ 45.1. MS [ESI$^+$] m/z: 633.2 [M + H$^+$]$^+$

Inhibitor **11a** was isolated as off-white solid. ^{1}H NMR (400 MHz, D_2O): δ 8.81 (s, 1H), 8.58 (d, *J* = 7.9 Hz, 1H), 8.06 (d, *J* = 7.8 Hz, 1H), 7.76 (t, *J* = 7.8 Hz, 1H), 7.66 – 7.63 (m, 3H), 7.56 – 7.52 (m, 3H), 7.36 (t, *J* = 7.4 Hz, 1H), 5.20 (t, *J* = 19.0 Hz, 1H). ^{31}P NMR (203 MHz, D_2O): δ 13.91 (s). ^{13}C NMR (126 MHz, D_2O): δ 169.4, 165.5, 159.7, 157.0, 138.3, 136.9, 134.4, 132.0, 129.4, 129.3, 129.2, 126.9, 126.0, 123.2, 123.0, 119.0, 115.9, 49.3. HRMS [ESI$^+$] calculated for $C_{20}H_{16}N_4Na_3O_7P_2S$ *m/z*, 586.9903; found 586.9903 [M + H]$^+$

(((2-(3-((4-methoxyphenyl)carbamoyl)phenyl)thieno[2,3-d]pyrimidin-4-yl)amino)methylene)bis-(phosphonic acid) (**11b**):

The tetraethyl (((2-(3-((4-methoxyphenyl)carbamoyl)phenyl)thieno[2,3-*d*]pyrimidin-4-yl)amino)methylene)bis(phosphonate) was isolated as a light yellow solid. ^{1}H NMR (500 MHz, $CDCl_3$ with ~0.1% CD_3OD): δ 9.01 (s, 1H), 8.67 (br_s, 1H), 8.59 (d, *J* = 7.8 Hz, 1H), 8.11 (d, *J* = 7.6 Hz, 1H), 7.68 (d, *J* = 8.8 Hz, 2H), 7.61 (t, *J* = 7.7 Hz, 1H), 7.45 (d, *J* = 5.3 Hz, 1H), 7.37 (d, *J* = 6.0 Hz, 1H), 6.92 (d, *J* = 9.0 Hz, 2H), 5.86 (t, *J* = 22.3 Hz, 1H), 4.27 – 4.10 (m, 8H), 3.82 (s, 3H), 1.26 (t, *J* = 7.1 Hz, 6H), 1.21 (t, *J* = 7.1 Hz, 6H). ^{31}P NMR (203 MHz, $CDCl_3$): δ 17.10 (s). MS [ESI$^+$] *m/z*: 663.4 $[M + H^+]^+$

Inhibitor **11b** was isolated as off-white solid. ^{1}H NMR (500 MHz, D_2O): δ 8.74 (s, 1H), 8.54 (d, *J* = 7.8 Hz, 1H), 8.00 (d, *J* = 7.7 Hz, 1H), 7.72 (t, *J* = 7.8 Hz, 1H), 7.62 (d, *J* = 5.9 Hz, 1H), 7.51 - 7.49 (m, 3H), 7.06 (d, *J* = 8.9 Hz, 2H), 5.18 (t, *J* = 18.9 Hz, 1H), 3.86 (s, 3H). ^{13}C NMR (126 MHz, D_2O): δ 169.3, 165.5, 159.7, 157.0, 156.7, 138.3, 134.3, 132.0, 130.1, 129.3, 129.3, 126.8, 124.8, 123.2, 118.9, 115.9, 114.4, 55.5. HSQC (^{1}H-^{13}C): ^{1}H at δ 5.18 correlates to ^{13}C-α at δ 49.3. ^{31}P NMR (203 MHz, D_2O): δ 13.91 (s). HRMS [ESI$^+$] calculated for $C_{21}H_{18}N_4Na_3O_8P_2S$ *m/z*, 617.00082; found 617.00090 $[M + H^+]^+$

(((2-(3-((3-fluoro-4-methoxyphenyl)carbamoyl)phenyl)thieno[2,3-d]pyrimidin-4-yl)amino)-methylene)bis(phosphonic acid) (**11c**):

The tetraethyl (((2-(3-((3-fluoro-4-methoxyphenyl)-carbamoyl)phenyl)thieno[2,3-*d*]pyrimidin-4-yl)amino)methylene)bis(phosphonate) was isolated as a yellow solid. ^{1}H NMR (500 MHz, $CDCl_3$): δ 9.28 (s, 1H), 9.10 (br_s, 1H), 8.62 (d, *J* = 7.8 Hz, 1H), 8.14 (d, *J* = 7.7 Hz, 1H), 7.70 (dd, *J* = 13.1, 2.3 Hz, 1H), 7.66 (d, *J* = 8.7 Hz, 1H), 7.59 (t, *J* = 7.7 Hz, 1H), 7.42 (d, *J* = 5.8 Hz, 1H), 7.27 (d, *J* = 6.0 Hz, 1H), 6.94 (t, *J* = 9.1 Hz, 1H), 6.77 (br_s, 1H), 5.63 (td, *J* = 22.9, 7.7 Hz, 1H), 4.24 – 4.11 (m, 8H), 1.24 - 1.20 (m, 12H). ^{31}P NMR (203 MHz, $CDCl_3$) δ 17.27 (s). ^{13}C NMR (126 MHz, $CDCl_3$): δ 168.4, 165.3, 158.5, 155.8 (t, *J* = 3.3 Hz), 152.2 (d, *J* = 244.1 Hz), 144.3 (d, *J* = 10.9 Hz), 138.0, 134.7, 132.6 (d, *J* = 9.4 Hz), 131.1, 130.2, 129.1, 126.8, 123.9, 117.9, 116.3 (d, *J* = 3.4 Hz), 115.5, 113.7 (d, *J* = 2.5 Hz), 109.7 (d, *J* = 22.6 Hz), 63.9 - 63.7 (m), 56.7, 46.9 (t, *J* = 147.9 Hz), 16.5 - 16.4 (m). MS [ESI$^+$] *m/z*: 681.3 $[M + H^+]^+$

Inhibitor **11c** was isolated as a pale yellow solid. ^{1}H NMR (500 MHz, D_2O): δ 8.77 (s, 1H), 8.55 (d, *J* = 7.8 Hz, 1H), 8.03 (d, *J* = 7.8 Hz, 1H), 7.74 (t, *J* = 7.8 Hz, 1H), 7.64 (d, *J* = 5.9 Hz, 1H), 7.53 - 7.51 (m, 2H), 7.34 (d, *J* = 8.5 Hz, 1H), 7.23 (t, *J* = 9.1 Hz, 1H), 5.21 (t, *J* = 18.5 Hz, 1H), 3.95 (s, 3H). ^{31}P NMR (203 MHz, D_2O): δ 13.90 (s). ^{13}C NMR (126 MHz, D_2O): δ 168.8, 165.5, 159.5, 157.0, 151.3 (d, *J* = 242.1 Hz), 144.3 (d, *J* = 10.9 Hz), 138.1, 133.9, 132.0, 130.5 (d, *J* = 9.4 Hz), 129.3, 129.2, 126.8, 123.2, 118.7, 118.7 (d, *J* = 3.1 Hz), 115.8, 113.9 (d, *J* = 1.9 Hz), 111.0 (d, *J* = 21.8 Hz), 56.3. . HSQC (^{1}H-^{13}C): ^{1}H at δ 5.19 correlates to ^{13}C-α at δ 49.0. HRMS [ESI$^+$] calculated for $C_{21}H_{17}O_8N_4FNa_3P_2S$ *m/z*, 634.99140; found 634.99164 $[M + H]^+$

Synthesis of (((6-(3-benzamidophenyl)thieno[2,3-d]pyrimidin-4-yl)amino)methylene)bis-(phosphonic acid) (**12**):

Suzuki cross-coupling between intermediate tetraethyl (((6-bromothieno[2,3-d]pyrimidin-4-yl)amino)methylene)bis(phosphonate), which was previously reported[239], and (3-benzamidophenyl)boronic acid (**ii**)[240] gave the tetraethyl (((6-(3-benzamidophenyl)thieno[2,3-*d*]pyrimidin-4-yl)amino)methylene)bis(phosphonate); isolated as a light yellow solid (82%).

^{1}H NMR (400 MHz, DMSO-d_6): δ 10.43 (s, -NH), 8.71 (d, *J* = 9.7 Hz, -NH), 8.54 (s, 1H), 8.45 (s, 1H), 8.31 (d, *J* = 2.3 Hz, 1H), 8.03 – 7.99 (m, 2H), 7.77 (d, *J* = 7.5 Hz, 1H), 7.64 – 7.44 (m, 5H), 5.81 (td, *J* = 23.5, 9.1 Hz, 1H), 4.16 – 4.02 (m, 8H), 1.23 – 1.11 (m, 12H). ^{31}P NMR (162 MHz, DMSO-d_6) δ 16.88 (s). MS [ESI$^+$] m/z: 633.2 $[M + H^+]^+$

Inhibitor **12** was isolated as a pale yellow solid. ^{1}H NMR (500 MHz, D_2O): δ 8.27 (s, 1H), 7.92 – 7.89 (m, 4H), 7.67 - 7.63 (m, 2H), 7.59 - 7.56 (m, 3H), 7.52 (t, *J* = 7.9 Hz, 1H). α-CH to the bisphosphonate overlaps with the solvent peak. ^{31}P NMR (203 MHz, D_2O): δ 13.53 (s). ^{13}C NMR (126 MHz, D_2O): δ 169.3, 163.2, 156.2, 153.5, 138.7, 137.9, 133.9, 133.5, 132.4, 129.9, 128.7, 127.3, 122.8, 121.8, 119.0, 118.6, 115.1, 50.8 (t, *J* = 125.7 Hz). HRMS [ESI$^+$] calculated for $C_{20}H_{16}N_4Na_3O_7P_2S$ *m/z*, 586.9903; found 586.9906 $[M + H]^+$

3.3.4. Expression, Purification and In Vitro Assay of Recombinant Human GGPPS.

A plasmid encoding N-terminally His_6-tagged human GGPPS (vector pNIC28-Bsa4, SGC Oxford) was transformed into *E. coli* BL21(DE3) cells as previously reported[241]. The protocols described by Kavanagh and co-workers[241] were also used for the purification and *in vitro* inhibition assay of hGGPPS.

3.3.5. Creation of Dimeric Y246D Mutant of hGGPPS.

The oligomeric complexation of hGGPPS was altered by introducing an amino acid with a charged side chain in place of one with a hydrophobic side chain at the dimer-dimer interface. Residue Tyr246 was changed to Asp246 by site-directed mutagenesis. The plasmid encoding the wild-type enzyme was used as the template; the sequence of the primers used for the site-directed mutagenesis are:

Y246D forward -
GGCTTTCCAGTGGCCCACAGCAGGTATGGAATCCCATCTGTCATCAATTCTGCC,

Y246D reverse -
TCCTCAAGATAATGTACACAGTCTTTTTTTATATCTATGTTTTCTGTTCTCTGGCGC.

Sequence-verified plasmids (with the newly introduced mutations) were transformed into *E. coli* BL21(DE3) cells. The Y246D mutant expressed well under the same condition used for the wild-type enzyme[241]. The oligomeric state of this mutant was confirmed to be dimeric by gel filtration.

3.3.6. Crystallization of the hGGPPS Y246D Mutant.

The enzyme was in the final purification buffer (10 mM HEPES (pH 7.5), 500 mM NaCl, 2 mM β-mercaptoethanol, and 5% glycerol). Inhibitor compounds were prepared as 25 mM solutions in 10 mM Tris (pH 7.0), and $MgCl_2$ as a 100 mM aqueous solution. The inhibitor and $MgCl_2$ solutions, if used at all, were added to the purified enzyme sample in different concentrations (**Table 3-1**). Crystals were obtained at 295 K by vapor diffusion in sitting drops composed of 1 μL protein solution and 1 μL crystallization buffer, and additional 0.5 μL microseed solution when added (**Table 3-1**). Seed solutions were prepared with Apo enzyme crystals and Seed Bead kits (Hampton Research). Two single crystals were transferred to a seed bead tube containing 50 μL crystallization buffer that produced these crystals (**Table 3-1**). The crystals were crushed by vortexing the tube contents for 3 minutes. The resulting microcrystal solution was added with additional 450 μL buffer and vortexed again for 3 minutes. The 500 μL stock solution was stored at room temperature and diluted 10^2-10^4 times for use in crystallization trials**.**

Table 3-1: Crystallization conditions

Data set	Apo	Inhibitor 10d
Composition of protein solution	0.01 M HEPES (pH 7.5), 0.5 M NaCl, 0.01 M -mercaptoethanol, 5% glycerol, 5 mM compound **8**, 20 mg/mL hGGPPS Y246D	0.01 M HEPES (pH 7.5), 0.5 M NaCl, 0.01 M -mercaptoethanol, 5% glycerol, 2 mM $MgCl_2$, 2 mM compound **10d**, 15 mg/mL hGGPPS Y246D
Composition of reservoir solution	0.26 M $(NH_4)_2HPO_4$, 35% glycerol	1.7 M $(NH_4)_2SO_4$, 4.25% isopropanol, 15% glycerol
Volume of reservoir, protein, and seed solution in crystallization drop (µL)	1:1	1:1:0.5
Volume of reservoir (µL)	80	80

3.3.7. X-ray Data Collection and Structure Determination.

Diffraction data were collected from single crystals at 100 K with a synchrotron radiation source (Beamline 08ID-1, Canadian Light Source, Saskatoon, SK, Canada). Data processing and anomalous signal calculation were carried out as described previously[225]. The structure models were initially built by molecular replacement with a ligand/solvent-omitted starting model generated from the PDB entry 2Q80. The models were improved through iterative rounds of manual and automated refinement, as described previously[225]. In order to model the ligand in the low-resolution structure (from the data set of Inhibitor **10d**; **Table 3-2**) in a bias-free manner, we first refined only the protein coordinates to near completion. A molecule of inhibitor **10d** was docked into the active site of this structure *in silico*, by using the program AutoDock vina[242]. Five of the top scoring docking output poses (**Figure 3-3**) were used in the subsequent steps: the inhibitor coordinates were added to the protein structure and real-space-rigid-body-refined against the ligand electron density once; the resulting protein-ligand structures were subjected to one final round of reciprocal-space refinement. Comparison of the refined maps indicated that starting (docking output) pose 1 agreed best with the electron density data (see the refined poses and electron density maps calculated; **Figure 3-4**). The final models were deposited in the PDB. Data

collection and structure refinement statistics, as well as the PDB codes for the final models, are summarized in **Table 3-2**. Structural data that support the findings of this study have been deposited in the RCSB Protein Data Bank (PDB; http://www.rcsb.org) with the accession numbers 6C56 and 6C57.

Table 3-2: Data collection and structure refinement statistics

Data set	**Apo**	**Inhibitor 10d**
PDB code	6C56	6C57
Data collection		
Wavelength (Å)	0.97949	1.38052
Space group	I422	I422
Unit cell dimension (Å)	a = b = 185.10, c = 115.20	a = b = 185.45, c = 114.20
Resolution range (Å)	54.39-2.80 (2.88-2.80)	97.24-3.50 (3.59-3.50)
Completeness (%)	99.9 (99.7)	100.0 (99.9)
Redundancy	9.9 (10.0)	12.9 (12.5)
I/σ(I)	36.5 (2.2)	26.9 (2.1)
R_{merge}	0.039 (1.129)	0.051 (1.271)
Refinement		
No. of reflections	23520	12192
R_{work}/R_{free}	0.185/0.238	0.198/0.252
No. of non-H atoms		
Protein	4317	4109
Ligand	24	34
Water	39	5
Total	4380	4148

R.m.s. deviations		
Bonds (Å)	0.021	0.018
Angles (°)	2.2	1.2
Ramachandran plot		
Most favored (%)	92.4	91.5
Allowed (%)	7.1	7.9
Outlier (%)	0.6	0.6

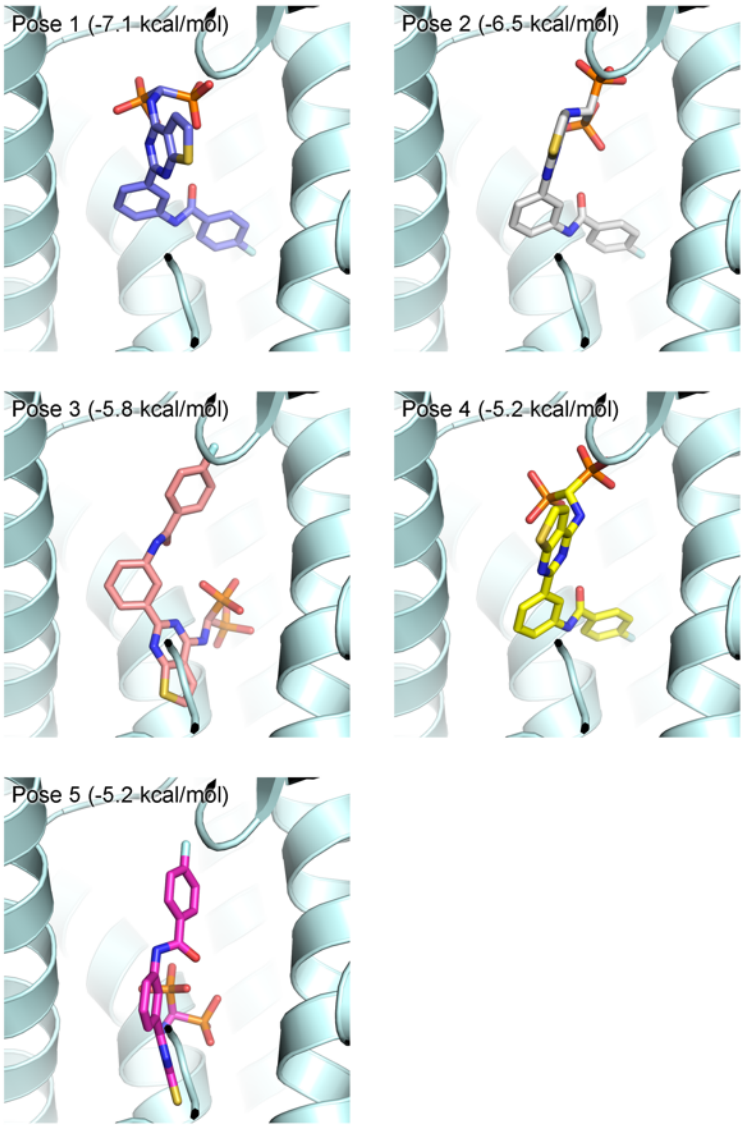

Figure 3-3: Binding poses of compound **10d** generated by *in silico* docking. The top five scoring poses are shown with their estimated binding energies.

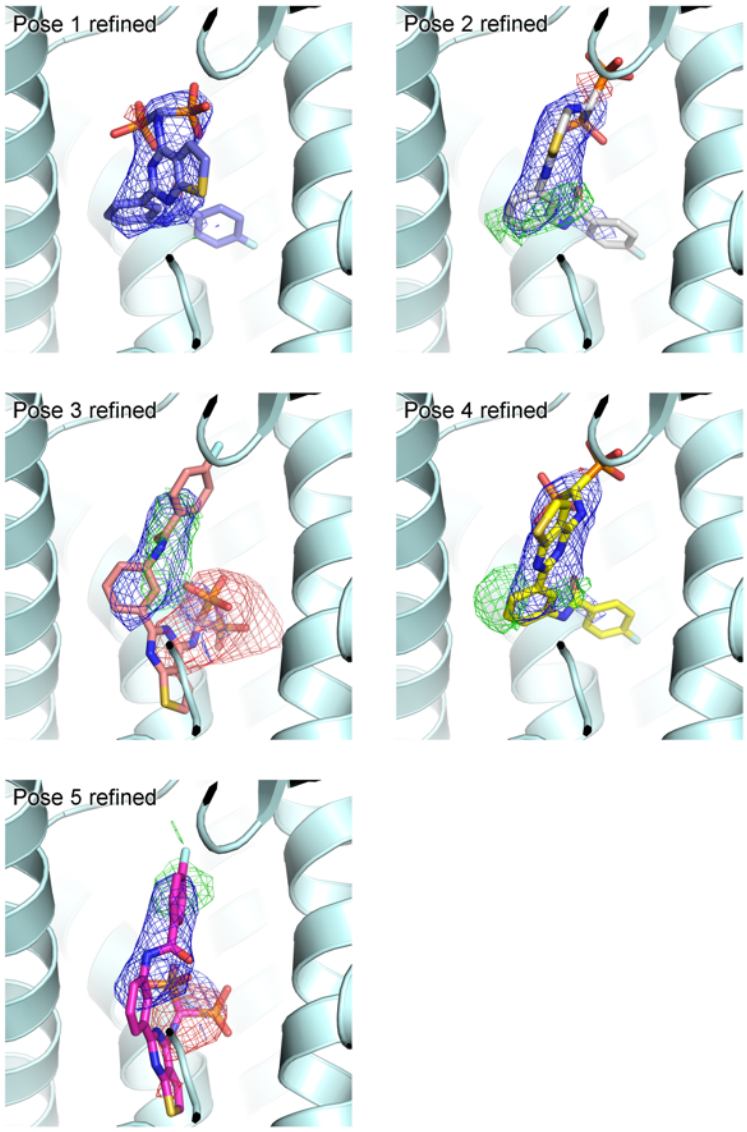

Figure 3-4: Crystallographically refined binding poses of compound **10d**. The density maps generated are shown as blue ($2F_o$-F_c contoured at 1σ) and green/red (positive and negative contours of F_o-F_c at 3σ) meshes.

3.3.8. Cell Culture and Viability Assays for MM Cell Lines.

Various MM cancer cell lines were cultured in RPMI-1640 medium supplemented with 10% fetal bovine serum (Gibco BRL, Gaithesburg, Md) supplemented with 2 mM L-glutamine in a 5% CO_2 atmosphere at 37°C. EC_{50} values for each target compound were determined using a commercial MTS proliferation assay (Promega, Madison, WI) following the manufacturer's instructions.

Briefly, compounds were diluted directly into culture medium and then applied to cells that were seeded in 96-well plates at a density of 5,000 cells per well. Cells were incubated with the indicated final concentration of compound in a total culture volume of 100 µl/well for 72 hours prior to the addition of the MTS reagent. Plates were incubated at 37 °C in the presence of 5% CO_2 for 2 hours prior to recording OD490 using a Tecan Infinite M200Pro microplate reader. Results were analyzed to obtain dose-response curves and EC_{50} determination was done using GraphPad PRISM version 5 (GraphPad Software, San Diego, CA).

3.3.9. Cell Culture for Various Cancer Cell Lines.

NCI-ADR-RES cells were obtained from National Cancer Institute (NCI) and all other cell lines were obtained from the American Type Culture Collection (ATCC). NHBE cells were maintained in Bronchial Epithelial Cell Growth Medium (BEGM) supplemented with 10% FBS (Multicell) and 2mM L-glutamine (Gibco/Life Technologies)**.** All other non-MM cells were maintained in culture using Roswell Park Memorial Institute (RPMI) 1640 media supplemented with 10% FBS (Multicell), Penicillin (100U/mL), Streptomycin (100ug/mL) and 2mM L-glutamine (Gibco/Life Technologies). Cells were plated in logarithmic growth phase in each well of clear bottom multiwell plates and cultured 16-24h before drug treatment. Serial dilutions of compounds were made in DMSO before dilution in proper media and then added to cultured cells in order to reach a maximum of 0.2% DMSO. Cells were incubated with drugs for 72 hours.

3.3.10. Determination of Cancer Cell Viability (other than MM).

Cell viability was determined by cellular quantitation of adenosine triphosphate (ATP) using the CellTiter-Glo Luminescent Cell Viability Assay Kit (Promega Corporation, Cat. No. G7571). Briefly, the CellTiter-Glo "one-mix-measure" reagent, containing both the cell permeabilizing agent and the Ultra-Glo luciferase, was added to the cell culture according to manufacturer's instructions allowing the free ATP to be released from viable cells and subsequently converted into luminescence. The luminescence generated in the reaction is directly proportional to cell viability and was quantified in a luminometer (PHERAstar FS, BMG Labtech). Data Analysis to calculate the relative growth inhibition induced by compound treatment, the mean value of relative light units (RLU) for replicate samples in the CellTiter-Glo assay at each dose was divided by the mean RLU value obtained from vehicle treated cells to give percent viability. Sigmoidal dose

response curves and EC_{50} values were generated using non-linear regression analysis (5 parameter fit) and GraphPad Prism Version 6 (GraphPad Software Inc., San Diego, CA).

3.3.11. Annexin-V Apoptosis Assays.

To assess the ability of compounds to induce apoptosis in cultured MM cell lines, cells were seeded at a density of $7.5x10^5$/mL in RPMI-1640 medium supplemented with 10% FBS and the indicated concentrations of compounds. After 72 hours of treatment, apoptosis was determined by double staining with APC Annexin V (BD Biosciences, Mississauga ON) and eFluor 780 Viability dye (ThermoFisher Scientific) according to the manufacturer's directions. Stained samples were acquired on a BD FACSCanto II instrument (BD Biosciences, Mississauga ON) and post-acquisition analyses were performed using FlowJo (V10) software. Apoptosis of multiple myeloma cells was also determined by flow cytometry by double staining cells with Allophycocyanin (APC) conjugated Annexin V and a V450 conjugated Mouse Anti-Human CD138 monoclonal antibody, following the manufacturer's instructions (BD Biosciences, Mississauga ON).

3.3.12. Western Blot Analysis.

MM cells were cultured in RPMI-1640 media supplemented with 10% FBS and L-glutamine and were maintained at 37°C in 5% CO_2 atmosphere in the presence and absence of the indicated concentration of hGGPPS inhibitor. Geranylgeraniol co-treatment (GGOH; 10 μM) served as a specificity control to demonstrate bypass of hGGPPS inhibitor treatment. Cells were harvested by centrifugation after the indicated treatment duration. Harvested cells were immediately washed with ice cold PBS, centrifuged, and then resuspended in ice cold RIPA lysis buffer (Pierce cat#89900). Equal amounts of cleared protein lysate were then separated by SDS-PAGE, transferred to PVDF membranes, and then membranes were incubated with primary antibody overnight at 4°C. The following primary antibodies were used: sXPB1 (Clone 143F) from Biolegend; GAPDH (sc-25778), p-AKT1/2/3 (sc-7985-R), and u-RAP1A (sc-1482) from Santa Cruz Biotechnology; total p44/42 (9102S), phospho-p44/42 (9101S), total eIF2α (9722S), phospho-eIF2α (9721S) and CHOP (2895S) from Cell Signaling Technology. After extensive washing, membranes were exposed to HRP-conjugated secondary antibodies for 1 hour at room temperature. After further extensive washing, ImmunoCruz (Santa Cruz Biotechnology)

chemiluminescence reagents were employed to visualize the remaining (bound) secondary antibodies.

3.3.13. XBP1 mRNA Splicing.

RPMI-8226 cells were seeded at a density of $7.5x10^5$/mL in RPMI-1640 medium supplemented with 10% FBS and the indicated concentrations of compounds. After 48 hours of treatment, cells were harvested by centrifugation and RNA extracted using Qiagen RNeasy Mini Kits. Purified RNA (1 μg) was converted into cDNA using a high capacity cDNA reverse transcription kit from Applied Biosystems (Foster City, CA). Semi-quantitative RT-PCR analysis of XBP1 mRNA splicing as well as quantitative real-time PCR detection of the spliced form of XBP1 mRNA were performed as described previously [(Back SH et al, 2005 PMID: 15804613) and (van Schadewijk A et al, 2012 PMID: 22038282), respectively]. GAPDH and 18S rRNA were used as loading and reference standards for semi-quantitative and real time PCR analyses, respectively.

3.3.14. Metabolic Stability.

Pooled male CD-1 mouse liver microsomes (lot C2F), Sprague-Dawley rat liver microsomes (lot NNK) and human liver microsomes (lot YAO) were purchased from BioreclamationIVT, Baltimore, Maryland. Loperamide, NADPH and DMSO were purchased from Sigma-Aldrich, Canada. Potassium phosphate buffer (100 mM) pH 7.4 was prepared freshly. HPLC grade methanol and acetonitrile, ACS grade ammonium formate and formic acid (98%) were obtained from Fisher Scientific. Water was purified by a Milli-Q ultrapure water system from Millipore (Bedford, MA, USA). Trimethylsilyl-diazomethane, 2 M solution in hexanes from ACROS Organics was purchased from Fisher Scientific. SPE cartridge, Strata- X 33um polymeric, 30mg, 96-well plate, were purchased from Phenomenex. After incubation of compound **11c** with liver microsomes, the parent molecule, as well as any metabolites with a bisphosphonate moiety, were converted to the corresponding trimethyl silyl esters, as previously reported[243]. Samples were analyzed by LC-MS/MS using loperamide as a reference control (half-life clearance of 8-15 min in all three liver microsomes).

3.3.15. Mice and *In Vivo* Experiment.

Vk*MYC/KaLwRij mice were bred and maintained in a pathogen-free standard animal facility with a light/dark cycle of 12 hours and provided with food and water *ad libitum*. Animals were

observed daily for any signs of overt toxicity, such as significant weight loss, decreased mobility, skin lesions, inflammation at the site of injection or morbidity. Animals were euthanized 4 hours after the last dose or as instructed by the experimental procedures protocol approved by the McGill University Animal Care Committee (protocol number 2012-7242). Briefly, mice with an M-peak higher than 15% (quantified by Serum Protein Electrophoresis) were used for this *in vivo* study. One group of mice was treated with vehicle (PBS, n=8) and the other group with 3 mg/kg of compound **11c** (n=8). All mice received a 14 day treatment (10 days treated daily plus weekend holiday followed by a two day re-treatment before sacrifice, a total of 12 doses) [age and gender matched and intraperitoneal injection]. All mice were euthanized after 4 hours of receiving the last dose or as instructed per protocol in case of toxicity effects.

3.3.16. Serum Protein Electrophoresis (SPEP).

SPEP was performed to quantify the M-peak in all mice before the start of the study and on the samples obtained on the day of sacrifice after complete treatment. SPEPs were performed using Hydragel agarose gel and HYDRASYS LC (Sebia, Lisses, France) following manufacturer's instructions. Resulting gels were scanned and band density was quantified using ImageJ (Version 1.48v). M-protein abundance was reported as percentage of the total protein.

3.3.17. Isolation of Peripheral Blood Mononuclear Cells (PBMCs).

Ammonium chloride was used to lyse red blood cells (RBCs) from whole blood collected while PBMCs were not thus lysed. Whole blood was diluted in 20 ml of ammonium chloride (155 mM NH_4Cl) and mixed by gentle vortexing for 10 minutes at room temperature. Cell solution was centrifuged at 400xg for 5 minutes and two washes with PBS were performed to remove ammonium chloride. PBMCs were harvested by centrifugation and Western Blot was performed to estimate inhibition of Rap1A geranylgeranylation (as described in the Western Blot analysis section above).

3.3.18. Differential Scanning Fluorimetry Studies.

These experiments were conducted as we previously reported, using the hGGPPS Y246D mutant enzyme at concentrations of 4 μM. It should be noted that the wild-type hGGPPS is not amenable to DSF studies since its melting temperature is (a) higher than allowed for safe operation of the RT-PCR (Bio-Rad iCycler iQ5) instrument (i.e. >90 ^{o}C) and exhibits multiple thermal transitions.

3.4. Results and Discussion

3.4.1. Identification of hGGPPS Inhibitors and Confirmation of Binding to the Active Site

Libraries of structurally diverse thienopyrimidine-based bisphosphonates (ThP-BPs), substituted at the C-2, C-5, and/or the C-6 carbon of the parent molecule **7** (**Figure 3-5**), were synthesized in order to probe the molecular recognition elements differentiating between binding to hFPPS versus hGGPPS[223,238,239].

Approximately 200 analogs were screened in our *in vitro* assays for their ability to inhibit hFPPS and/or hGGPPS. In general, compounds substituted at C-5 (~20 analogs) were found to be poor inhibitors of both enzymes; analogs more potent in inhibiting hFPPS were usually substituted at C-6 (~100 analogs), whereas analogs substituted at C-2 (~60 analogs) were inhibitors of hGGPPS with IC50 potency in the nanomolar range and exhibited selectivity against hFPPS. The synthesis of compounds having a C-2 substituent is briefly described in **Figure 3-1**. The synthesis of this library was achieved using slightly modified literature procedures, as described in the Experimental Section; select examples are shown in **Figure 3-5**.

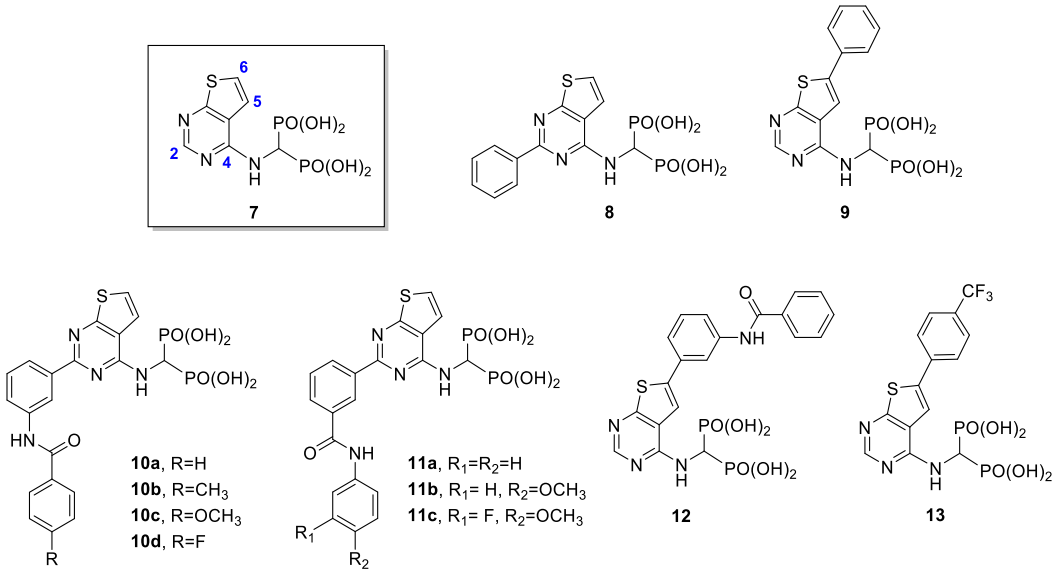

Figure 3-5: Examples of thienopyrimidine-based inhibitors of hFPPS/hGGPPS.

Initial structure−activity relationship (SAR) studies suggested that small substituents at either the C-2 or the C-6 position resulted in inhibitors with equivalent potency for both enzymes[223,238]. For example, the phenyl derivatives **8** and **9** (**Figure 3-5**) exhibited the same potency in inhibiting hGGPPS, with a narrow window of selectivity for hFPPS (**Table 3-3**). On the basis of these data,

we initially presumed that rotation around the C-4 amino linker, connecting the thienopyrimidine scaffold to the bisphosphonate moiety, could allow the side chains of **8** and **9** to adopt similar enzyme-bound conformations. However, SAR optimization proved that higher selectivity for hGGPPS could be achieved by extending the side chain attached to the C-2 position. Inhibitor **10a** was found to exhibit in vitro potency (IC50) of 64 nM in inhibiting hGGPPS and a selectivity window of approximately 30-fold against hFPPS (**Table 3-3**). In contrast, when the C-2 side chain of **10a** was transferred to the C-6 position of the thienopyrimidine core **7**, the resulting analog **12** was completely inactive in both *in vitro* inhibition assays at the highest concentration tested of 10 μM. These results confirmed that the molecular recognition elements involved in binding to hGGPPS (vs hFPPS) are not simply dictated by the presence of a bisphosphonate pharmacophore or the size and length of the side chain or the binding orientation of the thienopyrimidine scaffold. Further optimization of this class of compounds led to the identification of several hGGPPS inhibitors with IC50 values below 100 nM and a selectivity window of ≥15-fold. It is noteworthy that biological profiling of a 200-member library of ThP-BP compounds (a collection from this work and our previous studies[223,238,239]) clearly demonstrated that high potency in inhibiting hGGPPS, rather than hFPPS, is the critical factor in achieving nanomolar antitumor activity in human MM cells. Representative examples of ThP-BP hGGPPS inhibitors include analogs **10a-d** and the reversed amides **11a-c** (**Figure 3-5**).

Table 3-3: Enzyme inhibition (IC_{50}) and antiproliferation activity (EC_{50}) in MM RPMI-8226 cells of representative ThP-BP analogs

Compound	hFPPS [α] IC_{50} (μM)	hGGPPS [α] IC_{50} (μM)	*hGGPPS* Y246D IC_{50} (μM)	RPMI-8226 [β] EC_{50} (μM)
2	0.004	>100,000	nd	11
5	nd	0.43[γ]	0.59	nd
7	~0.8[δ]	>1.0[δ]	nd	nd
8	0.55	0.082	nd	nd
9	0.20	0.094	nd	nd
10a	2.0	0.064	0.039	0.50

10b	2.6	0.10	0.037	0.72
10c	1.0	0.085	0.092	nd
10d	>1.0[ε]	0.042	nd	0.70
11a	3.0	0.049	0.050	0.46
11b	1.3	0.075	nd	0.23
11c	1.4	0.086	0.075	0.14[ζ]
12	IN	IN	nd	IN
13	0.023	1.5	nd	>100

[a] IC_{50} values were determined with 10 min pre-incubation of the enzyme with each inhibitor; the values shown are average of n ≥3 determinations with standard deviation of ±5-10%.
[β] EC_{50} values were determined using an MTT assay after 72 hours of incubation of the cells with or without an inhibitor; the values shown are average of n ≥4 determinations with standard deviation of ≤ 2-fold.
IN: Inactive at the highest concentration tested of 10 μM
nd: not determined
[γ] IC_{50} value obtained in our own *in vitro* inhibition assays when compounds were tested in parallel with several other analogs in above table.
[δ] Estimated values based on 70% and 40% inhibition observed for hFPPS and hGGPPS, respectively, at 1 μM.
[ε] 20% inhibition was observed at 1 μM.
[ζ] Average of five independent determinations, each run in quadruplicate.

Binding of the ThP-BP inhibitors to the active site of hGGPPS was confirmed by crystallography and DSF studies. Crystallization of the wild-type human GGPPS has proven to be very challenging, with only one structure reported so far[241]. We assumed that the multimeric organization of this enzyme, forming a trimer of homodimers (**Figure 3-6A**), may be responsible for this challenge. A more readily crystallizable Y246D mutant was created, disrupting the interdimer contacts mediated by Tyr 246 (**Figure 3-6A**)[241]. This mutant is dimeric; it retains the same overall structure as the wild type enzyme (**Figure 3-6B**; PDB code 6C56; 2.80 Å resolution) and is catalytically competent (**Table 3-3**). We solved the cocrystal structure of inhibitor **10d** bound to the Y246D mutant, and despite lower resolution (PDB code 6C57; 3.50 Å resolution), we could observe the electron density for the inhibitor, as well as the anomalous signal from its sulfur atom, bound in the active site of one subunit (**Figure 3-6C**). While the exact binding

conformation is unclear, the bisphosphonate **10d** appears to bind between the aspartate-rich motifs, competing with the pyrophosphate of FPP (**Figure 3-6D**). Additionally, the p- fluorophenyl tail of **10d** appears to insert into the hydrophobic cavity formed between αD and αF, which typically accommodates the isoprenyl tail of FPP in the catalytic cycle. Binding of **10d** may also interfere with IPP binding, as the inhibitor's thienopyrimidine core extends into the second substrate site (**Figure 3-6D**). Binding of **10d** did not appear to involve Mg2+ ions (likely due to the low resolution), and it is plausible that direct interactions with residues Arg73, Gln185, and Lys212 can contribute to the stabilization of the charged bisphosphonate (**Figure 3-6C**). However, DSF studies clearly indicated that Mg2+ ions are required for the formation of the Y246D mutant/**10d** complex and an increase in thermal stability of the protein/inhibitor complex (**Figure 3-7**). Thus, our DSF data further corroborate that inhibitor **10d** binds to the active site of hGGPPS and must compete for binding with FPP.

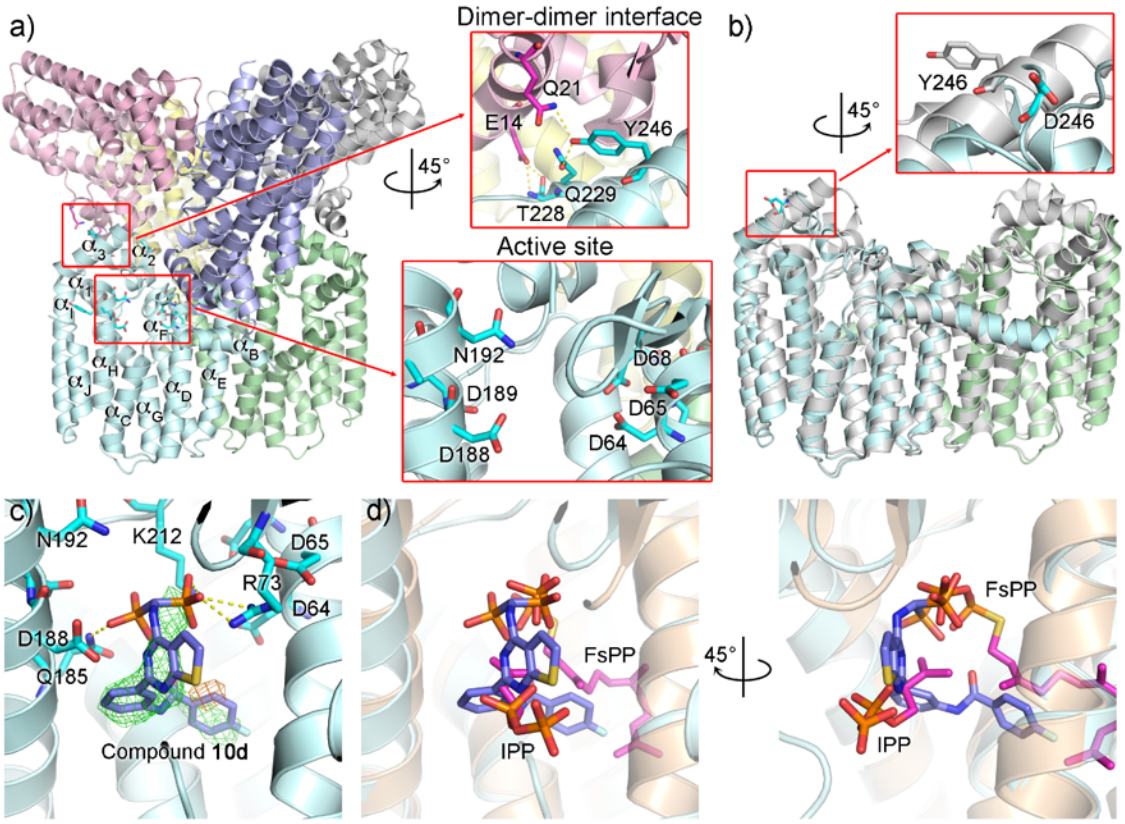

Figure 3-6: Crystal structure of wild type and mutant hGGPPS. (a) Hexameric wild type hGGPPS (PDB entry 2Q80); monomer units are indicated by different colors. (b) Dimeric hGGPPS mutant (Y246D; cyan and green; PDB entry 6C56); a dimer of the wild type enzyme (grey) is superposed (the inset highlights the

single amino acid mutation disrupting the dimer-dimer contact). (c) Dimeric hGGPPS in complex with **10d** (PDB entry 6C57). The green and orange meshes represent the ligand discovery map (F_o-F_c contoured at 3σ) and the anomalous signal map (3σ), respectively. (d) Superposition of **10d**, GGPPS substrate with the structure of a sulfur derivative of FPP (FsPP) and IPP bound to the yeast enzyme (ligands in magenta; protein in semi-transparent wheat; PDB entry 2E8T) are superimposed.

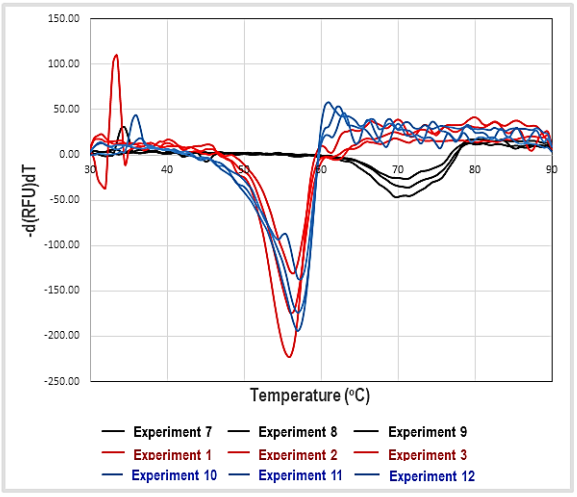

Experiment		Melting Temp (°C)	Average Tm (°C)
1	Y246D hGGPPS + Mg^{2+}	53.0	53.2
2	Y246D hGGPPS + Mg^{2+}	53.0	
3	Y246D hGGPPS + Mg^{2+}	53.5	
4	Y246D hGGPPS without Mg^{2+}	54.0	54.3
5	Y246D hGGPPS without Mg^{2+}	54.5	
6	Y246D hGGPPS without Mg^{2+}	54.5	
7	Y246D hGGPPS + Mg^{2+} + inhibitor 11c	70.0	70.7
8	Y246D hGGPPS + Mg^{2+} + inhibitor 11c	72.0	
9	Y246D hGGPPS + Mg^{2+} + inhibitor 11c	70.0	
10	Y246D hGGPPS + inhibitor 11c without Mg^{2+}	54.0	54.0
11	Y246D hGGPPS + inhibitor 11c without Mg^{2+}	54.0	
12	Y246D hGGPPS + inhibitor 11c without Mg^{2+}	54.0	

Figure 3-7: Differential scanning fluorimetry (DSF) data.

3.4.2. Inhibition of Cancer Cell Proliferation and Rap1A Prenylation

Inhibitors of hGGPPS are known to block the proliferation of MM RPMI-8226 cells (e.g., E/Z-6 was reported to exhibit an EC_{50} of 190 ± 58 nM)[233]. Initial profiling of our ThP-BP library was carried out only for analogs exhibiting $IC_{50} \leq 100$ nM in inhibiting hGGPPS and a minimum of a 10-fold selectivity against hFPPS. Compounds were tested up to a maximum concentration of 10 μM; higher concentrations can lead to aggregation and artifacts[239]. Several compounds were identified exhibiting submicromolar potency in inhibiting the proliferation of RPMI-8226 cells with inhibitors **11b** and **11c** identified as the most potent analogs (**Table 3-3**; **Figure 3-8A**). As was expected, no inhibition was observed with the structurally related, inactive compound **12** or with ThP-BP inhibitors that preferentially target hFPPS, such as analog **13**, despite similar lipophilicity (as estimated by their relative retention on a C_{18} reversed phase HPLC column). These results strongly suggest that neither the bisphosphonate moiety nor inhibition of hFPPS are responsible for the antiproliferation activity observed with our hGGPPS inhibitors.

The hGGPPS inhibitor **11c** was approximately equally toxic to RPMI-8226 cells as doxorubicin (**Figure 3-8A**) and ~80-fold more potent than zoledronic acid (EC_{50} ~ 11 μM). However, **11c** was significantly less toxic to normal bronchial cells (NHBE) than doxorubicin, which exhibited an EC_{50} of ~300 nM (**Figure 3-8B**). Antimyeloma potency (EC_{50} ~ 100−500 nM) was also observed in a genetically diverse panel of MM cell lines characteristic of the human disease, including cells carrying NF-κB activation mutations, RAS mutations, and p53 mutations/deletions (e.g., **Figure 3-9**)[244]. Given that cancers harboring genetic anomalies in p53 are commonly resistant to standard chemotherapy[245], the latter is an important observation. The antitumor effects of inhibitors **11b** and **11c** were also evaluated in a variety of other cancer cell lines with K-Ras/N-Ras overexpression and/or activating mutations, as well as an ovarian cancer cell line expressing high levels of multidrug resistant pumps (e.g., ADR-RES), along with doxorubicin as a control. In spite of their lower toxicity in normal cells, inhibitors **11b/11c** appeared to be as effective as (or better than) doxorubicin in blocking the proliferation of ADR-RES cells (**Figure 3-9B**). Antitumor activity was also observed in pancreatic cancer (MiaPaCa-2) and other cancer cells with several ThP-BP analogs (examples shown in **Figure 3-9C**). Interestingly, the toxicity of analog **11b** in MiaPaCa-2 cells was stronger than that of L-778,123 (3), in spite of its bisphosphonate chemical nature. L-778,123 was advanced to phase I clinical trials in patients with pancreatic cancer (90% K-Ras mutations), but was withdrawn from development due to toxicity[227].

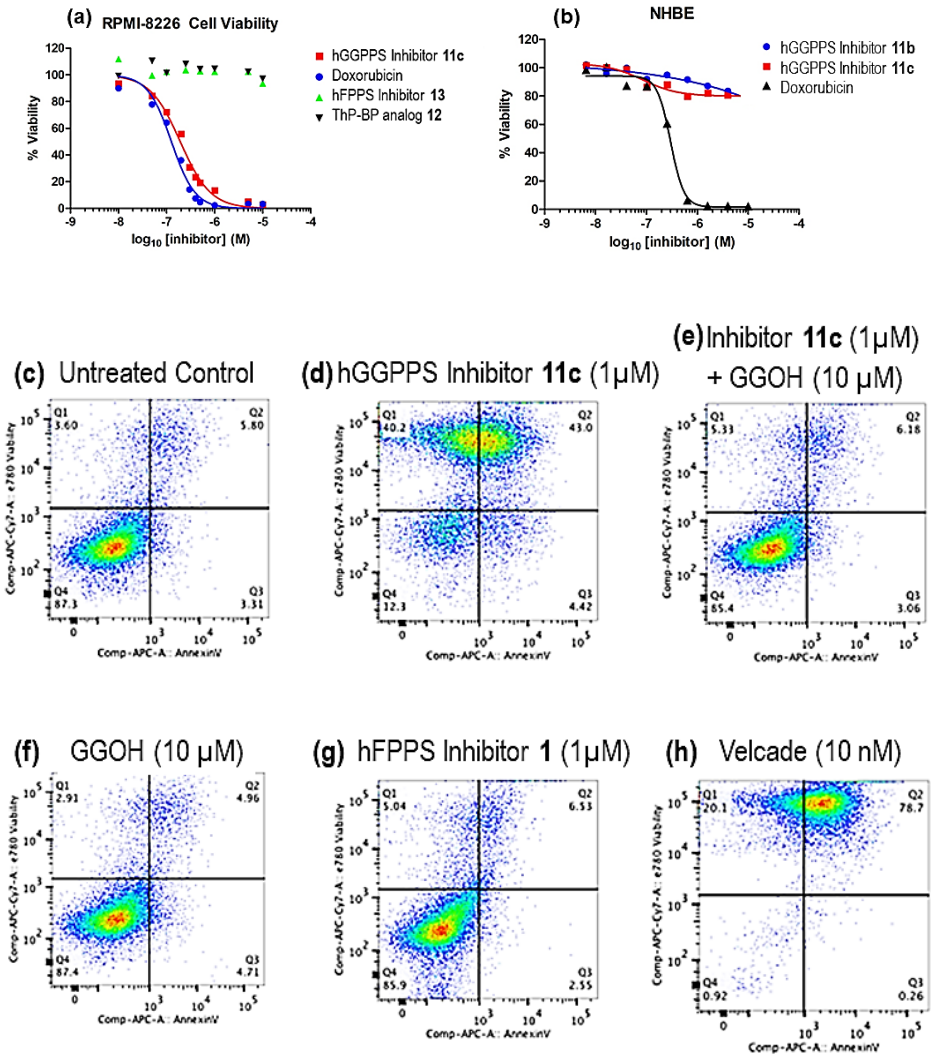

Figure 3-8: Antimyeloma properties of thienopyrimidine-based hGGPPS inhibitors. (a) Comparison of hGGPPS inhibitor **11c**, selective hFPPS inhibitor **13** and inactive ThP-BP compound **12**; doxorubicin was used as a positive control. (b) Toxicity effects on normal human bronchial cells (NHBE) induced by inhibitors **11b**, **11c** and doxorubicin. Apoptosis of MM RPMI-8226 cells after 72 hours of incubation with: (c) vehicle, (d) inhibitor **11c**, (e) GGOH and inhibitor **11c**, (f) GGOH alone, (g) ZOL (**1**) at the same concentration as **11c** and (h) velcade.

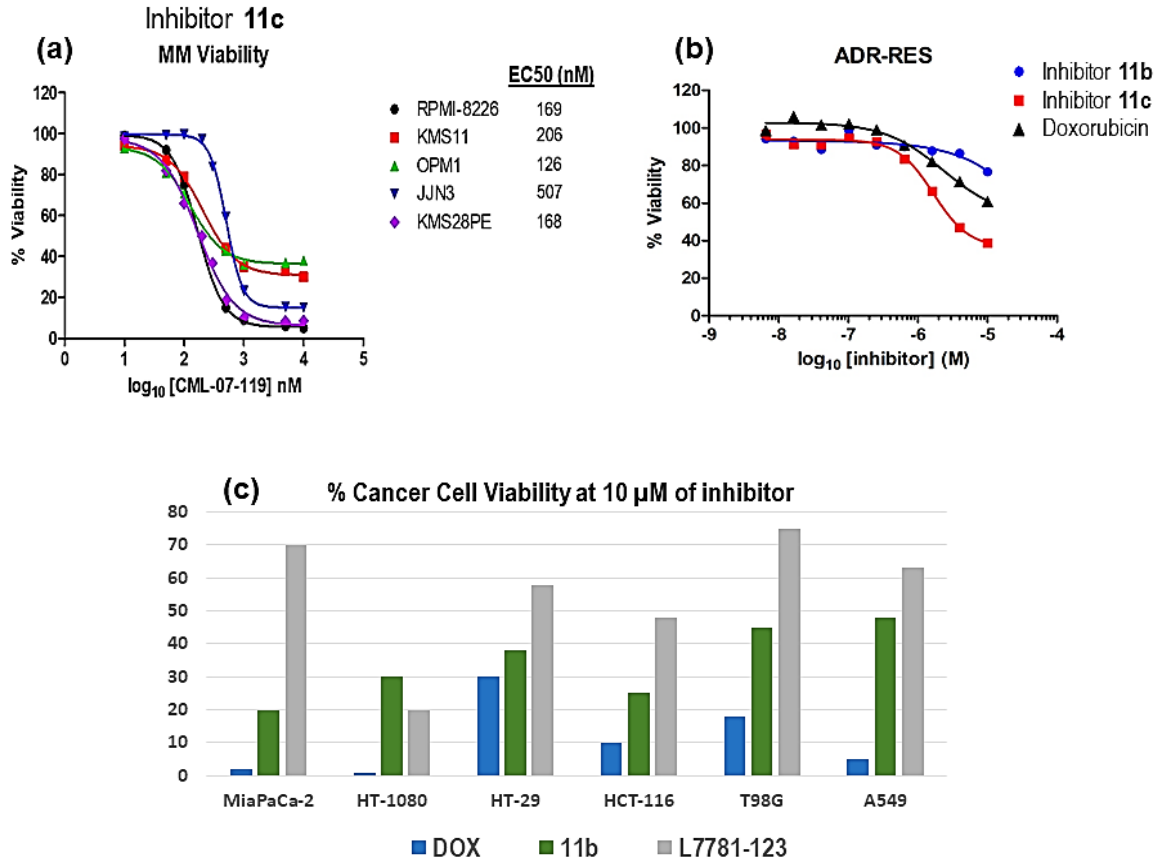

Figure 3-9: Comparison of the anti-proliferation effects on various cancer cell lines by doxorubicin, hGGPPS inhibitors **11b** and **11c**, and L7781-123 (3). (a) Representative examples of the antimyeloma effects of inhibitor **11c** on various human MM cells. (b) Comparison of the toxicity induced by **11b** and **11c** vs those of doxorubicin on an ovarian cancer line expressing high levels of multi-drug resistant pumps (ADR-RES). (c) Toxicity induced by inhibitor **11b** to pancreatic (MiaPaCa-2; K-RAS mutations), Fibrosarcoma (HT-1080; K-RAS mutations, N-RAS activation), colorectal (HT-29 and HCT-116; Wt- K-RAS overexpression and K-RAS mutation, respectively), brain (T98G), non-small cell lung (A549) cancer cell lines.

3.4.3. Intracellular Engagement of hGGPPS, Induction of Cell Apoptosis and Inhibition of Rap 1A Prenylation

Evaluation of several ThP-BP analogs by flow cytometry confirmed that they induce apoptosis in RPMI-8226 cells in a dose-depended manner; zoledronic acid (1) and the antimyeloma drug bortezomib (a proteasome inhibitor) were used as controls. Apoptosis of RPMI-8226 cells was observed with many hGGPPS inhibitors, including compounds **10b** (**Figure 3-10**) and **11c** (**Figure**

3-8D). In contrast, no apoptosis was observed with **1**, when tested in parallel at the same concentration (**Figure 3-8G**). Although induction of apoptosis in cancer cells treated with N-BP inhibitors of hFPPS has been previously reported (e.g., with incadronate in MM[152] and breast cancer[246] and with **1** in renal carcinoma[247] and mesothelioma[248] cells), these observations were possible only at very high concentrations of compound. Interestingly, in many of these studies greater reduction of toxicity was observed when cells were co-treated with geranylgeraniol (GGOH) than with farnesol (FOH)[249]. However, such observations cannot be interpreted as proof that intracellular depletion of GGPP is more toxic to cancer cells than depletion of FPP, since neither the relative cell permeability of FOH and GGOH nor their relative rates of bioconversion to their corresponding pyrophosphate metabolites are known. In our studies, complete rescue from apoptosis was observed when cells were simultaneously treated with a toxic dose of inhibitor **11c** and a nontoxic dose of geranylgeraniol (GGOH; **Figure 3-8E** and **Figure 3-8F,** respectively). These results are consistent with selective intracellular target engagement and a mechanism- based toxicity due to inhibition of hGGPPS. However, since bisphosphonates act as bioisosters of isoprenoid metabolites, it is conceivable that in addition to inhibiting hGGPPS, our ThP-BP compounds could also potentially inhibit the transferase enzymes (e.g., GGTase I and II), an effect that may be possible to overcome by high concentrations of GGOH. More in-depth studies are required to completely rule out any additional off-target effects. We also used bortezomib to induce apoptosis (**Figure 3-8H**) and observed no rescue when cells were co-treated with this drug and GGOH (**Figure 3-10**), consistent with a mechanism of action that is independent of protein prenylation.

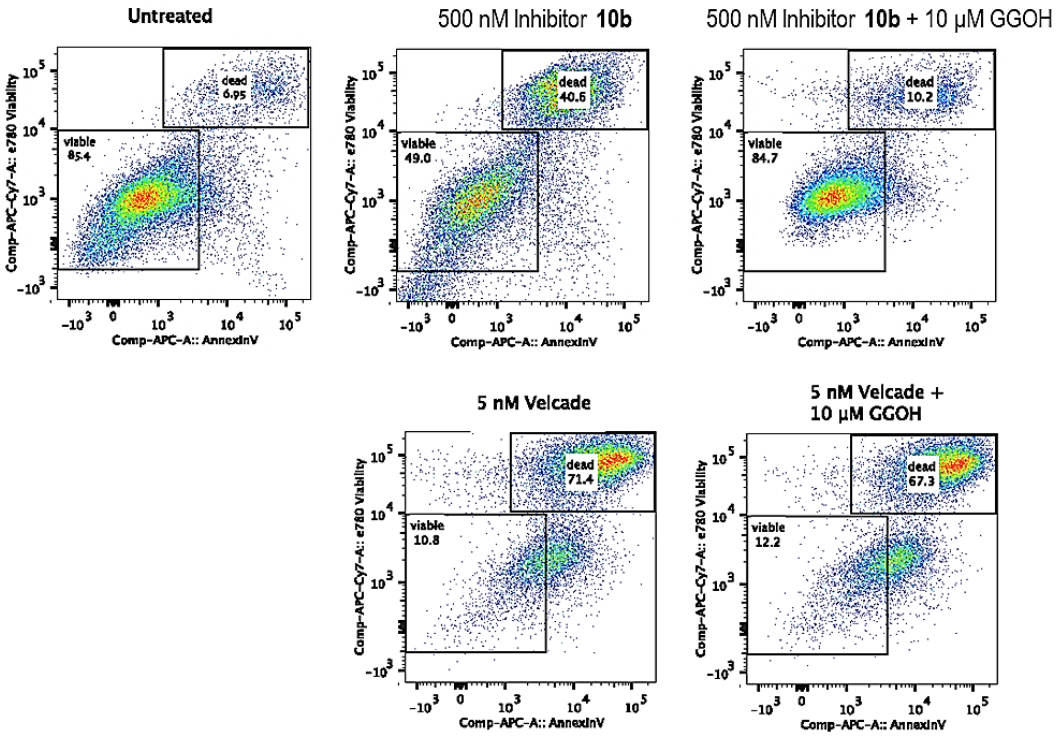

Figure 3-10: Apoptosis of multiple myeloma RPMI-8226 cells. Cell apoptosis observed after 72 hours of incubation with inhibitor **10b** and velcade as compared to the untreated control and cells co-treated with GGOH. Complete rescue from apoptosis was observed upon co-incubation of cells with GGOH to inhibitor **10b**, but for cells co-incubated with velcade and GGOH.

The ability of our hGGPPS inhibitors to disrupt intracellular geranylgeranylation of small GTPases was confirmed. For example, RPMI-8226 cells were incubated with increasing concentrations of inhibitor **11c** and their lysate was analyzed by Western Blotting, using a Rap 1A antibody that specifically binds to the unprenylated form of the protein. Dose-dependent inhibition of Rap 1A prenylation was observed at concentrations as low as 150−200 nM; similar results were observed with zoledronic acid (1) at approximately 0.5 µM concentration (**Figure 3-11**).

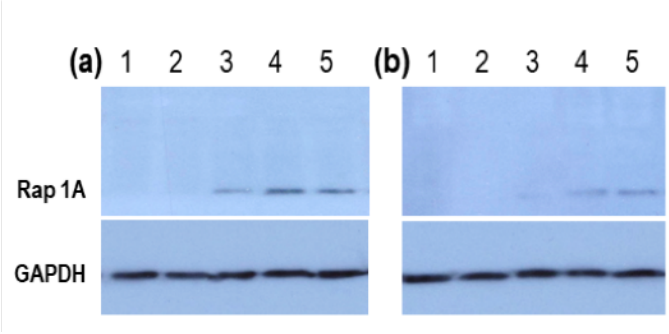

Figure 3-11: Western Blot analysis of intracellular levels of non-prenylated Rap 1A. RPMI-8226 cells were incubated with inhibitor **11c** (a) or ZOL (b); lanes 1: untreated control cells, lanes 2-5: treated with 100 nM, 200 nM, 400 nM and 500 nM, respectively.

Impairment of isoprenoid biosynthesis has been previously reported to also disrupt secretory pathway function in MM cells, leading to the accumulation of intracellular immunoglobulins and/or light chains in the endoplasmic reticulum (ER) that leads to ER stress-induced apoptosis[169]. We confirmed similar results with inhibitor **11c**, which induced increased splicing of XBP1 mRNA, as a consequence of ER stress (**Figure 3-12A**). Moreover, the increased XBP1 mRNA splicing caused by **11c** was largely subverted by simultaneous co-treatment with GGOH, consistent with ER stress induction due to hGGPPS inhibition. Western blot analysis also demonstrated that XBP1s (the protein product of spliced XBP1 mRNA) increased with hGGPPS inhibitor treatment, and this effect was also mitigated by GGOH co-treatment (**Figure 3-12B**). Increased and decreased phosphorylation of ERK and AKT, respectively, was also observed (**Figure 3-12B**). Collectively, these results suggest that intracellular inhibition of hGGPPS produces proapoptotic ERK signaling and concomitant loss of prosurvival AKT signaling in MM cells.

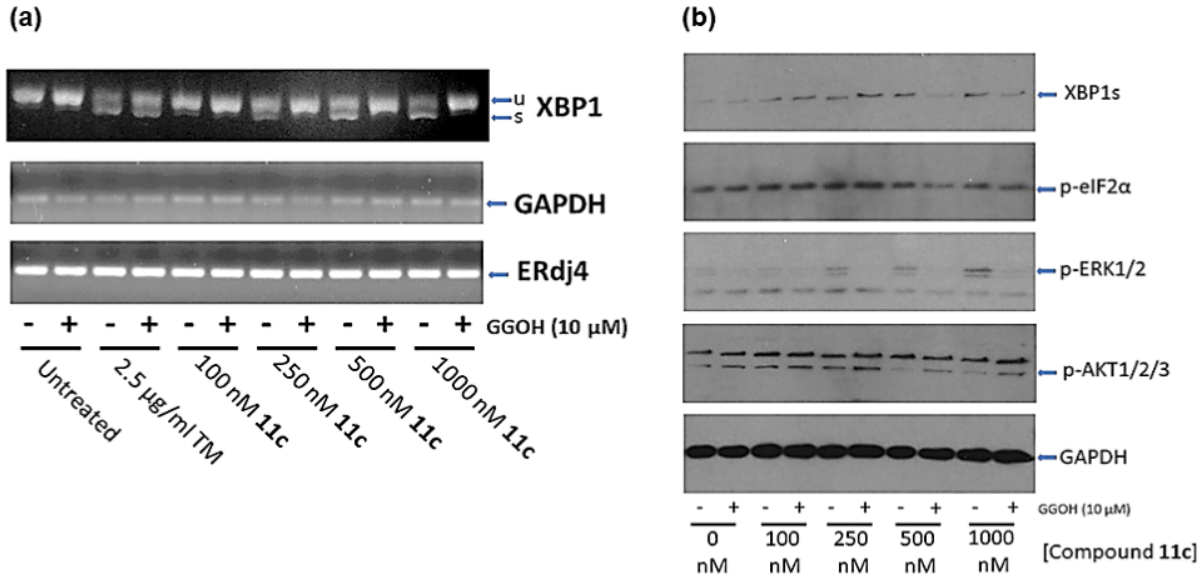

Figure 3-12: Induction of ER stress and modulation of ERK and AKT signaling by hGGPPS inhibitor treatment. (a) RT-PCR demonstrating specific (GGOH rescuable), dose-dependent, induction of XBP1 mRNA splicing by compound **11c**. (b) Western blotting results of RPMI-8226 lysates after 48 hours of treatment with the indicated concentration of hGGPPS inhibitor **11c** in the presence and absence of GGOH rescue for specificity assessment.

From a biochemical perspective, a reasonable first assumption is that the inhibition of hFPPS should block all downstream events in the mevalonate pathway, thus blocking prenylation of GTPases and inducing cell apoptosis. However, our results suggest that hGGPPS plays a more important role in cancer cell biology than hFPPS. Although the low cell-based potency of zoledronic acid (1) may be attributed to its poor physicochemical properties, we observed a dramatic difference in antimyeloma efficacy with structurally very similar ThP-BP compounds that preferentially inhibit hGGPPS vs hFPPS (e.g., hFPPS inhibitor **13** vs hGGPPS inhibitor **11c**; **Figure 3-8A**), suggesting that hGGPPS may be a better therapeutic target for oncology. To gain some insight into the reasons for our observations, we analyzed the intracellular level of these biological targets that potentially need to be engaged by an inhibitor, as can be inferred from the abundance of mRNA transcripts of each enzyme in cells[250]. We found that the mRNA levels of hFPPS are consistently higher than those of hGGPPS in all human MM cells (**Figure 3-13A**). Similar differences in the mRNA levels were observed in primary cancer cells, taken from bone marrow specimens (obtained at diagnosis) of over 700 MM patients participating in a large clinical

trial (**Figure 3-13B**; CoMMpass IA10 clinical trial data (NCT01454297))[251,252]. Collectively, the mRNA data strongly suggest that a lower dose of a drug would be required to achieve a much higher level of intracellular engagement of hGGPPS (thus potentially leading to better clinical efficacy and greater therapeutic index) than with an inhibitor of hFPPS. This conclusion is based on the assumption that the two inhibitors (for hGGPPS vs hFPPS) have equivalent potency and similar overall biopharmaceutical profiles.

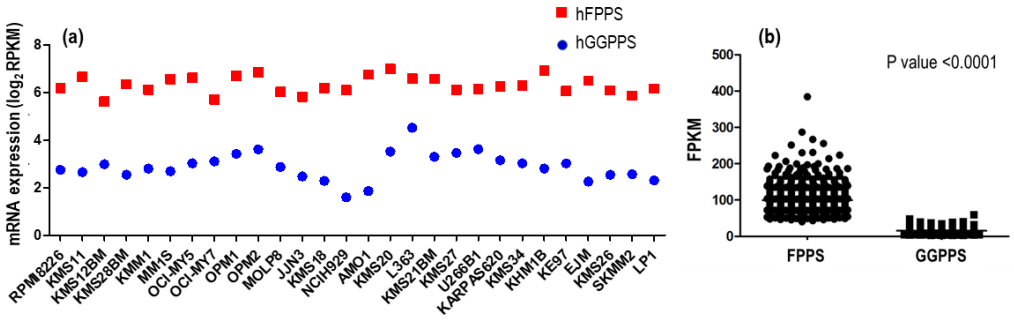

Figure 3-13: RNA transcript level (RNAseq) of hFPPS and hGGPPS. (a) mRNA expression (Log_2 RPKM) of hFPPS and hGGPPS in various human MM cell lines. (b) mRNA expression levels (FPKM) of hFPPS and hGGPPS in CD138-selected MM cells from patients' bone marrow specimens obtained at diagnosis.

3.4.4. Pre-Clinical Evaluation of a ThP-BP Inhibitor: Metabolic Stability, Bone Affinity and Proof-of-principle Studies

The half-life clearance of inhibitor **11c** in male CD-1 mouse (MLM), Sprague-Dawley rat (RLM), and human (HLM) liver microsomes was found to be 128 min, 187 min, and 154 min, respectively. Given the strong association between the MM malignancy and lytic bone disease, as well as the relationship between protein geranylgeranylation and bone resorbing osteoclasts[253], the affinity of our ThP-BP compounds for the bone mineral hydroxyapatite (HAP) was of significant importance. A validated ^{1}H NMR protocol was used to estimate the affinity of our compounds for bone[254]. The relative affinity of analogs **11a** and **11c** for hydroxyapatite (HAP) was found to be equivalent to that of zoledronic acid and slightly stronger than that of risedronic acid (^{1}H NMR data in **Figure 3-14**).

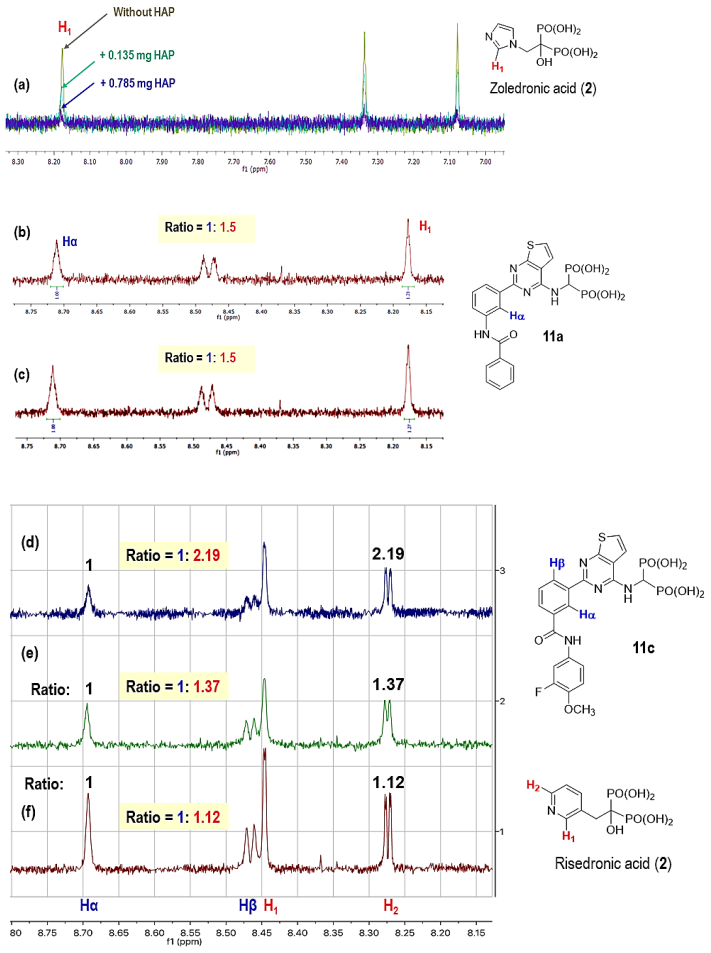

Figure 3-14: Comparison of the relative affinity of hGGPPS inhibitors **11a** and **11c** for hydroxyapatite *versus* the clinical *N*-BP drugs ZOL and RIS. ^{1}H NMR spectra of all compounds (at 50 µM concentration) were acquired in a solution of 50 mM Tris buffer at pH 7.5; for clarity, only select regions of the spectra are shown. (a) Control experiment with ZOL (1) without HAP and after pre-incubation with different amounts of HAP for 5 min. (b) ^{1}H NMR spectrum of **11a** and 1 mixture (~1:1 molar ratio) before any treatment with HAP and (c) the same sample of **11a** and 1 after incubation with 0.52 mg of HAP at room temperature for 5 min. (d) ^{1}H NMR spectrum of a mixture of **11c** and RIS (~1:1 molar ratio) after incubation with 0.40 mg of HAP at room temperature for 5 min, (e) the same sample of **11c** and RIS after incubation with 0.20 mg of HAP at room temperature for 5 min and (f) ^{1}H NMR spectrum of a mixture of **11c** and RIS (~1:1 molar ratio) before any treatment with HAP.

Encouraged by the above data, the in vivo efficacy of inhibitor **11c** was subsequently investigated in a validated MM mouse model that recapitulates the characteristics of the human MM disease and mimics the therapeutic responses of MM patients to clinically validate drugs[255].

Vk*MYC/KaLwRij transgenic mice were bred and maintained in a pathogen-free standard animal facility with a light/dark cycle of 12 h and provided with food and water ad libitum. They were observed daily for any signs of overt toxicity, such as significant weight loss, decreased mobility, skin lesions, inflammation at the site of injection, or morbidity, according to the Facility Animal Care Committees Protocol Number 2012-7242 from the Research Institute of McGill University Health Center (RI MUHC; Glen site) and in accordance with the Policies and Guidelines of the Canadian Council on Animal Care (CCAC).

Aged Vk*MYC/KaLwRij mice (average 50 weeks old)[256] with disease measurable by serum protein electrophoresis (i.e., M-protein levels higher than 15% of total serum proteins, a biomarker of MM disease burden) were treated with 3 mg kg^{-1} day^{-1} of compound **11c** or vehicle (phosphate buffered saline; PBS) by intraperitoneal injection (ip; n = 8 per group, age and gender matched) over a period of 14 days (a total of 12 doses, with a drug holiday during the weekends). Weight loss was observed in all animals over the treatment period, ranging from ~10% (n = 4) to 16% (n=2) in the control group and 15% (n=4) to 28% (n=1) for the animals treated with **11c** (two of the animals in the latter group were euthanized on day 13). Some of the weight loss was attributed to stress induced by daily intraperitoneal injections and manipulation of the animals. At the end of treatment with **11c**, Western blot analysis of peripheral blood mononuclear cell (PBMC) lysates clearly showed inhibition of Rap 1A geranylgeranylation, which is the expected and desired outcome of hGGPPS inhibition, providing evidence of systemic exposure and in vivo target engagement (**Figure 3-15A**). Encouraging antimyeloma efficacy was also observed with a decrease in serum M-protein for the mice treated with **11c** as compared to an increase for animals treated with vehicle (**Figure 3-15B,C**). Since the half-life of mouse immunoglobulins (i.e., M-protein) is approximately 7 days[257], the observed decrease in M-protein after less than 2 weeks of treatment (albeit moderate) is an exciting result that clearly proves the *in vivo* antimyeloma efficacy of inhibitor **11c**. It is noteworthy that for this study, daily dosing of compound **11c** (or vehicle) was carried out by ip injection, since daily dosing of mice by iv. is impractical and requires implanted slow delivery iv pumps. A disadvantage to ip administration of drugs is lower systemic exposure (as compared to iv dosing) and increased absorption into the liver (due to direct transport from the peritoneal cavity into the portal vein system); the latter leads to higher potential for hepatic toxicity. Blood chemistry assessment of plasma samples (collected at the end of the study)

confirmed increased alanine transaminase (ALT) and aspartate trans- aminase (AST) levels in some animals treated with **11c**, although the levels were highly variable (see **Table 3-4**). However, there was no correlation between the increase of liver enzymes, extent of weight loss, and decrease of M-protein levels for the animals treated with **11c** that could potentially imply a mechanism-based toxicity.

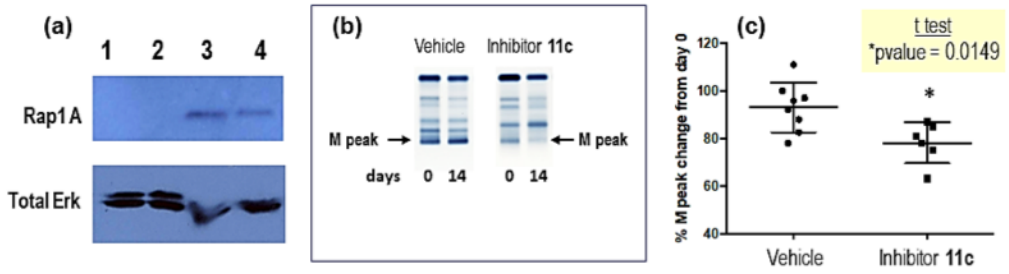

Figure 3-15: Results from *in vivo* treatment of Vk*MYC/KaLwRij mice with compound **11b**. (a) Western blot analysis of two representative PBMC samples from vehicle (lanes 1 and 2) and inhibitor **11c** treated mice (lanes 3 and 4). (b) Serum protein electrophoresis from animals treated with vehicle or inhibitor **11c**. Arrows indicated location of M-protein. (c) Analysis of M-protein as a percentage of total serum protein and expressed as a change from baseline (day 0) to day 14 for each respective mouse. Statistical analysis was performed using unpaired two tailed student's t-test.

Table 3-4: Blood Chemistry after treatment of aged Vk*MYC transgenic mice with inhibitor **11c** (4 hours after the last of the 10 doses of 3 mg/kg/day administered i.p.)

		Normal	**Mouse ID (mice treated with 11c)**						
	Units		**1348**	**1352**	**1377**	**1368**	**1395**	**1371**	**1393**
Bilirubin	µmol/L	2-15	10	3	3	36	3	6	11
Cholesterol	mmole/L	0.93-2.48	3.08	<1.29	2.34	<1.29	3.69	<1.29	2.61
ALT	U/L	28-132	978	176	1644	148	368	264	342
AST	U/L	59-247	2495	359	2656	522	713	574	3431
Decrease of M-protein			3%	8%	8%	3%	-1%	4%	5%
Weight loss			28%	17%	22%	15%	15%	15%	17

3.5. Conclusion

Multiple Myeloma (MM) is a malignancy of B lymphocytes, characterized by the accumulation of malignant plasma cells in the bone marrow that secrete monoclonal immunoglobulins (M-protein) and give rise to a constellation of target organ damage known as CRAB (hyper**C**alcemia, **R**enal failure, **A**nemia, **B**one disease)[16]. In the past, inhibition of protein prenylation of small GTPases that are intimately involved in oncogenesis was proposed as a plausible mechanism of MM therapy. However, strong clinical proof of efficacy with inhibitors of hFPPS, FTase and GGTase I inhibitors has been elusive. Currently, there are no known clinically validated inhibitors of hGGPPS. A new chemotype of hGGPPS inhibitors, represented by compound **11c**, was identified and found to induce antimyeloma effects both *in vitro* and in a reliable MM disease mouse model, which has been shown to accurately predict human drug response.

The studies herein also provide substantial evidence that the hGGPPS is a better therapeutic target for the treatment of MM than the upstream enzyme of the isoprenoid biosynthetic cascade (hFPPS). Support for this hypothesis was provided by antiproliferation data in human MM cells, which clearly showed a stronger response to compounds inhibiting hGGPPS, as compared to structurally related analogs (*i.e*. having very similar physicochemical properties) that are more potent at inhibiting hFPPS. Additionally, analysis of the mRNA levels of hFPPS and hGGPPS in MM cancer cells and bone marrow specimens of MM patients indicated much higher intracellular mRNA levels of hFPPS than hGGPPS. Collectively, these observations suggest that assuming selective hFPPS and hGGPPS inhibitors were identified that possessed equivalent biopharmaceutical properties, a more effective target engagement and better clinical outcome would be expected with therapeutic agents targeting hGGPPS. Furthermore, it has been proposed that the beneficial effect of *N*-BPs on bone resorption are more likely the result of indirect inhibition of geranylgeranylation (rather than direct farnesylation) of proteins in osteoclasts[149].[59] As one of the salient features of human MM is osteolytic bone disease, compounds such as **11c** that bind to bone with high affinity (thereby concentrating in the milieu of the MM disease), inhibit geranylgeranylation (thus blocking bone resorption) and exhibiting strong antimyeloma activity, may provide the ideal set of therapeutic properties for the treatment of multiple myeloma.

CONNECTING TEXT

Through the work done in Chapter 3, we presented the first GGPPS inhibitors with anti-proliferative properties in MM. These compounds show *in vitro* anti-cancer potency at nanomolar ranges in several MM cells lines and other cancer cell lines and promising anti-myeloma effects *in vivo*. The novel inhibitors demonstrated high GGPPS specificity and higher MM anti-proliferative potency than FPPS inhibitors such as acid zoledronic. Demonstrable anti-MM effects were also shown by these inhibitors in a novel mouse model of MM, the Vk*MYC/KaLwRij mouse model. After treating these mice, unprenylated Rap1A was observed in circulating peripheral blood cells indicating GGPPS target engagement as well as a significant decrease in the monoclonal protein proving efficacy in a model that develops MM.

The mechanism of action of BPs in general and more specifically of these novel GGPPS inhibitors it is yet not fully understood and requires further work. In brief, the last chapter places GGPPS as a valuable target in MM disease that needs to be further characterized. This next chapter presents novel data on the GGPPS genetic validation as a target. Successful knock-down of both GGPPS and FPPS in a specific MM cell line was achieved using shRNA lentiviral vectors. However, poor stability of knock-down led us to the use of CRISPR/Cas9 tool to obtain a more permanent knock-out of these two enzymes. Data will be presented on the next chapter on the study of GGPPS as a better target in the mevalonate pathway for anti-myeloma activity.

CHAPTER 4. MECHANISM OF ACTION OF INHIBITION OF TWO TARGETS WITHIN THE MEVALONATE PATHWAY

Mònica Gómez Palou†, Daniel D. Waller, Xian Fang Huang, Youla S. Tsantrizos, Michael Sebag

4.1. Abstract

Inhibition of the mevalonate pathway has long been a goal for the development of novel anti-cancer therapies. Bisphosphonates (BPs) act downstream to inhibit this pathway but were first developed to treat bone disorders, however while their potential as antitumor agents has been investigated in numerous studies *in vitro* and *in vivo* more recently in the last decade. Improved outcomes have been observed in clinical trials in breast cancer and multiple myeloma (MM) often in association with other anti-cancer drugs. The most potent BPs are nitrogen-containing BPs (*N*-BPs) which inhibit the farnesyl diphosphate synthase (FPPS) in the mevalonate pathway. It has been reported that inhibition of this pathway leads to cell apoptosis caused by accumulation of unprenylated small GTPases. Furthermore, novel BP inhibitors have been designed by our group that can target MM disease more potently. Instead of targeting FPPS like classic bisphosphonates, these novel compounds inhibit an enzyme further downstream within the same pathway, geranylgeranyl pyrophosphate synthase (GGPPS). The most prominent effect of these compounds is the inhibition of the mevalonate pathway leading to the inhibition of prenylation of small GTPases that are essential for cell survival. However, further research needs to be performed to completely elucidate how these compounds exert their anti-myeloma effects. In this report we look at the mevalonate pathway in further detail in the context of exploiting it for anti-MM therapies. We first generated GGPPS and FPPS knock-down (KD) MM cell lines by using lentiviral shRNA. Preliminary results from this knock-down revealed minimal cell apoptosis in GGPPS KD cells when GOOH was withdrawn from culture. However, knock-down of these two targets using shRNA was not shown to be permanent and CRISPR/Cas9 was used to generate a more permanent knock-out (KO) of GGPPS and FPPS in the RPMI8226 cell line. After confirming stable KO of GGPPS and FPPS by CRISPR/Cas9 we evaluated the proliferation rates of these cells in the presence and absence of exogenous GGOH. After 72 hours, only GGPPS KO cells with no GGOH in culture were shown to have substantially decreased viability. This data is very interesting because it is the first step towards the genetic validation of GGPPS as a target in the mevalonate pathway for MM therapy.

4.2. Introduction

Bisphosphonates (BPs) are used as the mainstay of treatment for Multiple Myeloma (MM) bone disease[32]. BPs are inhibitors of osteoclastic bone resorption and are used for the treatment of

several skeletal disorders such as osteoporosis or heritable skeletal disorders in children (e.g. osteogenesis imperfecta)[258]. There are two types of BPs currently being used, the nonnitrogen containing BPs (e.g. etidronate and clodronate) and the nitrogen-containing BPs (*N*-BPs, e.g. pamidronate, alendronate, risedronate and zoledronic acid). The mechanism of action of these two types of BPs differ and it has been reported that *N*-BPs are more potent molecules[143]. The mechanism of action of *N*-BPs is based on the inhibition of the mevalonate pathway (**Figure 4-1**).

The use of BPs for their anti-cancer properties has had increased attention in the past few years. The mechanism of action for the anti-proliferative activity of *N*-BPs is still under investigation but it has been reported that it is through the inhibition of the mevalonate pathway that these compounds have anti-cancer effects and they do so in a dose-dependent manner[259,260].

The mevalonate pathway is known to play an important role in myeloma cell survival. The end products of the mevalonate pathway are cholesterol which is crucial for the membrane and steroid synthesis and non-sterol products such as farnesyl pyrophosphate (FPP) and geranylgeranyl pyrophosphate (GGPP) (**Figure 4-1**)[261]. GGPP and FPP are necessary for the prenylation of small GTPases such as Ras, Rho, Rab, Rac and Rap which are involved in proliferation, signal transduction and apoptosis[262]. The mevalonate pathway is highly regulated and it is dysregulated in tumor cells by a variety of mechanisms. The different levels of pathway dysregulation suggest that cancer cells are particularly dependent on mevalonate-derived end products and therefore preferentially sensitive to inhibition of the mevalonate pathway[263]. For instance, inhibition of the mevalonate pathway by statins has shown to be a promising venue to target myeloma cells although the results show mix efficacy with only a subset of tumors being highly responsive[264]. A report showed that genes of the mevalonate pathway were identified as top-scoring targets after a pooled genome-wide short hairpin RNA screen. The screen was performed in order to unravel novel targets that could potentiate statin-induced apoptosis when knock-down was done. Amongst these targets were sterol regulatory element binding transcription factor 2 or geranylgeranyl diphosphate synthase (GGPPS)[263]. Inhibition of the mevalonate pathway by *N*-BPs has been shown to reduce cell viability mainly by inhibiting cell proliferation in myeloma cells[265]. The inhibition of FPPS, which is upstream of GGPPS in the mevalonate pathway, by *N*-BPs such as zoledronic acid leads to the inhibition of prenylation of small GTPases which are important for cell survival and cytoskeletal organization[155]. As a consequence of inhibiting protein prenylation there are several downstream effects that are thought to contribute to the mechanism of action of BPs in

causing cell apoptosis. The most prominent effect is an increase in the stress of the endoplasmic reticulum (ER) and the subsequent activation of the unfolded protein response (UPR). Myeloma cells rely heavily in this machinery in order to process the high degree of antibodies produced (e.g. monoclonal protein)[168]. When the mevalonate pathway is targeted with inhibitors such as *N*-BPs (e.g. zoledronic acid) there is accumulation of unprenylated proteins in the ER which will in turn cause chronic activation of the UPR leading to apoptosis of myeloma cells[167].

Until today many efforts have been directed to target FPPS and the prenyl transferase FTase and GGTase I in the mevalonate pathway in order to inhibit cancer cell proliferation. However, results showed modest clinical antitumoral efficacy of zoledronic acid[159,160] (**Figure 4-1**). A variety of structurally diverse compounds have been tested over the years, albeit with little to no significant antitumor potency. One of the reasons behind this is the poor biopharmaceutical properties of these compounds. *N*-BPs are not lipophilic compounds and they have difficulty reaching their intended intracellular targets. Furthermore, it is possible that FPPS is not the appropriate molecule to be targeted in the mevalonate pathway. A report were genome-wide shRNA screening was performed to uncover novel targets revealed that genes of the mevalonate pathway are amongst the top-scoring targets and one example is the geranylgeranyl pyrophosphate synthase (GGPPS)[263].

The geranylgeranyl pyrophosphate synthase in the mevalonate pathway is still not yet clinically validated and only few selective inhibitors have advanced to pre-clinical development (**Figure 4-1**). As described in Chapter 3, it was shown that GGPPS mRNA levels were lower in both myeloma cell lines and in myeloma cells from patients newly diagnosed and we believe that this makes GGPPS an easier molecule to target than FPPS. In this case a lower concentration of inhibitor will be needed to achieve better anti-myeloma results[266]. Our group has reported a new class of bisphosphonate-like compounds that are specific inhibitors of GGPPS in the mevalonate pathway. These compounds have shown to present effective anti-proliferative activity against MM and other cancer cell types. These novel BPs have shown to induce myeloma cell apoptosis *in vitro* as well as *in vivo* downregulation of Rap1A geranylgeranylation and reduction of M-protein in the serum in the MM mouse model, Vk*MYC/KaLwRij[266].

The inhibition of FPPS and GGPPS in the mevalonate pathway needs to be further assessed to fully comprehend the mechanism of action by which these compounds exert their anti-cancer effects. In this report, we performed the genetic knock-down of both FPPS and GGPPS *in vitro* in

a MM cell line to understand the consequences of genetically targeting these two enzymes. This work presents two strategies used to knock-down or knock-out GGPPS and FPPS genes using shRNA or CRISPR/Cas9, respectively. The main goal of this article is to validate these targets by analyzing the viability of GGPPS KO and FPPS KO cells after withdrawal of geranylgeraniol (GGOH) from cell culture. GGOH is a product from the mevalonate pathway and functions as an essential compound for cell proliferation and differentiation[267]. When GGOH is supplemented exogenously to myeloma cells that have been treated with inhibitors of GGPPS, it is able to exert a protective action by rescuing the pathway at the GGPP level (**Figure 4-1**). It is by analyzing the response to GGOH presence and absence in the novel GGPPS KO and FPPS KO cell lines that we can establish the validity of these molecules as valuable targets in the mevalonate pathway.

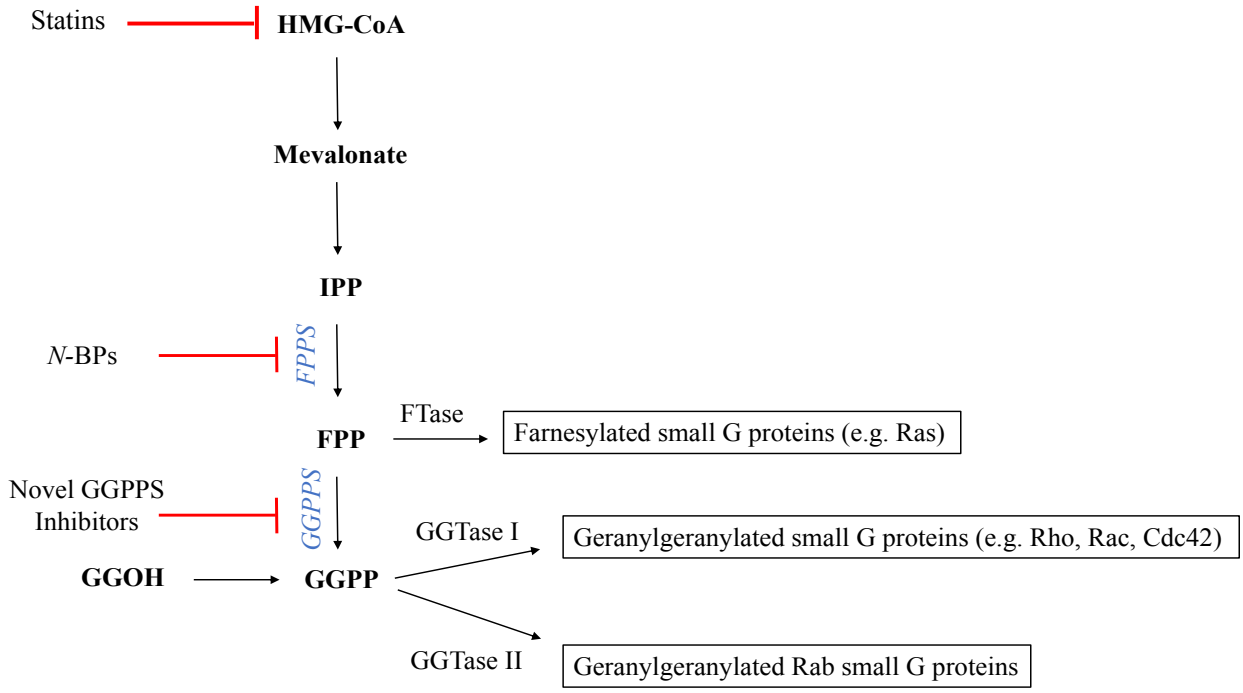

Figure 4-1: The mevalonate pathway and its inhibitors.

4.3. Materials & Methods

4.3.1. Cell Culture for RPMI8226 and HEK293FT cells

RPMI8226 cell line was cultured in RPMI-1640 medium (Multicell) supplemented with 10% fetal bovine serum (Gibco, Gaithesburg, MD) supplemented with 2 mM L-glutamine in a 5% CO_2 atmosphere at 37ºC. HEK293FT cells were cultured with DMEM (Multicell) supplemented with 10% fetal bovine serum (Gibco, Gaithesburg, MD) supplemented with 2 mM L-glutamine in a 5% CO_2 atmosphere at 37ºC.

4.3.2. shRNAs Obtained to Induce Knock-down

To knock-down GGPPS and FPPS, shRNAs cloned into the pLKO.1 vector (**Figure 4-2**) were obtained from the High Throughput Screening Facility-Life Science Complex McGill University (Sigma Mission).

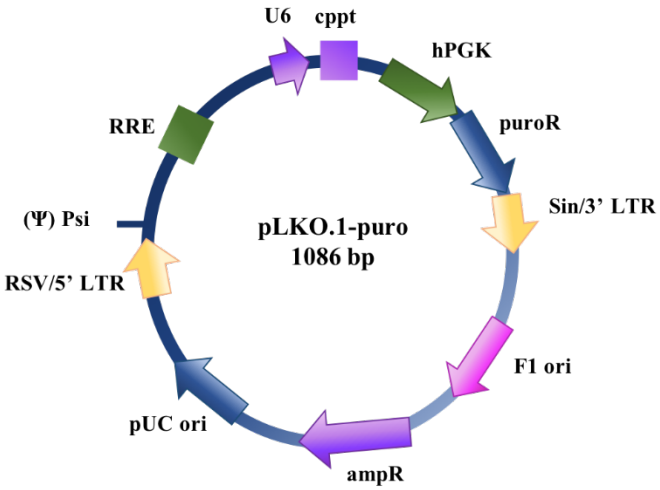

Figure 4-2: TRC1 Vector Map (pLKO.1-puro). *Cppt*: central polyurine tract; *hPGK*: human phosphoglycerate kinase eukaryotic promoter; *puroR*: puromycin resistance gene for mammalian selection; *SIN/3' LTR*: 3' self-inactivating long terminal repeat; *Fi ori*: f1 origin of replication; *ampR*: ampicillin resistance gene for bacterial selection; *pUC ori*: pUC origin of replication; *RSV/5' LTR*: 5' long terminal repeat; *Psi*: RNA packaging signal; *RRE*: Rev response element; *U6*: U6 promoter.

One clone for each of the shRNAs was obtained and they are identified as follows (**Table 4-1**):

Table 4-1: Identification of GGPPS1 and FPPS shRNA clones.

Clone #	TRC Clone ID	Symbol	Gene ID
R-413-2	TRCN0000045788	GGPPS1	9453
R-413-4	TRCN0000299722	FPPS	2224

One Shot™ Stbl3™ Chemically Competent *E. coli* cells (ThermoFisher Scientific, MA, USA) were transformed with DNA from plasmids containing GGPPS1 and FPPS shRNAs according to manufacturer's instructions. The pLKO.1-puro backbone of the shRNAs shown in **Figure 4-2** contains a cassette for puromycin resistance. In addition, DNA from pLKO.1 empty vector was used as negative control and a vector containing GFP (1394G) was used to visualize positive transduction into our cell line of choice. Positive transformed cells were then selected by plating on LB agar containing ampicillin and grown overnight at 37ºC. One clone was selected from each culture and used to inoculate 5.5 ml in LB broth plus ampicillin. These cultures were then grown shaking overnight at 37ºC. After sufficient growth, 500 µl of solution was frozen in glycerol at -80ºC to keep as a stock and the rest was diluted 1:100 in LB broth for expansion. Once LB broth was inoculated, expansion of culture was performed shaking at 37ºC for approximately 16 hours. Extraction of plasmid DNA from expanded cultures was performed using the E.Z.N.A plasmid DNA Maxi kit (Omega Bio-Tek, Norcos, GA, USA) as per manufacturer's instructions.

4.3.3. Lentiviral Production

For production of self-inactivating lentiviral vectors, HEK293FT (human embryonal kidney cells) helper cells were co-transfected with each specific shRNA (GGPPS or FPPS) and the lentivirus packaging plasmids pMDLg/pRRE (Addgene plasmid #12251), RSV-rev (Addgene plasmid #12253), and pMD2.G (Addgene plasmid #12259)[268]. In brief, competent Stbl3 cells were transformed with each specific shRNA and packaging plasmids and after expansion of cultures plasmid DNA was extracted and used for lentiviral production. Cells were co-transfected at 75% confluency with the plasmid DNA extracted from the three packaging plasmids plus each specific shRNA. Calcium phosphate was used for transfection (CalPhos ™ Mammalian Transfection Kit, Clontech, Mountain View, CA, USA). Overnight transfection of cells was performed with cells in incubator at 37ºC and 5% CO_2 followed by fresh media replacement after 24 hours. Cells were left

in incubator for 72 hours post-transfection after changing media. Supernatant was collected after 72 hours and filtered (0.45 μm filter). Concentrated virus was obtained from filtered supernatant by ultracentrifugation at 22,000 rpm for 2 hours. Following centrifugation, concentrated virus particles were resuspended in PBS and either used directly for transduction or stored in -80ºC freezer.

4.3.4. Transduction of RPMI8226 Cells with Lentivirus Containing shRNAs

Transduction of shRNAs contained in the lentiviral particles was performed in MM RPMI8226 cells. Briefly, RPMI8226 cells were seeded in 12-well plates at a confluency of 1 x 10^5 cells per well. In order to increase efficiency polybrene (Sigma-Aldrich, St. Louis, MO, USA) was added to the cell culture at a concentration of 4 μg/ml. Culture of RPMI8226 cells was performed since day 1 of transduction in the presence of geranylgeraniol (GGOH, Sigma-Aldrich, St. Louis, MO, USA) at a concentration of 10 μM. Following protocol optimization, a dilution of 1:5 of lentivirus in media was chosen to perform transduction of shRNAs. RPMI8226 cells were in culture with the presence of each shRNA lentivirus for 16 hours until media was replaced. After 72 hours of infection, selection of positively transduced cells was performed using puromycin (Thermo Fisher Scientific, Waltham, MA, USA) at a concentration of 2 μg/ml. Cells were passaged every 3-4 days for 2 weeks before gene expression was analyzed.

4.3.5. CRISPR/Cas9 Genome Editing

Integration of Cas9 into RPMI8226 MM cell line was performed using the lentiCas9-Blast plasmid (Addgene plasmid #52962), a separate lentiviral construct that delivers hSpCas9 and blasticidin resistance into the cell line. Cas9 plasmid DNA was extracted from Cas9 transformed competent Stbl3 cells using the E.Z.N.A plasmid DNA Maxi kit (Omega Bio-Tek, Norcos, GA, USA) and the steps performed to achieve Cas9 expression in RPMI8226 cell line were followed as described in "Lentiviral Production" section. After transduction of RPMI8226 cells with Cas9, selection of resistant cells was performed using blasticidin at a concentration of 4 μg/ml for 14 days. Confirmation of Cas9 expression was done by western blot and aliquots were frozen to be used for the final transduction. For CRISPR/Cas9 genome editing in RPMI8226/Cas9 cells the lentiGuide-Puro (Addgene plasmid #52963) vector was used. This plasmid expresses only the chimeric guide RNA. The vector was digested using *BsmBI*, and a pair of annealed oligos were cloned into the single guide RNA scaffold. The oligos were designed based on the target site sequence and had to

be flanked on the 3' end by a 3bp NGG PAM sequence[269,270]. The oligos used in this report were designed using CRISPR tools from Feng Shang's lab and they are the following:

GGPPS1(Exon 4):

Oligo 1: 5'-CACCGGACAACTCAAAACTCCGACG-3'

Oligo 2: 5'-AAACCGTCGGAGTTTTGAGTTGTCC-3'

FPPS (Exon 4):

Oligo 1: 5'-CACCGGTATAACCGGGGTTTGACGG-3'

Oligo 2: 5'-AAACCCGTCAAACCCCGGTTATACC-3'

Once the lentiviral vector digestion, oligo annealing and ligation were performed, plasmids were transformed into competent Stbl3 bacteria (ThermoFisher Scientific, MA, USA).

Plasmid DNA for each of the gRNAs was extracted from Stbl3 bacteria and the same steps performed in "Lentiviral Production" section were performed using the lentiviral packaging plasmids. Selection using puromycin at a concentration of 2 μg/ml was started on the fifth day after transfection and continued over several weeks.

4.3.6. Gene Expression Analysis

RPMI8226 cells transduced with each specific shRNA were collected and lysed at different time points. Total RNA was extracted from the samples (Qiagen RNeasy Mini Kit, Germantown, MD) and reverse-transcribed into cDNA (Applied Biosystems High-capacity cDNA Reverse Transcription kit, Foster City, CA) prior to gene expression analysis. Quantitative real-time PCR (qRT-PCR) was performed using the Applied Biosystems StepOne Plus Real Time PCR System and SYBR Green Master Mix (Foster City, CA). Changes in relative gene expression were calculated using the $2^{-\Delta\Delta CT}$ method with normalization to GAPDH. The following primer sets were used: GGPPS1, forward primer (5'- CCAGGTAAACAAGTGAGAACCAA-3') and reverse primer (5'- CGTCGGAGTTTTGAGTTGTCT-3'); FPPS, forward primer (5'- CACCCAGAGATAGGAGATGC-3') and reverse primer (5'- AGCTCCCGGAATGCTACTA-3'); GAPDH, forward primer (5'- AATCCCATCACCATCTTCC-3') and reverse primer (5'- TTCTCCATGGTGGTGAAGA-3').

4.3.7. GFP Expression and Annexin V apoptosis assay

After 72 hours of transducing GFP in RPMI8226 cells, flow cytometry analysis was performed to assess GFP expression. To assess the apoptotic effect of retrieving GGOH from GGPPS knocked-down cells, flow cytometry was performed using Annexin V. Cells were seeded at a density of $5x10^5$ cells/well in 6-well plates in RPMI-1640 medium supplemented with 10% FBS and treated with or without GGOH for 96 hours. After 96 hours of treatment, apoptosis was determined by double staining with APC Annexin V (BD Biosciences, Mississauga, ON) and eFLuor780 Viability dye (ThermoFisher Scientific) according to manufacturer's directions. Stained samples were acquired on a BD FACSCanto II instrument (BD Biosciences, Mississauga ON) and post-acquisition analyses were performed using FlowJo (V10) software.

4.3.8. Western Blot Analysis

RPMI8226 cells were transduced with the lentiCas9-Blast vector and selected using blasticidin at a concentration of 4 μg/ml. After two weeks of culture (14 days post-infection), cells were harvested by centrifugation and immediately washed with ice cold PBS. Next, cells were centrifuged and resuspended in ice cold RIPA lysis buffer (Pierce cat#89900). RPMI8226 cells non-transduced were used as a negative control for this assay. Equal amounts of cleared protein lysate were then separated by SDS-PAGE, transferred to PVDF membranes, and then membranes were incubated with primary antibody overnight at 4°C. The following primary antibody was used: anti-FLAG (Sigma-Aldrich, F-7425). After extensive washing, the membrane was exposed to HRP-conjugated secondary antibody for 1 hour at room temperature. After further extensive washing, ImmunoCruz (Santa Cruz Biotechnology) chemiluminescence reagents were employed to visualize the remaining (bound) secondary antibody.

4.3.9. Viability Assay for KO Cell Lines

Cell were seeded in 96-well plates at a density of 5,000 cells per well with 9 replicates per condition. Cells were incubated with or without GGOH and when indicated with final concentration of **11b** compound of 1 μM. Final culture volume was 100 μl/well and incubation was performed for 72 hours prior to the addition of the MTS proliferation assay reagent (Promega, Madison, WI). Plates were incubated at 37ºC in the presence of 5% CO_2 for 2 hours prior to recording OD490 using Tecan Infinite M200Pro microplate reader.

4.3.10. Screening for GGPPS Genome Edited DNA

First, genomic DNA from KO cell lines was extracted using QiAamp DNA Blood Mini Kit (Qiagen, Germantown, MD) and Alt-R Genome Editing Detection Kit (Integrated DNA technologies, Coralville, IA) was used to verify mis-match editing in GGPPS target gene in KO cell lines. PCR amplification of GGPPS (777 bp) was done using the following primer sequences (Integrated DNA technologies, Coralville, IA) and cycling conditions:

Forward: 3'- CACACCTGAGACTTTCATAATCTGT-5'

Reverse: 5' – GTGCATCAATCTGTTTATAGGCTTTAG -5'

Cycling conditions: 94ºC for 15 min, 40 cycles of 92ºC for 30 sec, 55ºC for 1 min, 72ºC for 1 min and 30 sec, followed by 72ºC for 10 min.

Visualization of digestion-derived restriction bands for verification of genome edited KO cell lines was performed using DNA gel electrophoresis (1.6% agarose gel) and ethidium bromide (Sigma, St. Louis, MO).

4.3.11. Statistical Analysis

Comparison between groups was accomplished using standard Student's T test and ANOVA regression analysis where appropriate

4.4. Results

4.4.1. Positive Transduction of GFP in RPMI8226 Using Lentiviral Packaging Plasmids

Myeloma cell lines have been shown to be challenging to transfect with nucleic acids and several transfection methodologies have been used over the years to improve upon the efficiency of transfection[271]. Here, knock-down of GGPPS and FPPS in the RPMI8226 MM cell line was done using lentiviral transduction of shRNA for GGPPS and FDPPS to achieve a more efficient knock-down of these two genes.

Transduction of GFP into the RPMI8226 cells was first performed to test the lentiviral packaging plasmids (pMDLg/pRRE, RSV-rev and pMD2.G) in our cell line. Positive GFP was observed after 72 hours of transduction (**Figure 4-3A**). To quantify the number of GFP positive cells, flow

cytometry was performed in the same cells after 72 hours of transduction and results showed that 90% of the cell population expressed GFP positively (**Figure 4-3B**).

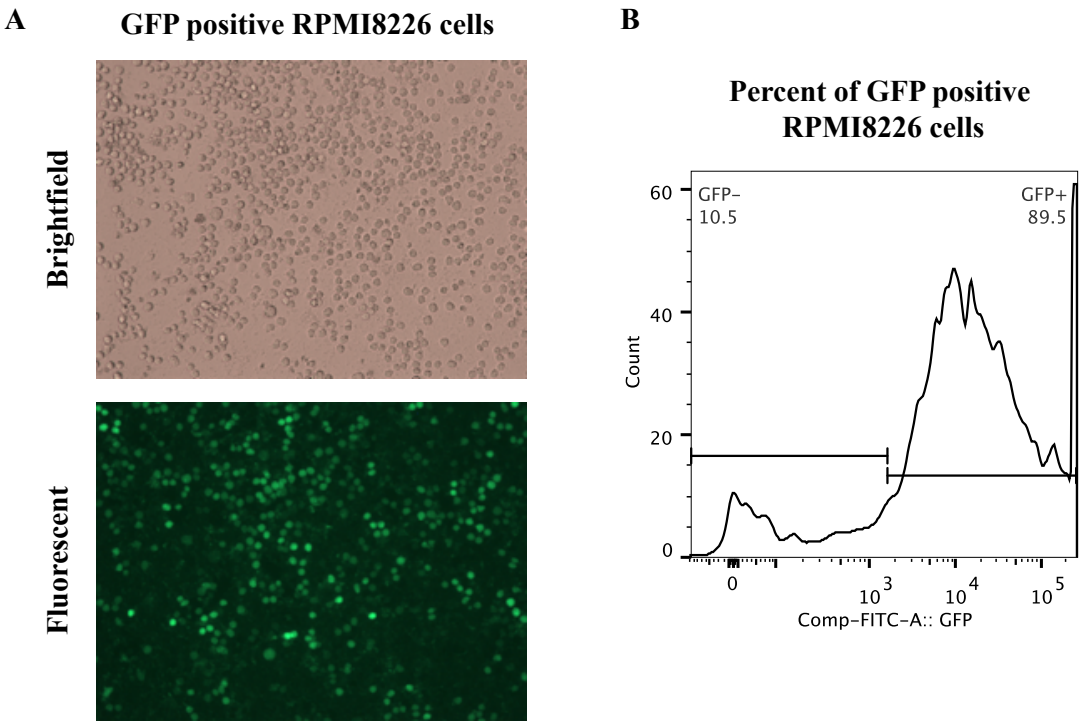

Figure 4-3: GFP transduction of RPMI8226 MM cells. (*A*) Microscopy images of RPMI8226 cells transduced with GFP after 72 hours of transduction. Comparison of the same area of cells using brightfield versus fluorescent to approximate efficiency of transduction. (*B*) Percentage of RPMI8226 GFP positive cells using flow cytometry analysis.

4.4.2. Knock-down of GGPPS and FPPS in RPMI8226 Cell Line Using shRNA

Once it was confirmed that GFP transduced successfully in the RPMI8226 cells using the lentiviral packaging plasmids, knock-down of GGPPS and FPPS was performed RPMI8226 cells following the same procedures. Cells were infected with lentivirus containing shRNAs and after 5 days of infection, selection with puromycin antibiotic was started. Interestingly, in many studies including our last report, reduction of BP induced toxicity was observed when MM cells were co-treated with geranylgeraniol (GGOH) and BPs[249,266]. We hypothesized that presence of GGOH in culture was necessary for RPMI8226 cell survival after knock-down of GGPPS and FPPS genes. GGOH is a downstream product of the mevalonate pathway and when this substrate is added exogenously

in the cell cultures is able to rescue the pathway at the GGPP step (**Figure 4-1**). For this reason, all cells cultured during knock-down were supplemented with GGOH at a concentration of 10 μM. Once the cell cultures achieved a growth phase without observable death, gene expression analysis of GGPPS and FPPS was performed using qPCR. RPMI8226 cells that had been transduced with GGPPS shRNA showed 80% knock-down of GGPPS while FPPS levels were maintained similar to the control after 14 days post-infection (**Figure 4-4A**). RPMI8226 cells that had been transduced with FPPS shRNA also showed 80% knock-down of FPPS while GGPPS gene levels were maintained similar to the control after 14 days post-infection (**Figure 4-4B**).

Cells were kept in culture over time in order to test the stability of the knock-downs achieved with the shRNAs. In the GGPPS KD cell line, 70% of knock-down was observed for GGPPS after 5 weeks of culture. After two months of cell culture the percentage of cells with GGPPS knock-down decreased to 40% (**Figure 4-4C**) possibly indicating a growth advantage for cells not harboring the shRNA or without effective suppression of mRNA target and this despite continuous GGOH rescue.

In the FPPS KD cell line, the knock-down of FPPS was below 50% after one month of cell culture and it had decreased to 20% after 2 months indicating poor stability of the knock-down by shRNA (**Figure 4-4D)**.

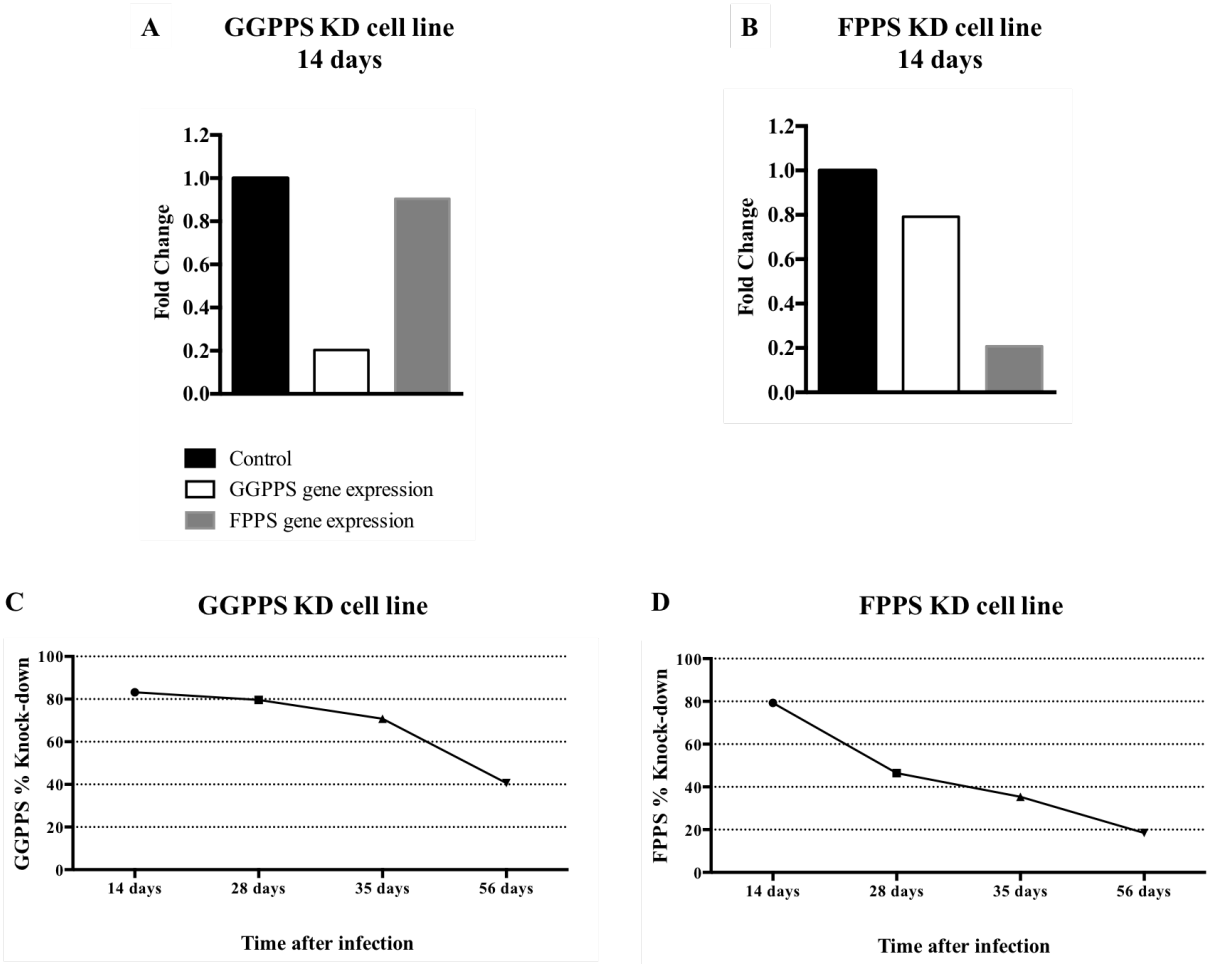

Figure 4-4: shRNA knock-down of GGPPS and FPPS in RPMI8226 MM cell line. (*A*) Gene expression of GGPPS and FPPS in GGPPS KD cell line with shRNA after 14 days of infection versus control pLKO.1 empty vector using GAPDH as endogenous control in all cases, (*B*) Gene expression of GGPPS and FPPS in FPPS KD cell line with shRNA after 14 days of infection versus control pLKO.1 empty vector, (*C*) GGPPS gene expression over time in GGPPS KD cell line. (*D*) FPPS gene expression over time in GGPPS KD cell line.

4.4.3. Apoptosis of RPMI8226 KD Cell Line after GGOH Withdrawal

After GGOH withdrawal, we looked at cellular apoptosis in RPMI8226 cells infected with shRNAs to knockdown GGPPS, FDPS or control vectors. We observed that in the control cells, 96 hours of withdrawal from GGOH was not accompanied by an increase in apoptotic cell death (**Figure 4-5A and B**). Results show that withdrawal of GGOH from GGPPS KD cells caused an increase in apoptosis of only 3%. (**Figure 4-5C and D**). Results from this same assay in FPPS KD

cells did not show any differences between groups (data not shown), indicating that GGOH is only able to rescue the pathway at the GGPPS level.

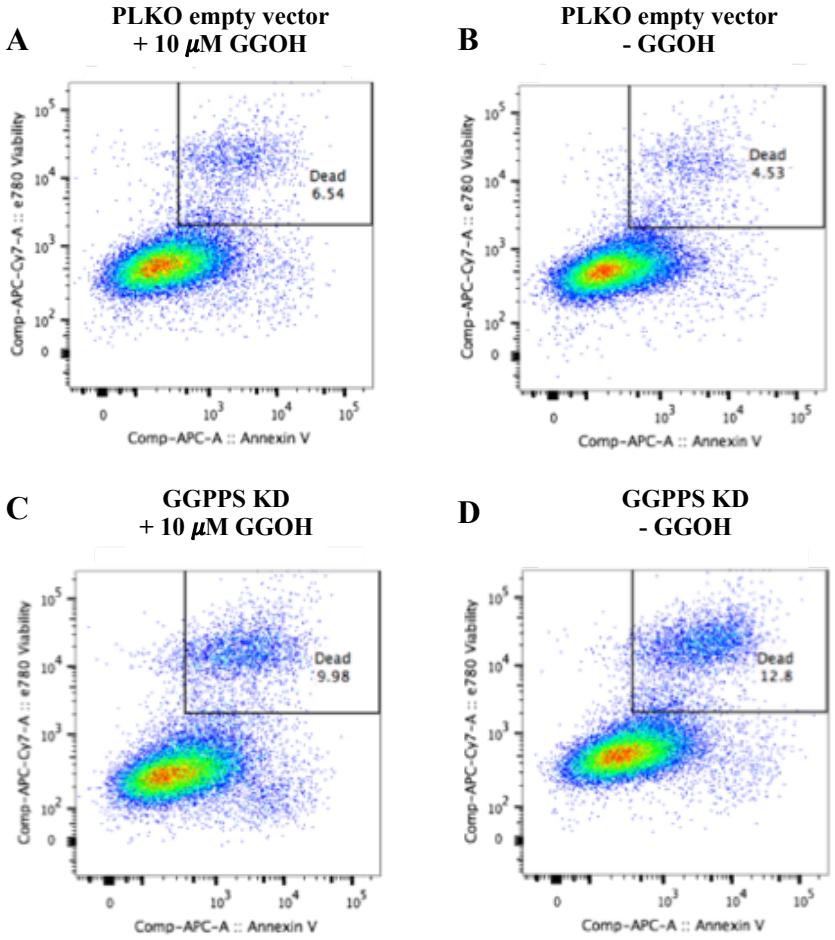

Figure 4-5: Apoptosis of MM RPMI8226 GGPPS KD cells after 96 hours in culture. (*A*) pLKO.1 empty vector treated with GGOH at 10 μM for 96 hours, (*B*) pLKO.1 empty vector without GGOH for 96 hours, (*C*) RPMI8226 GGPPS KD cell line treated with GGOH at 10 μM for 96 hours, (*D*) RPMI8226 GGPPS KD cell line without GGOH for 96 hours.

4.4.4. Knock-out of GGPPS and FPPS in RPMI8226 Cell Line using CRISPR/Cas9

In order to generate a more efficient knock-down and a more permanent one, CRISPR/Cas9 was employed.

The first step towards knocking out GGPPS and FPPS was generating a cell line which expresses Cas9 in order to use the CRISPR strategy. RPMI8226 cells were transduced with the lentiCas9-Blast vector and Cas9 expression was confirmed using western blot analysis at two different

lentiviral concentrations. Non-transduced RPMI8226 cells were used as negative control (**Figure 4-6**). After positive expression of Cas9 in the RPMI8226 cell line, transduction of each specific guide sequence (GGPPS or FPPS) was performed in order to generate the knock-out (KO) cell lines. Selection using puromycin was performed in order to isolate positively transduced clones. In addition, all cell cultures that were transduced to achieve knock-out of GGPPS or FPPS were maintained with GGOH to prevent premature cell death.

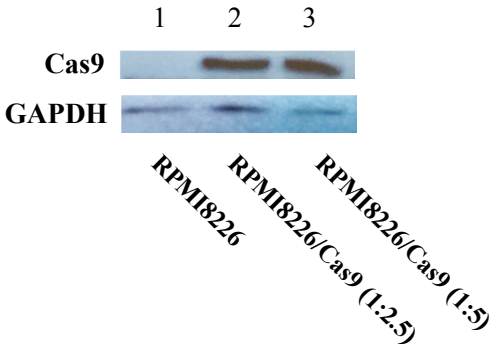

Figure 4-6: Cas9 expression in RPMI8226 transduced cell line. Lane 1: RPMI8226 cell line (negative control); lane 2: RPMI8226 transduced cell line with Cas9 (1:2.5 virus dilution); lane 3: RPMI8226 transduced cell line with Cas9 (1:5 virus dilution).

Assessment of GGPPS and FPPS knock-out was performed using gene expression analysis by qPCR. After 7 days post-infection, RPMI8226 KO cell line presented 80% knock-down of GGPPS and interestingly, FPPS gene was shown to be up-regulated as a consequence of the knock-down (**Figure 4-7A**). In the FPPS KO cell line, 70% knock-down was shown for FPPS gene expression after 7 days post-infection (**Figure 4-7D**).

Gene expression analysis was performed after 4 weeks post-infection in the cultured cells to test for stability of knock-outs. Maintenance of knock-down of GGPPS and FPPS was achieved for each cell line respectively, with knock-downs increasing up to 90% in both cell lines, respectively (**Figure 4-7B, C and E, F**). To our surprise, we observed that in RPMI8226 cells with GGPPS knock-out, FPPS expression decreased significantly after 4 weeks (**Figure 4-7B**). In addition, in the FPPS KO cell line, GGPPS gene expression was significantly decreased as well after 4 weeks (**Figure 4-7E**) and we surmise that this may be an effect of the continuous long-term presence of GGOH inducing a negative feedback mechanism on GGPPS and FPPS respectively.

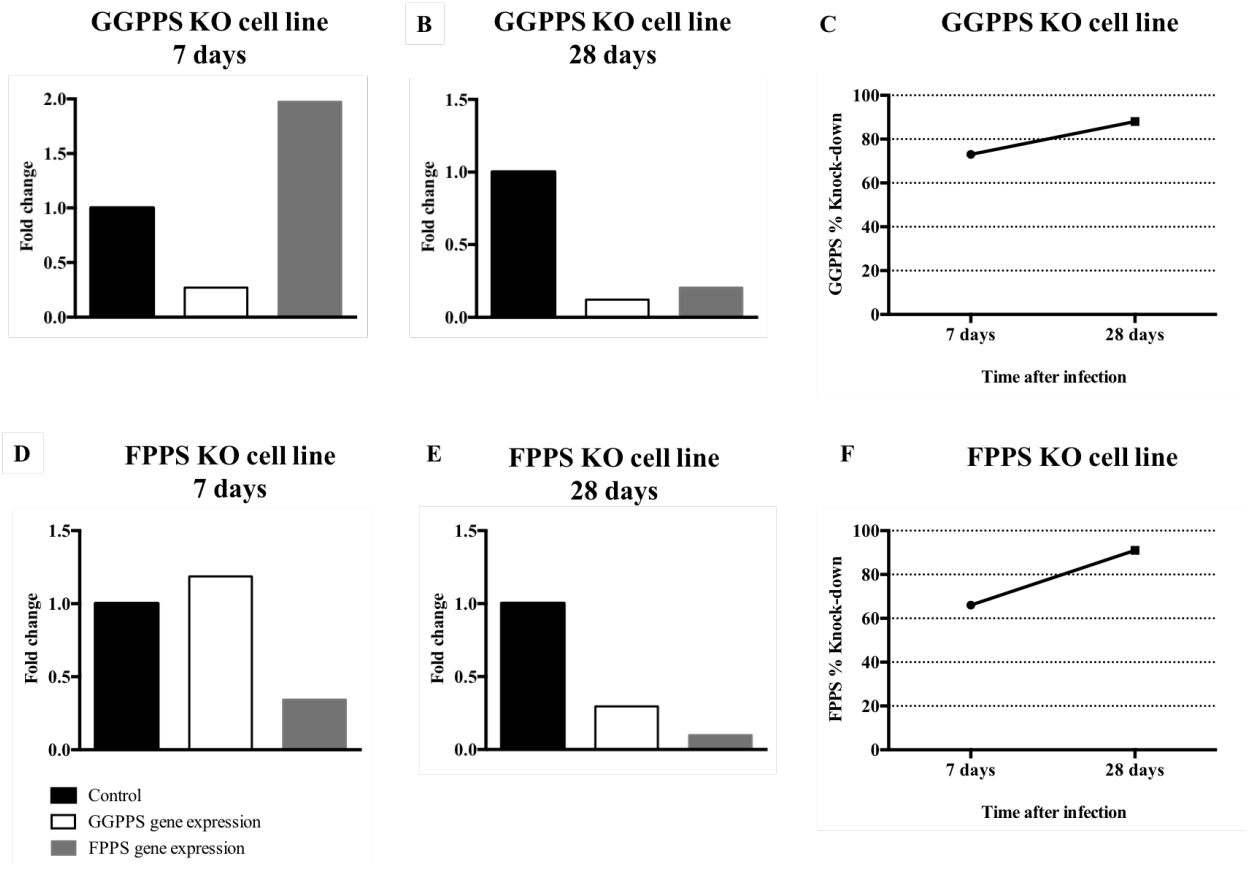

Figure 4-7: CRISPR/Cas9 knock-out of GGPPS and FPPS in RPMI8226 MM cell line. (*A,B*) Gene expression of GGPPS and FPPS in GGPPS KO cell line with shRNA after 7 days and 1 month of infection versus RPMI8226/Cas9 cells using GAPDH as endogenous control in all cases, (*C*) GGPPS gene expression over time in GGPPS KO cell line. (*D,E*) Gene expression of GGPPS and FPPS in FPPS KO cell line with shRNA after 7 days and 1 month of infection versus RPMI8226/Cas9 cells, (*F*) FPPS gene expression over time in FPPS KO cell line.

4.4.5. Successful Genetic Validation of GGPPS as a Target in the Mevalonate Pathway

After confirming knock-down of GGPPS and FPPS in their respective cell lines after using CRISPR/Cas9, validation of GGPPS as a target was performed by analyzing proliferation of KO cells in the presence or absence of GGOH. We observed a significantly reduced proliferative capacity in the GGPPS KO cells after withdrawing GGOH from culture for 72 hours (**Figure 4-8A**). Interestingly, we observed no reduction in the proliferative capacity of FPPS KO cells after GGOH withdrawal (**Figure 4-8A**).

We next treated our FPPS and GGPPS knocked out cells with our specific and novel GPPS inhibitor, **11b** (refer to chapter 3). Our goal is to see whether knockdown of the target would shift our IC50 curve with our specific inhibitors, thereby validating the specificity of our approach. Results show that GGPPS and FPPS KO cells proliferate normally when co-treated with GGOH and **11b**. When GGOH is absent from the media, treatment with compound **11b** of GGPPS KO and FPPS KO cells, causes decreased proliferation rates in all cases (**Figure 4-8B**).

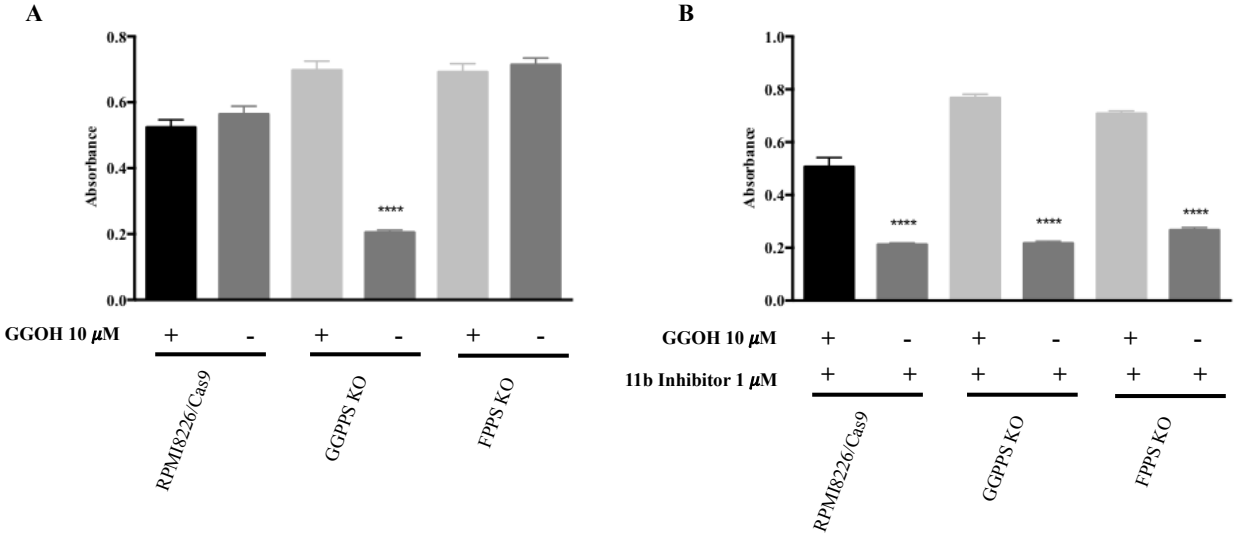

Figure 4-8: Proliferation assay of GGPPS and FPPS KO cell lines with and without GGOH treatment. (*A*) MTS assay absorbance of RPMI8226/Cas9, GGPPS KO, and FPPS KO cell lines with and without GGOH for 72 hours. (*B*) MTS assay absorbance of RPMI8226/Cas9, GGPPS KO, and FPPS KO cell lines with and without GGOH for 72 hours. All cells were co-treated with inhibitor **11b** at a concentration of 1 μM. Error bars represent standard deviations. $^{****}P \leq 0.0001$

4.4.6. Creation of GGPPS KO Cell Lines from Single Clones

As shown in Figure 4-7B, GGPS knock-down levels in GGPS KO cells were shown to be around 90% after 1 month of culture. It is challenging to observe a full knock-out of our gene of interest using qPCR since our cultures present at least 10% of cells that do not show knock-down of GGPPS. We suspect that cells grow better with GGPPS intact and that any attempt at suppressing its expression leads to a selective pressure favoring cells that maintain their expression of this gene. Since our focus is the validation of GGPPS as a target, our goal was to isolate clones in order to obtain a pure GGPPS KO cell line, free from long term selection pressures favoring GGPPS retention. In order to achieve this aim, GGPPS KO cells were diluted to one cell per well in 96-

well plates and wells with one cell were grown (single clones). In order to verify that our new cell lines grown from single clones had the desired editing we performed a T7 endonuclease I mismatch cleavage assay which detects on-target genome editing and can estimate genome editing efficiency in CRISPR-treated cells. After several attempts, two different cell lines that show edited GGPPS were identified (**Figure 4-9, lane 2 and 3**). Further analysis of these two new KO cell lines will be of great importance for the advance on the validation of GGPPS.

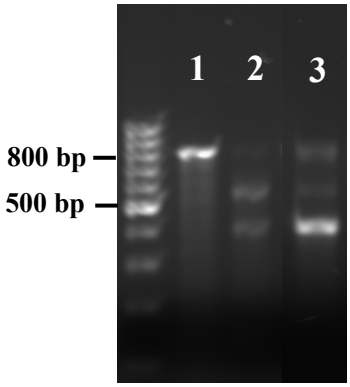

Figure 4-9: Detection of genome editing of GGPPS gene in two novel GGPPS KO cell lines created using CRISPR/Cas9 (lane 2 and 3). Detection of genome editing was performed using a T7 endonuclease I mismatch assay and visualization was performed using DNA gel electrophoresis. Lane 1 shows the negative control for edited GGPPS obtained from RPMI8226/Cas9 cell line (777 bp). Lane 2 shows mismatch-derived restriction bands of novel GGPPS KO cell line derived from single cells (600 bp and 400 bp approximately). Lane 3 shows mismatch-derived restriction bands in second new GGPPS KO cell line derived from single cells (600 bp and 400 bp approximately).

4.5. Discussion

Here we focus on the mevalonate pathway and more specifically on the GGPPS and FPPS mediated steps of this pathway. This pathway has become an interesting therapeutic target in MM disease since novel BPs have shown anti-myeloma effects both *in vitro* and *in vivo*[83,266]. The arrays of techniques available nowadays to perform KDs or KOs of specific genes are numerous and appropriate selection needs careful consideration for each case[271]. Our goal was to obtain a permanent knock-out of GGPPS and FPPS in the RPMI8226 cells. Results showed good knock-down of GGPPS and FPPS respectively using CRISPR/Cas9 as a tool and in this case the knock-

downs were stable. To our surprise, after culturing GGPPS KO cells for over a month gene expression analysis showed that FPPS was affected. In parallel, KO of FPPS was performed in the RPMI8226/Cas9 cell line as comparison. FPPS KO was also successful and permanent, however, GGPPS gene expression seemed to be downregulated after cells being cultured for one month. Our hypothesis is that this is caused by culturing these KO cells in the presence of GGOH since the first day. It is possible that the mevalonate pathway is getting overactivated due to the constant presence of GGOH. Due to each specific KO the pathway is downregulating the expression of FPPS and GGPPS as a negative feedback. These results open the discussion to the consequences of knocking-out enzymes in the same pathway and how that can affect other enzymes upstream and downstream in the mevalonate pathway.

The results in the last section of this report are specially interesting because they totally validate our choice of GGPPS as a target. Withdrawal of GGOH was accompanied by a marked decrease in proliferation rates of cells harboring the GGPPS KO proving that this enzyme is crucial for cell survival. When there is no GGOH in culture and GGPPS is targeted genetically results are the same as when we target this enzyme pharmaceutically with our novel inhibitors.

There are several unresolved aspects that need some attention and deserve to be further investigated in the future in this project. The first is the presumed homeostatic feedback regulation of GGPPS and FPPS mRNA in response to extended culture in the presence of exogenous GGOH in the FPPS KO and GGPPS KO cell lines, respectively. This has first been observed in our preliminary data and can complicate interpretation of the viability findings knowing that even the FPPS KO cell line has decreased mRNA levels of GGPPS as well. It is possible that the GGPPS gene expression left in the FPPS KO cell line is enough for the cells to survive even without GGOH in culture. The number of GGPPS transcript copies left in the FPPS KO need to be measured in order to elucidate the minimal amount of GGPPS needed for survival without the presence of GGOH in culture. This complicated feedback observed here goes to show how much more there is to learn about the regulation of the mevalonate pathway and their enzymes.

Finally, the creation of a RPMI8226/Cas9 cell line that presents a complete KO of GGPPS might be the missing key to fully understand the intricacies of this pathway. In order to generate this cell line, dilution of GGPPS KO cells was performed down to single clones per well. Following weeks of culture, surviving clones were looked at in order to assess genetic KO of GGPPS. A T7

endonuclease I mismatch assay was used and two cell lines presented positive editing of GGPPS confirming the isolation of two novel cell lines without expression of GGPPS. The characterization of these novel cell lines will open the door for a better understanding of the role of GGPPS in the mevalonate pathway and how to better target it. This work is of great importance in light of the successful generation of novel bisphosphonate-like inhibitors that inhibit the GGPPS enzyme and which present powerful anti-myeloma effects.

The anti-myeloma effects of BPs have been shown to impact survival of this disease. The mechanism by which this survival advantage is observed remains mysterious. It is thought that BPs could act either directly on the tumors, though their poor bioavailability is their limiting factor. They could act by changing the microenvironmental milieu of the bone marrow in which MM cells live, as they are toxic to at least one of this milieu's cellular components, the osteoclast. It is interesting to note that their lethal effects on osteoclasts may indeed be mediated by the inhibition of GGPPS rather than FPPS, although classic BPs have far better inhibitory profile for FPPS, again highlighting the poor performance of classic BPs as anti-cancer agents. Finally, the role of the immune environment in BPs anti-cancer properties has been suggested[272], however, which enzyme plays a greater role in the context has not yet been well elucidated.

CHAPTER 5. GENERAL DISCUSSION AND ORIGINAL CONTRIBUTIONS TO KNOWLEDGE

There is a big diversity of mouse models that have been used over the years to study MM myeloma disease[117]. Each animal model presents its own advantages and limitations due to their characteristics and the form in which MM disease develops. It is for these reasons that researchers need to take care on choosing the appropriate type of model for their studies. The first contribution of this thesis is the generation of the Vk*MYC/KaLwRij mouse model that has shown to be clinically very similar to the human MM. MM disease develops as the mice age with earlier development of gammopathies compared to the Vk*MYC model and higher disease burden as well. Disease burden is exacerbated in this model as expected but plasma cells still exhibit the same sensitivity to anti-MM drugs such as bortezomib. In addition to creating a model that resembles human MM another goal was to generate a model with bone disease similar to what is observed clinically in MM patients. The Vk*MYC/KaLwRij model presents abnormal trabecular architecture as well as some bone surface changes. However, characteristic MM bone lesions were not apparent in this model. Further investigation revealed significantly decreased number and function of osteoblasts and osteoclasts in Vk*MYC/KaLwRij mice. In MM, osteoclastic stimulation is a prominent feature that is observed in conjunction with osteoblastic inhibition[51]. As described previously, the RANKL/OPG system is a key player in MM bone disease. OPG levels have been reported to be significantly decreased in MM patients which leads to increased osteoclast activity in this setting[52]. Surprisingly, the Vk*MYC/KaLwRij mice show decreased osteoclastic activity and a novel contribution to knowledge exposed in this model is the unexpected and significantly increased OPG serum levels in the Vk*MYC/KaLwRij mice. OPG appears to originate from the MM cells themselves and what these results suggest is that despite other mechanisms of osteoclastic stimulation, an intact RANKL-OPG axis is essential for osteoclastic function. It is important to understand how the RANKL/OPG system is behaving in MM mouse models. Serum concentrations of OPG have been measured in the past in naïve mice and compared to mice bearing 5T2 MM and 5T33 MM cells originating from KaLwRij mice. Results showed that sRANKL was not detectable in the serum of naïve mice or in 5T33 MM mice but were significantly higher in serum of 5T2 MM mice. On the other hand, serum concentrations of OPG in 5T2 MM mice and naïve mice were not significantly different but were significantly increased in 5T33 MM mice[194]. The differences in sRANKL and OPG serum levels might explain the lack of detectable bone disease seen in the 5T33 MM model and explain the difference between the 5T2 and the 5T33 models. It is possible that the bone disease observed in the 5T2 MM model

might be due to the lower levels of OPG in this model and when OPG expression is higher only "diffuse" osteolytic lesions are observed like in the 5T33 MM model[194]. It seems that the Vk*MYC/KaLwRij model resembles the 5T33 MM model were no prominent lytic lesions are observed but trabecular bone is affected and might be caused by high levels of OPG preventing full stimulation of osteoclasts. By contrast, we reported osteoblastic inhibition through the impairment of their differentiation from mesenchymal stem cells. Osteoblastic inhibition is a reported feature in MM patients that this model does recapitulate[68]. RNA sequencing revealed a number of upregulated inflammatory pathways which include TNF-α and NF-κB signaling pathways. We believe that the MSC impairment to differentiation into osteoblasts is the result of cytokine exposure in the bone marrow compartment. It has been previously reported that when TNF-α is present it can inhibit the recruitment of osteoblastic precursors from progenitor cells as well as suppress RUNX2 leading to impairment of osteoblastic differentiation[197,198]. In this mouse model, it may be that NF-κB and TNF-a play a far more important role in osteoblastic impairment than does DKK1 in human MM, though the end result and the mechanisms for that end result are likely very similar. In summary, a unique model and interesting platform for the study of MM bone disease has been presented in this thesis. The Vk*MYC/KaLwRij model is of great interest thanks to the uncoupling of osteoblasts from osteoclasts observed and represents a novel opportunity to study and possibly intervene using strategies that target osteoblastic function.

MM bone disease is a main clinical feature of MM and up to 80% of MM patients suffer from it with very challenging complications[32]. BPs have been used for a long time as the main treatment for MM bone disease and other bone disorders[9]. In the last decade, anti-cancer effects of BPs have been examined with promising results[258]. An original contribution to knowledge from this thesis has been the design and testing of novel BPs to target MM disease *in vitro* and *in vivo*. Inhibition of protein prenylation of small GTPases has been linked to oncogenesis and a possible mechanism of MM therapy[235]. Mostly all studies performed until today have been with BPs that are inhibitors of FPPS in the mevalonate pathway which leads to inhibition of protein prenylation. However, strong clinical proof of efficacy with inhibitors of FPPS or FTase, and GGTase I has not been achieved. In this thesis we present a new type of GGPPS inhibitors that were identified and found to induce antimyeloma effects both *in vitro* and *in vivo*. *In vitro* proliferation assays in several MM cell lines clearly showed stronger response to treatments with GGPPS inhibitors compared to analogs that are more potent inhibitors of FPPS. In order to understand the reasons behind these

observations, we analyzed the intracellular levels of these two targets by looking at the expression levels of mRNA transcripts of each enzyme in cells. FPPS levels are shown to be consistently higher than those of GGPPS in all human MM cell lines. These same results are observed in primary cancer cells taken from bone marrow specimens at diagnosis of over 700 MM patients participating in the CoMMpass clinical trial[251]. These data suggest that a lower concentration of a drug would be required to achieve much higher level of intracellular engagement of GGPPS that with an inhibitor of FPPS. These data indicate that GGPPS is a better therapeutic target for the treatment of MM than FPPS. Furthermore, suppression of osteoclasts by *N*-BPs that inhibit FPPS is not caused by a direct effect but by a consequent depletion of FPP and of GGPP in the osteoclast[273]. These results suggest that the anti-cancer effects observed by FPPS inhibition are a consequence of indirect inhibition of GGPPS downstream which would explain why *N*-BPs have little to no anti-tumor effect compared to our novel inhibitors. Again, this reinforces the notion that GGPPS may actually be the superior target in this pathway.

The mechanism of action of these novel BPs needs to be further studied. We have shown that the (Chapter 3) impairment of isoprenoid biosynthesis disrupts the secretory pathway function of cells. This process leads to the inevitable accumulation of intracellular immunoglobulins in the endoplasmic reticulum which will lead to ER stress-induced apoptosis. XBP1 mRNA and protein levels were increased as a consequence of ER stress after cell treatment with the novel inhibitors and mitigation of this effect was observed by GGOH co-treatment. Increased and decreased phosphorylation of ERK and AKT, respectively, was also observed. In summary, these results suggest that intracellular inhibition of hGGPPS produces proapoptotic ERK signaling and concomitant loss of prosurvival AKT signaling in MM cells. Finally, another original contribution from this work was to successfully show *in vivo* efficacy of these novel GGPPS inhibitors in the treatment of a MM model, the Vk*MYC/KaLwRij. After a dose escalation assay, an *in vivo* experiment was carried out to determine if the novel compound would be effective decreasing the disease burden in the Vk*MYC/KaLwRij mice. M-protein in serum of mice decreased compared to animals treated with vehicle. In addition, *in vivo* target engagement was confirmed after showing inhibition of Rap 1A geranylgeranylation by western blot in PBMCs of treated mice. These results clearly show the *in vivo* antimyeloma efficacy of our the novel GGPPS inhibitors. Furthermore, these novel inhibitors not only present anti-cancer properties but maintain the beneficial effects on bone resorption as we have shown a retained affinity for hydroxyapatite (in bone). These

compounds have proved to be ideal candidates for the treatment of both MM and potentially its bone disease, although definitive proof of the latter will undoubtedly follow.

The next chapter of this thesis focused the attention on genetically validating GGPPS as a target for anti-myeloma drug development as we have already demonstrated that effective pharmacologic blockade leads to MM cell death. Two different approaches were used to permanently block the expression of these enzymes in a MM cell line, the RPMI8226. The first approach was to use lentiviral shRNA to knock-down of GGPPS and FPPS expression. Approximately 80% knock-down of GGPPS and FPPS was achieved using shRNA. More permanently inhibited GGPPS and FPPS gene expression using the CRISPR/Cas9 tool was also achieved. Our results using this latter technique demonstrate over 80% decreased gene expression of GGPPS and FPPS for each cell line. Transfected cells maintained in GGOH for longer periods of time showed even higher percentage of knock-down (about 90%) which confirms that CRISPR/Cas9 achieved more permanent knock-out status of cells. We incidentally noted that in cells in which GGPPS was knocked-out, over time levels of FPPS mRNA also decreased while levels of GGPPS mRNA were also found to be diminished in cells cultured over time in which FPPS was knocked-out. Both these enzymes are in the same signaling pathway and a negative feedback mechanism induced by the presence of GGOH could be playing a role was our paradoxical observation. The regulatory mechanisms governing the expression and control of various components of the mevalonate pathway are not clearly understood or even known and this would be one of the first observations of a negative feedback mechanism.

We also examined the proliferation rate of GGPPS KO and FPPS KO cells in the presence and absence of GGOH. As explained previously, the use of exogenous GGOH in culture acts by feeding into the GGPP step of the mevalonate pathway which allows cells to proliferate when GGPPS is inhibited. We showed that withdrawal of GGOH from GGPPS KO cells in culture for 72 hours caused decreased proliferation of these cells in the same way that we had observed in Chapter 3 when treating the RPMI8226 cells with our novel BPs. However, when withdrawing GGOH from FPPS KO cells, no decrease in viability was observed. Although mRNA levels of each FPPS and GGPPS are convincing for knock-out, we do not know if even small amount of residual FPPS transcripts may be enough to sustain protein production and the viability seen once GGOH was withdrawn. However, we note that these knocked-out cultures were maintained for several weeks showing decreasing mRNA levels of both respective targets making it unlikely that

residual FPPS transcription plays a role in the lack of toxicity in the FPPS KO cells. We also note that mRNA levels of FPPS decrease in cells cultured in the presence of GGOH even in absence of any attempt to knock-down FPPS and yet despite the presence of GGOH and decreased transcript levels from a KO attempt and negative feedback regulation, MM cells survived well on GGOH withdrawal. This is completely different from what was observed with GGPPS. Taken as a whole, we believe that GGPPS is likely a more interesting target for anti-myeloma therapy than FPPS, shifting away from what was traditionally believed to be the real target of *N*-BPs.

In vivo, we can speculate that targeting GGPPS can have anti-myeloma effect at the direct cellular level and, as has been shown with *N*-BPs, the microenvironment of the MM cells can lead to decreased viability. The bone marrow microenvironment plays a significant role both in the development of MM disease but also in the mechanisms of resistance in this disease[16]. Consequences of the inhibition of protein prenylation by GGPPS inhibition should be considered not only for the effects on myeloma cells but also for all other exposed cell types in the bone marrow of patients and/or animal models.

The final goal of the fourth chapter was the creation of a GGPPS knock-out cell line starting from a single clone so we can obtain and homogenous cell population. It will be providential to have a cell line with a complete KO of GGPPS to further asses the mechanism of action of these molecules without interference of other genetic cell types. GGPPS KO cells were diluted to one cell per well and successful isolation and proliferation of this cell led to the creation of a unique cell line with GGPPS KO. Due to the fact that not all clones isolated presented our preferred KO, gene editing detection was performed. Out of all isolated and grown cells, two of them grew healthy cell lines with positive gene editing of GGPPS. The newly created GGPS KO cell lines will be of great use to further investigate the consequences of inhibiting the mevalonate pathway. Additionally, the possibility of performing synergy assays with our new inhibitors opens the door to further asses how the mevalonate pathway inhibition is involved in cancer and how it can be targeted therapeutically.

5.1. Summary of Original Contributions to Knowledge

- Generation of a novel mouse model of MM and MM bone disease, the Vk*MYC/KaLwRij model, that similarly recapitulated the human MM disease to its parent mouse line:
  - Characterization of the MM disease in this model and verification of sensitivity to clinically used anti-MM drugs (bortezomib).
  - Characterization of the MM bone disease in this model:
    - Study of the bone phenotype revealed abnormal trabecular architecture and changes in bone surface.
    - Discovery of decreased osteoclastic number and function in this model:
      - Significantly increased levels of OPG observed to possibly account for the lack of outright lytic bone lesions in this model.
      - The source of OPG in this model was found to be malignant plasma cells. Unlike plasma cells in human disease which do not produce OPG. Plasma cell production of OPG is a major barrier of the development of flagrant bone disease in mouse models of MM.
    - Impaired osteoblastic differentiation in the Vk*MYC/KaLwRij:
      - RNA sequencing of MSCs revealed a number of inflammatory signaling pathways significantly upregulated in the Vk*MYC/KaLwRij MSCs cells which inhibit MSC differentiation into osteoblasts.
      - Inflammatory cytokines might be the reason behind the differentiation impairment observed in this model.
- Design and testing of novel GGPPS inhibitors of the mevalonate pathway that successfully target MM disease *in vitro* and *in vivo*:
  - Successful design of inhibitors with high GGPPS specificity
  - *In vitro* test of efficacy of novel inhibitors in several MM cell lines showed potency of anti-proliferation at nanomolar ranges.
  - Rap 1A unprenylation due to GGPPS inhibition in cells by novel inhibitors.

- Endoplasmic reticulum stress and activation of ER-induced apoptosis was reported as an effect of the treatment with GGPPS inhibitors. Rescue of the mevalonate pathway was achieved by co-treatment with GGOH.
- *In vivo* test of efficacy of novel inhibitors was performed in the Vk*MYC/KaLwRij and results showed decreased levels of M-protein in this model and decreased Rap 1A prenylation proving *in vivo* target engagement.

- Genetic validation of GGPPS as a target for anti-myeloma drug development:
  - Knock-down of both GGPPS and FPPS were achieved in RPMI8226 MM cell line using lentiviral shRNA:
    - Some apoptosis of GGPPS knock-down cells was observed after withdrawal of GGOH confirming the importance of this target for the survival of the cells but poor sustained knock-down limited this observation.
  - Superior inhibition of GGPPS and FPPS expression using CRISPR/Cas9:
    - Permanent knock-down of GGPPS and FPPS in RPMI8226 cells by qPCR is observed after 1 month of cells in culture.
    - Inhibition of MM cellular growth in cells with GGPPS KO but not in cells with FPPS KO, confirming GGPPS as a superior target for drug development.
    - Creation of two novel cell lines that present positive genomic editing for GGPPS gene to be used for further research into the development of novel inhibitors of the mevalonate pathway.

CONCLUSIONS

The work presented on this thesis has generated significant contributions: (a) characterizing a novel transgenic mouse model of MM and MM bone disease, the Vk*MYC/KaLwRij model, (b) successful design and testing of efficient and potent GGPPS inhibitors that can target MM *in vitro* and *in vivo*, and (c) successful generation of a novel GGPPS KO cell line by using CRISPR/Cas9 as a tool. Further characterization of the novel GGPPS inhibitors and a deeper understanding of the involvement of the mevalonate pathway in cancer, specifically in MM, is essential to generate more potent and targeted therapies. Finally, the availability of such models such as the one presented in this thesis is of outmost importance in order to have appropriate platforms on which to study MM and that can serve to test novel chemical entities.

References

1. Rajkumar, S.V.*, et al.* International Myeloma Working Group updated criteria for the diagnosis of multiple myeloma. *Lancet Oncol* **15**, e538-548 (2014).
2. Landgren, O.*, et al.* Monoclonal gammopathy of undetermined significance (MGUS) consistently precedes multiple myeloma: a prospective study. *Blood* **113**, 5412-5417 (2009).
3. Waxman, A.J.*, et al.* Racial disparities in incidence and outcome in multiple myeloma: a population-based study. *Blood* **116**, 5501-5506 (2010).
4. Huang, S.Y.*, et al.* Epidemiology of multiple myeloma in Taiwan: increasing incidence for the past 25 years and higher prevalence of extramedullary myeloma in patients younger than 55 years. (2007).
5. Canadian Cancer Statistics 2017. *Canadian Cancer Society's Advisory Committee on Cancer Statistics. Toronto: ON: Canadian Cancer Society* (2017).
6. Mitsiades, C.S., Mitsiades Ns Fau - Munshi, N.C., Munshi Nc Fau - Richardson, P.G., Richardson Pg Fau - Anderson, K.C. & Anderson, K.C. The role of the bone microenvironment in the pathophysiology and therapeutic management of multiple myeloma: interplay of growth factors, their receptors and stromal interactions. (2006).
7. Gonzalez, D.*, et al.* Immunoglobulin gene rearrangements and the pathogenesis of multiple myeloma. *Blood* **110**, 3112-3121 (2007).
8. Maul, R.W. & Gearhart, P.J. AID and somatic hypermutation. *Adv Immunol* **105**, 159-191 (2010).
9. Kumar, S.K.*, et al.* Multiple myeloma. *Nature Reviews Disease Primers* **3**, 17046 (2017).
10. Bergsagel, P.L. & Kuehl, W.M. Chromosome translocations in multiple myeloma. *Oncogene* **20**, 5611-5622 (2001).
11. Rajkumar, S.V.*, et al.* Impact of primary molecular cytogenetic abnormalities and risk of progression in smoldering multiple myeloma. *Leukemia* **27**, 1738-1744 (2013).

12. Morgan, G.J., Walker, B.A. & Davies, F.E. The genetic architecture of multiple myeloma. *Nat Rev Cancer* **12**, 335-348 (2012).

13. Shou, Y.*, et al.* Diverse karyotypic abnormalities of the c-myc locus associated with c-myc dysregulation and tumor progression in multiple myeloma. *Proc Natl Acad Sci U S A* **97**, 228-233 (2000).

14. Debes-Marun, C.S.*, et al.* Chromosome abnormalities clustering and its implications for pathogenesis and prognosis in myeloma. *Leukemia* **17**, 427-436 (2003).

15. Keats, J.J.*, et al.* Clonal competition with alternating dominance in multiple myeloma. *Blood* **120**, 1067-1076 (2012).

16. Bianchi, G. & Munshi, N.C. Pathogenesis beyond the cancer clone(s) in multiple myeloma. *Blood* **125**, 3049-3058 (2015).

17. Panaroni, C., Yee, A.J. & Raje, N.S. Myeloma and Bone Disease. *Curr Osteoporos Rep* (2017).

18. Hideshima, T., Mitsiades, C., Tonon, G., Richardson, P.G. & Anderson, K.C. Understanding multiple myeloma pathogenesis in the bone marrow to identify new therapeutic targets. *Nat Rev Cancer* **7**, 585-598 (2007).

19. Ribatti, D., Nico, B. & Vacca, A. Importance of the bone marrow microenvironment in inducing the angiogenic response in multiple myeloma. *Oncogene* **25**, 4257-4266 (2006).

20. Jourdan, M.*, et al.* A major role for Mcl-1 antiapoptotic protein in the IL-6-induced survival of human myeloma cells. *Oncogene* **22**, 2950-2959 (2003).

21. Child, J.A.*, et al.* High-dose chemotherapy with hematopoietic stem-cell rescue for multiple myeloma. *N Engl J Med* **348**, 1875-1883 (2003).

22. Mitsiades, C.S.*, et al.* Activation of NF-kappaB and upregulation of intracellular anti-apoptotic proteins via the IGF-1/Akt signaling in human multiple myeloma cells: therapeutic implications. *Oncogene* **21**, 5673-5683 (2002).

23. Palumbo, A.*, et al.* Autologous transplantation and maintenance therapy in multiple myeloma. *N Engl J Med* **371**, 895-905 (2014).

24. Lipe, B., Vukas, R. & Mikhael, J. The role of maintenance therapy in multiple myeloma. *Blood Cancer J* **6**, e485 (2016).

25. Rajkumar, S.V.*, et al.* Lenalidomide plus high-dose dexamethasone versus lenalidomide plus low-dose dexamethasone as initial therapy for newly diagnosed multiple myeloma: an open-label randomised controlled trial. (2010).

26. Cavo, M.*, et al.* Bortezomib with thalidomide plus dexamethasone compared with thalidomide plus dexamethasone as induction therapy before, and consolidation therapy after, double autologous stem-cell transplantation in newly diagnosed multiple myeloma: a randomised phase 3 study. (2010).

27. Kumar, S.*, et al.* Randomized, multicenter, phase 2 study (EVOLUTION) of combinations of bortezomib, dexamethasone, cyclophosphamide, and lenalidomide in previously untreated multiple myeloma. *Blood* **119**, 4375-4382 (2012).

28. Benboubker, L.*, et al.* Lenalidomide and dexamethasone in transplant-ineligible patients with myeloma. *N Engl J Med* **371**, 906-917 (2014).

29. Ma, J.*, et al.* Immunotherapy Strategies Against Multiple Myeloma. *Technology in Cancer Research & Treatment* **16**, 717-726 (2017).

30. Stewart, A.K.*, et al.* Health-Related Quality-of-Life Results From the Open-Label, Randomized, Phase III ASPIRE Trial Evaluating Carfilzomib, Lenalidomide, and Dexamethasone Versus Lenalidomide and Dexamethasone in Patients With Relapsed Multiple Myeloma. *J Clin Oncol* **34**, 3921-3930 (2016).

31. Snowden, J.A.*, et al.* Guidelines for supportive care in multiple myeloma 2011. *Br J Haematol* **154**, 76-103 (2011).

32. Terpos, E.*, et al.* International Myeloma Working Group recommendations for the treatment of multiple myeloma-related bone disease. *J Clin Oncol* **31**, 2347-2357 (2013).

33. Terpos, E., Ntanasis-Stathopoulos, I., Gavriatopoulou, M. & Dimopoulos, M.A. Pathogenesis of bone disease in multiple myeloma: from bench to bedside. *Blood Cancer J* **8**, 7 (2018).

34. Sims, N.A. & Martin, T.J. Coupling the activities of bone formation and resorption: a multitude of signals within the basic multicellular unit. (2014).

35. Katsimbri, P. The biology of normal bone remodelling. *Eur J Cancer Care (Engl)* **26**(2017).

36. Andersen, T.L.*, et al.* A physical mechanism for coupling bone resorption and formation in adult human bone. *Am J Pathol* **174**, 239-247 (2009).

37. Hadjidakis, D.J. & Androulakis, II. Bone remodeling. (2006).

38. Raggatt, L.J. & Partridge, N.C. Cellular and molecular mechanisms of bone remodeling. *J Biol Chem* **285**, 25103-25108 (2010).

39. Tamma, R. & Zallone, A. Osteoblast and osteoclast crosstalks: from OAF to Ephrin. *Inflamm Allergy Drug Targets* **11**, 196-200 (2012).

40. Matsuoka, K., Park, K.A., Ito, M., Ikeda, K. & Takeshita, S. Osteoclast-derived complement component 3a stimulates osteoblast differentiation. *J Bone Miner Res* **29**, 1522-1530 (2014).

41. Wang, L.*, et al.* Osteoblast-induced osteoclast apoptosis by fas ligand/FAS pathway is required for maintenance of bone mass. (2015).

42. Boyle, W.J., Simonet, W.S. & Lacey, D.L. Osteoclast differentiation and activation. *Nature* **423**, 337-342 (2003).

43. Zhao, C.*, et al.* Bidirectional ephrinB2-EphB4 signaling controls bone homeostasis. *Cell Metab* **4**, 111-121 (2006).

44. Hayashi, M.*, et al.* Osteoprotection by semaphorin 3A. *Nature* **485**, 69-74 (2012).

45. Chen, X.*, et al.* Osteoblast-osteoclast interactions. *Connect Tissue Res* **59**, 99-107 (2018).

46. Balemans, W.*, et al.* Increased bone density in sclerosteosis is due to the deficiency of a novel secreted protein (SOST). (2001).

47. Negishi-Koga, T.*, et al.* Suppression of bone formation by osteoclastic expression of semaphorin 4D. *Nat Med* **17**, 1473-1480 (2011).

48. Li, D.*, et al.* Osteoclast-derived exosomal miR-214-3p inhibits osteoblastic bone formation. *Nat Commun* **7**, 10872 (2016).

49. Zaidi, M. Skeletal remodeling in health and disease. *Nat Med* **13**, 791-801 (2007).

50. Hameed, A., Brady, J.J., Dowling, P., Clynes, M. & O'Gorman, P. Bone disease in multiple myeloma: pathophysiology and management. *Cancer Growth Metastasis* **7**, 33-42 (2014).

51. Terpos, E., Christoulas, D., Gavriatopoulou, M. & Dimopoulos, M.A. Mechanisms of bone destruction in multiple myeloma. *Eur J Cancer Care (Engl)* **26**(2017).

52. Sezer, O., Heider, U., Zavrski, I., Kuhne, C.A. & Hofbauer, L.C. RANK ligand and osteoprotegerin in myeloma bone disease. *Blood* **101**, 2094-2098 (2003).

53. Giuliani, N., Colla S Fau - Rizzoli, V. & Rizzoli, V. New insight in the mechanism of osteoclast activation and formation in multiple myeloma: focus on the receptor activator of NF-kappaB ligand (RANKL). (2004).

54. Houde, C.*, et al.* Overexpression of the NOTCH ligand JAG2 in malignant plasma cells from multiple myeloma patients and cell lines. *Blood* **104**, 3697-3704 (2004).

55. Colombo, M.*, et al.* Notch-directed microenvironment reprogramming in myeloma: a single path to multiple outcomes. *Leukemia* **27**, 1009-1018 (2013).

56. Roodman, G.D. & Choi, S.J. MIP-1 alpha and myeloma bone disease. *Cancer Treat Res* **118**, 83-100 (2004).

57. Palma, B.D.*, et al.* Osteolytic lesions, cytogenetic features and bone marrow levels of cytokines and chemokines in multiple myeloma patients: Role of chemokine (C-C motif) ligand 20. *Leukemia* **30**, 409-416 (2016).

58. Lentzsch, S.*, et al.* Macrophage inflammatory protein 1-alpha (MIP-1 alpha) triggers migration and signaling cascades mediating survival and proliferation in multiple myeloma (MM) cells. (2002).

59. Kyrstsonis, M.C., Dedoussis G Fau - Baxevanis, C., Baxevanis C Fau - Stamatelou, M., Stamatelou M Fau - Maniatis, A. & Maniatis, A. Serum interleukin-6 (IL-6) and interleukin-4 (IL-4) in patients with multiple myeloma (MM). (1996).

60. Terpos, E., Berenson, J., Raje, N. & Roodman, G.D. Management of bone disease in multiple myeloma. *Expert Rev Hematol* **7**, 113-125 (2014).

61. Fulciniti, M.*, et al.* A high-affinity fully human anti-IL-6 mAb, 1339, for the treatment of multiple myeloma. *Clin Cancer Res* **15**, 7144-7152 (2009).

62. Lee, J.W.*, et al.* IL-3 expression by myeloma cells increases both osteoclast formation and growth of myeloma cells. (2004).

63. Ehrlich, L.A.*, et al.* IL-3 is a potential inhibitor of osteoblast differentiation in multiple myeloma. (2005).

64. Chen, J.*, et al.* BAFF is involved in macrophage-induced bortezomib resistance in myeloma. (2017).

65. Tanaka, Y.*, et al.* Myeloma cell-osteoclast interaction enhances angiogenesis together with bone resorption: a role for vascular endothelial cell growth factor and osteopontin. *Clin Cancer Res* **13**, 816-823 (2007).

66. Wang, C.*, et al.* Differentiation of Bone Marrow Mesenchymal Stem Cells in Osteoblasts and Adipocytes and its Role in Treatment of Osteoporosis. *Med Sci Monit* **22**, 226-233 (2016).

67. Reagan, M.R., Liaw, L., Rosen, C.J. & Ghobrial, I.M. Dynamic Interplay between Bone and Multiple Myeloma: Emerging Roles of the Osteoblast. *Bone* **75**, 161-169 (2015).

68. Xu, S., De Veirman, K., De Becker, A., Vanderkerken, K. & Van Riet, I. Mesenchymal stem cells in multiple myeloma: a therapeutical tool or target? *Leukemia* (2018).

69. Xu S Fau - Evans, H.*, et al.* Impaired osteogenic differentiation of mesenchymal stem cells derived from multiple myeloma patients is associated with a blockade in the deactivation of the Notch signaling pathway. (2012).

70. Silvestris, F., Lombardi, L., De Matteo, M., Bruno, A. & Dammacco, F. Myeloma bone disease: pathogenetic mechanisms and clinical assessment. *Leuk Res* **31**, 129-138 (2007).

71. Garcia-Gomez, A., Sanchez-Guijo, F., Del Canizo, M.C., San Miguel, J.F. & Garayoa, M. Multiple myeloma mesenchymal stromal cells: Contribution to myeloma bone disease and therapeutics. *World J Stem Cells* **6**, 322-343 (2014).

72. Monroe, D.G., McGee-Lawrence, M.E., Oursler, M.J. & Westendorf, J.J. Update on Wnt signaling in bone cell biology and bone disease. *Gene* **492**, 1-18 (2012).

73. Politou, M.C.*, et al.* Serum concentrations of Dickkopf-1 protein are increased in patients with multiple myeloma and reduced after autologous stem cell transplantation. *Int J Cancer* **119**, 1728-1731 (2006).

74. Tian, E.*, et al.* The role of the Wnt-signaling antagonist DKK1 in the development of osteolytic lesions in multiple myeloma. *N Engl J Med* **349**, 2483-2494 (2003).

75. Terpos, E.*, et al.* Elevated circulating sclerostin correlates with advanced disease features and abnormal bone remodeling in symptomatic myeloma: reduction post-bortezomib monotherapy. *Int J Cancer* **131**, 1466-1471 (2012).

76. Sutherland, M.K.*, et al.* Sclerostin promotes the apoptosis of human osteoblastic cells: a novel regulation of bone formation. *Bone* **35**, 828-835 (2004).

77. Baron, R. & Kneissel, M. WNT signaling in bone homeostasis and disease: from human mutations to treatments. *Nat Med* **19**, 179-192 (2013).

78. Brunetti, G.*, et al.* Sclerostin is overexpressed by plasma cells from multiple myeloma patients. (2011).

79. Qiang, Y.W.*, et al.* Myeloma-derived Dickkopf-1 disrupts Wnt-regulated osteoprotegerin and RANKL production by osteoblasts: a potential mechanism underlying osteolytic bone lesions in multiple myeloma. *Blood* **112**, 196-207 (2008).

80. Colucci S Fau - Brunetti, G.*, et al.* Myeloma cells suppress osteoblasts through sclerostin secretion. (2011).

81. Giuliani, N.*, et al.* Myeloma cells block RUNX2/CBFA1 activity in human bone marrow osteoblast progenitors and inhibit osteoblast formation and differentiation. *Blood* **106**, 2472-2483 (2005).

82. Fleisch, H. Development of bisphosphonates. *Breast Cancer Res* **4**, 30-34 (2002).

83. Morgan, G.J.*, et al.* First-line treatment with zoledronic acid as compared with clodronic acid in multiple myeloma (MRC Myeloma IX): a randomised controlled trial. (2010).

84. Modi, N.D. & Lentzsch, S. Bisphosphonates as antimyeloma drugs. *Leukemia* **26**, 589-594 (2012).

85. Stresing, V., Daubine, F., Benzaid, I., Monkkonen, H. & Clezardin, P. Bisphosphonates in cancer therapy. *Cancer Lett* **257**, 16-35 (2007).

86. Zangari, M.*, et al.* Response to bortezomib is associated to osteoblastic activation in patients with multiple myeloma. (2005).

87. Gandolfi, S.*, et al.* The proteasome and proteasome inhibitors in multiple myeloma. *Cancer Metastasis Rev* **36**, 561-584 (2017).

88. Miller, P.D. Denosumab: anti-RANKL antibody. *Curr Osteoporos Rep* **7**, 18-22 (2009).

89. Gavriatopoulou, M., Dimopoulos, M.A., Kastritis, E. & Terpos, E. Emerging treatment approaches for myeloma-related bone disease. *Expert Rev Hematol* **10**, 217-228 (2017).

90. Fulciniti, M.*, et al.* Anti-DKK1 mAb (BHQ880) as a potential therapeutic agent for multiple myeloma. (2009).

91. McClung, M.R.*, et al.* Romosozumab in postmenopausal women with low bone mineral density. *N Engl J Med* **370**, 412-420 (2014).

92. Mitsiades, C.S., Anderson, K.C. & Carrasco, D.R. Mouse models of human myeloma. *Hematol Oncol Clin North Am* **21**, 1051-1069, viii (2007).

93. Sanchez, E., Chen, H. & Berenson, J.R. In vivo models of multiple myeloma (MM). (2014).

94. Hofgaard, P.O.*, et al.* A Novel Mouse Model for Multiple Myeloma (MOPC315.BM) That Allows Noninvasive Spatiotemporal Detection of Osteolytic Disease. *PLOS ONE* **7**, e51892 (2012).

95. Amend, S.R.*, et al.* Whole Genome Sequence of Multiple Myeloma-Prone C57BL/KaLwRij Mouse Strain Suggests the Origin of Disease Involves Multiple Cell Types. *PLoS One* **10**, e0127828 (2015).

96. Radl, J., Croese, J.W., Zurcher, C., Van den Enden-Vieveen, M.H. & de Leeuw, A.M. Animal model of human disease. Multiple myeloma. *Am J Pathol* **132**, 593-597 (1988).

97. Croucher, P.I., *et al.* Zoledronic acid treatment of 5T2MM-bearing mice inhibits the development of myeloma bone disease: evidence for decreased osteolysis, tumor burden and angiogenesis, and increased survival. *J Bone Miner Res* **18**, 482-492 (2003).

98. Paton-Hough, J., Chantry, A.D. & Lawson, M.A. A review of current murine models of multiple myeloma used to assess the efficacy of therapeutic agents on tumour growth and bone disease. (2015).

99. Vanderkerken, K., *et al.* Organ involvement and phenotypic adhesion profile of 5T2 and 5T33 myeloma cells in the C57BL/KaLwRij mouse. *Br J Cancer* **76**, 451-460 (1997).

100. Asosingh, K., Radl, J., Van Riet, I., Van Camp, B. & Vanderkerken, K. The 5TMM series: a useful in vivo mouse model of human multiple myeloma. *Hematol J* **1**, 351-356 (2000).

101. Alici, E., Konstantinidis, K.V., Aints, A., Dilber, M.S. & Abedi-Valugerdi, M. Visualization of 5T33 myeloma cells in the C57BL/KaLwRij mouse: establishment of a new syngeneic murine model of multiple myeloma. *Exp Hematol* **32**, 1064-1072 (2004).

102. Dallas, S.L., *et al.* Ibandronate reduces osteolytic lesions but not tumor burden in a murine model of myeloma bone disease. (1999).

103. Gado, K., Domjan, G., Hegyesi, H. & Falus, A. Role of INTERLEUKIN-6 in the pathogenesis of multiple myeloma. *Cell Biol Int* **24**, 195-209 (2000).

104. Suematsu, S., *et al.* Generation of plasmacytomas with the chromosomal translocation t(12;15) in interleukin 6 transgenic mice. *Proc Natl Acad Sci U S A* **89**, 232-235 (1992).

105. Chesi, M., *et al.* AID-dependent activation of a MYC transgene induces multiple myeloma in a conditional mouse model of post-germinal center malignancies. *Cancer Cell* **13**, 167-180 (2008).

106. Carrasco, D.R., *et al.* The differentiation and stress response factor XBP-1 drives multiple myeloma pathogenesis. *Cancer Cell* **11**, 349-360 (2007).

107. Munshi, N.C., *et al.* Identification of genes modulated in multiple myeloma using genetically identical twin samples. (2004).

108. Wen, X.Y., *et al.* Identification of c-myc promoter-binding protein and X-box binding protein 1 as interleukin-6 target genes in human multiple myeloma cells. (1999).

109. Gambella, M.*, et al.* High XBP1 expression is a marker of better outcome in multiple myeloma patients treated with bortezomib. *Haematologica* **99**, e14-e16 (2014).

110. Huang, Y.W.*, et al.* Disseminated growth of a human multiple myeloma cell line in mice with severe combined immunodeficiency disease. *Cancer Res* **53**, 1392-1396 (1993).

111. Doran, P.M.*, et al.* Native osteoprotegerin gene transfer inhibits the development of murine osteolytic bone disease induced by tumor xenografts. *Exp Hematol* **32**, 351-359 (2004).

112. Kikuchi, J.*, et al.* The novel orally active proteasome inhibitor K-7174 exerts anti-myeloma activity in vitro and in vivo by down-regulating the expression of class I histone deacetylases. *J Biol Chem* **288**, 25593-25602 (2013).

113. Mirandola, L.*, et al.* Galectin-3C inhibits tumor growth and increases the anticancer activity of bortezomib in a murine model of human multiple myeloma. *PLoS One* **6**, e21811 (2011).

114. Carlo-Stella, C.*, et al.* CD52 antigen expressed by malignant plasma cells can be targeted by alemtuzumab in vivo in NOD/SCID mice. (2006).

115. Rabin, N.*, et al.* A new xenograft model of myeloma bone disease demonstrating the efficacy of human mesenchymal stem cells expressing osteoprotegerin by lentiviral gene transfer. *Leukemia* **21**, 2181-2191 (2007).

116. Zhang, Y.*, et al.* Pyk2 promotes tumor progression in multiple myeloma. *Blood* **124**, 2675-2686 (2014).

117. Rossi, M.*, et al.* Mouse models of multiple myeloma: technologic platforms and perspectives. *Oncotarget* **9**, 20119-20133 (2018).

118. Mitsiades, C.S.*, et al.* Fluorescence imaging of multiple myeloma cells in a clinically relevant SCID/NOD in vivo model: biologic and clinical implications. *Cancer Res* **63**, 6689-6696 (2003).

119. Urashima, M.*, et al.* The development of a model for the homing of multiple myeloma cells to human bone marrow. *Blood* **90**, 754-765 (1997).

120. Yaccoby, S., Barlogie, B. & Epstein, J. Primary myeloma cells growing in SCID-hu mice: a model for studying the biology and treatment of myeloma and its manifestations. *Blood* **92**, 2908-2913 (1998).

121. Tassone, P.*, et al.* A clinically relevant SCID-hu in vivo model of human multiple myeloma. *Blood* **106**, 713-716 (2005).

122. Yang, J.*, et al.* Constitutive activation of p38 MAPK in tumor cells contributes to osteolytic bone lesions in multiple myeloma. *Leukemia* **26**, 2114-2123 (2012).

123. Yaccoby, S.*, et al.* Myeloma interacts with the bone marrow microenvironment to induce osteoclastogenesis and is dependent on osteoclast activity. (2002).

124. Yata, K. & Yaccoby, S. The SCID-rab model: a novel in vivo system for primary human myeloma demonstrating growth of CD138-expressing malignant cells. *Leukemia* **18**, 1891-1897 (2004).

125. Pennisi, A.*, et al.* The proteasome inhibitor, bortezomib suppresses primary myeloma and stimulates bone formation in myelomatous and nonmyelomatous bones in vivo. *Am J Hematol* **84**, 6-14 (2009).

126. Calimeri, T.*, et al.* A unique three-dimensional SCID-polymeric scaffold (SCID-synth-hu) model for in vivo expansion of human primary multiple myeloma cells. *Leukemia* **25**, 707-711 (2011).

127. Lwin, S.T., Edwards, C.M. & Silbermann, R. Preclinical animal models of multiple myeloma. *Bonekey Rep* **5**, 772 (2016).

128. Hoyos, V. & Borrello, I. The immunotherapy era of myeloma: monoclonal antibodies, vaccines, and adoptive T-cell therapies. *Blood* **128**, 1679-1687 (2016).

129. Van Valckenborgh, E.*, et al.* Multiple myeloma induces the immunosuppressive capacity of distinct myeloid-derived suppressor cell subpopulations in the bone marrow. *Leukemia* **26**, 2424-2428 (2012).

130. Iwai, Y.*, et al.* Involvement of PD-L1 on tumor cells in the escape from host immune system and tumor immunotherapy by PD-L1 blockade. *Proc Natl Acad Sci U S A* **99**, 12293-12297 (2002).

131. Cooke, R.E.*, et al.* Spontaneous onset and transplant models of the Vk*MYC mouse show immunological sequelae comparable to human multiple myeloma. *Journal of Translational Medicine* **14**, 259 (2016).

132. Botta, C.*, et al.* MiR-29b antagonizes the pro-inflammatory tumor-promoting activity of multiple myeloma-educated dendritic cells. *Leukemia* **32**, 1003-1015 (2018).

133. Lahtinen, R., Laakso, M., Palva, I., Virkkunen, P. & Elomaa, I. Randomised, placebo-controlled multicentre trial of clodronate in multiple myeloma. Finnish Leukaemia Group. *Lancet* **340**, 1049-1052 (1992).

134. Berenson, J.R.*, et al.* Efficacy of pamidronate in reducing skeletal events in patients with advanced multiple myeloma. Myeloma Aredia Study Group. *N Engl J Med* **334**, 488-493 (1996).

135. Sanfilippo, K.M.*, et al.* Comparative effectiveness on survival of zoledronic acid versus pamidronate in multiple myeloma. *Leuk Lymphoma* **56**, 615-621 (2015).

136. Widler, L.*, et al.* Highly potent geminal bisphosphonates. From pamidronate disodium (Aredia) to zoledronic acid (Zometa). *J Med Chem* **45**, 3721-3738 (2002).

137. Mhaskar, R.*, et al.* Bisphosphonates in multiple myeloma: a network meta-analysis. *Cochrane Database Syst Rev*, CD003188 (2012).

138. Shipman, C.M., Rogers, M.J., Apperley, J.F., Russell, R.G. & Croucher, P.I. Bisphosphonates induce apoptosis in human myeloma cell lines: a novel anti-tumour activity. *Br J Haematol* **98**, 665-672 (1997).

139. Aparicio, A.*, et al.* In vitro cytoreductive effects on multiple myeloma cells induced by bisphosphonates. *Leukemia* **12**, 220-229 (1998).

140. Derenne, S.*, et al.* Zoledronate is a potent inhibitor of myeloma cell growth and secretion of IL-6 and MMP-1 by the tumoral environment. (1999).

141. Tassone, P.*, et al.* Growth inhibition and synergistic induction of apoptosis by zoledronate and dexamethasone in human myeloma cell lines. *Leukemia* **14**, 841-844 (2000).

142. Shinoda H Fau - Adamek, G.*, et al.* Structure-activity relationships of various bisphosphonates. (1983).

143. Drake, M.T., Clarke, B.L. & Khosla, S. Bisphosphonates: mechanism of action and role in clinical practice. *Mayo Clin Proc* **83**, 1032-1045 (2008).

144. Coleman, R.E. Bisphosphonates: clinical experience. *Oncologist* **9 Suppl 4**, 14-27 (2004).

145. Kavanagh, K.L*., et al.* The molecular mechanism of nitrogen-containing bisphosphonates as antiosteoporosis drugs. (2006).

146. Buhaescu, I. & Izzedine, H. Mevalonate pathway: a review of clinical and therapeutical implications. *Clin Biochem* **40**, 575-584 (2007).

147. Goldstein, J.L. & Brown, M.S. Regulation of the mevalonate pathway. *Nature* **343**, 425-430 (1990).

148. van Beek, E., Pieterman E Fau - Cohen, L., Cohen L Fau - Lowik, C., Lowik C Fau - Papapoulos, S. & Papapoulos, S. Farnesyl pyrophosphate synthase is the molecular target of nitrogen-containing bisphosphonates. (1999).

149. Coxon, F.P*., et al.* Protein geranylgeranylation is required for osteoclast formation, function, and survival: inhibition by bisphosphonates and GGTI-298. (2000).

150. Zhang, D*., et al.* The small GTP-binding protein, rho p21, is involved in bone resorption by regulating cytoskeletal organization in osteoclasts. (1995).

151. Li, B., Ling Chau, J.F., Wang, X. & Leong, W.F. Bisphosphonates, specific inhibitors of osteoclast function and a class of drugs for osteoporosis therapy. *J Cell Biochem* **112**, 1229-1242 (2011).

152. Shipman, C.M., Croucher, P.I., Russell, R.G., Helfrich, M.H. & Rogers, M.J. The bisphosphonate incadronate (YM175) causes apoptosis of human myeloma cells in vitro by inhibiting the mevalonate pathway. *Cancer Res* **58**, 5294-5297 (1998).

153. Senaratne, S.G., Pirianov, G., Mansi, J.L., Arnett, T.R. & Colston, K.W. Bisphosphonates induce apoptosis in human breast cancer cell lines. *Br J Cancer* **82**, 1459-1468 (2000).

154. Lee, M.V., Fong, E.M., Singer, F.R. & Guenette, R.S. Bisphosphonate treatment inhibits the growth of prostate cancer cells. *Cancer Res* **61**, 2602-2608 (2001).

155. Zekri, J., Mansour, M. & Karim, S.M. The anti-tumour effects of zoledronic acid. *J Bone Oncol* **3**, 25-35 (2014).

156. Roelofs, A.J., Thompson, K., Gordon, S. & Rogers, M.J. Molecular mechanisms of action of bisphosphonates: current status. *Clin Cancer Res* **12**, 6222s-6230s (2006).

157. Green, J.R. Antitumor effects of bisphosphonates. *Cancer* **97**, 840-847 (2003).

158. Wood, J.*, et al.* Novel antiangiogenic effects of the bisphosphonate compound zoledronic acid. (2002).

159. Skerjanec, A.*, et al.* The pharmacokinetics and pharmacodynamics of zoledronic acid in cancer patients with varying degrees of renal function. *J Clin Pharmacol* **43**, 154-162 (2003).

160. Weiss, H.M.*, et al.* Biodistribution and plasma protein binding of zoledronic acid. *Drug Metab Dispos* **36**, 2043-2049 (2008).

161. Sasaki, A.*, et al.* Bisphosphonate risedronate reduces metastatic human breast cancer burden in bone in nude mice. *Cancer Res* **55**, 3551-3557 (1995).

162. Hiraga, T., Williams, P.J., Mundy, G.R. & Yoneda, T. The bisphosphonate ibandronate promotes apoptosis in MDA-MB-231 human breast cancer cells in bone metastases. *Cancer Res* **61**, 4418-4424 (2001).

163. Kakonen, S.M. & Mundy, G.R. Mechanisms of osteolytic bone metastases in breast carcinoma. *Cancer* **97**, 834-839 (2003).

164. Matsumoto, T. & Abe, M. Bone destruction in multiple myeloma. *Ann N Y Acad Sci* **1068**, 319-326 (2006).

165. Gordon, S.*, et al.* Pamidronate causes apoptosis of plasma cells in vivo in patients with multiple myeloma. *Br J Haematol* **119**, 475-483 (2002).

166. Brewer, J.W. & Hendershot, L.M. Building an antibody factory: a job for the unfolded protein response. *Nat Immunol* **6**, 23-29 (2005).

167. Malhotra, J.D. & Kaufman, R.J. The endoplasmic reticulum and the unfolded protein response. *Semin Cell Dev Biol* **18**, 716-731 (2007).

168. Vincenz, L., Jager, R., O'Dwyer, M. & Samali, A. Endoplasmic reticulum stress and the unfolded protein response: targeting the Achilles heel of multiple myeloma. *Mol Cancer Ther* **12**, 831-843 (2013).

169. Holstein, S.A. & Hohl, R.J. Isoprenoid biosynthetic pathway inhibition disrupts monoclonal protein secretion and induces the unfolded protein response pathway in multiple myeloma cells. (2011).

170. Lin, J.H. Bisphosphonates: a review of their pharmacokinetic properties. (1996).

171. Corso, A.*, et al.* A different schedule of zoledronic acid can reduce the risk of the osteonecrosis of the jaw in patients with multiple myeloma. *Leukemia* **21**, 1545 (2007).

172. Siegel, R.L., Miller, K.D. & Jemal, A. Cancer Statistics, 2017. *CA Cancer J Clin* **67**, 7-30 (2017).

173. Kawano, Y.*, et al.* Targeting the bone marrow microenvironment in multiple myeloma. *Immunol Rev* **263**, 160-172 (2015).

174. Giuliani, N., Bataille, R., Mancini, C., Lazzaretti, M. & Barille, S. Myeloma cells induce imbalance in the osteoprotegerin/osteoprotegerin ligand system in the human bone marrow environment. *Blood* **98**, 3527-3533 (2001).

175. Roodman, G.D. Pathogenesis of myeloma bone disease. *Leukemia* **23**, 435-441 (2009).

176. Evans, C.E., Ward C Fau - Rathour, L., Rathour L Fau - Galasko, C.B. & Galasko, C.B. Myeloma affects both the growth and function of human osteoblast-like cells. (1992).

177. Kristensen, I.B.*, et al.* Expression of osteoblast and osteoclast regulatory genes in the bone marrow microenvironment in multiple myeloma: only up-regulation of Wnt inhibitors SFRP3 and DKK1 is associated with lytic bone disease. (2013).

178. Galson, D.L., Silbermann, R. & Roodman, G.D. Mechanisms of multiple myeloma bone disease. *Bonekey Rep* **1**, 135 (2012).

179. Terpos, E.*, et al.* Circulating activin-A is elevated in patients with advanced multiple myeloma and correlates with extensive bone involvement and inferior survival; no alterations post-lenalidomide and dexamethasone therapy. (2012).

180. Harada, S. & Rodan, G.A. Control of osteoblast function and regulation of bone mass. *Nature* **423**, 349-355 (2003).

181. Yun, T.J.*, et al.* Osteoprotegerin, a crucial regulator of bone metabolism, also regulates B cell development and function. (2001).

182. Marulanda, J., Gao, C., Roman, H., Henderson, J.E. & Murshed, M. Prevention of arterial calcification corrects the low bone mass phenotype in MGP-deficient mice. *Bone* **57**, 499-508 (2013).

183. Soleimani, M. & Nadri, S. A protocol for isolation and culture of mesenchymal stem cells from mouse bone marrow. *Nat Protoc* **4**, 102-106 (2009).

184. Schneider, C.A., Rasband, W.S. & Eliceiri, K.W. NIH Image to ImageJ: 25 years of image analysis. *Nat Methods* **9**, 671-675 (2012).

185. Dobin, A.*, et al.* STAR: ultrafast universal RNA-seq aligner. *Bioinformatics* **29**, 15-21 (2013).

186. Love, M.I., Huber, W. & Anders, S. Moderated estimation of fold change and dispersion for RNA-seq data with DESeq2. *Genome Biol* **15**, 550 (2014).

187. Luo, W., Friedman, M.S., Shedden, K., Hankenson, K.D. & Woolf, P.J. GAGE: generally applicable gene set enrichment for pathway analysis. *BMC Bioinformatics* **10**, 161 (2009).

188. Gu, Z., Eils, R. & Schlesner, M. Complex heatmaps reveal patterns and correlations in multidimensional genomic data. *Bioinformatics* **32**, 2847-2849 (2016).

189. Bordini, J.*, et al.* Erythroblast apoptosis and microenvironmental iron restriction trigger anemia in the VK*MYC model of multiple myeloma. *Haematologica* **100**, 834-841 (2015).

190. Chang, J.*, et al.* NF-kappaB inhibits osteogenic differentiation of mesenchymal stem cells by promoting beta-catenin degradation. *Proc Natl Acad Sci U S A* **110**, 9469-9474 (2013).

191. Radl J Fau - Hollander, C.F., Hollander Cf Fau - van den Berg, P., van den Berg P Fau - de Glopper, E. & de Glopper, E. Idiopathic paraproteinaemia. I. Studies in an animal model--the ageing C57BL/KaLwRij mouse. *Clinical and Experimental Immunology* **33(3)**, 395-402 (1978).

192. Terpos, E. & Dimopoulos, M.A. Interaction between the skeletal and immune systems in cancer: mechanisms and clinical implications. *Cancer Immunology, Immunotherapy* (2011).

193. Garrett, I.R., Dallas, S., Radl, J. & Mundy, G.R. A murine model of human myeloma bone disease. *Bone* **20**, 515-520 (1997).

194. Buckle, C.H., *et al.* Soluble rank ligand produced by myeloma cells causes generalised bone loss in multiple myeloma. *PLoS One* **7**, e41127 (2012).

195. Li, Y., *et al.* B cells and T cells are critical for the preservation of bone homeostasis and attainment of peak bone mass in vivo. *Blood* **109**, 3839-3848 (2007).

196. Qiang, Y.-W., Shaughnessy, J.D. & Yaccoby, S. Wnt3a signaling within bone inhibits multiple myeloma bone disease and tumor growth. *Blood* **112**, 374-382 (2008).

197. Osta, B., Benedetti, G. & Miossec, P. Classical and Paradoxical Effects of TNF-alpha on Bone Homeostasis. *Front Immunol* **5**, 48 (2014).

198. Algate, K., Haynes, D.R., Bartold, P.M., Crotti, T.N. & Cantley, M.D. The effects of tumour necrosis factor-alpha on bone cells involved in periodontal alveolar bone loss; osteoclasts, osteoblasts and osteocytes. *J Periodontal Res* **51**, 549-566 (2016).

199. Shinoda, Y., *et al.* Regulation of bone formation by adiponectin through autocrine/paracrine and endocrine pathways. *J Cell Biochem* **99**, 196-208 (2006).

200. Thirunavukkarasu, K., *et al.* Stimulation of osteoprotegerin (OPG) gene expression by transforming growth factor-beta (TGF-beta). Mapping of the OPG promoter region that mediates TGF-beta effects. *J Biol Chem* **276(39)**, 36241-36250 (2001).

201. Fournier, P.G., Stresing V Fau - Ebetino, F.H., Ebetino Fh Fau - Clezardin, P. & Clezardin, P. How do bisphosphonates inhibit bone metastasis in vivo? (2010).

202. Nguyen, U.T., *et al.* Analysis of the eukaryotic prenylome by isoprenoid affinity tagging. *Nat Chem Biol* **5**, 227-235 (2009).

203. Kho, Y., *et al.* A tagging-via-substrate technology for detection and proteomics of farnesylated proteins. *Proc Natl Acad Sci U S A* **101**, 12479-12484 (2004).

204. Stark, J.L., *et al.* Structure and function of human DnaJ homologue subfamily a member 1 (DNAJA1) and its relationship to pancreatic cancer. *Biochemistry* **53**, 1360-1372 (2014).

205. Kampinga, H.H. & Craig, E.A. The HSP70 chaperone machinery: J proteins as drivers of functional specificity. (2010).

206. Young, S.G., Fong Lg Fau - Michaelis, S. & Michaelis, S. Prelamin A, Zmpste24, misshapen cell nuclei, and progeria--new evidence suggesting that protein farnesylation could be important for disease pathogenesis. (2005).

207. Takai, Y., Sasaki, T. & Matozaki, T. Small GTP-binding proteins. *Physiol Rev* **81**, 153-208 (2001).

208. Mullen, P.J., Yu, R., Longo, J., Archer, M.C. & Penn, L.Z. The interplay between cell signalling and the mevalonate pathway in cancer. (2016).

209. Clendening, J.W.*, et al.* Dysregulation of the mevalonate pathway promotes transformation. *Proc Natl Acad Sci U S A* **107**, 15051-15056 (2010).

210. Sorrentino, G.*, et al.* Metabolic control of YAP and TAZ by the mevalonate pathway. *Nat Cell Biol* **16**, 357-366 (2014).

211. Nielsen Sf Fau - Nordestgaard, B.G.*, et al.* Statin use and reduced cancer-related mortality. (2013).

212. Garwood, E.R.*, et al.* Fluvastatin reduces proliferation and increases apoptosis in women with high grade breast cancer. *Breast Cancer Res Treat* **119**, 137-144 (2010).

213. Kubatka, P., Kruzliak, P., Rotrekl, V., Jelinkova, S. & Mladosievicova, B. Statins in oncological research: from experimental studies to clinical practice. *Crit Rev Oncol Hematol* **92**, 296-311 (2014).

214. Sanfilippo, K.M.*, et al.* Statins Are Associated With Reduced Mortality in Multiple Myeloma. *J Clin Oncol* **34**, 4008-4014 (2016).

215. Dunford, J.E. Molecular targets of the nitrogen containing bisphosphonates: the molecular pharmacology of prenyl synthase inhibition. *Curr Pharm Des* **16**, 2961-2969 (2010).

216. Ebetino, F.H.*, et al.* The relationship between the chemistry and biological activity of the bisphosphonates. (2011).

217. Coleman, R.E.*, et al.* Breast-cancer adjuvant therapy with zoledronic acid. (2011).

218. Gnant, M.*, et al.* Adjuvant endocrine therapy plus zoledronic acid in premenopausal women with early-stage breast cancer: 62-month follow-up from the ABCSG-12 randomised trial. *Lancet Oncol* **12**, 631-641 (2011).

219. Gnant, M.*, et al.* Endocrine therapy plus zoledronic acid in premenopausal breast cancer. *N Engl J Med* **360**, 679-691 (2009).

220. Coleman, R.*, et al.* Zoledronic acid (zoledronate) for postmenopausal women with early breast cancer receiving adjuvant letrozole (ZO-FAST study): final 60-month results. *Ann Oncol* **24**, 398-405 (2013).

221. Morgan, G.J.*, et al.* Effects of induction and maintenance plus long-term bisphosphonates on bone disease in patients with multiple myeloma: the Medical Research Council Myeloma IX Trial. *Blood* **119**, 5374-5383 (2012).

222. Jahnke, W.*, et al.* Allosteric non-bisphosphonate FPPS inhibitors identified by fragment-based discovery. *Nat Chem Biol* **6**, 660-666 (2010).

223. De Schutter, J.W.*, et al.* Multistage screening reveals chameleon ligands of the human farnesyl pyrophosphate synthase: implications to drug discovery for neurodegenerative diseases. *J Med Chem* **57**, 5764-5776 (2014).

224. Marzinzik, A.L.*, et al.* Discovery of Novel Allosteric Non-Bisphosphonate Inhibitors of Farnesyl Pyrophosphate Synthase by Integrated Lead Finding. *ChemMedChem* **10**, 1884-1891 (2015).

225. Park, J.*, et al.* Pharmacophore Mapping of Thienopyrimidine-Based Monophosphonate (ThP-MP) Inhibitors of the Human Farnesyl Pyrophosphate Synthase. *J Med Chem* **60**, 2119-2134 (2017).

226. Lobell, R.B.*, et al.* Preclinical and clinical pharmacodynamic assessment of L-778,123, a dual inhibitor of farnesyl:protein transferase and geranylgeranyl:protein transferase type-I. *Mol Cancer Ther* **1**, 747-758 (2002).

227. Martin, N.E.*, et al.* A phase I trial of the dual farnesyltransferase and geranylgeranyltransferase inhibitor L-778,123 and radiotherapy for locally advanced pancreatic cancer. *Clin Cancer Res* **10**, 5447-5454 (2004).

228. Yokoyama, K., Zimmerman, K., Scholten, J. & Gelb, M.H. Differential prenyl pyrophosphate binding to mammalian protein geranylgeranyltransferase-I and protein farnesyltransferase and its consequence on the specificity of protein prenylation. *J Biol Chem* **272**, 3944-3952 (1997).

229. Rowinsky, E.K. Lately, it occurs to me what a long, strange trip it's been for the farnesyltransferase inhibitors. (2006).

230. Zhang, Y.*, et al.* Lipophilic pyridinium bisphosphonates: potent gammadelta T cell stimulators. *Angew Chem Int Ed Engl* **49**, 1136-1138 (2010).

231. Zhang, Y.*, et al.* Lipophilic bisphosphonates as dual farnesyl/geranylgeranyl diphosphate synthase inhibitors: an X-ray and NMR investigation. (2009).

232. Shull, L.W., Wiemer, A.J., Hohl, R.J. & Wiemer, D.F. Synthesis and biological activity of isoprenoid bisphosphonates. *Bioorg Med Chem* **14**, 4130-4136 (2006).

233. Wills, V.S., Allen, C., Holstein, S.A. & Wiemer, D.F. Potent Triazole Bisphosphonate Inhibitor of Geranylgeranyl Diphosphate Synthase. (2015).

234. Wills, V.S.*, et al.* Bishomoisoprenoid triazole bisphosphonates as inhibitors of geranylgeranyl diphosphate synthase. (2017).

235. Guenther, A.*, et al.* The bisphosphonate zoledronic acid has antimyeloma activity in vivo by inhibition of protein prenylation. (2010).

236. J. Kent Barbay, D.C., Brian Christopher Shook, Aihua Wang Methylene amines of thieno [2,3-d] pyrimidine and their use as adenosine a2a receptor antagonists. *WO 2010/045006 A1*.

237. Liebeskind, L.S. & Srogl, J. Heteroaromatic thioether-boronic acid cross-coupling under neutral reaction conditions. *Org Lett* **4**, 979-981 (2002).

238. Leung, C.Y., Langille, A.M., Mancuso, J. & Tsantrizos, Y.S. Discovery of thienopyrimidine-based inhibitors of the human farnesyl pyrophosphate synthase--parallel synthesis of analogs via a trimethylsilyl ylidene intermediate. (2013).

239. Leung, C.Y.*, et al.* Thienopyrimidine bisphosphonate (ThPBP) inhibitors of the human farnesyl pyrophosphate synthase: optimization and characterization of the mode of inhibition. *J Med Chem* **56**, 7939-7950 (2013).

240. Wetzel, M., Marchais-Oberwinkler, S. & Hartmann, R.W. 17beta-HSD2 inhibitors for the treatment of osteoporosis: Identification of a promising scaffold. *Bioorg Med Chem* **19**, 807-815 (2011).

241. Kavanagh, K.L., Dunford, J.E., Bunkoczi, G., Russell, R.G. & Oppermann, U. The crystal structure of human geranylgeranyl pyrophosphate synthase reveals a novel hexameric arrangement and inhibitory product binding. *J Biol Chem* **281**, 22004-22012 (2006).

242. Trott, O. & Olson, A.J. AutoDock Vina: improving the speed and accuracy of docking with a new scoring function, efficient optimization, and multithreading. *J Comput Chem* **31**, 455-461 (2010).

243. Ghassabian, S., Wright La Fau - Dejager, A.D., Dejager Ad Fau - Smith, M.T. & Smith, M.T. Development and validation of a sensitive solid-phase-extraction (SPE) method using high-performance liquid chromatography/tandem mass spectrometry (LC-MS/MS) for determination of risedronate concentrations in human plasma. (2012).

244. For details on the characterization of MM cell lines, refer to Keats Lab website: http://www.keatslab.org/projects/mm-cell-line-characterization/cell-line-characterization-status.

245. Hideshima, T.*, et al.* p53-related protein kinase confers poor prognosis and represents a novel therapeutic target in multiple myeloma. (2017).

246. Jagdev, S.P., Coleman, R.E., Shipman, C.M., Rostami, H.A. & Croucher, P.I. The bisphosphonate, zoledronic acid, induces apoptosis of breast cancer cells: evidence for synergy with paclitaxel. *Br J Cancer* **84**, 1126-1134 (2001).

247. Fujita, M.*, et al.* Involvement of the mevalonate pathway in the antiproliferative effect of zoledronate on ACHN renal cell carcinoma cells. *Oncol Rep* **27**, 1371-1376 (2012).

248. Okamoto, S.*, et al.* Zoledronic acid induces apoptosis and S-phase arrest in mesothelioma through inhibiting Rab family proteins and topoisomerase II actions. (2014).

249. van de Donk, N.W., Lokhorst, H.M., Nijhuis, E.H., Kamphuis, M.M. & Bloem, A.C. Geranylgeranylated proteins are involved in the regulation of myeloma cell growth. *Clin Cancer Res* **11**, 429-439 (2005).

250. The Cancer Cell Line Encyclopedia and Genomics of Drug Sensitivity in Cancer Investigators. Pharmacogenomic agreement between two cancer cell line data sets. *Nature* 84-87 (2015).

251. Lonial, S.*, et al.* Interim Analysis of the Mmrf Commpass Trial: Identification of Novel Rearrangements Potentially Associated with Disease Initiation and Progression. *Blood* **124**, 722 (2014).

252. Keats, J.J.*, et al.* Molecular Predictors of Outcome and Drug Response in Multiple Myeloma: An Interim Analysis of the Mmrf CoMMpass Study. *Blood* **128**, 194 (2016).

253. Van Beek, E.R., Lowik Cw Fau - Papapoulos, S.E. & Papapoulos, S.E. Bisphosphonates suppress bone resorption by a direct effect on early osteoclast precursors without affecting the osteoclastogenic capacity of osteogenic cells: the role of protein geranylgeranylation in the action of nitrogen-containing bisphosphonates on osteoclast precursors. (2002).

254. Jahnke, W. & Henry, C. An in vitro assay to measure targeted drug delivery to bone mineral. *ChemMedChem* **5**, 770-776 (2010).

255. Chesi, M.*, et al.* Drug response in a genetically engineered mouse model of multiple myeloma is predictive of clinical efficacy. (2012).

256. Gomez-Palou, M.F., H.; Kremer, R.; Sebag, M. A transgenic model of multiple myeloma bone disease shows profound mesenchymal stem cell impairment. *Blood* **112**(2013).

257. Vieira, P. & Rajewsky, K. The half-lives of serum immunoglobulins in adult mice. *Eur J Immunol* **18**, 313-316 (1988).

258. Van Acker, H.H., Anguille, S., Willemen, Y., Smits, E.L. & Van Tendeloo, V.F. Bisphosphonates for cancer treatment: Mechanisms of action and lessons from clinical trials. *Pharmacol Ther* **158**, 24-40 (2016).

259. Corso, A.*, et al.* Zoledronic acid down-regulates adhesion molecules of bone marrow stromal cells in multiple myeloma: a possible mechanism for its antitumor effect. *Cancer* **104**, 118-125 (2005).

260. van de Donk, N.W., Kamphuis, M.M., van Kessel, B., Lokhorst, H.M. & Bloem, A.C. Inhibition of protein geranylgeranylation induces apoptosis in myeloma plasma cells by reducing Mcl-1 protein levels. *Blood* **102**, 3354-3362 (2003).

261. van der Spek, E. Targeting the mevalonate pathway in multiple myeloma. *Leuk Res* **34**, 267-268 (2010).

262. Zhang, F.L. & Casey, P.J. Protein prenylation: molecular mechanisms and functional consequences. *Annu Rev Biochem* **65**, 241-269 (1996).

263. Pandyra, A.A.*, et al.* Genome-wide RNAi analysis reveals that simultaneous inhibition of specific mevalonate pathway genes potentiates tumor cell death. *Oncotarget* **6**, 26909-26921 (2015).

264. Clendening, J.W.*, et al.* Exploiting the mevalonate pathway to distinguish statin-sensitive multiple myeloma. *Blood* **115**, 4787-4797 (2010).

265. Ural, A.U.*, et al.* The bisphosphonate zoledronic acid induces cytotoxicity in human myeloma cell lines with enhancing effects of dexamethasone and thalidomide. *Int J Hematol* **78**, 443-449 (2003).

266. Lacbay, C.M.*, et al.* Unraveling the Prenylation-Cancer Paradox in Multiple Myeloma with Novel Geranylgeranyl Pyrophosphate Synthase (GGPPS) Inhibitors. *J Med Chem* (2018).

267. Takeda, Y.*, et al.* Geranylgeraniol, an intermediate product in mevalonate pathway, induces apoptotic cell death in human hepatoma cells: death receptor-independent activation of caspase-8 with down-regulation of Bcl-xL expression. *Jpn J Cancer Res* **92**, 918-925 (2001).

268. Dull, T.*, et al.* A third-generation lentivirus vector with a conditional packaging system. *J Virol* **72**, 8463-8471 (1998).

269. Sanjana, N.E., Shalem, O. & Zhang, F. Improved vectors and genome-wide libraries for CRISPR screening. *Nature methods* **11**, 783-784 (2014).

270. Shalem, O.*, et al.* Genome-scale CRISPR-Cas9 knockout screening in human cells. *Science* **343**, 84-87 (2014).

271. Steinbrunn, T., Chatterjee, M., Bargou, R.C. & Stuhmer, T. Efficient transient transfection of human multiple myeloma cells by electroporation--an appraisal. *PLoS One* **9**, e97443 (2014).

272. Nussbaumer, O.*, et al.* Essential requirements of zoledronate-induced cytokine and gammadelta T cell proliferative responses. *J Immunol* **191**, 1346-1355 (2013).

273. Coxon, F.P., Thompson, K. & Rogers, M.J. Recent advances in understanding the mechanism of action of bisphosphonates. *Curr Opin Pharmacol* **6**, 307-312 (2006).